Western Graduate&PostdoctoralStudies

Western University
Scholarship@Western

Electronic Thesis and Dissertation Repository

10-26-2018 2:30 PM

Pressure Tuning Of Energy Storage Materials Probed By In-situ Vibrational Spectroscopy And Synchrotron Radiation

Pan Wang
The University of Western Ontario

Supervisor
Song, Yang
The University of Western Ontario

Graduate Program in Chemistry
A thesis submitted in partial fulfillment of the requirements for the degree in Doctor of Philosophy
© Pan Wang 2018

Follow this and additional works at: https://ir.lib.uwo.ca/etd

Part of the Analytical Chemistry Commons, Inorganic Chemistry Commons, and the Materials Chemistry Commons

Recommended Citation

Wang, Pan, "Pressure Tuning Of Energy Storage Materials Probed By In-situ Vibrational Spectroscopy And Synchrotron Radiation" (2018). *Electronic Thesis and Dissertation Repository*. 5823.
https://ir.lib.uwo.ca/etd/5823

This Dissertation/Thesis is brought to you for free and open access by Scholarship@Western. It has been accepted for inclusion in Electronic Thesis and Dissertation Repository by an authorized administrator of Scholarship@Western. For more information, please contact wlswadmin@uwo.ca.

www.manaraa.com

Abstract

Clean and renewable energy has drawn much attention recently due to the increasing demand for more energy and environmental issues. New materials have been developed and the improved performance of such materials have been achieved in the past decades. It has been proved that application of external high pressure can significantly tune the structure of materials. Consequently, the properties of the materials could also be modified. Therefore, in this thesis, we focused on the high-pressure studies of two classes of energy storage materials, hydrogen storage materials and solar cell materials. Ammonia borane (AB) has been extensively investigated as an excellent hydrogen storage material, and abundant derivatives of AB with lower dehydrogenation temperatures and better kinetics have been obtained. Three AB derivatives, sodium amidoborane (NaAB), hydrazine borane (HB), and ethane 1,2-diamineborane (EDAB) have been studied under high pressure for the first time using *in-situ* vibrational spectroscopy and synchrotron X-ray diffraction. Structural transformations and interactions between molecules in the crystals have been explored for all three materials. It was also found that the ionic interaction, dihydrogen bonding and hydrogen bonding existing between the molecules in the crystals, which stabilize the crystal structures and may play an important role in the process of the dehydrogenation of materials. Significantly, our studies could also be a guidance for the designing of the new hydrogen storage material by substituting the hydrogen atoms on either B or N atoms to modify the reactivity of B-H and N-H bonds. Formamidinium lead iodide ($FAPbI_3$) perovskite as a superior solar cell material was investigated under high pressure using in situ synchrotron X-ray diffraction, FTIR spectroscopy, photoluminescence (PL) spectroscopy, electrical conductivity (EC) measurements, and ab initio calculations. Structural stabilities of two polymorphs of $FAPbI_3$ and the interactions between organic and inorganic moieties have been explored on compression, and pressure tuned optoelectric properties of $FAPbI_3$ were also studied. Moreover, our investigation thus provides valuable insight into the design and engineering of organolead halide perovskite-based solar cell materials. Overall, our high-pressure studies of energy storage materials could provide the insight into the pressure-tuned structures and properties of the materials.

www.manaraa.com

Keywords

Organo-lead halide Perovskite, hydrogen storage materials, sodium amidoborane, hydrazine borane, ethane 1,2-diamineborane, high pressure, synchrotron radiation, vibrational spectroscopy, phase transitions, hydrogen bonding

www.manaraa.com

Co-Authorship Statement

This thesis contains materials from previously published manuscript authored by Pan Wang and co-authored or edited by others mentioned below. Dr. Yang Song is the corresponding author on the presented paper and is responsible for the supervision of Pan Wang over the course of his Ph.D. study. He also played a major role in the editing and revision of the materials presented in all chapters.

In chapter 3, Dr. Yansun Yao did the theoretical calculations about the high-pressure structures of sodium amidoborane. Nilesh Shinde collected the synchrotron XRD patterns in APS. Pan Wang is responsible for the synthesis of the material, data collection of vibrational spectroscopy and data analysis.

In chapter 4 and 5, Pan Wang is responsible for the sample preparation, data collection and data analysis. The IR and Raman measurements were performed in Dr. Song's lab; the Synchrotron XRD patters were collected in APS.

Chapter 6 is from the publication authored by Pan Wang, Jiwen Guan, Draven T. K. Galeschuk, Yansun Yao, Cindy F. He, Shan Jiang, Sijia Zhang, Ying Liu, Meiling Jin, Changqing Jin, and Yang Song (J. Phys. Chem. Lett. 2017, 8, 2119−2125). Pan Wang and Cindy F. He are responsible for the synthesis of the samples and IR and PL measurements. Synchrotron XRD patters were collected by Pan Wang, Jiwen Guan and Shan Jiang in APS. Draven T. K. Galeschuk and Dr. Yansun Yao performed all the calculations. Sijia Zhang, Ying Liu, Meiling Jin, Changqing Jin performed the Electrical resistance measurements in Institute of Physics, Chinese Academy of Sciences, Beijing. All data analysis was done by Pan Wang except for the Band structures and projected DOS of $FAPbI_3$, which was performed by Dr. Yansun Yao and Dr. Yang Song.

I am aware of the University of Western Ontario Policy on Authorship, and I certify that I have properly acknowledged the contribution of other researchers to my thesis.

www.manaraa.com

Acknowledgments

First and foremost, I would like to express my great gratitude to my supervisor Prof. Yang Song. My Ph.D. study would not have been possible without his exceptional supervision, patient guidance and inspiring advice. I am truly grateful to study and work under his supervision.

I would like to thank Dr. T. K. Sham, Dr. Yining Huang, Dr. François Lagugné-Labarthet, Dr. Yang Song and Dr. Paul D. Boyle for their excellent graduate courses. Also, I would like to thank Jan Mathers, Sandra Zakaria Holtslag, and Susan England in First Year Chemistry Lab, whom I spent lots of time working with, and it was the greatest experience I ever had. Also, I appreciate all the input from my collaborators, Draven T. K. Galeschuk and Dr. Yansun Yao (University of Saskatchewan), Sijia Zhang, Ying Liu, Meiling Jin and Dr. Changqing Jin (Institute of Physics, Chinese Academy of Sciences). I would also like to thank the beamline scientists in APS, Dr. Zou Finfrock and Dr. ChangYong Park for their help and technical support.

I would also like to thank all my group members: Dr. Jiwen Guan, Miss. Shan Jiang, Miss. Fengping Xiao, Miss. Cindy F. He and Mr. Heng Xiang. They have been providing great help to me since the start of my graduate study. Four years company makes them my lifetime friends.

I would like to thank my good friends in Western, Dr. Nazhen Liu, Dr. Jun Li, Miss. Mengnan Guo, Mr. Zitong Wang, Mr. Yue Zhang, Mr. Dan Guo, Miss. Mi Li, Mr. Jiatang Chen and Mr. Shoushun Chen. It is you who drive my loneliness away and leave me a colorful and joyful Canadian life.

Finally, I would like to give my special thanks to my parents and all the members of my family. Thanks for your unconditional love, support and understanding in the last four years.

www.manaraa.com

Table of Contents

Abstract i

Co-Authorship Statement iii

Acknowledgments iv

Table of Contents v

List of Tables x

List of Figures xii

List of Abbreviations xix

Chapter 1 1

1 Introduction 1

1.1 Energy storage materials 1

1.1.1 Energy source 1

1.1.2 Hydrogen storage materials 2

1.1.3 Perovskite solar cell materials 4

1.2 High-pressure science 8

1.2.1 High-pressure phenomena 8

1.2.2 High-pressure chemistry 8

1.3 High-pressure studies on energy storage materials 9

1.3.1 High-pressure studies on hydrogen storage materials 9

1.3.2 High-pressure studies on perovskite solar cell materials 12

1.4 Motivation and outline of the thesis 15

1.5 References 16

Chapter 2 35

2 Experimental 35

www.manaraa.com

2.1 Materials preparation 35

2.1.1 Mechanochemistry and ball milling synthetic method 35

2.1.2 Wet chemistry method 36

2.2 High-pressure apparatus 36

2.2.1 Diamond anvil cells 36

2.2.2 Pressure gauge 38

2.2.3 Pressure transmitting medium 39

2.3 *In-situ* high-pressure characterizations 40

2.3.1 Vibrational spectroscopy 40

2.3.2 IR spectroscopy system 42

2.3.3 Raman spectroscopy system 43

2.3.4 Photoluminescence spectroscopy 44

2.3.5 Synchrotron X-ray diffraction 45

2.3.6 Structural refinement 48

2.4 References 49

Chapter 3 52

3 Pressure-induced phase transitions and evolution of dihydrogen bonding in sodium amidoborane by *in-situ* vibrational spectroscopy and synchrotron X-ray diffraction . 52

3.1 Introduction 52

3.2 Experimental 53

3.2.1 Materials and methods 53

3.2.2 Powder X-ray diffraction 54

3.2.3 In-situ high-pressure FTIR spectroscopy 54

3.2.4 In-situ high-pressure Raman spectroscopy 54

3.2.5 In-situ high-pressure X-ray diffraction 55

3.3 Results and discussion 55

www.manaraa.com

3.3.1 XRD pattern of NaAB under ambient pressure 55

3.3.2 Raman and IR spectra of NaAB under ambient pressure 57

3.3.3 In-situ high-pressure IR spectroscopy 60

3.3.4 In-situ high-pressure Raman spectroscopy 63

3.3.5 Pressure effects on IR and Raman modes 65

3.3.6 In-situ Synchrotron X-ray diffraction 68

3.3.7 Discussion 74

3.4 Conclusions 75

3.5 References 76

Chapter 4 81

4 Pressure effects on structure and dihydrogen bonding in hydrazine borane probed by *in- situ* vibrational spectroscopy and synchrotron X-ray diffraction 81

4.1 Introduction 81

4.2 Experimental 83

4.2.1 Synthesis of hydrazine borane 83

4.2.2 Powder X-ray diffraction 83

4.2.3 In-situ FTIR spectroscopy 84

4.2.4 In-situ Raman spectroscopy 84

4.2.5 In-situ synchrotron X-ray diffraction 84

4.3 Results and Discussion 84

4.3.1 XRD pattern under ambient conditions 84

4.3.2 IR and Raman spectra under ambient conditions 87

4.3.3 IR spectra under high pressure 89

4.3.4 Raman spectra under high pressure 94

4.3.5 Synchrotron XRD patterns under high pressure 98

4.3.6 Discussion 104

www.manaraa.com

4.4 Conclusions 105

4.5 References 105

Chapter 5 111

5 High-pressure structural study of ethane 1,2-diamineborane using in-situ vibrational spectroscopy and synchrotron X-ray diffraction and insight into dihydrogen bonding 111

5.1 Introduction 111

5.2 Materials and Characterizations 112

5.2.1 Materials and preparation 112

5.2.2 Powder X-ray diffraction 113

5.2.3 In-situ FTIR spectroscopy 113

5.2.4 In-situ Raman spectroscopy 113

5.2.5 In-situ synchrotron X-ray diffraction 113

5.3 Results and discussions 114

5.3.1 XRD pattern under ambient conditions 114

5.3.2 IR and Raman spectra under ambient conditions 114

5.3.3 IR spectra under high pressure 118

5.3.4 Raman spectra under high pressure 123

5.3.5 Synchrotron XRD patterns under high pressure 129

5.3.6 Discussion 134

5.4 Conclusions 134

5.5 References 135

Chapter 6 142

6 Pressure-induced polymorphic, optical and electronic transitions of formamidinium lead Iodide perovskite 142

6.1 Introduction 142

6.2 Experimental 143

www.manaraa.com

6.2.1 Materials 143
6.2.2 Powder X-ray diffraction 144
6.2.3 In situ high-pressure X-ray diffraction 144
6.2.4 FTIR spectroscopy 144
6.2.5 Photoluminescence measurements 145
6.2.6 Electrical conductivity measurements 145
6.2.7 Computational Methods 146
6.3 Results and discussion 146
6.3.1 XRD analysis of $FAPbI_3$ 146
6.3.2 IR analysis of $FAPbI_3$ 155
6.3.3 Optical response of $FAPbI_3$ 163
6.3.4 Electrical measurements of $FAPbI_3$ 168
6.4 Conclusions and Summary 171
6.5 References 172
Chapter 7 177
7 Summary and future work 177
7.1 Summary 177
7.2 Future work 179
7.3 References 179
Appendix A Refinement results of NaAB 181
Appendix B Refinement results of HB 185
Appendix C Refinement results of EDAB 193
Appendix D Copyright Permission 196
Curriculum Vitae 197

www.manaraa.com

List of Tables

Table 1.1 Summary of most investigated perovskite materials 7

Table 1.2 Summary of selected high-pressure studies on hydrogen storage materials[34]..... 11

Table 1.3 The recent high-pressure studies on perovskite solar cell materials..... 14

Table 2.1 The common PTMs and their highest pressure maintaining the hydrostatic condition[14-15] 40

Table 3.1 Assignments and vibrational frequencies of $NaNH_2BH_3$ and NH_3BH_3 at ambient pressure[33]..... 60

Table 3.2 Pressure dependence of vibrational modes of $NaNH_2BH_3$ on compression from IR spectra 67

Table 3.3 Pressure dependence of vibrational modes of $NaNH_2BH_3$ on compression from Raman spectra..... 68

Table 3.4 Unit cell parameters of $NaNH_2BH_3$ at presentative pressures..... 74

Table 4.1 Assignments and vibrational frequencies (cm^{-1}) of HB at ambient pressure[12, 23]... 89

Table 4.2 The pressure dependence of characteristic IR modes of HB on compression..... 94

Table 4.3 The pressure dependence of characteristic Raman modes of HB on compression 95

Table 4.4 Refined cell parameters of HB at presentative pressures 103

Table 5.1 Assignments and vibrational frequencies (cm^{-1}) of EDAB and AB at ambient pressure[25, 36]..... 117

Table 5.2 Pressure dependence of the selected IR modes of EDAB on compression..... 122

Table 5.3 Pressure dependence of the selected Raman modes of EDAB on compression... 127

www.manaraa.com

Table 5.4 Proposed new crystal structures of EDAB on compression and calculated cell parameters of EDAB under different pressures 133

Table 6.1 Unit cell parameters of α-$FAPbI_3$ and δ-$FAPbI_3$ at presentative pressures 150

Table 6.2 Assignment of IR peaks of α-$FAPbI_3$ and δ-$FAPbI_3$ 159

Table 6.3 Pressure dependence of selected IR modes of α-$FAPbI_3$ on compression 161

Table 6.4 Pressure dependence of selected IR modes of δ-$FAPbI_3$ on compression..... 162

www.manaraa.com

List of Figures

Figure 1.1 Crystal structure of cubic halide perovskite and the BX_6^{2-} octahedrons 5

Figure 1.2 Examples of various high-pressure phenomena[68] 9

Figure 1.3 band gap energy of $MAPbBr_3$ (a) and $FAPbI_3$ (b) as a function of pressure[147, 149] 13

Figure 1.4 In situ high-pressure optical micrographs of $FAPbBr_3$ crystal in a DAC[149] 13

Figure 2.1 Photos of Retsch PM 200 planetary ball mill and grinding jars and balls 36

Figure 2.2 The photo of a DAC and a schematic draw of DAC with the diamond anvils enlarged[7] 37

Figure 2.3 Ruby luminescence measured at different pressures (1.5 and 2.1 GPa) with two sharp luminescent peaks (R_1 and R_2)[7] 39

Figure 2.4 Illustration of IR absorption, Rayleigh scattering and Raman scattering 41

Figure 2.5 Schematic diagram of the IR micro-spectroscopy system[17] 43

Figure 2.6 Schematic illustration of the Raman system[7] 44

Figure 2.7 Illustration of the process of Photoluminescence 45

Figure 2.8 Illustration of the emission of synchrotron radiation 47

Figure 2.9 Set up of 20ID at APS. 1, 2, 3 labeled in this figure represent the detector, sample stage and X-ray beam, respectively. 47

Figure 2.10 2D and 1D patterns of CeO_2 collected in APS (λ = 0.4592 Å) 48

Figure 3.1 XRD pattern of $NaNH_2BH_3$ sample under ambient conditions (a) and calculated XRD patterns in comparison with experimental results using Rietveld refinement (b). The purple square and red triangle in (a) represent the plastic wrap and unreacted NaH 56

www.manaraa.com

Figure 3.2 The crystal structure of $NaNH_2BH_3$ under ambient pressure in a unit cell and the coordination of Na atom with one NH_2^- and three BH_3 units..... 57

Figure 3.3 Raman spectra between NH_3BH_3 and $NaNH_2BH_3$ under ambient pressure and room temperature. The inset figure is the lattice modes region for $NaNH_2BH_3$. 58

Figure 3.4 IR spectra between NH_3BH_3 and $NaNH_2BH_3$ under ambient pressure and room temperature. 59

Figure 3.5 IR spectra of NaAB collected at room temperature in the region of 600-3500 cm^{-1}. The peak around 3250 and 3302 cm^{-1} in (b) belongs to the N-H stretching mode of unreacted NH_3BH_3..... 62

Figure 3.6 Raman spectra of NaAB collected at room temperature in the region of 100-3500 cm^{-1}. The peaks around 3255 and 3281 cm^{-1} in (c) belong to the N-H stretching mode of unreacted NH_3BH_3. 64

Figure 3.7 Pressure dependence of selected IR modes of NaAB on compression. The vertical dashed lines indicate the proposed phase boundaries. 66

Figure 3.8 Pressure dependence of selected Raman modes of NaAB on compression. The vertical dashed lines indicate the proposed phase boundaries. 66

Figure 3.9 XRD patterns of $NaNH_2BH_3$ upon compression, the square and triangle symbols at ambient pressure represent the plastic wrap and unreacted NaH..... 70

Figure 3.10 Calculated XRD patterns in comparison with experimental results at 1.75 (a) and 3.27 GPa (c) using Rietveld refinement. Proposed crystal structures of high-pressure phase II (b) and phase III (d) based on MD simulations. 71

Figure 3.11 Enthalpies of several new possible crystal structures for phase III as a function of pressure. Note that the $P2_1/c$ structure always has the lowest enthalpy at high pressure region 72

Figure 3.12 Cell parameters (a) and volume (b) of $NaNH_2BH_3$ as a function of pressure..... 73

www.manaraa.com

Figure 4.1 Indexed XRD pattern of Hydrazine borane under ambient conditions (a) and calculated XRD patterns in comparison with experimental results under ambient conditions using Le Bail refinement (b) 85

Figure 4.2 Structure of HB unit cell and the network of the HB molecules building by dihydrogen bonds and hydrogen bonds (a), an HB molecule with its nearest neighboring molecules (b). The N−H···H−B dihydrogen bonds were indicated by red dashed lines, while the N−H···N classical hydrogen bonds were presented by blue dashed lines. 86

Figure 4.3 Raman and IR spectrum of HB collected at room temperature under ambient pressure 88

Figure 4.4 IR spectra of HB collected at room temperature on compression in the region of 630-3400 cm^{-1}. The pressures in GPa are labeled for each spectrum and the assignments are labeled for selected IR modes. 91

Figure 4.5 Selected IR spectra of HB collected at room temperature on decompression 92

Figure 4.6 Pressure dependence of selected IR modes of HB on compression. Different symbols represent IR modes with different origins. 93

Figure 4.7 Raman spectra of HB collected at room temperature on compression in the region of 50-3400 cm^{-1}. The pressures in GPa are labeled for each spectrum and the assignments are labeled for selected Raman modes. 96

Figure 4.8 Selected Raman spectra of HB collected at room temperature on decompression, the pressures in GPa are labeled for each spectrum. 97

Figure 4.9 Pressure dependence of selected Raman modes of HB on compression. Different symbols represent Raman modes with different origins. 98

Figure 4.10 In-situ high-pressure Synchrotron XRD patterns of HB on compression 99

Figure 4.11 Calculated XRD patterns in comparison with experimental results at 0.82 (a) and 19.68 GPa (b) using Le Bail refinement 100

www.manaraa.com

Figure 4.12 The recovered XRD pattern of HB in comparison with the initial one 101

Figure 4.13 Cell parameters of HB as a function of pressure (a), and experimental cell volume of HB in comparison with calculated result using the third-order Birch–Murnaghan isothermal equation of state upon compression (b). 102

Figure 5.1 XRD pattern of EDAB under ambient conditions (a) and calculated XRD patterns in comparison with experimental results using Rietveld refinement (b) 115

Figure 5.2 Structure of EDAB unit cell 116

Figure 5.3 IR (a) and Raman (b) spectra of EDAB collected at room temperature under ambient pressure, most of the vibrational modes have been assigned and labeled. 118

Figure 5.4 IR spectra of EDAB collected at room temperature on compression in the region of 670-3400 cm^{-1}. The pressures in GPa are labeled for each spectrum, and the assignments are labeled for selected IR modes. * and # represent the appearance of new peaks in phase II and phase III. 120

Figure 5.5 Pressure dependence of selected IR modes of HB on compression. Different symbols represent IR modes with different origins. 121

Figure 5.6 Recovered IR spectrum in comparison with the initial one 123

Figure 5.7 Raman spectra of EDAB collected at room temperature on compression in the region of 250-3300 cm^{-1}. The pressures in GPa are labeled for each spectrum, and the assignments are labeled for selected Raman modes. * and # represent the appearance of new peaks in phase II and phase III. 125

Figure 5.8 Pressure dependence of selected Raman modes of HB on compression. Different symbols represent Raman modes with different origins. 126

Figure 5.9 Recovered Raman spectrum in comparison with the initial one 128

Figure 5.10 Synchrotron XRD patters of EDAB upon compression in room temperature. * and # represent the appearance of new peaks in phase II and phase III. 130

www.manaraa.com

Figure 5.11 Calculated XRD patters in comparison with experimental results of EDAB at 1.72 (a) and 7.88 (b) GPa using Le Bail refinement 131

Figure 5.12 Cell parameters and volumes as a function of pressure of EDAB during compression 132

Figure 6.1 X-ray diffraction patterns of α- (a) and δ- (b) $FAPbI_3$ at ambient conditions using Co $K\alpha$ radiation of λ=1.7890 Å in comparison with structural refinement using $Pm\bar{3}m$ (c) and $P6_3mc$ (d) crystal structures respectively. 148

Figure 6.2 XRD patterns of α-$FAPbI_3$ upon compression and decompression (a), proposed crystal structures of high-pressure phase II (b) and phase III (c) based on MD simulations, and calculated XRD patterns in comparison with experimental results at 0.34 GPa (d) and 1.67 GPa (e) using Rietveld refinement. 149

Figure 6.3 Enthalpies of new crystal structures for α- (a) and δ- (b) phase of $FAPbI_3$ as a function of pressure. Note that the *Imm*2/*Immm* structure always has a lower enthalpy than the cubic α-phase even at ambient pressure. This could be due to an inadequate estimate of the enthalpy of the cubic α-phase by a static calculation. The cubic α-phase has free molecule rotations which cannot be accounted for in this calculation. 152

Figure 6.4 Reduced unit cell parameters and volumes of α- (a) and δ- (b) phase of $FAPbI_3$ as a function of pressure. 152

Figure 6.5 XRD patterns of δ-$FAPbI_3$ upon compression and decompression (a). Calculated XRD patterns of $FAPbI_3$ in comparison with experimental results at 0.34 GPa for δ-$FAPbI_3$ (b) and the corresponding crystal structure in *C*2/*c* (c) and primitive cell representations (d). 154

Figure 6.6 The relationship between original hexagonal structure (a) and monoclinic *C*2/*c* structure (b) for δ-phase of $FAPbI_3$ upon compression. The *C*2/*c* structure is shown in the primitive unit cell for comparison. 155

www.manaraa.com

Figure 6.7 FTIR spectra of α-$FAPbI_3$ upon compression (a) and pressure dependence of selected IR modes (b) and (c). 157

Figure 6.8 FTIR spectra of δ-phase of $FAPbI_3$ upon compression and decompression, (a) and pressure dependence of selected IR modes for δ-phase (b) and (c). 158

Figure 6.9 Schematic hydrogen bonding interactions between FA and PbI_6 polyhedra in *Imm*2 structure at 0.34 GPa (a) and in *Immm* structure at 1.67GPa (b). The distances of H···I ranging from 2.4 Å to 3.2 Å, i.e., those in strong to moderate hydrogen bonding region, are highlighted by yellow lines. Hydrogen bonds are clearly more populated and symmetric, in the *Immm* structure. 160

Figure 6.10 Optical micrographs of α-$FAPbI_3$ upon compression and recovery (a), PL spectra of α-$FAPbI_3$ upon compression and decompression (b) and the corresponding pressure dependence (c). 164

Figure 6.11 In situ high-pressure optical micrographs of δ-$FAPbI_3$ in a diamond anvil cell. 165

Figure 6.12 Band structures and projected DOS of α-$FAPbI_3$ (a) at ambient pressure and calculated bandgap energy vs pressure (b). 166

Figure 6.13 Band structures and projected density of states (DOS) of α-$FAPbI_3$ for phase II at ambient pressure (a) and 1.6 GPa (b), and for phase III at ambient pressure (c) and 2.0 GPa (d). 166

Figure 6.14 Band structures and projected density of states (DOS) of δ-$FAPbI_3$ for the hexagonal phase at ambient pressure (a) and 1.4 GPa (b), and for the *C*2/*c* phase at 1.7 GPa (c) and 3.0 GPa (d), as well as the calculated bandgap energy as a function of pressure (e). 167

Figure 6.15 Electrical resistance of α- and δ-phase of $FAPbI_3$ as a function of pressure. The inset shows detailed comparison of the electrical resistance of α- and δ-phase of $FAPbI_3$ in the pressure region of 0-5 GPa..... 168

www.manaraa.com

Figure 6.16 Temperature dependence of DC electrical resistance of α- (a) and δ- (b) phase $FAPbI_3$ measured at different pressures. The inset shows the DC electrical resistance of α (a) and δ (b) at 32 GPa and 27 GPa respectively. 170

www.manaraa.com

List of Abbreviations

AB Ammonia borane

ANL Argonne National Laboratory

APS Advanced Photon Source

CCD charge coupled device

DAC diamond anvil cell

EC electrical conductivity

EDAB ethane 1,2-diamineborane

FA formamidinium

FTIR Fourier transform infrared

GPa gigapascal

HB hydrazine borane

IR infrared

MA methylammonium

MCT mercury cadmium telluride

NaAB sodium amidoborane

PL photoluminescence

PTM Pressure transmitting medium

XRD X-ray diffraction

www.manaraa.com

Chapter 1

1 Introduction

1.1 Energy storage materials

1.1.1 Energy source

Over the past several decades, the prosperous economy has been witnessed all over the world due to the high speed of industrial development and the progress of new technologies. However, the rapid growth of the global economy leads to various kinds of scientific and social problems, such as the energy crisis and the environmental deterioration. Nowadays, we rely on oil, natural gas and coal (the fossil fuels) for nearly 85% of our current energy needs, and such fossil fuels will eventually run out in the near future, considering that the consumption of global energy is still increasing year by year.[1-3] Moreover, the combustion and utilization of fossil fuels not only produces massive greenhouse gas CO_2 and other hazardous emissions, but also requires a wealth of consumption of other energies. Thus, replacement of the traditional energy source by clean and renewable energy is in urgent demand.

Accordingly, the development of renewable energy has received much attention. Substantial progress has been made on the investigation of alternative energy sources, including hydrogen energy, solar energy, nuclear energy, wind energy, and so on.[4-7] According to REN21 (renewable energy policy network for the 21st century) global status report,[8] the renewable energy in power generation grew by 17% in 2017, higher than the 10-year average rate (16.2%). Even more, renewable energies provided 26% of global electricity and accounted for an estimated 70% of net additions to global power generation capacity in last year, which shows the strong promises for the global energy transition from fossil fuels to renewable energy in the future.[1, 8] Particularly, hydrogen and solar energy sources are attractive due to their excellent properties among all forms of renewable energy.

www.manaraa.com

Hydrogen is one promising energy carrier because it is highly efficient and nontoxic. Moreover, the oxidation product of hydrogen is only water, which is environmentally friendly. Furthermore, hydrogen has extraordinary high energy density with 142 MJ/Kg, three times as high as liquid hydrocarbon based fuels.[9] Such outstanding properties make hydrogen one of the most promising candidates for portable applications.[10-11]

Another option to replace the fossil fuels is solar energy, as the annual amount of solar energy reaching the surface of the Earth is 1,575 – 49,837 EJ (EJ = 10^{18} J), which is several times larger than the total world energy consumption in one year.[8] Solar energy could be directly converted into electricity by solar cells, based on photovoltaics effect, which is the creation of voltage and electric current in a material upon exposure to light.[12-14] Another benefit of solar energy is that both home and business users can easily deploy it as it does not require any huge setup, which makes it one of the most widely used renewable energy source.

1.1.2 Hydrogen storage materials

In order to achieve the goal of wide utilization of hydrogen energy source, hydrogen storage is considered to be the first and most important step. However, the efficient and safe hydrogen storage has long been a technological barrier before the usage of hydrogen energy.[15] Traditionally, the high-pressure tank technique and cryogenic technique are the most commercialized methods, which are impractical for the wide application of hydrogen due to the safety concerns and volumetric constraints. Therefore, developing hydrogen storage materials is regarded as a key point for portable applications of hydrogen energy. In order to guide the research of hydrogen storage materials, the U.S. Department of Energy (DOE) developed a target, i.e., a hydrogen storage system should meet a gravimetric capacity of 7.5 wt% usable H_2 and a volumetric capacity of 0.07 kg usable H_2 L^{-1}.[16] Besides, other preferred factors affecting the commercial applications of hydrogen storage materials are adequate hydrogenation-dehydrogenation temperature/rate, cycling stability and low cost.[4, 17] There are typically two types of hydrogen storage materials currently: physical storage materials and chemical storage materials.[15, 18-19]

www.manaraa.com

In the category of physical storage materials, metal organic frameworks (MOFs) has been considered as a promising hydrogen storage material. In such cases, hydrogen is adsorbed on the surface and channels via van der Waals force, so the hydrogen storage capacity mainly depends on the surface area of MOFs.[18] In contrast to the physical hydrogen storage materials, chemical storage materials show completely different interaction with hydrogen. Usually, this kind of materials consist of hydrogen atoms and other elements, such as simple hydrides, (e.g. NaH), complex hydrides, (e.g. $Mg(AlH_4)_2$) and chemical hydrides, (e.g. NH_3BH_3), hydrogen would be released when the materials are heated. These chemical storage materials have high hydrogen gravimetric densities and could serve as the basis for rechargeable hydrogen storage systems. In addition, easy synthesis method and low price make them more attractive and commercially available compared to MOFs. Among these hydrogen storage materials, compounds with B-N bond have recently received considerable attention as potential hydrogen storage materials, such as ammonia borane and its derivatives.[11, 20]

Ammonia borane (AB) is one of the most promising solid-state materials for potential hydrogen storage.[21] This molecular material is stable at room temperature and pressure, neither flammable nor explosive. Moreover, it possesses a high hydrogen content of 19.6 %, which makes it competitive among all these candidates. AB has been extensively investigated by vibrational spectroscopy, neutron diffraction and synchrotron XRD, the researches on AB revealed a characteristic feature in its structure, the dihydrogen bond N−H···H−B, which is the interaction between the hydrogen atoms bonded respectively to B and N atoms, such hydrogen atoms have opposite charges due to the different electronegativity of the B and N atoms.[21-22] In the molecule of AB, because of the stronger electronegativity of N atoms, the hydrogen atoms bonded to nitrogen atoms are protonic in character. Whereas boron is less electronegative than hydrogen, the hydrogen atoms bonded to boron atoms are hydridic in character (the electronegativity of N, B and H are 3.04, 2.04 and 2.20). These two different charged hydrogen species form a network of N−H···H−B dihydrogen bonds, which stabilize the structure of NH_3BH_3 as a molecular solid with much higher melting point (104 °C). Besides, the dihydrogen bonds also

www.manaraa.com

participate in the dehydrogenation process of AB to lower the decomposition temperature. The thermal decomposition of AB follows three steps:

$$NH_3BH_3\ (s) \rightarrow [NH_2BH_2]\ (s) + H_2\ (g) \quad (1)$$

$$[NH_2BH_2]\ (s) \rightarrow [NHBH]\ (s) + H_2\ (g) \quad (2)$$

$$[NHBH]\ (s) \rightarrow BN\ (s) + H_2\ (g) \quad (3)$$

The first step occurs between 70 °C and 112 °C, followed by the decomposition of $[NH_2BH_2]$ from about 110 °C to nearly 200 °C. The last step occurs at temperatures in excess of 500 °C, which is thus not considered practical for hydrogen storage.[23-24]

However, two main drawbacks of ammonia borane still hold back the practical use of it, i.e., the high decomposition temperature and releasing of toxic borazine during the decomposition process.[25] Many approaches have been developed to overcome these two obstacles, such as nanoconfining ammonia borane into SBA-15,[26] doping other base-metal catalysts[27] and using ionic liquid medium.[28] Moreover, a series of derivatives of AB by substituting the H atom with alkali or alkaline earth metal element has been synthesized to improve the performance, specifically metal amidoborane, such as $LiNH_2BH_3$ and $NaNH_2BH_3$, which possess total H_2 content of 11 wt% and 7.4 wt%, respectively, have been reported.[24, 29] Additionally, hydrazine borane (HB, $N_2H_4BH_3$) and ethane 1,2-diamineborane (EDAB, $BH_3NH_2CH_2CH_2NH_2BH_3$) are also promising hydrogen storage materials, with the hydrogen content of 15.4 wt% and 16.0 wt%, respectively. In these molecules, they all have hydridic and protonic H atoms, which could also benefit the release of hydrogen during the decomposition process without the emission of borazine.[21, 30-33]

1.1.3 Perovskite solar cell materials

In order to achieve high power conversion efficiency (PCE) from solar energy, the solar cell materials have been investigated extensively over the past decades. According to the different generations, solar cell materials can be classified into crystalline silicon, thin film-based materials like CdTe, CIGS (copper indium gallium selenide) and perovskite

www.manaraa.com

solar cell materials.[6, 34-35] Among them, perovskite solar cell (PSC) materials have drawn much attention recently due to their low cost, high efficiency, easy fabrication and tunable photovoltaic performance.[36-39] In particular, halide perovskite materials have become the most promising candidate in the field of photovoltaics due to the high PCE, which increased from 3.8 % in 2009 to 22.1% in 2017.[36, 40-42] In comparison with other high efficiency materials, i.e., monocrystalline Si cells, thin-fill single-crystalline GaAs cells, polycrystalline CdTe thin-film cells and $Cu(In,Ga)(Se,S)_2$ (CIGS) cells, whose highest efficiency are 25.6%, 28.8%, 21.5%, and 21.7%, respectively,[6] halide perovskites show the comparable high PCE.[40] Additionally, higher efficiency of halide perovskites is still expected in the future.[40, 43-44] Moreover, halide perovskites have been popularized in recent investigations due to their facile synthesis procedure, low cost and easy fabrication, in contrast to Si, GaAs, CdTe and CIGS solar cells, which require high capital investment.[45] Therefore, the halide perovskites constituting of a brand new class of materials with excellent performance still await further exploration.

Normally, perovskites adopt a cubic structure of ABX_3 (the unit cell of ABX_3 is shown in Figure 1.1), where A is a monovalent, non-coordinating cation, usually Cs and organic cation. B is a bivalent p-block metal, typically Pb and Sn. X is a halide anion coordinated to B. As shown in Figure 1.1, cation B has 6 nearest neighboring anions X, while cation A has 12 nearest neighbors X.[45] The crystal of ABX_3 consists of a 3D network of corner-sharing BX_6^{4-} octahedra, and cation A locates in a cage surrounded by octahedrons.

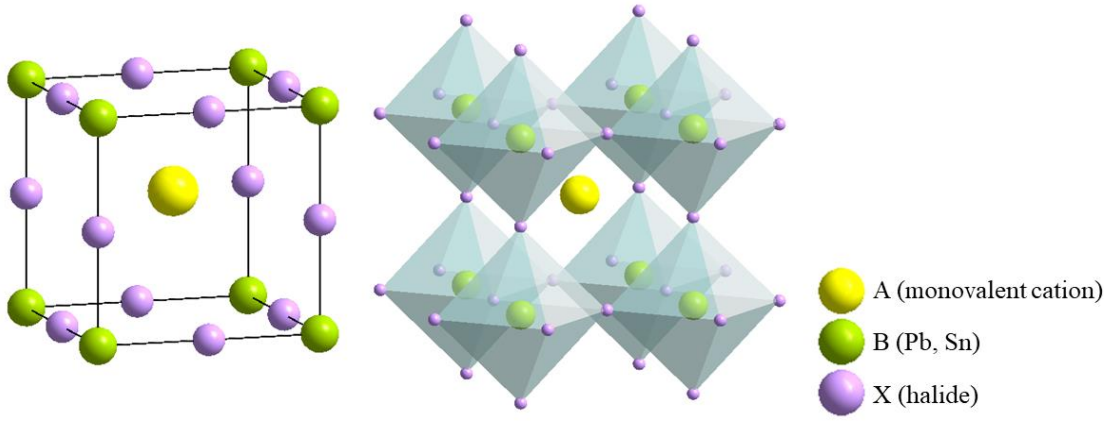

Figure 1.1 Crystal structure of cubic halide perovskite and the BX_6^{2-} octahedrons

www.manaraa.com

To stabilize the perovskite structure, a proper size of cation A should be taken into account, which is restrained by Goldschmidt tolerance factor *t*,[46] as shown in Equation 1.1, where R_A, R_B, R_X are the ionic radii of the corresponding ions.[44, 47-48] It is well studied that the tolerance factor *t* should be in the range of 0.8 to 1.0 to maintain a stable perovskite structure. Otherwise, the structure will be highly distorted and the stability will be reduced.[49] Under this criterion, only 3 cations for A site, Cs^+, $CH_3NH_3^+$ (MA) and $HC(NH_2)_2^+$ (FA) are mostly investigated in perovskite materials. As listed in Table 1.1, the structures and band gaps of such materials are summarized.

$$t = \frac{R_A + R_B}{\sqrt{2}(R_X + R_B)} \qquad \text{Equation 1.1}$$

Compared to inorganic $CsPbX_3$, the organic-inorganic hybrid lead halide perovskites show the higher stability and better photovoltaic performance. Therefore, extensive studies on $MAPbX_3$ and $FAPbX_3$ have been performed.[44, 50-51] Moreover, the theoretical studies have revealed that the band gap of the perovskites is mainly defined by the overlap between the p orbital of X and the p orbital of Pb. As a result, the band gap can be tuned by replacing the halide anion.[46, 49] As shown in Table 1.1, the values of band gap of $APbBr_3$ (A = Cs, MA, FA) are very close, and the band gap of $MAPbI_3$ could be tuned from 1.57 to 2.23 eV by the exchange of the halide ions.[52-53] Even though the cation A has no direct contribution to band gap, it can still affect the electronic structure through the steric effect.[54-55] Compared to MA, FA has a stronger steric size, leading to a narrower band gap (1.45 eV for $FAPbI_3$), broader absorption spectrum, higher efficiency and better chemical stability. Therefore, $FAPbI_3$ has been investigated extensively in recent years.[41, 54, 56-57]

www.manaraa.com

Table 1.1 Summary of most investigated perovskite materials

Materials	Crystal system	Space group	Temperature	Band gap (eV)	References
$CsPbCl_3$	Orthorhombic	*Pbnm*	20 °C	2.97	58-59
$CsPbBr_3$	Orthorhombic	*Pnma*	20 °C	2.25	60-61
δ-$CsPbI_3$	Orthorhombic	*Pnma*	20 °C	2.82	61-62
α-$CsPbI_3$	Cubic	$Pm\bar{3}m$	335 °C	1.73	63
$MAPbBr_3$	Cubic	$Pm\bar{3}m$	20 °C	2.23	64
$MAPbI_3$	Tetragonal	*I*4/*mcm*	20 °C	1.55	64
$MAPbI_{3-x}Br_x$			20 °C	1.57-2.23	53
$FAPbBr_3$	Cubic	$Pm\bar{3}m$	20 °C	2.23	65
α-$FAPbI_3$	Trigonal	*P*3*m*1	170 °C	1.45	41
α-$FAPbI_3$	Cubic	$Pm\bar{3}m$	170 °C	1.45	66

www.manaraa.com

1.2 High-pressure science

1.2.1 High-pressure phenomena

Pressure is an important parameter controlling the chemical equilibrium and determining a chemical reaction, which is defined as a measure of how the internal energy of a system changes when it expands or contracts, as shown in Equation 1.2, where P, E, V are pressure, internal energy and volume.[67] When applying pressure to materials, the inter-atomic and intra-atomic distance will be shortened, leading to a reduced volume and an increased internal energy of the system. Particularly, in extremely high-pressure region, which is in gigapascal range (1 GPa = 10^9 Pa = 10^4 bar), the high-pressure induced volume contraction results in some unusual behaviors of the materials and some novel materials with exotic structures and properties are generated under high pressure, as illustrated in Figure 1.2, some examples of such high-pressure phenomena and new materials are highlighted.[68]

$$P = -\frac{\partial E}{\partial V} \qquad \text{Equation 1.2}$$

1.2.2 High-pressure chemistry

By altering the intermolecular distances and the chemical bonding, high pressure enables the structural changes of the materials, such as phase transitions, polymerization, amorphization and so on.[68] Various possible structures can be generated under high pressure, such as synthetic diamond, which is made by the compression of graphite. Moreover, Pressure can also effectively modify the composition of the materials, leading to the formation of compounds with unusual stoichiometry, which could not be synthesized by conventional chemical routines.[69-71] For instance, a number of hydrogen-rich metal hydrides, LiH_x, NaH_x, were synthesized under the high pressure.[70, 72] Furthermore, high pressure has been demonstrated to make some significant improvement in applied material science by tuning the electronic and optical properties of materials for novel applications, such features will be discussed in the following part.[73]

www.manaraa.com

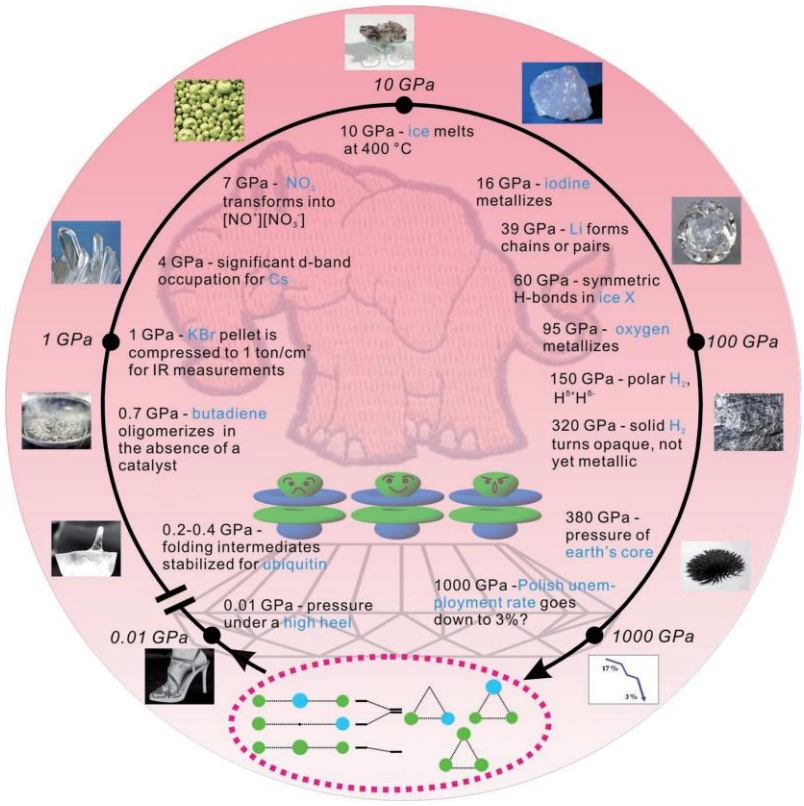

Figure 1.2 Examples of various high-pressure phenomena[68]

1.3 High-pressure studies on energy storage materials

1.3.1 High-pressure studies on hydrogen storage materials

The high-pressure technique has been demonstrated as an effective and promising approach for developing potential hydrogen storage materials by providing a unique chance to reveal the pressure-induced phase transitions and thus guiding the design of new hydrogen storage materials.[74-86] For instance, Metal hydrides are the simplest hydrogen storage materials, such as MgH_2, which exhibits multiple polymorphs under high pressure. Under ambient conditions, it crystallized into α-MgH_2 structure with space group $P4_2/mnm$, then γ-MgH_2 with an orthorhombic structure (*Pbcn*) was formed at 2 GPa,[87-88] and a γ- to β-MgH_2 transition was found at 3.8 GPa, as well as a δ structure at higher pressures with the respective structures of cubic ($Pa\bar{3}$) and orthorhombic types

www.manaraa.com

(*Pbca*).[89-91] Some recent high-pressure studies of different hydrogen storage materials are summarized in Table 1.2.

As a highly promising hydrogen storage material, the high-pressure effect on ammonia borane has been investigated extensively. AB adopts a tetragonal structure with space group *I*4*mm* under ambient conditions, and undergoes a phase transition to an orthorhombic structure when cooled to 225 K with the space group $Pmn2_1$.[20, 92-97] AB transformed to a new ordered orthorhombic structure at 1.5 GPa, followed by another phase transition at 8 GPa.[98-103] Furthermore, a new high-pressure phase (space group $P2_1$) at above 12.9 GPa was characterized by in situ synchrotron X-ray powder diffraction.[104] Moreover, the dihydrogen bond was confirmed by the high-pressure studies on AB using IR and Raman spectroscopy, which contributes to the abnormal high melting point of molecular AB crystal and the dehydrogenation process.[105-106]

In addition to phase transitions, the formation of novel hydrogen-containing complexes under high pressure has been drawn much attention in recent years due to their extremely high hydrogen content without the limitations of conventional stoichiometry. These complexes are typically supermolecular compounds, or clathrate materials, with guest–host structures, where H_2 could be stored in the framework structures of host. Pressure can drive the formation of such novel complexes between H_2 and other simple molecules, such as CH_4, NH_3, H_2O, SiH_4 and even noble gases.[107-122] The first such system was reported to be CH_4-H_2 system by Somayazulu *et al.* in 1996, and four molecular compounds, $CH_4(H_2)_2$, $(CH_4)_2H_2$, $CH_4(H_2)_4$, and CH_4H_2 were observed at pressures up to 10 GPa.[123-124] Among them, $CH_4(H_2)_4$ holds an outstanding 33.4 wt% H_2 (and a total of 50 mass% H), which is far beyond the US DOE target. Similarly, ammonia borane has been found to be able to form such complex with H_2 under high pressure. Lin *et al.* obtained a novel solid $NH_3BH_3(H_2)_x$, where x = 1.3–2, at above 6.2 GPa, revealing 8–12 wt% of additional H_2 in this new phase, which makes this new complex one of the most H_2-rich materials (with ～30 wt% H_2).[125] The subsequent researches on NH_3BH_3–H_2 system under high pressure shed light on the design of new complexes for practical hydrogen storage applications.[126-127]

www.manaraa.com

Table 1.2 Summary of selected high-pressure studies on hydrogen storage materials[34]

Materials	Hydrogen content	Crystal structure	Pressure range (GPa)[a]	Temperature range (°C)[a]	References
Simple hydride					
LiH	12.6%	$Fm\bar{3}m$	250	25	128
MgH_2	7.7%	$P4_2/mnm$ (α), $Pa\bar{3}$ (β), $Pbcn$ (γ), $Pbca$(δ)	16	797	87-90
AlH_3	10.0%	$R\bar{3}c$ (α), Cmcm (α'), $Fd\bar{3}m$ (β), Pnnm (γ) P2 (α-II), $Pm\bar{3}n$ (α-III)	164	-269	129-131
Complex hydride					
$LiAlH_4$	10.6%	$P2_1/c$ (α), $I2/b$ (β)	7	500	132-133
$LiBH_4$	18.4%	$Pnma$, $P6_3mc$, $Ama2$, $Fm\bar{3}m$	10	227	77, 83, 134
$Ca(BH_4)_2$	11.5%	Fddd(α), $P\bar{4}$ (β), Pbca (γ), $I\bar{4}2d$ (α')	10	-193 - 400	82, 135-136
$LiNH_2$	8.7%	$I\bar{4}$ (α), $P2_1$(β)	16	25	137-138
Chemical hydride					
NH_3BH_3	19.6%	$I4mm$, $Pmn2_1$, $Cmc2_1$, $P2_1$	65	-258 - 77	20, 98, 103-105
H_2 containing complex					
CH_4-H_2	50.0%	$CH_4(H_2)_2$ – $P6_3/mmc$	60	-263	123-124
NH_3BH_3-H_2	28.7%	$NH_3BH_3(H_2)_x$, x = 1.3-2	60	140	125

[a] The pressure range goes from ambient to the given value; for temperature, the values refer to either the maximum or the minimum or to a range of temperatures under which the materials were investigated under simultaneous high-pressure conditions.

www.manaraa.com

1.3.2 High-pressure studies on perovskite solar cell materials

Power conversion efficiency is a crucial factor to evaluate the solar cells. According to Shockley–Queisser limit theory, the limiting power conversion efficiency for a single-junction solar cell is 33.7%, for an optimum semiconductor band gap energy of 1.34 eV.[139-141] However, the band gaps of almost all perovskite solar cells are higher than this limit, as indicated in Table 1.1. Therefore, it is essential to find an effective method to narrow the band gap of perovskites, such as by applying high pressure.[142-143] The mechanical compression can effectively modify the crystal structures and tune the electronic structures of the materials, resulting in a narrower band gap during the compression.[139, 144-145] The pressure-tuned structures and band gaps of selected perovskite solar cell materials are summarized in Table 1.3.

The high-pressure studies on hybrid perovskites $APbX_3$ revealed that various structural changes could be induced upon compression, such as phase transitions, local distortions in the inorganic lattice, and partial amorphization.[144] As shown in Table 1.3, $MAPbCl_3$, $MAPbBr_3$ and $FAPbBr_3$ exhibit the similar phase transitions upon compression. These materials transform from $Pm\bar{3}m$ space group to the final *Pnma* space group, followed by a reversible amorphization, which could be attributed to the tilting and shrinking of PbX_6 octahedra and destroying of long-range ordering of MA or FA cations, respectively.[146-149] Additionally, $MAPbI_3$ and $FAPbI_3$ shown the different structural changes, $MAPbI_3$ undergoes the transition from *I*4/*mcm* to $Im\bar{3}$, then to *Immm*, while no phase transition was observed in the study of $FAPbI_3$ with the space group of *P*3*m*1.[150-151]

Moreover, another significant pressure effect on perovskite materials is tuning the electronic structures, leading to the modified optoelectronic properties, such as the color changes of materials, the optical absorption and photoluminescence evolutions, the electronic conductivity modifications and metallization.[144, 146-163] The high-pressure studies on $MAPbBr_3$ revealed the anomalous band gap evolution during compression with red-shift followed by blue-shift, which was explained by the competition between compression effect and pressure-induced amorphization.[147] As shown in Figure 1.3 (a),

www.manaraa.com

the band gap of $MAPbBr_3$ decreases from 2.36 eV at ambient pressure to 2.32 eV at 0.8 GPa, followed by an increase.[147] The electric resistance and photocurrent measurements showed the increasing resistance of material and considerable response to the visible light irradiation upon compression.[147] Moreover, $FAPbBr_3$ also exhibits the pressure-induced band gap evolution, which decreases from 2.27 eV at ambient pressure to near 2.10 eV at 2.20 GPa, as shown in Figure 1.3 (b).[149] Meanwhile, optical properties can be tuned by pressure as well, such as, the color of $FAPbBr_3$. It gradually changes from orange to red, followed by yellow and finally becomes colorless upon compression (figure 1.4).[149]

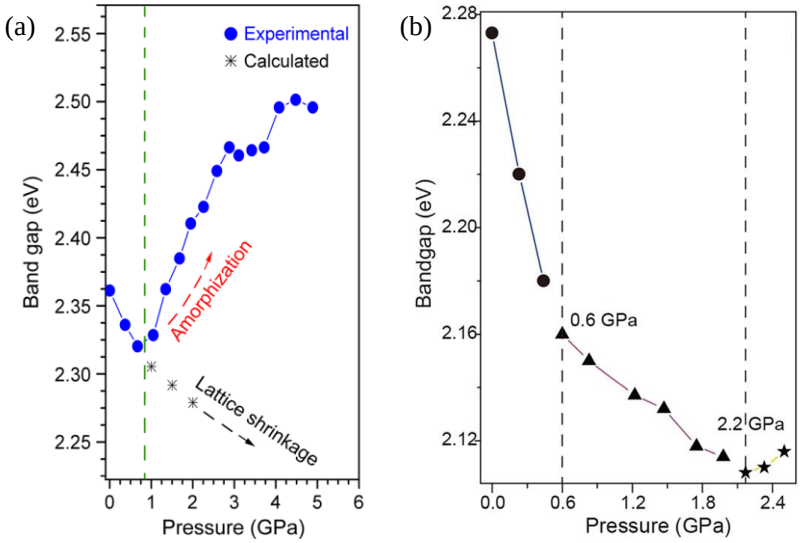

Figure 1.3 band gap energy of $MAPbBr_3$ (a) and $FAPbI_3$ (b) as a function of pressure[147, 149]

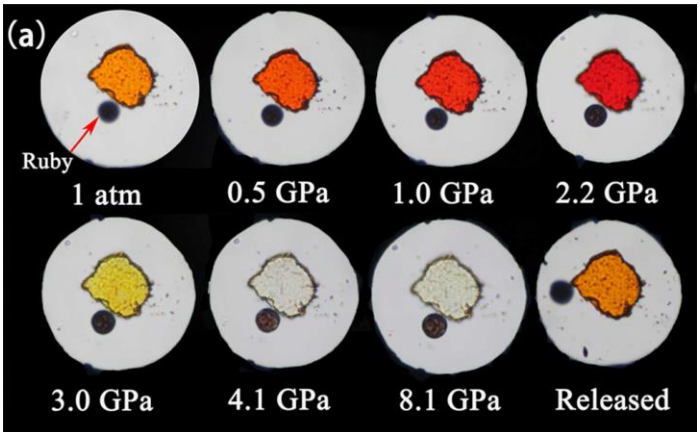

Figure 1.4 In situ high-pressure optical micrographs of $FAPbBr_3$ crystal in a DAC[149]

www.manaraa.com

Table 1.3 The recent high-pressure studies on perovskite solar cell materials

Materials	Phase transitions	Band gap evolution (eV)	Methods	Pressure range (GPa)[a]	References
$MAPbCl_3$	$Pm\bar{3}m$ to an isostructural $Pm\bar{3}m$, then to *Pnma*	3.06 to 3.01, then to 3.15	Synchrotron XRD, Raman spectroscopy and PL	20	158
$MAPbBr_3$	$Pm\bar{3}m$ to $Im\bar{3}$, to *Pnma*	2.36 to 2.32, then to 2.50	Synchrotron XRD, PL, Electrical resistance and photocurrent	46	146-147, 162
$MAPbI_3$	$I4/mcm$ to $Im\bar{3}$, then to *Immm*	1.58 to 1.56, then to 1.79	Synchrotron XRD, Raman and PL	47	148, 150, 152-155
$FAPbBr_3$	$Pm\bar{3}m$ to $Im\bar{3}$, then to *Pnma*	2.27 to 2.10, then to 2.12	Synchrotron XRD, optical micrographs, optical absorption and PL	30	149
$FAPbI_3$	No phase transition for $P3m1$	1.49 to 1.38, then to 1.40	Synchrotron XRD, optical absorption and PL	7	151

[a] Pressure range goes from ambient pressure to the highest pressure in the investigations

www.manaraa.com

1.4 Motivation and outline of the thesis

Because the potential application of NH_3BH_3 on hydrogen storage has been restricted due to its two main drawbacks, the desire for new AB derivatives with better dehydrogenation performance has been aroused. Consequently, abundant researches on such materials have been conducted under ambient conditions and by the theoretical calculations with respect to the structure and dehydrogenation behavior. Applying high pressure on hydrogen storage materials could induce the new polymorphs, and thus exploring the evolution of the bond behaviors could aid in understanding the mechanism of dehydrogenation precess and the synthesis of novel materials. Therefore, it's important to investigate the hydrogen storage materials under high pressure.

In this thesis, we study three AB derivatives (sodium amidoborane $NaNH_2BH_3$, hydrazine borane $N_2H_4BH_3$ and ethane 1,2-diamineborane $BH_3NH_2CH_2CH_2NH_2BH_3$) under high pressure using IR, Raman spectroscopy and synchrotron X-ray diffraction, as described in chapters 3, 4 and 5, respectively. The structural stability and the evolution of cell parameters for each material are investiaged under high pressure. The possible new high-pressure phases of the materials are also proposed. Moreover, we examine the high-pressure effect on hydrogen bonding and dihydrogen bonding for all materials by monitoring the shift of N-H stretching modes using IR and Raman spectroscopy, which may play an important role in the dehydrogenation process. High-pressure studies on such materials will be helpful to understand the correlation between the structures and performance. Furthermore, the investigations may guide the improvement of the hydrogen storage properties of the potential material and the design of new materials for hydrogen storage applications.

The fact that the band gap of α-$FAPbI_3$ is very close to the Shockley-Queisser limit makes high pressure an promising method to narrow the band gap. Therefore, it is extremely beneficial to study the high-pressure effect on the electronic structure of α-$FAPbI_3$ and examine the stability of the new high-pressure phases. Furthermore, the influence of the FA moiety in the perovskite materials remains unclear. Therefore, in Chapter 6, we report the high-pressure study of α-$FAPbI_3$ and δ-$FAPbI_3$ perovskite

www.manaraa.com

materials comparatively. The crystal structures and band gaps are characterized by in-situ synchrotron radiation XRD, IR spectroscopy, photoluminescence and electronic measurements. The information will also provide us with the opportunity to understand the structural stability and the pressure dependent optoelectrical properties, which may lead to the development of new perovskite-based solar cell materials.

1.5 References

(1) BP Statistical review of world energy 2018.

(2) Dresselhaus, M. S.; Thomas, I. L. Alternative energy technologies. *Nature* **2001,** *414*, 332-337.

(3) Ellabban, O.; Abu-Rub, H.; Blaabjerg, F. Renewable energy resources: Current status, future prospects and their enabling technology. *Renewable & Sustainable Energy Reviews* **2014,** *39*, 748-764.

(4) Durbin, D. J.; Malardier-Jugroot, C. Review of hydrogen storage techniques for on board vehicle applications. *International Journal of Hydrogen Energy* **2013,** *38*, 14595-14617.

(5) Dunn, S. Hydrogen futures: toward a sustainable energy system. *International Journal of Hydrogen Energy* **2002,** *27*, 235-264.

(6) Polman, A.; Knight, M.; Garnett, E. C.; Ehrler, B.; Sinke, W. C. Photovoltaic materials: Present efficiencies and future challenges. *Science* **2016,** *352*, 307.

(7) Detz, R.; Reek, J.; van der Zwaan, B. The future of solar fuels: when could they become competitive? *Energy & Environmental Science* **2018,** *11*, 1653-1669.

(8) REN21 Renewables 2018 Global Status Report.

(9) Mazloomi, K.; Gomes, C. Hydrogen as an energy carrier: Prospects and challenges. *Renewable & Sustainable Energy Reviews* **2012,** *16*, 3024-3033.

www.manaraa.com

(10) Eberle, U.; Felderhoff, M.; Schuth, F. Chemical and physical solutions for hydrogen storage. *Angewandte Chemie-International Edition* **2009,** *48*, 6608-6630.

(11) Hamilton, C. W.; Baker, R. T.; Staubitz, A.; Manners, I. B-N compounds for chemical hydrogen storage. *Chemical Society Reviews* **2009,** *38*, 279-293.

(12) Jean, J.; Brown, P. R.; Jaffe, R. L.; Buonassisi, T.; Bulovic, V. Pathways for solar photovoltaics. *Energy & Environmental Science* **2015,** *8*, 1200-1219.

(13) Curtright, A. E.; Morgan, M. G.; Keith, D. W. Expert assessments of future photovoltaic technologies. *Environmental Science & Technology* **2008,** *42*, 9031-9038.

(14) Green, M. A. Third generation photovoltaics: Ultra-high conversion efficiency at low cost. *Progressin Photovoltaics* **2001,** *9*, 123-135.

(15) Schlapbach, L.; Zuttel, A. Hydrogen-storage materials for mobile applications. *Nature* **2001,** *414*, 353-358.

(16) Churchard, A. J.; Banach, E.; Borgschulte, A.; Caputo, R.; Chen, J. C.; Clary, D. C.; Fijalkowski, K. J.; Geerlings, H.; Genova, R. V.; Grochala, W., et al. A multifaceted approach to hydrogen storage. *Physical Chemistry Chemical Physics* **2011,** *13*, 16955-16972.

(17) Li, H. W.; Yan, Y. G.; Orimo, S.; Zuttel, A.; Jensen, C. M. Recent progress in metal borohydrides for hydrogen storage. *Energies* **2011,** *4*, 185-214.

(18) Dutta, S. A review on production, storage of hydrogen and its utilization as an energy resource. *Journal of Industrial and Engineering Chemistry* **2014,** *20*, 1148-1156.

(19) van den Berg, A. W. C.; Arean, C. O. Materials for hydrogen storage: current research trends and perspectives. *Chemical Communications* **2008**, *6*, 668-681.

(20) Bowden, M. E.; Gainsford, G. J.; Robinson, W. T. Room-temperature structure of ammonia borane. *Australian Journal of Chemistry* **2007,** *60*, 149-153.

www.manaraa.com

(21) Staubitz, A.; Robertson, A. P. M.; Manners, I. Ammonia-borane and related compounds as dihydrogen sources. *Chemical Reviews* **2010,** *110*, 4079-4124.

(22) Morrison, C. A.; Siddick, M. M. Dihydrogen bonds in solid BH_3NH_3. *Angewandte Chemie-International Edition* **2004,** *43*, 4780-4782.

(23) Hu, M.; Geanangel, R.; Wendlandt, W. The thermal decomposition of ammonia borane. *Thermochimica Acta* **1978,** *23*, 249-255.

(24) Xiong, Z. T.; Yong, C. K.; Wu, G. T.; Chen, P.; Shaw, W.; Karkamkar, A.; Autrey, T.; Jones, M. O.; Johnson, S. R.; Edwards, P. P., et al. High-capacity hydrogen storage in lithium and sodium amidoboranes. *Nature Materials* **2008,** *7*, 138-141.

(25) Chua, Y. S.; Chen, P.; Wu, G. T.; Xiong, Z. T. Development of amidoboranes for hydrogen storage. *Chemical Communications* **2011,** *47*, 5116-5129.

(26) Gutowska, A.; Li, L. Y.; Shin, Y. S.; Wang, C. M. M.; Li, X. H. S.; Linehan, J. C.; Smith, R. S.; Kay, B. D.; Schmid, B.; Shaw, W., et al. Nanoscaffold mediates hydrogen release and the reactivity of ammonia borane. *Angewandte Chemie-International Edition* **2005,** *44*, 3578-3582.

(27) Keaton, R. J.; Blacquiere, J. M.; Baker, R. T. Base metal catalyzed dehydrogenation of ammonia-borane for chemical hydrogen storage. *Journal of the American Chemical Society* **2007,** *129*, 1844-1845.

(28) Bluhm, M. E.; Bradley, M. G.; Butterick, R.; Kusari, U.; Sneddon, L. G. Amineborane-based chemical hydrogen storage: Enhanced ammonia borane dehydrogenation in ionic liquids. *Journal of the American Chemical Society* **2006,** *128*, 7748-7749.

(29) Diyabalanage, H. V. K.; Shrestha, R. P.; Semelsberger, T. A.; Scott, B. L.; Bowden, M. E.; Davis, B. L.; Burrell, A. K. Calcium amidotrihydroborate: A hydrogen storage material. *Angewandte Chemie-International Edition* **2007,** *46*, 8995-8997.

www.manaraa.com

(30) Hugle, T.; Kuhnel, M. F.; Lentz, D. Hydrazine borane: A promising hydrogen storage material. *Journal of the American Chemical Society* **2009,** *131*, 7444-7446.

(31) Moury, R.; Moussa, G.; Demirci, U. B.; Hannauer, J.; Bernard, S.; Petit, E.; van der Lee, A.; Miele, P. Hydrazine borane: synthesis, characterization, and application prospects in chemical hydrogen storage. *Physical Chemistry Chemical Physics* **2012,** *14*, 1768-1777.

(32) Leardini, F.; Valero-Pedraza, M. J.; Perez-Mayoral, E.; Cantelli, R.; Banares, M. A. Thermolytic decomposition of ethane 1,2-diamineborane investigated by thermoanalytical methods and in Situ vibrational spectroscopy. *Journal of Physical Chemistry C* **2014,** *118*, 17221-17230.

(33) Neiner, D.; Karkamkar, A.; Bowden, M.; Choi, Y. J.; Luedtke, A.; Holladay, J.; Fisher, A.; Szymczak, N.; Autrey, T. Kinetic and thermodynamic investigation of hydrogen release from ethane 1,2-di-amineborane. *Energy & Environmental Science* **2011,** *4*, 4187-4193.

(34) Assadi, M. K.; Bakhoda, S.; Saidur, R.; Hanaei, H. Recent progress in perovskite solar cells. *Renewable & Sustainable Energy Reviews* **2018,** *81*, 2812-2822.

(35) Britt, J.; Ferekides, C. Thin-film CdS/CdTe solar cell with 15.8% efficiency. *Applied Physics Letters.* **1993,** *62*, 2851-2852.

(36) Mesquita, I.; Andrade, L.; Mendes, A. Perovskite solar cells: Materials, configurations and stability. *Renewable & Sustainable Energy Reviews* **2018,** *82*, 2471-2489.

(37) Djurisic, A. B.; Liu, F. Z.; Tam, H. W.; Wong, M. K.; Ng, A.; Surya, C.; Chen, W.; He, Z. B. Perovskite solar cells - An overview of critical issues. *Progress in Quantum Electronics* **2017,** *53*, 1-37.

www.manaraa.com

(38) Correa-Baena, J. P.; Saliba, M.; Buonassisi, T.; Gratzel, M.; Abate, A.; Tress, W.; Hagfeldt, A. Promises and challenges of perovskite solar cells. *Science* **2017,** *358*, 739-744.

(39) Kovalenko, M. V.; Protesescu, L.; Bodnarchuk, M. I. Properties and potential optoelectronic applications of lead halide perovskite nanocrystals. *Science* **2017,** *358*, 745-750.

(40) Service, R. F. Perovskite solar cells keep on surging. *Science* **2014,** *344*, 458-458.

(41) Jeon, N. J.; Noh, J. H.; Yang, W. S.; Kim, Y. C.; Ryu, S.; Seo, J.; Seok, S. I. Compositional engineering of perovskite materials for high-performance solar cells. *Nature* **2015,** *517*, 476-480.

(42) Saliba, M.; Matsui, T.; Seo, J. Y.; Domanski, K.; Correa-Baena, J. P.; Nazeeruddin, M. K.; Zakeeruddin, S. M.; Tress, W.; Abate, A.; Hagfeldt, A., et al. Cesium-containing triple cation perovskite solar cells: improved stability, reproducibility and high efficiency. *Energy & Environmental Science* **2016,** *9*, 1989-1997.

(43) Hailegnaw, B.; Kirmayer, S.; Edri, E.; Hodes, G.; Cahen, D. Rain on methylammonium lead iodide based perovskites: Possible environmental effects of perovskite solar cells. *Journal of Physical Chemistry Letters* **2015,** *6*, 1543-1547.

(44) Zhao, Y. X.; Zhu, K. Organic-inorganic hybrid lead halide perovskites for optoelectronic and electronic applications. *Chemical Society Reviews* **2016,** *45*, 655-689.

(45) Stoumpos, C. C.; Kanatzidis, M. G. Halide perovskites: Poor man's high-performance semiconductors. *Advanced Materials* **2016,** *28*, 5778-5793.

(46) Stoumpos, C. C.; Kanatzidis, M. G. The renaissance of halide perovskites and their evolution as emerging semiconductors. *Accounts of Chemical Research* **2015,** *48*, 2791-2802.

www.manaraa.com

(47) Kim, H. S.; Im, S. H.; Park, N. G. Organolead halide perovskite: New horizons in solar cell research. *Journal of Physical Chemistry C* **2014,** *118*, 5615-5625.

(48) Kieslich, G.; Sun, S. J.; Cheetham, A. K. Solid-state principles applied to organic-inorganic perovskites: new tricks for an old dog. *Chemical Science* **2014,** *5*, 4712-4715.

(49) Yin, W. J.; Yang, J. H.; Kang, J.; Yan, Y. F.; Wei, S. H. Halide perovskite materials for solar cells: a theoretical review. *Journal of Materials Chemistry A* **2015,** *3*, 8926-8942.

(50) Saparov, B.; Mitzi, D. B. Organic-inorganic perovskites: Structural versatility for functional materials design. *Chemical Reviews* **2016,** *116*, 4558-4596.

(51) Green, M. A.; Ho-Baillie, A.; Snaith, H. J. The emergence of perovskite solar cells. *Nature Photonics* **2014,** *8*, 506-514.

(52) Zhou, H. P.; Chen, Q.; Li, G.; Luo, S.; Song, T. B.; Duan, H. S.; Hong, Z. R.; You, J. B.; Liu, Y. S.; Yang, Y. Interface engineering of highly efficient perovskite solar cells. *Science* **2014,** *345*, 542-546.

(53) Noh, J. H.; Im, S. H.; Heo, J. H.; Mandal, T. N.; Seok, S. I. Chemical management for colorful, efficient, and stable inorganic-organic hybrid nanostructured solar cells. *Nano Letters* **2013,** *13*, 1764-1769.

(54) Filip, M. R.; Eperon, G. E.; Snaith, H. J.; Giustino, F. Steric engineering of metal-halide perovskites with tunable optical band gaps. *Nature Communications* **2014,** *5*, 5757.

(55) Green, M. A.; Hishikawa, Y.; Dunlop, E. D.; Levi, D. H.; Hohl-Ebinger, J.; Ho-Baillie, A. W. Y. Solar cell efficiency tables (version 52). *Progress in Photovoltaics* **2018,** *26*, 427-436.

www.manaraa.com

(56) Pang, S. P.; Hu, H.; Zhang, J. L.; Lv, S. L.; Yu, Y. M.; Wei, F.; Qin, T. S.; Xu, H. X.; Liu, Z. H.; Cui, G. L. $NH_2CH=NH_2PbI_3$: An alternative organolead iodide perovskite sensitizer for mesoscopic solar cells. *Chemistry of Materials* **2014,** *26*, 1485-1491.

(57) Yang, W. S.; Noh, J. H.; Jeon, N. J.; Kim, Y. C.; Ryu, S.; Seo, J.; Seok, S. I. High-performance photovoltaic perovskite layers fabricated through intramolecular exchange. *Science* **2015,** *348*, 1234-1237.

(58) Zhang, L.; Wang, L.; Wang, K.; Zou, B. Pressure-induced structural evolution and optical properties of metal halide perovskite $CsPbCl_3$. *The Journal of Physical Chemistry C* **2018,** *122*, 15220–15225.

(59) Sakuma, T.; Mutou, M.; Ohki, K.; Arai, M.; Takahashi, H.; Ishii, Y. Low-energy excitation in $CsPbX_3$ (X=Cl, Br). *Solid State Ionics* **2002,** *154*, 237-242.

(60) Stoumpos, C. C.; Malliakas, C. D.; Peters, J. A.; Liu, Z. F.; Sebastian, M.; Im, J.; Chasapis, T. C.; Wibowo, A. C.; Chung, D. Y.; Freeman, A. J., et al. Crystal growth of the perovskite semiconductor $CsPbBr_3$: A new material for high-energy radiation detection. *Crystal Growth & Design* **2013,** *13*, 2722-2727.

(61) Cottingham, P.; Brutchey, R. L. On the crystal structure of colloidally prepared $CsPbBr_3$ quantum dots. *Chemical Communications* **2016,** *52*, 5246-5249.

(62) Stoumpos, C. C.; Malliakas, C. D.; Kanatzidis, M. G. Semiconducting tin and lead iodide perovskites with organic cations: Phase transitions, high mobilities, and near-Infrared photoluminescent properties. *Inorganic Chemistry* **2013,** *52*, 9019-9038.

(63) Eperon, G. E.; Paterno, G. M.; Sutton, R. J.; Zampetti, A.; Haghighirad, A. A.; Cacialli, F.; Snaith, H. J. Inorganic caesium lead iodide perovskite solar cells. *Journal of Materials Chemistry A* **2015,** *3*, 19688-19695.

(64) Kojima, A.; Teshima, K.; Shirai, Y.; Miyasaka, T. Organometal halide perovskites as visible-light sensitizers for photovoltaic cells. *Journal of the American Chemical Society* **2009,** *131*, 6050-6051.

www.manaraa.com

(65) Hanusch, F. C.; Wiesenmayer, E.; Mankel, E.; Binek, A.; Angloher, P.; Fraunhofer, C.; Giesbrecht, N.; Feckl, J. M.; Jaegermann, W.; Johrendt, D., et al. Efficient planar heterojunction perovskite solar cells based on formamidinium lead bromide. *Journal of Physical Chemistry Letters* **2014,** *5*, 2791-2795.

(66) Weller, M. T.; Weber, O. J.; Frost, J. M.; Walsh, A. Cubic perovskite structure of black formamidinium lead iodide, alpha-$HC(NH_2)_2PbI_3$, at 298 K. *Journal of Physical Chemistry Letters* **2015,** *6*, 3209-3212.

(67) Shen, G. Y.; Mao, H. K. High-pressure studies with x-rays using diamond anvil cells. *Reports on Progress in Physics* **2017,** *80*, 1-53.

(68) Grochala, W.; Hoffmann, R.; Feng, J.; Ashcroft, N. W. The chemical imagination at work in very tight places. *Angewandte Chemie-International Edition* **2007,** *46*, 3620-3642.

(69) Zhang, L.; Wang, Y.; Lv, J.; Ma, Y. Materials discovery at high pressures. *Nature Reviews Materials* **2017,** *2*, 17005.

(70) Kuno, K.; Matsuoka, T.; Nakagawa, T.; Hirao, N.; Ohishi, Y.; Shimizu, K.; Takahama, K.; Ohta, K.; Sakata, M.; Nakamoto, Y. Heating of Li in hydrogen: possible synthesis of LiHx. *Journal of Materials Chemistry A* **2015,** *35*, 16-21.

(71) Zhang, W.; Oganov, A. R.; Goncharov, A. F.; Zhu, Q.; Boulfelfel, S. E.; Lyakhov, A. O.; Stavrou, E.; Somayazulu, M.; Prakapenka, V. B.; Konôpková, Z. Unexpected stable stoichiometries of sodium chlorides. *Science* **2013,** *342*, 1502-1505.

(72) Struzhkin, V. V.; Kim, D. Y.; Stavrou, E.; Muramatsu, T.; Mao, H.-k.; Pickard, C. J.; Needs, R. J.; Prakapenka, V. B.; Goncharov, A. F. Synthesis of sodium polyhydrides at high pressures. *Nature Communications* **2016,** *7*, 12267.

(73) Song, Y.; Manaa, M. R., New trends in chemistry and materials science in extremely tight space. *The Journal of Physical Chemistry C* **2012,** *116*, 2059-2060.

www.manaraa.com

(74) Ramzan, M.; Hussain, T.; Ahuja, R. High pressure phase determination and electronic properties of lithiumamidoborane. *Applied Physics Letters* **2012,** *101*, 111902.

(75) Najiba, S.; Chen, J. H. High-pressure study of lithium amidoborane using Raman spectroscopy and insight into dihydrogen bonding absence. *Proceedings of the National Academy of Sciences of the United States of America* **2012,** *109*, 19140-19144.

(76) Filinchuk, Y.; Talyzin, A. V.; Chernyshov, D.; Dmitriev, V. High-pressure phase of $NaBH_4$: Crystal structure from synchrotron powder diffraction data. *Physical Review B* **2007,** *76*, 092104.

(77) Talyzin, A. V.; Andersson, O.; Sundqvist, B.; Kurnosov, A.; Dubrovinsky, L. High-pressure phase transition in $LiBH_4$. *Journal of Solid State Chemistry* **2007,** *180*, 510-517.

(78) Fallas, J. C.; Chien, W. M.; Chandra, D.; Kamisetty, V. K.; Emmons, E. D.; Covington, A. M.; Chellappa, R.; Gramsch, S. A.; Hemley, R. J.; Hagemann, H. Raman spectroscopy measurements of the pressure-temperature behavior of $LiAlH_4$. *Journal of Physical Chemistry C* **2010,** *114*, 11991-11997.

(79) Talyzin, A.; Sundqvist, B. High-pressure study of $NaAlH_4$ by Raman spectroscopy up to 17 GPa. *High Pressure Research* **2006,** *26*, 165-173.

(80) Kumar, R. S.; Ke, X.; Cornelius, A. L.; Chen, C. F. Effect of pressure and temperature on structural stability of potential hydrogen storage compound Li_3AlH_6. *Chemical Physics Letters* **2008,** *460*, 442-446.

(81) Talyzin, A. V.; Sundqvist, B. Reversible phase transition in $LiAlH_4$ under high-pressure conditions. *Physical Review B* **2004,** *70*, 180101.

(82) Liu, A.; Xie, S. T.; Dabiran-Zohoory, S.; Song, Y. High-pressure structures and transformations of calcium borohydride probed by combined Raman and Infrared spectroscopies. *Journal of Physical Chemistry C* **2010,** *114*, 11635-11642.

www.manaraa.com

(83) Filinchuk, Y.; Chernyshov, D.; Nevidomskyy, A.; Dmitriev, V. High-pressure polymorphism as a step towards destabilization of $LiBH_4$. *Angewandte Chemie-International Edition* **2008,** *47*, 529-532.

(84) George, L.; Drozd, V.; Saxena, S. K.; Bardaji, E. G.; Fichtner, M. Structural phase transitions of $Mg(BH_4)_2$ under pressure. *Journal of Physical Chemistry C* **2009,** *113*, 486-492.

(85) Tumanov, N. A.; Roedern, E.; Lodziana, Z.; Nielsen, D. B.; Jensen, T. R.; Talyzin, A. V.; Cerny, R.; Chernyshov, D.; Dmitriev, V.; Palasyuk, T., et al. High-pressure study of $Mn(BH4)_2$ reveals a stable polymorph with high hydrogen density. *Chemistry of Materials* **2016,** *28*, 274-283.

(86) Qi, G. Y.; Wang, K.; Li, X. D.; Zou, B. High pressure behavior of hydrogen storage material guanidinium borohydride. *Journal of Physical Chemistry C* **2016,** *120*, 13414-13420.

(87) Kohlmann, H.; Zhao, Y. S.; Nicol, M. F.; McClure, J. The crystal structure of alpha-MgD_2 under high pressure by neutron powder diffraction. *Zeitschrift Fur Kristallographie* **2008,** *223*, 706-710.

(88) Bortz, M.; Bertheville, B.; Bottger, G.; Yvon, K. Structure of the high pressure phase gamma-MgH_2 by neutron powder diffraction. *Journal of Alloys and Compounds* **1999,** *287*, L4-L6.

(89) Vajeeston, P.; Ravindran, P.; Kjekshus, A.; Fjellvag, H. Pressure-induced structural transitions in MgH_2. *Physical Review Letters* **2002,** *89*, 175506.

(90) Vajeeston, P.; Ravindran, P.; Hauback, B. C.; Fjellvag, H.; Kjekshus, A.; Furuseth, S.; Hanfland, M. Structural stability and pressure-induced phase transitions in MgH_2. *Physical Review B* **2006,** *73*, 224102.

www.manaraa.com

(91) Cui, S. X.; Feng, W. X.; Hu, H. Q.; Feng, Z. B.; Wang, Y. X. Structural phase transitions in MgH_2 under high pressure. *Solid State Communications* **2008,** *148*, 403-405.

(92) Allis, D. G.; Kosmowski, M. E.; Hudson, B. S. The inelastic neutron scattering spectrum of $H_3B : NH_3$ and the reproduction of its solid-state features by periodic DFT. *Journal of the American Chemical Society* **2004,** *126*, 7756-7757.

(93) Hess, N. J.; Bowden, M. E.; Parvanov, V. M.; Mundy, C.; Kathmann, S. M.; Schenter, G. K.; Autrey, T. Spectroscopic studies of the phase transition in ammonia borane: Raman spectroscopy of single crystal NH_3BH_3 as a function of temperature from 88 to 330 K. *Journal of Chemical Physics* **2008,** *128*, 034508.

(94) Cho, H.; Shaw, W. J.; Parvanov, V.; Schenter, G. K.; Karkamkar, A.; Hess, N. J.; Mundy, C.; Kathmann, S.; Sears, J.; Lipton, A. S., et al. Molecular structure and dynamics in the low temperature (orthorhombic) phase of NH_3BH_3. *Journal of Physical Chemistry A* **2008,** *112*, 4277-4283.

(95) Kathmann, S. M.; Parvanov, V.; Schenter, G. K.; Stowe, A. C.; Daemen, L. L.; Hartl, M.; Linehan, J.; Hess, N. J.; Karkamkar, A.; Autrey, T. Experimental and computational studies on collective hydrogen dynamics in ammonia borane: Incoherent inelastic neutron scattering. *Journal of Chemical Physics* **2009,** *130*, 024507.

(96) Ziparo, C.; Colognesi, D.; Giannasi, A.; Zoppi, M. Raman spectra of ammonia borane: Low frequency lattice modes. *Journal of Physical Chemistry A* **2012,** *116*, 8827-8832.

(97) Klooster, W. T.; Koetzle, T. F.; Siegbahn, P. E. M.; Richardson, T. B.; Crabtree, R. H. Study of the N-H···H-B dihydrogen bond including the crystal structure of BH_3NH_3 by neutron diffraction. *Journal of the American Chemical Society* **1999,** *121*, 6337-6343.

www.manaraa.com

(98) Lin, Y.; Mao, W. L.; Drozd, V.; Chen, J. H.; Daemen, L. L. Raman spectroscopy study of ammonia borane at high pressure. *Journal of Chemical Physics* **2008,** *129*, 234509.

(99) Xie, S. T.; Song, Y.; Liu, Z. X. In situ high-pressure study of ammonia borane by Raman and IR spectroscopy. *Canadian Journal of Chemistry-Revue Canadienne De Chimie* **2009,** *87*, 1235-1247.

(100) Filinchuk, Y.; Nevidomskyy, A. H.; Chernyshov, D.; Dmitriev, V. High-pressure phase and transition phenomena in ammonia borane NH_3BH_3 from x-ray diffraction, Landau theory, and ab initio calculations. *Physical Review B* **2009,** *79*, 214111.

(101) Chen, J. H.; Couvy, H.; Liu, H. Z.; Drozd, V.; Daemen, L. L.; Zhao, Y. S.; Kao, C. C. In situ X-ray study of ammonia borane at high pressures. *International Journal of Hydrogen Energy* **2010,** *35*, 11064-11070.

(102) Wang, L. C.; Bao, K.; Meng, X.; Wang, X. L.; Jiang, T. T.; Cui, T. A.; Liu, B. B.; Zou, G. T. Structural and dynamical properties of solid ammonia borane under high pressure. *Journal of Chemical Physics* **2011,** *134*, 024517.

(103) Liu, A.; Song, Y. In Situ high-pressure and low-temperature study of ammonia borane by Raman spectroscopy. *Journal of Physical Chemistry C* **2012,** *116*, 2123-2131.

(104) Lin, Y.; Ma, H. W.; Matthews, C. W.; Kolb, B.; Sinogeikin, S.; Thonhauser, T.; Mao, W. L. Experimental and theoretical studies on a high pressure monoclinic phase of ammonia borane. *Journal of Physical Chemistry C* **2012,** *116*, 2172-2178.

(105) Trudel, S.; Gilson, D. F. R. High-pressure Raman spectroscopic study of the ammonia-borane complex. Evidence for the dihydrogen bond. *Inorganic Chemistry* **2003,** *42*, 2814-2816.

(106) Custelcean, R.; Dreger, Z. A. Dihydrogen bonding under high pressure: A Raman study of BH_3NH_3 molecular crystal. *Journal of Physical Chemistry B* **2003,** *107*, 9231-9235.

www.manaraa.com

(107) Mao, W. L.; Koh, C. A.; Sloan, E. D. Clathrate, hydrates under pressure. *Physics Today* **2007,** *60*, 42-47.

(108) Struzhkin, V. V.; Militzer, B.; Mao, W. L.; Mao, H. K.; Hemley, R. J. Hydrogen storage in molecular clathrates. *Chemical Reviews* **2007,** *107*, 4133-4151.

(109) Strobel, T. A.; Hester, K. C.; Koh, C. A.; Sum, A. K.; Sloan, E. D. Properties of the clathrates of hydrogen and developments in their applicability for hydrogen storage. *Chemical Physics Letters* **2009,** *478*, 97-109.

(110) Chidester, B. A.; Strobel, T. A. The ammonia-hydrogen system under pressure. *Journal of Physical Chemistry A* **2011,** *115*, 10433-10437.

(111) Mao, W. L.; Mao, H. K.; Goncharov, A. F.; Struzhkin, V. V.; Guo, Q. Z.; Hu, J. Z.; Shu, J. F.; Hemley, R. J.; Somayazulu, M.; Zhao, Y. S. Hydrogen clusters in clathrate hydrate. *Science* **2002,** *297*, 2247-2249.

(112) Vos, W. L.; Finger, L. W.; Hemley, R. J.; Mao, H. K. Novel H_2-H_2O clathrates at high-pressures. *Physical Review Letters* **1993,** *71*, 3150-3153.

(113) Vos, W. L.; Finger, L. W.; Hemley, R. J.; Mao, H. K. Pressure dependence of hydrogen bonding in a novel H_2O-H_2 clathrate. *Chemical Physics Letters* **1996,** *257*, 524-530.

(114) Lokshin, K. A.; Zhao, Y. S.; He, D. W.; Mao, W. L.; Mao, H. K.; Hemley, R. J.; Lobanov, M. V.; Greenblatt, M. Structure and dynamics of hydrogen molecules in the novel clathrate hydrate by high pressure neutron diffraction. *Physical Review Letters* **2004,** *93*, 125503.

(115) Lu, H. L.; Wang, J. W.; Liu, C. L.; Ratcliffe, C. I.; Becker, U.; Kumar, R.; Ripmeester, J. Multiple H_2 occupancy of cages of clathrate hydrate under mild conditions. *Journal of the American Chemical Society* **2012,** *134*, 9160-9162.

www.manaraa.com

(116) Hakim, L.; Koga, K.; Tanaka, H. Phase behavior of different forms of ice filled with hydrogen molecules. *Physical Review Letters* **2010,** *104*, 115701.

(117) Chen, X. J.; Struzhkin, V. V.; Song, Y.; Goncharov, A. F.; Ahart, M.; Liu, Z. X.; Mao, H.; Hemley, R. J. Pressure-induced metallization of silane. *Proceedings of the National Academy of Sciences of the United States of America* **2008,** *105*, 20-23.

(118) Eremets, M. I.; Trojan, I. A.; Medvedev, S. A.; Tse, J. S.; Yao, Y. Superconductivity in hydrogen dominant materials: Silane. *Science* **2008,** *319*, 1506-1509.

(119) Strobel, T. A.; Somayazulu, M.; Hemley, R. J. Novel pressure-induced interactions in silane-hydrogen. *Physical Review Letters* **2009,** *103*, 065701.

(120) Wang, S. B.; Mao, H. K.; Chen, X. J.; Mao, W. L. High pressure chemistry in the H_2-SiH_4 system. *Proceedings of the National Academy of Sciences of the United States of America* **2009,** *106*, 14763-14767.

(121) Li, Y. W.; Gao, G. Y.; Xie, Y.; Ma, Y. M.; Cui, T. A.; Zou, G. T. Superconductivity at similar to 100 K in dense $SiH_4(H_2)_2$ predicted by first principles. *Proceedings of the National Academy of Sciences of the United States of America* **2010,** *107*, 15708-15711.

(122) Yim, W. L.; Tse, J. S.; Iitaka, T. Pressure-induced intermolecular interactions in crystalline silane-hydrogen. *Physical Review Letters* **2010,** *105*, 215501.

(123) Somayazulu, M. S.; Finger, L. W.; Hemley, R. J.; Mao, H. K. High-pressure compounds in methane-hydrogen mixtures. *Science* **1996,** *271*, 1400-1402.

(124) Somayazulu, M. S.; Hemley, R. J.; Goncharov, A. F.; Mao, H. K.; Finger, L. W. High-pressure compounds in the methane-hydrogen system: X-ray, infrared and Raman studies on $CH_4(H_2)_2$. *European Journal of Solid State and Inorganic Chemistry* **1997,** *34*, 705-713.

www.manaraa.com

(125) Lin, Y.; Mao, W. L.; Mao, H. K. Storage of molecular hydrogen in an ammonia borane compound at high pressure. *Proceedings of the National Academy of Sciences of the United States of America* **2009,** *106*, 8113-8116.

(126) Wang, S. B.; Mao, W. L.; Autrey, T. Bonding in boranes and their interaction with molecular hydrogen at extreme conditions. *Journal of Chemical Physics* **2009,** *131*, 144508.

(127) Chellappa, R. S.; Somayazulu, M.; Struzhkin, V. V.; Autrey, T.; Hemley, R. J. Pressure-induced complexation of NH_3BH_3-H_2. *Journal of Chemical Physics* **2009,** *131*, 224515.

(128) Lazicki, A.; Loubeyre, P.; Occelli, F.; Hemley, R. J.; Mezouar, M. Static compression of LiH to 250 GPa. *Physical Review B* **2012,** *85*, 054103.

(129) Drozd, V.; Garimella, S.; Saxena, S.; Chen, J.; Palasyuk, T. High-pressure Raman and X-ray diffraction study of β-and γ-polymorphs of aluminum hydride. *The Journal of Physical Chemistry C* **2012,** *116*, 3808-3816.

(130) Graetz, J.; Chaudhuri, S.; Lee, Y.; Vogt, T.; Muckerman, J.; Reilly, J. Pressure-induced structural and electronic changes in α− AlH_3. *Physical Review B* **2006,** *74*, 214114.

(131) Goncharenko, I. I. Goncharenko, MI Eremets, M. Hanfland, JS Tse, M. Amboage, Y. Yao, and IA Trojan. Pressure-induced hydrogen-dominant metallic state in aluminum hydride. *Physical Review Letters* **2008,** *100*, 045504.

(132) Yan, S.; Lee, J. Y. Excess electrons in $LiAlH_4$ clusters: Implication for hydrogen storage. *The Journal of Physical Chemistry C* **2008,** *113*, 1104-1108.

(133) Pitt, M.; Blanchard, D.; Hauback, B.; Fjellvåg, H.; Marshall, W. Pressure-induced phase transitions of the $LiAlD_4$ system. *Physical Review B* **2005,** *72*, 214113.

www.manaraa.com

(134) Soulié, J.-P.; Renaudin, G.; Černý, R.; Yvon, K. Lithium boro-hydride $LiBH_4$: I. Crystal structure. *Journal of Alloys and Compounds* **2002,** *346*, 200-205.

(135) Miwa, K.; Aoki, M.; Noritake, T.; Ohba, N.; Nakamori, Y.; Towata, S.-i.; Züttel, A.; Orimo, S.-i. Thermodynamical stability of calcium borohydride $Ca(BH_4)_2$. *Physical Review B* **2006,** *74*, 155122.

(136) Filinchuk, Y.; Rönnebro, E.; Chandra, D. Crystal structures and phase transformations in $Ca(BH_4)_2$. *Acta Materialia* **2009,** *57*, 732-738.

(137) Chellappa, R. S.; Chandra, D.; Somayazulu, M.; Gramsch, S. A.; Hemley, R. J. Pressure-induced phase transitions in $LiNH_2$. *The Journal of Physical Chemistry B* **2007,** *111*, 10785-10789.

(138) Huang, X.; Li, D.; Li, F.; Jin, X.; Jiang, S.; Li, W.; Yang, X.; Zhou, Q.; Zou, B.; Cui, Q. Large volume collapse during pressure-induced phase transition in lithium amide. *The Journal of Physical Chemistry C* **2012,** *116*, 9744-9749.

(139) Szafranski, M.; Katrusiak, A. Photovoltaic hybrid perovskites under pressure. *Journal of Physical Chemistry Letters* **2017,** *8*, 2496-2506.

(140) Shockley, W.; Queisser, H. J. Detailed balance limit of efficiency of p-n junction solar cells. *Journal of Applied Physics* **1961,** *32*, 510-519.

(141) Sha, W. E. I.; Ren, X. G.; Chen, L. Z.; Choy, W. C. H. The efficiency limit of $CH_3NH_3PbI_3$ perovskite solar cells. *Applied Physics Letters* **2015,** *106*, 221104.

(142) Colella, S.; Mosconi, E.; Fedeli, P.; Listorti, A.; Gazza, F.; Orlandi, F.; Ferro, P.; Besagni, T.; Rizzo, A.; Calestani, G., et al. $MAPbI_{3-x}Cl_x$ mixed halide perovskite for hybrid solar cells: The role of chloride as dopant on the transport and structural properties. *Chemistry of Materials* **2013,** *25*, 4613-4618.

www.manaraa.com

(143) Li, Q.; Li, S. R.; Wang, K.; Quan, Z. W.; Meng, Y.; Zou, B. High-pressure study of perovskite-like organometal halide: Band-gap narrowing and structural evolution of $NH_3(CH_2)_4NH_3CuCl_4$. *Journal of Physical Chemistry Letters* **2017,** *8*, 500-506.

(144) Jaffe, A.; Lin, Y.; Karunadasa, H. I. Halide perovskites under pressure: Accessing new properties through lattice compression. *Acs Energy Letters* **2017,** *2*, 1549-1555.

(145) Postorino, P.; Malavasi, L. Pressure-induced effects in organic-inorganic hybrid perovskites. *Journal of Physical Chemistry Letters* **2017,** *8*, 2613-2622.

(146) Swainson, I. P.; Tucker, M. G.; Wilson, D. J.; Winkler, B.; Milman, V. Pressure response of an organic-inorganic perovskite: Methylammonium lead bromide. *Chemistry of Materials* **2007,** *19*, 2401-2405.

(147) Wang, Y. H.; Lu, X. J.; Yang, W. G.; Wen, T.; Yang, L. X.; Ren, X. T.; Wang, L.; Lin, Z. S.; Zhao, Y. S. Pressure-induced phase transformation, reversible amorphization, and anomalous visible light response in organolead bromide perovskite. *Journal of the American Chemical Society* **2015,** *137*, 11144-11149.

(148) Jaffe, A.; Lin, Y.; Beavers, C. M.; Voss, J.; Mao, W. L.; Karunadasa, H. I. High-pressure single-crystal structures of 3D lead-halide hybrid perovskites and pressure effects on their electronic and optical properties. *Acs Central Science* **2016,** *2*, 201-209.

(149) Wang, L. R.; Wang, K.; Zou, B. Pressure-induced structural and optical properties of organometal halide perovskite-based formamidinium lead bromide. *Journal of Physical Chemistry Letters* **2016,** *7*, 2556-2562.

(150) Capitani, F.; Marini, C.; Caramazza, S.; Postorino, P.; Garbarino, G.; Hanfland, M.; Pisanu, A.; Quadrelli, P.; Malavasi, L. High-pressure behavior of methylammonium lead iodide ($MAPbI_3$) hybrid perovskite. *Journal of Applied Physics* **2016,** *119*, 185901.

(151) Liu, G.; Kong, L. P.; Gong, J.; Yang, W. G.; Mao, H. K.; Hu, Q. Y.; Liu, Z. X.; Schaller, R. D.; Zhang, D. Z.; Xu, T. Pressure-induced bandgap optimization in lead-

www.manaraa.com

based perovskites with prolonged carrier lifetime and ambient retainability. *Advanced Functional Materials* **2017,** *27*, 1604208.

(152) Jiang, S. J.; Fang, Y. A.; Li, R. P.; Xiao, H.; Crowley, J.; Wang, C. Y.; White, T. J.; Goddard, W. A.; Wang, Z. W.; Baikie, T., et al. Pressure-dependent polymorphism and band-gap tuning of methylammonium lead iodide perovskite. *Angewandte Chemie-International Edition* **2016,** *55*, 6540-6544.

(153) Ou, T. J.; Yan, J. J.; Xiao, C. H.; Shen, W. S.; Liu, C. L.; Liu, X. Z.; Han, Y. H.; Ma, Y. Z.; Gao, C. X. Visible light response, electrical transport, and amorphization in compressed organolead iodine perovskites. *Nanoscale* **2016,** *8*, 11426-11431.

(154) Szafranski, M.; Katrusiak, A. Mechanism of pressure-induced phase transitions, amorphization, and absorption-edge shift in photovoltaic methylammonium lead iodide. *Journal of Physical Chemistry Letters* **2016,** *7*, 3458-3466.

(155) Wang, K.; Liu, R.; Qiao, Y.; Cui, J.; Song, B.; Liu, B.; Zou, B. Pressure-induced reversible phase transition and amorphization of $CH_3NH_3PbI_3$. *Acta Physica Sinica* **2015,** *66*, 030701.

(156) Lee, Y.; Mitzi, D. B.; Barnes, P. W.; Vogt, T. Pressure-induced phase transitions and templating effect in three-dimensional organic-inorganic hybrid perovskites. *Physical Review B* **2003,** *68*, 020103.

(157) Lu, X. J.; Wang, Y. G.; Stoumpos, C. C.; Hu, Q. Y.; Guo, X. F.; Chen, H. J.; Yang, L. X.; Smith, J. S.; Yang, W. G.; Zhao, Y. S., et al. Enhanced structural stability and photo responsiveness of $CH_3NH_3SnI_3$ perovskite via pressure-induced amorphization and recrystallization. *Advanced Materials* **2016,** *28*, 8663-8668.

(158) Wang, L. R.; Wang, K.; Xiao, G. J.; Zeng, Q. S.; Zou, B. Pressure-induced structural evolution and band gap shifts of organometal halide perovskite-based methylammonium lead chloride. *Journal of Physical Chemistry Letters* **2016,** *7*, 5273-5279.

www.manaraa.com

(159) Jaffe, A.; Lin, Y.; Mao, W. L.; Karunadasa, H. I. Pressure-induced conductivity and yellow-to-black piezochromism in a layered Cu-Cl hybrid perovskite. *Journal of the American Chemical Society* **2015,** *137*, 1673-1678.

(160) Sun, S. J.; Deng, Z. Y.; Wu, Y.; Wei, F. X.; Isikgor, F. H.; Brivio, F.; Gaultois, M. W.; Ouyang, J. Y.; Bristowe, P. D.; Cheetham, A. K., et al. Variable temperature and high-pressure crystal chemistry of perovskite formamidinium lead iodide: a single crystal X-ray diffraction and computational study. *Chemical Communications* **2017,** *53*, 7537-7540.

(161) Gesi, K. Effect of hydrostatic pressure on the structural phase transitions in $CH_3NH_3PbX_3$ (X = Cl, Br, I). *Ferroelectrics* **1997,** *203*, 249-268.

(162) Matsuishi, K.; Ishihara, T.; Onari, S.; Chang, Y. H.; Park, C. H. Optical properties and structural phase transitions of lead-halide based inorganic-organic 3D and 2D perovskite semiconductors under high pressure. *Physica Status Solidi B-Basic Research* **2004,** *241*, 3328-3333.

(163) Jaffe, A.; Lin, Y.; Mao, W. L.; Karunadasa, H. I. Pressure-induced metallization of the halide perovskite $(CH_3NH_3)PbI_3$. *Journal of the American Chemical Society* **2017,** *139*, 4330-4333.

www.manaraa.com

Chapter 2

2 Experimental

2.1 Materials preparation

2.1.1 Mechanochemistry and ball milling synthetic method

Mechanochemistry is the combination of mechanical and chemical processes on a molecular scale, which was defined by IUPAC as a chemical reaction that is induced by the direct absorption of mechanical energy, the process of shearing, stretching and grinding could generate the reactive sites for the chemical reactions.[1] Nowadays, the employment of ball mills for materials synthesis has been a strong emerging field of research. Moreover, it has been widely employed in industry to synthesize a variety of commercially useful materials including a wide variety of chemical hydrides.[2] The advantages of using ball mills instead of conventional processing routes are the reduction of reaction time, the gain of higher yield and without the need for purification.[3-4]

A ball mill is a type of grinder, which is widely used to grind or mix metals or other raw materials for further processing. It consists of a hollow cylindrical jar rotating about its axis and some balls as the grinding media, which could be made of hardened steel, stainless steel, tungsten carbide, agate and zirconium oxide. Among various kinds of ball mills, planetary ball mills have become the most frequently used apparatus due to several benefits, for instance, the ease of simple set up, the excellent cleanability, moderate cost of the device[2] and grinding particles down to the nanometer size range.[5]

As shown in Figure 2.1, a Retsch planetary ball mill was used to synthesize $NaNH_2BH_3$. The jars and the grinding balls are made of stainless steel. The reactants were sealed in the jars in glovebox due to their air sensitivity. Besides, several grinding balls were also placed into the jars according to a specific ratio of ball to sample. Once two grinding jars are clamped tightly eccentrically on the wheel of the planetary ball mill, the reaction proceeds, without the addition of solvents. The grinding balls in the grinding jars are

www.manaraa.com

subjected to superimposed rotational movements under the ultra-high speed (up to 250 rpm), which releases high dynamic energies.

Figure 2.1 Photos of Retsch PM 200 planetary ball mill and grinding jars and balls

2.1.2 Wet chemistry method

Even though it is convenient to synthesize the materials via ball milling method, it still limits to one-step reactions. Therefore, we synthesized other materials by wet chemistry method. In this thesis, hydrazine borane and two polymorphs of $FAPbI_3$ were synthesized by wet chemistry method. The details are provided in Chapter 4 and Chapter 6.

2.2 High-pressure apparatus

2.2.1 Diamond anvil cells

The recent advances of high-pressure techniques provide the researchers with the opportunities for a deeper understanding of matters, such as diamond anvil technology. Diamonds are the hardest material in nature, which makes them applicable for the generation of high pressure, reaching as high as 400 GPa.[6] Moreover, diamonds are transparent to a broad spectral range of electromagnetic radiation. Therefore, the diamond anvil cells (DAC) are widely used in the high-pressure area using various *in-situ* characterizations, such as vibrational spectroscopy and X-ray diffraction.

As shown in Figure 2.2, a symmetrical DAC consists of two opposing diamond anvils, which are mounted on the two supporting seats, usually made of tungsten carbide. The

www.manaraa.com

culet of the diamonds are normally tens to hundreds of microns in diameter. A pre-indented stainless steel gasket with a hole drilled at the center is placed between two diamonds, which was used as the sample chamber. A few ruby balls are also loaded in the sample chamber as the pressure calibrant. High pressure can be generated by tightening screws which are embedded in the pistons, and the range of the pressure is determined by the culet size of diamonds.

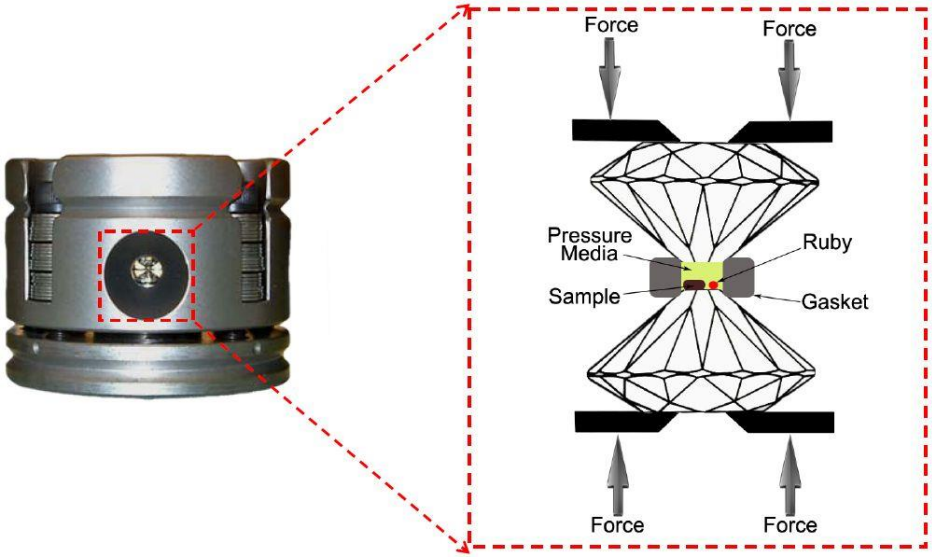

Figure 2.2 The photo of a DAC and a schematic draw of DAC with the diamond anvils enlarged[7]

Generally, there are two different types of diamonds according to the level and type of their chemical impurities, namely type I and type II. Both types of diamonds contain nitrogen atoms as their main impurity, which are within the crystal lattice of carbon atoms and could be detected by vibrational spectroscopy.[8] The purity of type II is higher than type I. They both have a strong first order Raman line at 1332 cm^{-1}, and type I diamond has two absorption region at around 1000-1350 cm^{-1} and 2000 cm^{-1} for IR absorption, while there is only one absorption region at around 2000 cm^{-1} in the IR spectrum of type II diamond.[8-9] Therefore, type I diamonds can only be used in Raman spectroscopy, and type II diamonds could be satisfied in IR spectroscopy.

www.manaraa.com

2.2.2 Pressure gauge

Ruby luminescence method has been used to determine the pressure inside the DAC since 1972, which supports the widespread application of DAC for in situ high-pressure investigations. This optical pressure sensing method is still the most common technique in high-pressure experiments nowadays.[10-13]

When alumina is doped with chromium, the substitution of Al^{3+} by Cr^{3+} ions leads to the formation of ruby, which has two intense luminescent peaks R_1 and R_2 when it was excited by laser, as shown in Figure 2.3. The positions of R_1 and R_2 show the redshift with the increasing pressure. The use of the R-line luminescence to measure pressure was established after the method calibrated by other primary pressure standards, such as Au, Cu, Mo and Pt, under quasi-hydrostatic conditions in argon or neon medium.[10-11] Using this method, the relation between applied hydrostatic pressure P and wavelength change $\Delta\lambda$ of the R-line emission, as shown in Equation 2.1, could be applied up to 80 GPa, and the resolution of the pressure can be achieved to ± 0.05 GPa.[11] In this equation, P is the *in-situ* pressure in GPa, $\Delta\lambda$ is the wavelength shift of R_1 peak in nm, the parameter B equals 7.665 under the quasi-hydrostatic condition.

$$P = \frac{1904}{B}\left[\left(1+\frac{\Delta\lambda}{694.24}\right)^{B}-1\right] \qquad \text{Equation 2.1}$$

www.manaraa.com

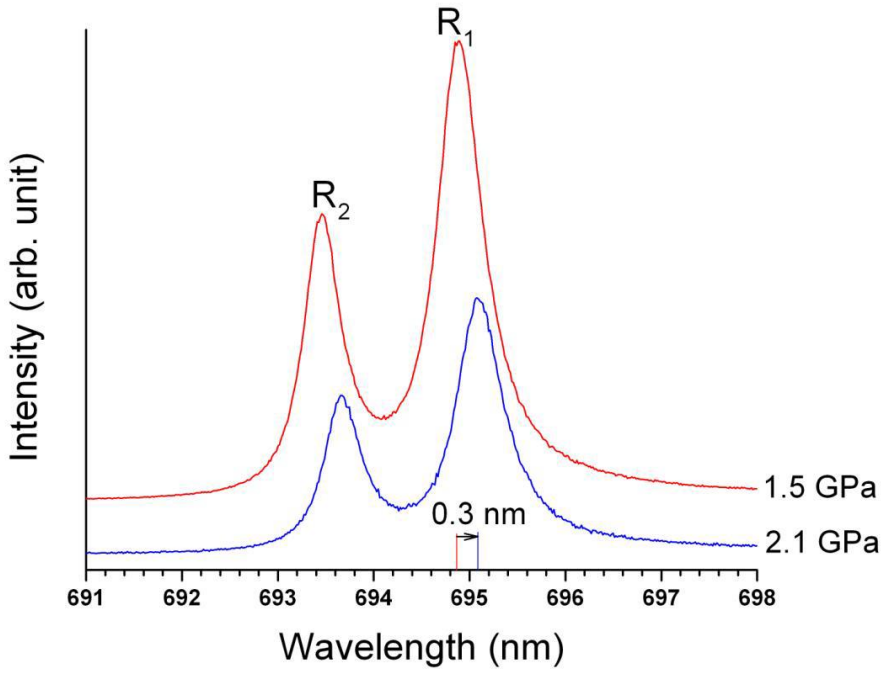

Figure 2.3 Ruby luminescence measured at different pressures (1.5 and 2.1 GPa) with two sharp luminescent peaks (R_1 and R_2)[7]

2.2.3 Pressure transmitting medium

Hydrostatic pressure is preferred for the high-pressure experiments, which means no pressure gradient in the entire sample area during the compression. Otherwise, the variation in strain throughout the sample can lead to distorted observations of different behaviors. In order to maintain the hydrostatic conditions, a pressure transmitting medium (PTM) is used to load into the sample chamber, which is a compressible fluid. A proper PTM should satisfy several requirements, such as low shear strength, low thermal conductivity, not reacting with the sample and maintaining hydrostatic condition to as high pressure as possible. The common used PTMs are listed in Table 2.1 with the highest pressure they can achieve under hydrostatic condition. Accordingly, the choice of PTM depends on the highest pressure in the experiment. In this thesis, no PTM was used for hydrogen storage materials due to the pressure range in the experiments and the air

www.manaraa.com

sensitivity of samples. Neon was used as PTM loaded together with $FAPbI_3$ using the gas loading system at GSECARS of APS.

Table 2.1 The common PTMs and their highest pressure maintaining the hydrostatic condition[14-15]

Pressure transmitting medium	P_{max} maintaining the hydrostatic condition
Methanol	8.6 GPa
4:1 methanol-ethanol	10.5 GPa
16:3:1 methanol-ethanol-H_2O	10.5 GPa
silicon oil	20 GPa
Ne	50 GPa

2.3 *In-situ* high-pressure characterizations

2.3.1 Vibrational spectroscopy

Vibrational spectroscopy is a non-destructive identification method that measures the vibrational energy in a compound. Each chemical bond has unique vibrational energy, which could be recorded by vibrational spectroscopy when a molecule interacts with the light. Such information could provide the information regarding molecular structures, chemical bonding and changes in crystal structures. In particular, high-pressure studies of materials using vibrational spectroscopy could provide the pressure effects on chemical bonding and local structures, which are investigated in this thesis.

The most common techniques for vibrational spectroscopy are Infrared (IR) and Raman spectroscopy, based on the different selection rules. In infrared spectroscopy, infrared light over broad frequencies is passed through a sample. The IR absorption can be detected when the molecular dipole moment changes during the vibration, according to the equation 2.2.

www.manaraa.com

$$\frac{\delta\mu}{\delta q} \neq 0 \qquad \text{Equation 2.2}$$

Where $\delta\mu$ is the variation of the dipolar moment, δq is the variation of the normal coordinates. A change of the position of the atoms relative to each other must induce a change of the electric dipole, and the interactions between the change of dipole and the incoming light lead to the absorption when $h\nu = \Delta E$, as shown in Figure 2.4.

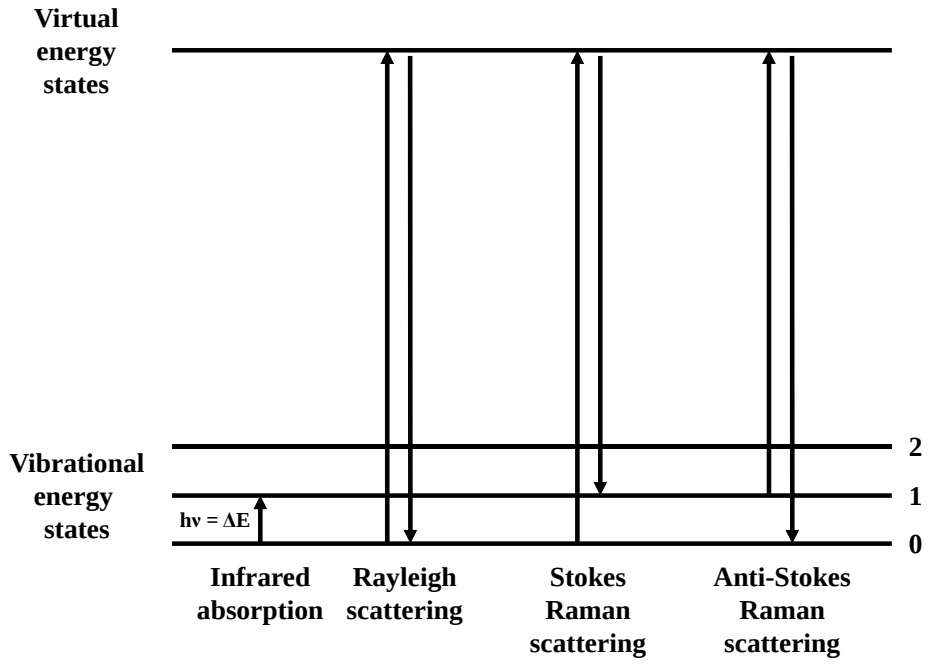

Figure 2.4 Illustration of IR absorption, Rayleigh scattering and Raman scattering

Similar to IR, Raman spectroscopy could also be used to collect the information of the molecular structures and the chemical bonding. In Raman spectroscopy, the sample is irradiated by an intense laser beam, and a part of the light will be scattered along different directions. The scattered light consists of two types, Rayleigh scattering, which is strong and has the same frequency as the incident beam. The other one is Raman scattering, which is very weak (10^{-5} of intensity of the incident beam) and has a different frequency from the incident beam. As illustrated in Figure 2.4, there are two kinds of Raman scattering, stokes and anti-stokes Raman scattering. When the molecule comes back from

www.manaraa.com

virtual state, if the energy of scattered photon is less than the incident photon, it is stokes scattering and the molecule absorbs energy; if the energy of scattered photon is greater than the incident photon, it is anti-stokes scattering and the molecule loses energy. Typically, most molecules are initially in their ground state. Therefore, stokes scattering is stronger than anti-Stokes scattering, which makes stokes scattering mainly measured in Raman spectroscopy.

The Raman effect is based on the interaction between the electron cloud of a molecule and the external electrical field of the monochromatic light, which can create an induced dipole moment within the molecule based on its polarizability. The selection rule for Raman scattering is that the polarizability of the molecule should change as it vibrates, as shown in Equation 2.3, where $\delta\alpha$ is the variation of polarizability, δq is the variation of the normal coordinates.

$$\frac{\delta\alpha}{\delta q} \neq 0 \qquad \text{Equation 2.3}$$

For the Raman measurements of solid with the crystal structure, the lattice vibrations could also be detected, and these modes are weak in energy and are found at low frequencies (approximately in the region of $400 - 10\ cm^{-1}$). Lattice modes are further classified as translations and rotations, and occur in ionic or molecular crystals.[16]

2.3.2 IR spectroscopy system

A customized IR micro-spectroscopy system was set up in our lab for the IR measurements, as shown in Figure 2.5. The main parts of the IR micro-spectroscopy system are a commercial Fourier transform infrared (FTIR) spectrometer, which was from Bruker Optics Inc. (model Vertex 80v), and a Globar IR light source. The system is operated under a vacuum of less than 5 mbar in order to remove the interference from H_2O and CO_2. An IR beam is collimated and directed into a relay box through a KBr window on the spectrometer. The beam is then focused onto the sample by iris optics and 15× reflective objective lens. After the DAC is placed on the sample stage and aligned with the aid of an optical microscope, the size of the IR beam is adjusted to be identical

www.manaraa.com

to the sample size (150 μm) by a series of iris apertures. Then the transmitted IR beam is collected and reflected by a condenser and several mirrors, and directed to a midband mercury cadmium telluride (MCT) detector allowing measurements in the spectral range of 600 cm^{-1} to 12000 cm^{-1}. A reference spectrum was collected as the background, which is the spectrum of diamonds and KBr loaded in the sample hole. Subsequently, the spectrum of each sample could be collected with a resolution of 4 cm^{-1} and 512 scans.

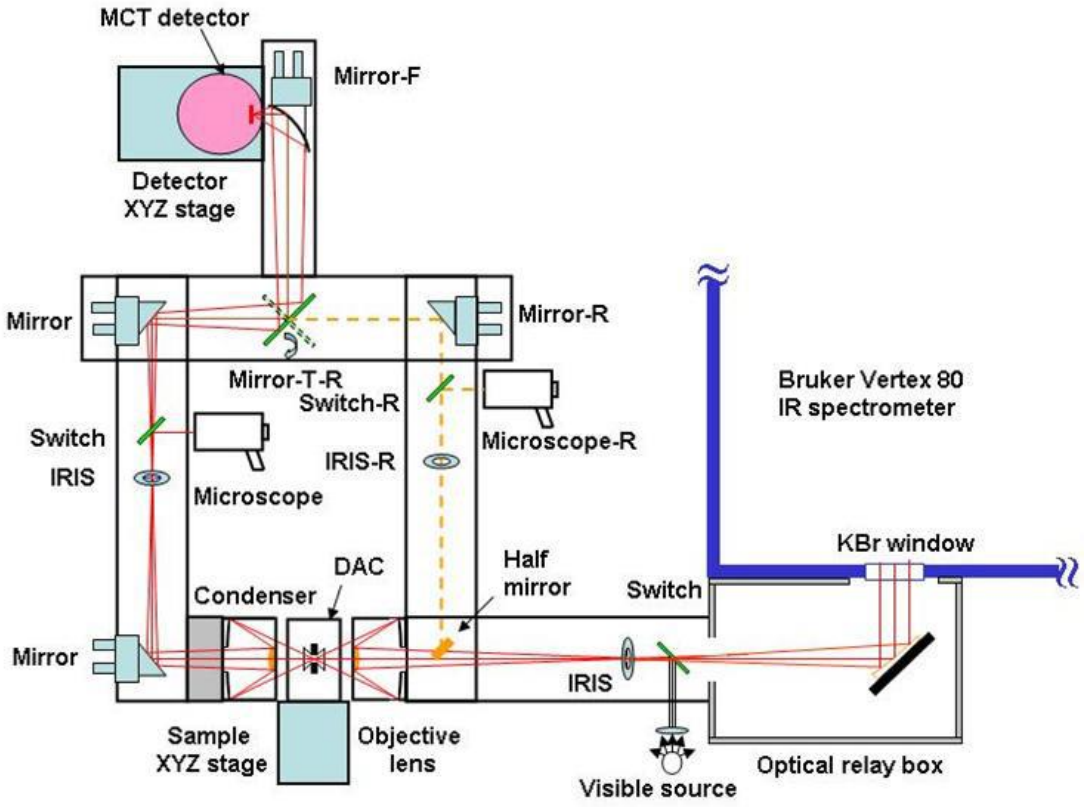

Figure 2.5 Schematic diagram of the IR micro-spectroscopy system[17]

2.3.3 Raman spectroscopy system

Same as IR spectroscopy, a user-customized Raman system was used for our Raman measurements and the schematic diagram of this Raman system in our lab is shown in Figure 2.6. The system consists of several parts, such as the laser source, a microscope system, and a CCD detector. A solid state laser with a wavelength of 532 nm is used as the excitation source in this thesis. The DAC is placed on the sample stage and is aligned

www.manaraa.com

under the microscope manually, followed by the focus of the laser beam onto the sample. The laser is focused to < 5 μm on the sample by a 20× objective. The Raman signal is detected with backscattering geometry by the same objective lens. A grating with 1200 lines/mm is used for all measurements. The Raman spectrum is recorded by a CCD detector (charge-coupled device), which is cooled by liquid nitrogen to maintain the -120 °C operation condition. A WinSpec software is used to control and collect the spectrum, which could be obtained by setting a proper accumulation time. The system is calibrated by using standard neon lines with the resolution of ± 1 cm^{-1}.

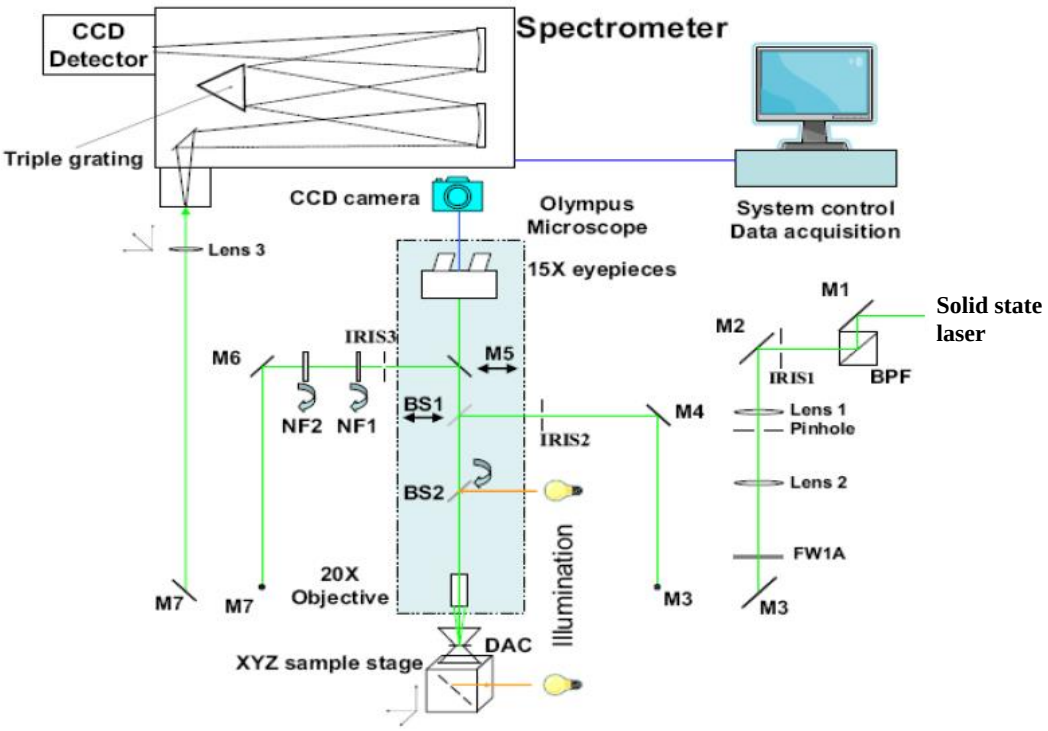

Figure 2.6 Schematic illustration of the Raman system[7]

2.3.4 Photoluminescence spectroscopy

Photoluminescence (PL) is one of the most important experimental techniques for the characterization of semiconductors. As shown in Figure 2.7, PL is a process in which a molecule absorbs a photon to excite one electron in the valence band to the conduction

www.manaraa.com

band, followed by the electron eventually falling back down to the valence band with the emission of a luminescent photon.[18] Thus the energy of the emitted photon is equal to the band gap energy, E_g. Therefore, PL spectroscopy can be used to measure the band gap of semiconductors. In this thesis, PL measurements of $FAPbI_3$ were carried out using the customized Raman spectrometer with a 532 nm diode pumped solid stat laser as the excitation laser.

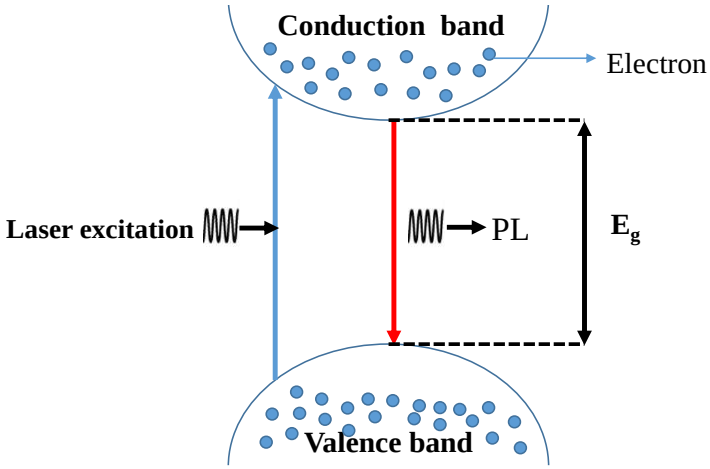

Figure 2.7 Illustration of the process of Photoluminescence

2.3.5 Synchrotron X-ray diffraction

X-ray diffraction technique is widely used in the structure analysis of matters, the basic principle of XRD is given by Bragg's law (Equation 2.4), where λ is the wavelength of X-ray, d_{hkl} is the spacing of the lattice planes with the Miller indices h, k, l, θ is the angle of Bragg reflection with respect to these planes.

$$n\lambda = 2d_{hkl}\sin\theta \qquad \text{Equation 2.4}$$

X-ray diffraction is a powerful tool to investigate the crystal structures and chemical compositions. However, the hydrogen storage materials investigated in this thesis are not suitable for the local X-ray source due to the small atomic scattering factor of low Z elements. Moreover, for the high-pressure XRD measurements, the sample is sealed in the diamond anvil cells, due to the small size of the sample, it requires the intense high energy X-ray beam and the small beam size to characterize the sample, which can hardly

www.manaraa.com

be achieved in the local XRD facilities. Therefore, synchrotron radiation (SR) becomes the best X-ray source in the high-pressure studies. Compared to the local sources, synchrotron radiation has many extraordinary advantages. Firstly, the brilliance of the X-ray beam achieved in SR is four to twelve orders of magnitude higher than that from a conventional X-ray source. Moreover, the resolution of XRD patterns is significantly increased in powder diffraction applications and the tunability of SR makes the researchers choose any desired wavelength easily. Furthermore, the highly collimated X-ray beam and a tiny opening angle realize the most satisfactory choice for high-pressure research due to the tiny size of the sample. Therefore, synchrotron radiation becomes the most effective method to investigate the materials under high pressure, even though its availability is restricted to several existing synchrotron sites.[19]

Synchrotron radiation is generated by accelerated electrons with energy E bent by a magnetic field H along a circular orbit, and SR is directed along the tangent to the orbit of the electron, as illustrated in Figure 2.8. Such radiation is extremely intense and highly tunable over a broad energy range from the infrared to hard x-ray regions. Moreover, it also gives a high spatial resolution and better signal-to-noise ratio, which makes SR a highly efficient and powerful tool for the structure analysis of materials.

The XRD patterns in this thesis were collected as Debye-Scherrer rings by a 2D detector at beam-line 16 and 20ID at Advanced Photon Source (APS) in Argonne National Laboratory (ANL), and the setup of beam-line 20ID is shown in Figure 2.9. The 2D Debye-Scherrer diffraction patterns were collected using a MARCCD detector and integrated by using Fit2D or Dioptas programs for further analysis.[20] Figure 2.10 shows the 2D and 1D patterns of CeO_2 collected in APS, which was used as a calibrant in the measurement of synchrotron XRD.

www.manaraa.com

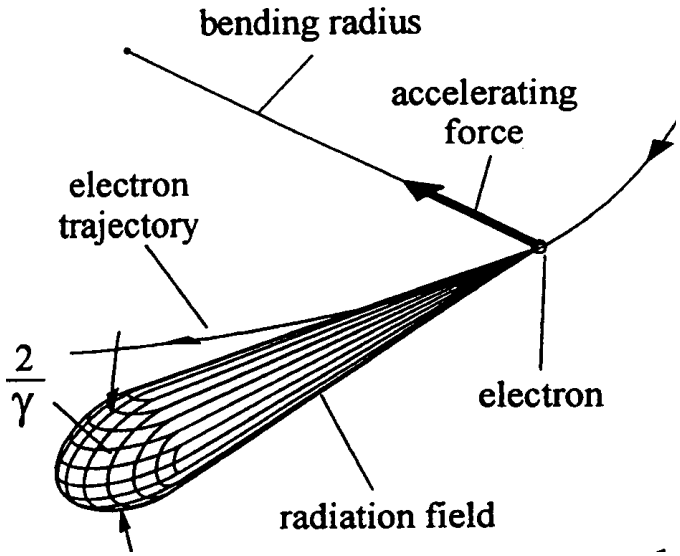

Figure 2.8 Illustration of the emission of synchrotron radiation

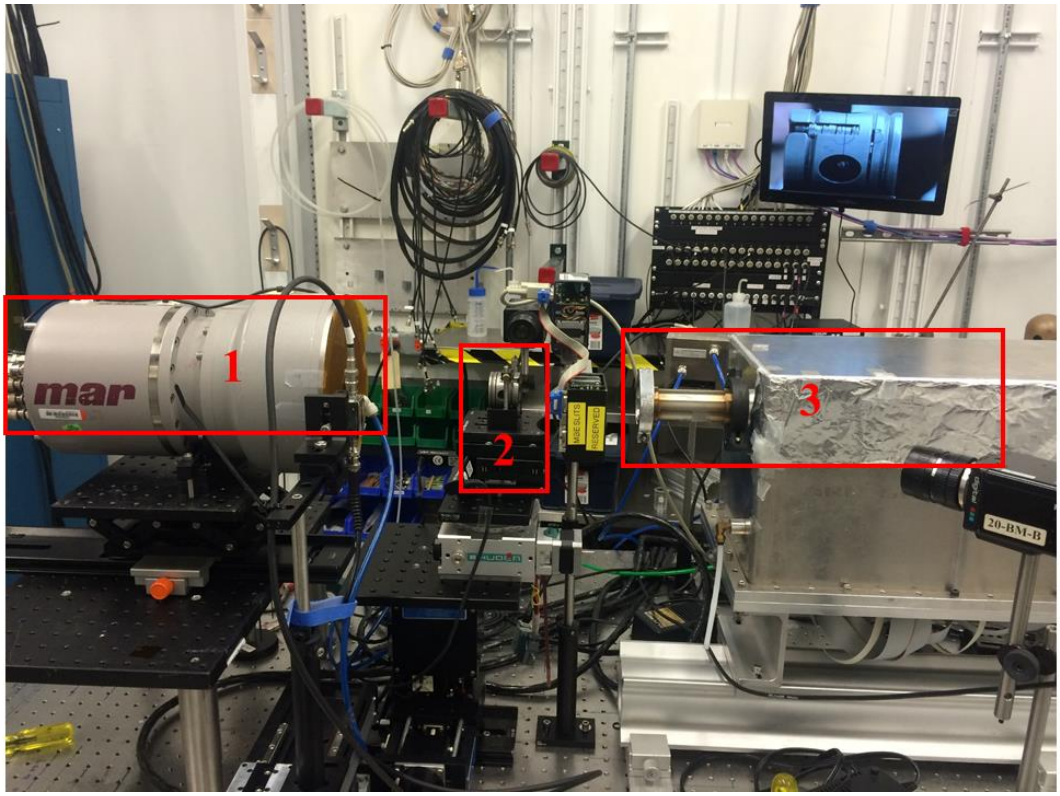

Figure 2.9 Set up of 20ID at APS. 1, 2, 3 labeled in this figure represent the detector, sample stage and X-ray beam, respectively.

www.manaraa.com

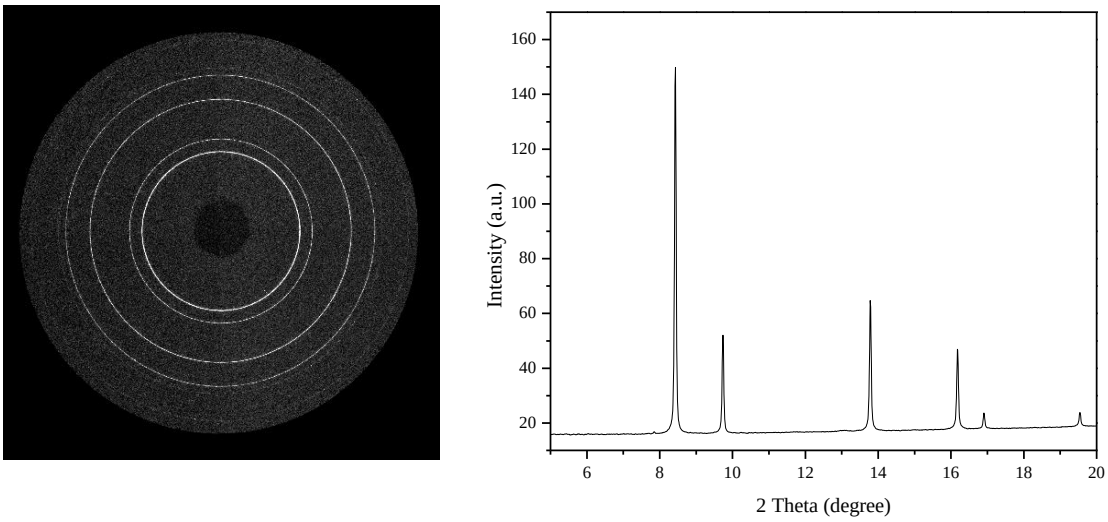

Figure 2.10 2D and 1D patterns of CeO_2 collected in APS (λ = 0.4592 Å)

2.3.6 Structural refinement

X-ray diffraction patterns are analyzed using structural refinement programs. Rietveld refinement is a technique for the use in the characterization of crystalline materials. It is a standard treatment of powder diffraction data to make the final structural model to achieve the accepted criterion. After the Rietveld refinement, the information about the crystal structures can be obtained, such as the lattice parameters, the atomic positions, the crystallinity, and so on.[19] To obtain the best match between observed and calculated full powder diffraction profile, the profile residual factor R_p and the weighted profile residual R_{wp} should be as small as possible. The principle of Rietveld method is to use a least squares approach to refine a theoretical line profile until it matches the observed profile.[19] The most popular platform for Rietveld refinement is GSAS (General Structure Analysis System). In this thesis, the GSAS + EXPGUI program is used to process the refinements of XRD data.

Le Bail analysis is an alternative to Rietveld refinement when available structure information is limited or intensity of diffraction pattern is not reliable. Le Bail fitting is just doing a Rietveld fit without the atomic information being present, the intensities of the individual peaks are no longer treated as least-squares parameters and are never

www.manaraa.com

refined. Consequently, each cycle of least-squares is very fast, only background, peak shape, and lattice parameters are refined during each least squares cycle.[19] The required crystal structure information for Le Bail refinement is the cell parameters and space group. In this thesis, due to the low Z elements of hydrogen storage materials, the atomic coordinates and the intensity of the XRD patterns were extremely difficult to be refined using Rietveld refinement. Therefore, several XRD patterns of these materials were refined by Le Bail method.

2.4 References

(1) James, S. L.; Adams, C. J.; Bolm, C.; Braga, D.; Collier, P.; Friscic, T.; Grepioni, F.; Harris, K. D. M.; Hyett, G.; Jones, W., et al. Mechanochemistry: opportunities for new and cleaner synthesis. *Chemical Society Reviews* **2012,** *41*, 413-447.

(2) Burmeister, C. F.; Kwade, A. Process engineering with planetary ball mills. *Chemical Society Reviews* **2013,** *42*, 7660-7667.

(3) Patil, P. R.; Kartha, K. P. R. Solvent-free synthesis of thioglycosides by ball milling. *Green Chemistry* **2009,** *11*, 953-956.

(4) Bruckmann, A.; Krebs, A.; Bolm, C. Organocatalytic reactions: effects of ball milling, microwave and ultrasound irradiation. *Green Chemistry* **2008,** *10*, 1131-1141.

(5) Karagedov, G.; Lyakhov, N. Mechanochemical grinding of inorganic oxides. *KONA Powder and Particle Journal* **2003,** *21*, 76-87.

(6) Shen, G.; Mao, H. K. High-pressure studies with x-rays using diamond anvil cells. *Reports on Progress in Physics* **2016,** *80*, 016101.

(7) Dong, Z. High-pressure study of molecular solids and 1D nanostructures by vibrational spectroscopy and synchrotron x-ray diffraction. *Thesis* **2012**.

www.manaraa.com

(8) Walker, J. Optical absorption and luminescence in diamond. *Reports on Progress in Physics* **1979,** *42*, 1605-1659.

(9) Solin, S. A.; Ramdas, A. K. Raman spectrum of diamond. *Physical Review B* **1970,** *1*, 1687.

(10) Syassen, K. Ruby under pressure. *High Pressure Research* **2008,** *28*, 75-126.

(11) Mao, H. K.; Xu, J.; Bell, P. M. Calibration of the ruby pressure gauge to 800 kbar under quasi-hydrostatic conditions. *Journal of Geophysical Research-Solid Earth and Planets* **1986,** *91*, 4673-4676.

(12) Forman, R. A.; Piermarini, G. J.; Barnett, J. D.; Block, S. Pressure measurement made by the utilization of ruby sharp-line luminescence. *Science* **1972,** *176*, 284-285.

(13) Mao, H. K.; Bell, P. M. High-pressure physics: the 1-megabar mark on the ruby R1 static pressure scale. *Science* **1976,** *191*, 851-852.

(14) Marshall, W. G.; Francis, D. J. Attainment of near-hydrostatic compression conditions using the Paris–Edinburgh cell. *Journal of Applied Crystallography* **2002,** *35*, 122-125.

(15) Angel, R. J.; Bujak, M.; Zhao, J.; Gatta, G. D.; Jacobsen, S. D. Effective hydrostatic limits of pressure media for high-pressure crystallographic studies. *Journal of Applied Crystallography* **2007,** *40*, 26-32.

(16) Ferraro, J. R., *Introductory raman spectroscopy*. Elsevier: 2003.

(17) Dong, Z.; Song, Y. Transformations of cold-compressed multiwalled boron nitride nanotubes probed by infrared spectroscopy. *The Journal of Physical Chemistry C* **2010,** *114*, 1782-1788.

(18) Bebb, H. B.; Williams, E., Photoluminescence I: theory. In *Semiconductors and semimetals*, Elsevier: **1972**, *8*, 181-320.

www.manaraa.com

(19) Pecharsky, V.; Zavalij, P., *Fundamentals of powder diffraction and structural characterization of materials*. Springer Science & Business Media: 2008.

(20) Prescher, C.; Prakapenka, V. B. DIOPTAS: a program for reduction of two-dimensional X-ray diffraction data and data exploration. *High Pressure Research* **2015,** *35*, 223-230.

www.manaraa.com

Chapter 3

3 Pressure-induced phase transitions and evolution of dihydrogen bonding in sodium amidoborane by *in-situ* vibrational spectroscopy and synchrotron X-ray diffraction

3.1 Introduction

With the increasing consumption of fossil fuel sources, the new energy systems are required urgently. In particular, hydrogen-rich materials have been gaining much attention due to their high hydrogen content and renewability.[1,2,3] Ammonia borane (NH_3BH_3) is one of the most promising solid-state materials for potential hydrogen storage because this molecular material is stable at atmospheric conditions with a high hydrogen content of 19.6 %.[4,5] However, the high decomposition temperature (~150 ℃) and releasing of toxic borazine during the decomposition process constrain its applications.[6] Recently, chemical compositional modification has been found to show significantly enhanced dehydrogenation performance, leading to the formation of a series of derivatives of NH_3BH_3.[5, 7-16] Particularly, substituting one of the hydrogen atoms bonded with N atom in NH_3BH_3 with alkali or alkaline earth metal element leads to the formation of a new series of materials, namely metal amidoborane, such as $LiNH_2BH_3$, $NaNH_2BH_3$ and $Ca(NH_2BH_3)_2$.[5,7] $LiNH_2BH_3$ and $NaNH_2BH_3$ are found to be isostructural and crystallize in an orthorhombic space group *Pbca*.[5] Compared to NH_3BH_3, the improved dehydrogenation properties have been achieved in $LiNH_2BH_3$ and $NaNH_2BH_3$, such as lower dehydrogenation temperature and no borazine emission during the dehydrogenation process. They begin to release H_2 upon heating to ~85 ℃ and reached a maximum at around 90 ℃, and the total of 11 wt% and 7.4 wt% of H_2 can be released from $LiNH_2BH_3$ and $NaNH_2BH_3$, respectively.[5]

For developing potential hydrogen storage materials, high-pressure technique has been demonstrated as an effective and promising approach, which can provide a unique chance to reveal the atomic, electronic and structural information, and could guide the design of

www.manaraa.com

new hydrogen storage materials.[17-20] Over the past several years, there has been an increasing number of high-pressure studies on NH_3BH_3 and its derivatives. The bond behaviors and new structures of these materials were investigated under high pressure. The Raman spectra of the NH_3BH_3 as a function of pressure provided the evidence of the dihydrogen bond, which contributes to the unusual high melting point (104 ℃) and the mechanism of dehydrogenation.[21-23] Two phase transitions for NH_3BH_3 were observed at room temperature by in situ XRD. The structure transforms from *I*4*mm* at ambient pressure into *Cmc*2_1 and *P*2_1 under high pressure.[24] Moreover, the high-pressure study on $LiNH_2BH_3$ indicated that the N-H stretching modes shifted to higher frequency with the increase of pressure, implying that there is no dihydrogen bond in $LiNH_2BH_3$, different from NH_3BH_3.[25]

Isostructural to $LiNH_2BH_3$, $NaNH_2BH_3$ shows very similar properties on dehydrogenation process, but the theoretical studies have shown that there are some difference between these two compounds in respect of phase stability and electronic structure.[26-28] Thus it is necessary to investigate the high-pressure behavior of $NaNH_2BH_3$ to supply direct evidences of possible phase transitions and the variation of dihydrogen bond, which will be helpful to understand the correlations between the structures and the dehydrogenation performance. Here we report an investigation of $NaNH_2BH_3$ by synchrotron X-ray diffraction, *in situ* Fourier transform infrared (FTIR) spectroscopy and Raman spectroscopy, the pressure-induced new polymorphs of $NaNH_2BH_3$ with structural stabilities and bond behavior are discussed. Interestingly, our results reveal that no evidence shows the negative linear compressibility, which is totally different from the previous study on $NaNH_2BH_3$.[29]

3.2 Experimental

3.2.1 Materials and methods

NaH and NH_3BH_3 powder were purchased from Sigma Aldrich with claimed purity of 97% and 95%, respectively, and used as received. $NaNH_2BH_3$ was synthesized according to the literature[5]. Briefly, a mixture of NaH and NH_3BH_3 in a 1:1 molar ratio (0.063 g

www.manaraa.com

NaH and 0.080 g NH_3BH_3) with six steel balls (ball-to-sample weight ratio is 180:1) were sealed in two stainless steel jars, respectively, which was operated in a N_2-filled MBraun LAB Master 130 glovebox with H_2O content of < 1 ppm and O_2 content of < 5 ppm. Then the milling process in two jars was carried out in a Retsch PM200 planetary ball mill at 250 rpm for 70 min with 10 minutes interval every 30 minutes. After milling, the mixture was stored in a N_2-filled glovebox for further structural and vibrational spectroscopy characterization.

3.2.2 Powder X-ray diffraction

The crystallinity and purity of the as-synthesized products was investigated by a Rigaku X-ray diffractometer using Co Kα radiation (λ = 1.78890 Å), the scan range was from 2θ = 10 to 80 ° with a step size of 0.02. Sample was loaded on a glass slide in a N_2-filled MBraun LAB Master 130 glovebox, then a piece of plastic wrap, which is made of Low-Density Polyethylene, was used to cover on the sample to prevent the exposure to air and moisture.

3.2.3 In-situ high-pressure FTIR spectroscopy

A symmetrical diamond anvil cell (DAC) with two type-II diamonds with 400 μm culets was used for the high-pressure IR measurements. Then the sample and a ruby ball were carefully placed in the sample chamber and spectral quality KBr powder was also loaded into the sample chamber. The in-situ IR absorption experiments were carried out by a customized IR micro-spectroscopy system with details described in Chapter 2.

3.2.4 In-situ high-pressure Raman spectroscopy

For in-situ high pressure Raman measurements, a symmetrical DAC with two type-I diamonds with 400 μm culets was used and the sample was loaded into sample chamber with a ruby ball, and no pressure transmitting medium was used. Then in situ high-pressure Raman experiments were carried out by a customized Raman spectrometer with a 532 nm excitation laser. The signal was recorded using an ultrasensitive, liquid nitrogen cooled, back-illuminated, charge-coupled device (CCD) detector from Acton.

www.manaraa.com

3.2.5 In-situ high-pressure X-ray diffraction

A symmetrical diamond anvil cell with 400 μm culet size was used for high-pressure study, and a stainless steel gasket was preindented to 50 μm in thickness, then a hole with diameter of 150 μm was drilled in the center of it as a sample chamber, and a ruby ball was loaded into it as pressure calibrant. For synchrotron XRD, the sample was loaded into the sample chamber and no pressure transmitting medium was used due to the air sensitivity of the sample. The experiment was performed in Advanced Photon Source (APS), Argonne, USA using the beamline of HPCAT. The wavelength of beamline is 0.4246 Å, and the 2D Debye-Scherrer diffraction patterns were integrated by using Fit2D program for further analysis.

3.3 Results and discussion

3.3.1 XRD pattern of NaAB under ambient pressure

$NaNH_2BH_3$ was synthesized according to the reference[5] and the product was stored in a N_2-filled MBraun LAB Master 130 glovebox with H_2O content of < 1 ppm and O_2 content of < 5 ppm. As illustrated in Figure 3.1, X-ray diffraction pattern of NaAB was collected and the major peaks have been indexed. The XRD result shows that our sample mainly consists of sodium amidoborane, with little uncompleted reactants. From XRD patterns and the indexed peaks of the product, the structure of $NaNH_2BH_3$ was found to be orthorhombic crystal with space group *Pbca*. The unit cell of $NaNH_2BH_3$ is showed in Figure 3.2. The cell parameters were refined to be a = 7.4741 Å, b = 14.6590 Å, c = 5.6625 Å, V = 620.41 $Å^3$, using Rietveld refinement, which are consistence with those in the reference.[5]

www.manaraa.com

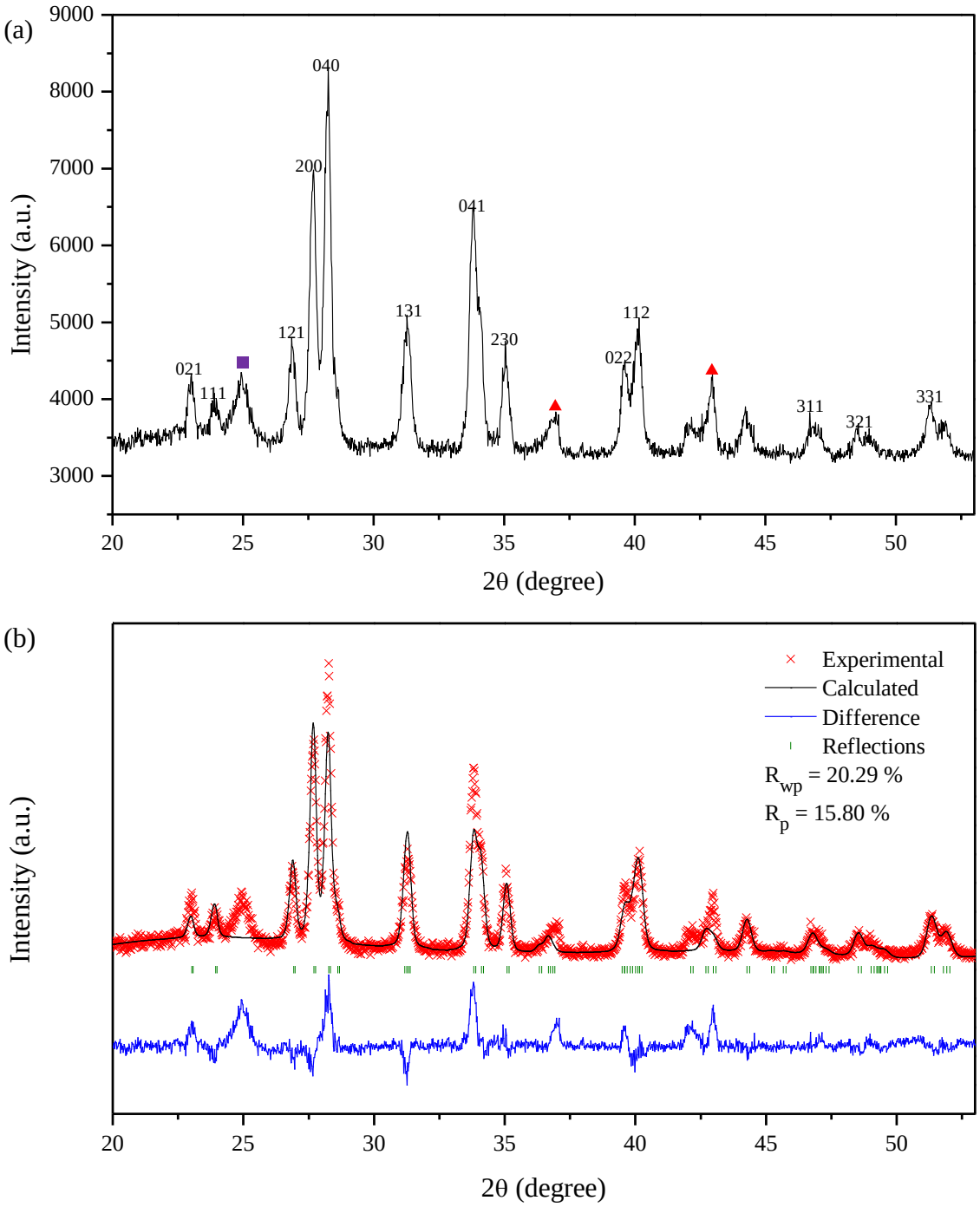

Figure 3.1 XRD pattern of $NaNH_2BH_3$ sample under ambient conditions (a) and calculated XRD patterns in comparison with experimental results using Rietveld refinement (b). The purple square and red triangle in (a) represent the plastic wrap and unreacted NaH, respectively.

www.manaraa.com

The previous theoretical studies show that the structure and bonding natures of $NaNH_2BH_3$ are dramatically altered from that of NH_3BH_3. Substituting by Na atoms, $NaNH_2BH_3$ shows more ionic character, similar with its isostructure $LiNH_2BH_3$. As shown in Figure 3.2, each Na^+ is tetrahedrally coordinated by one NH_2^- and three BH_3 units. The interactions between these species stabilize the structure of $NaNH_2BH_3$ and form the basis of framework.[9, 30] Compared to NH_3BH_3, the B-N bond decreases from 1.59 Å in NH_3BH_3 to 1.56 Å in $NaNH_2BH_3$, due to the increasing electron density on the nitrogen in $NH_2BH_3^-$, resulting in a stronger and shorter B-N bond.[5, 31] In addition, there is an increase in B-H bond length from 1.18 Å to 1.23 Å. While the N-H bond length decreases from 1.07 Å to 1.03 Å.[28, 31]

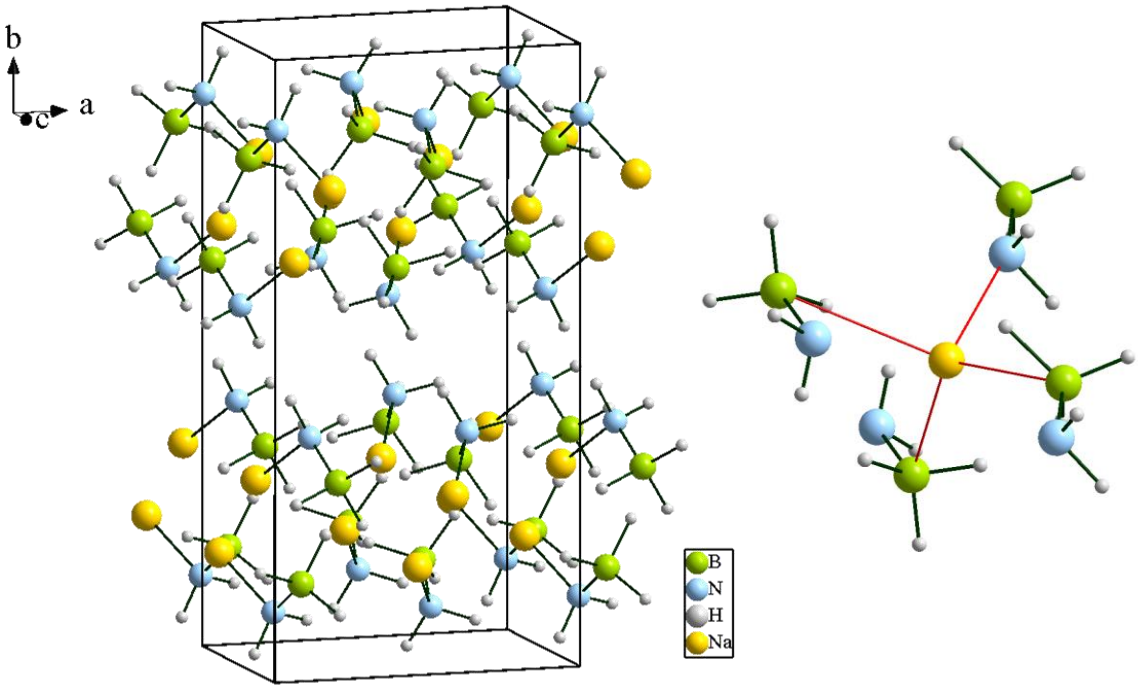

Figure 3.2 The crystal structure of $NaNH_2BH_3$ under ambient pressure in a unit cell and the coordination of Na atom with one NH_2^- and three BH_3 units.

3.3.2 Raman and IR spectra of NaAB under ambient pressure

Raman and IR spectra of NaAB were collected under ambient conditions and shown in Figure 3.3 and 3.4. The main peaks of $NaNH_2BH_3$ have been assigned preliminarily, in

www.manaraa.com

reference to the peak assignments of NH_3BH_3 and $LiNH_2BH_3$.[32,33,34] Both Raman and IR spectra of NH_3BH_3 and $NaNH_2BH_3$ consist of several bands in B-N stretching (760-900 cm^{-1}), B-H deformation (1000-1300 cm^{-1}), N-H deformation (1300-1700 cm^{-1}), B-H stretching (2000-2600 cm^{-1}) and N-H stretching (3000-3600 cm^{-1}) regions.[32]

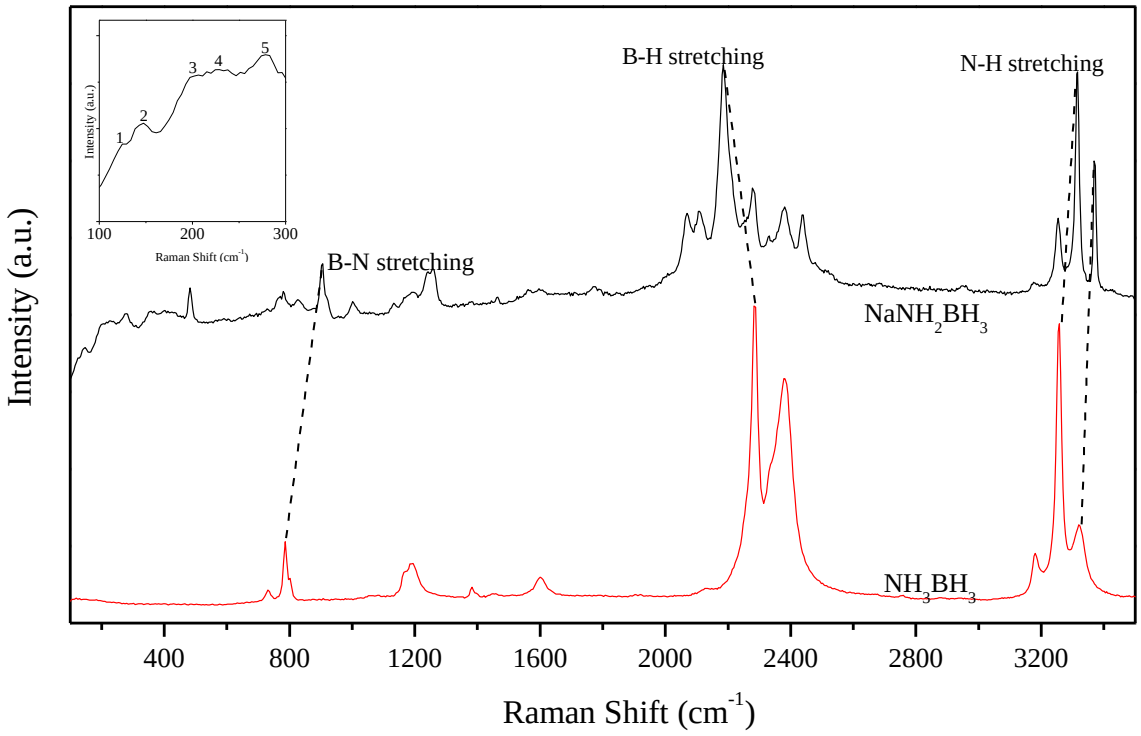

Figure 3.3 Raman spectra between NH_3BH_3 and $NaNH_2BH_3$ under ambient pressure and room temperature. The inset figure is the lattice modes region for $NaNH_2BH_3$.

The position of these modes for $NaNH_2BH_3$ are quite different from those measured from NH_3BH_3. In Figure 3.3, the B-H stretching modes are red-shifted by 99 cm^{-1} whereas the N-H stretching modes are blue-shifted by 58 cm^{-1} and 50 cm^{-1}. The N-B stretching modes are also blue-shifted by 120 cm^{-1}, which implies that $NaNH_2BH_3$ has weaker B-H bonds than NH_3BH_3. Moreover, both of the N-H and B-N bonds become stronger in $NaNH_2BH_3$ with respect to NH_3BH_3, consistent with the XRD analysis. The same trend was also observed in IR spectra (Figure 3.4). Additionally, this observation is also consistent with

www.manaraa.com

the previous study on $LiNH_2BH_3$[25]. The partial assignments and vibrational frequencies of $NaNH_2BH_3$ and NH_3BH_3 at ambient pressure were listed in Table 3.1.

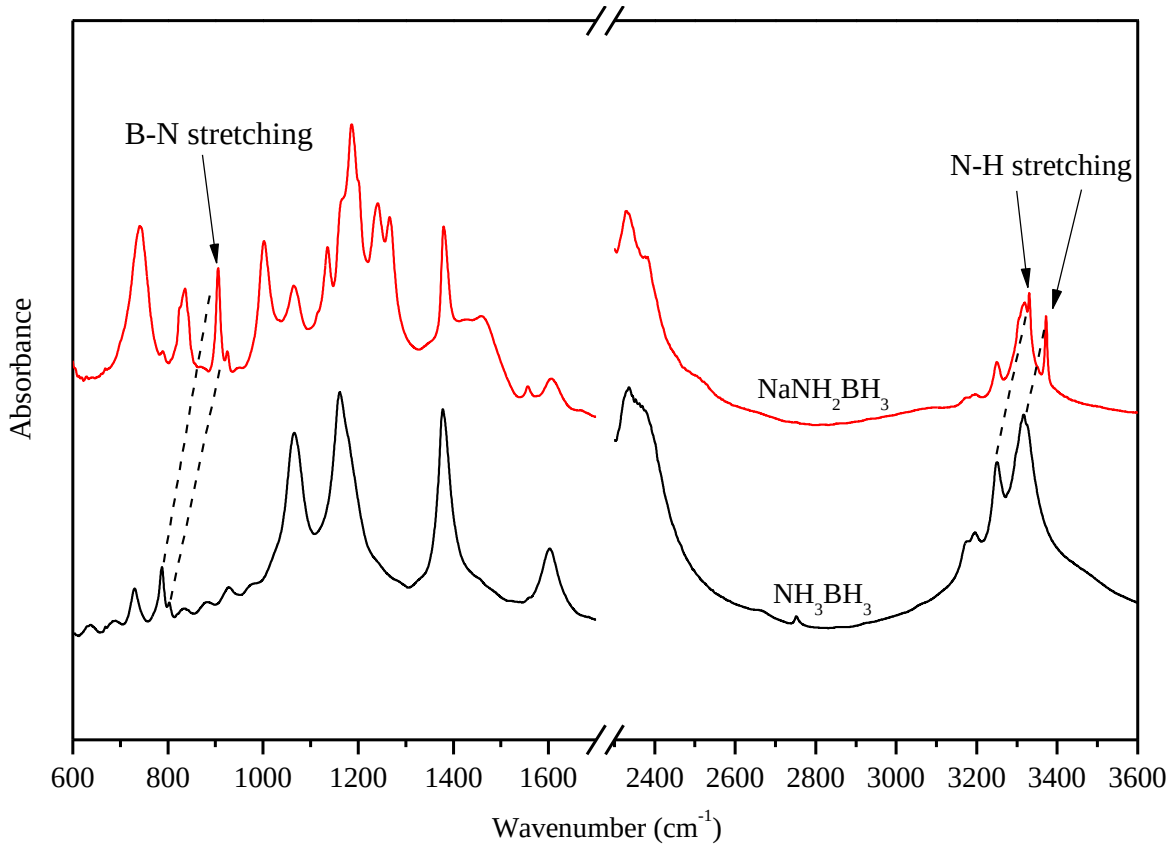

Figure 3.4 IR spectra between NH_3BH_3 and $NaNH_2BH_3$ under ambient pressure and room temperature.

www.manaraa.com

Table 3.1 Assignments and vibrational frequencies of $NaNH_2BH_3$ and NH_3BH_3 at ambient pressure[33]

Assignment	Raman shift (cm^{-1})		IR frequency (cm^{-1})	
	$NaNH_2BH_3$	NH_3BH_3	$NaNH_2BH_3$	NH_3BH_3
v (N-H) str (a)	3370	3320	3372	3317
v (N-H) str (b)	3316	3258	3330	3250
v (B-H) str (a)		2380		
v (B-H) str (b)	2185	2284		
v (N-H) def (a)		1601	1606	1602
v (N-H) def (b)		1383	1380	1378
v (B-H) def		1190	1185	1161
v (N-B) str (a)		802	924	803
v (N-B) str (b)	906	786	906	787
NBH rocking		730	741	730

3.3.3 In-situ high-pressure IR spectroscopy

IR spectra of NaAB were collected upon compression in the region of 600 – 3500 cm^{-1}, as shown in Figure 3.5. Upon compression to 1.05 GPa, N-H deformation mode at 1380 cm^{-1} splits into a doublet with reduced intensity. In addition, another peak in this region at 1606 cm^{-1} develops into a sharp peak from a previously broad band. Meanwhile, in the B-H stretching region, it is noticeable that a new peak at 2399 cm^{-1} appears. All these

www.manaraa.com

evidences indicate a phase transition at around 1.05 GPa. Upon further compression to 3.43 GPa, abundant changes were observed, which demonstrates the second phase transition. Firstly, the NBH rocking motion at 741 cm^{-1} vanishes in contrast to the appearance of a new peak at 895 cm^{-1}. Moreover, in B-H deformation region, the peak at 1263 cm^{-1} splits into two weaker components, and the peak at 1309 cm^{-1} disappears at the same time. At last, the N-H stretching mode at 3372 cm^{-1} turns from a sharp peak to a broad band. With the further compression to 11.08 GPa, no significant changes were observed and all bands became broadened. Moreover, the spectrum on decompression to near ambient pressure exhibits a different profile from phase I, indicating the irreversible pressure-induced phase transitions of $NaNH_2BH_3$.

www.manaraa.com

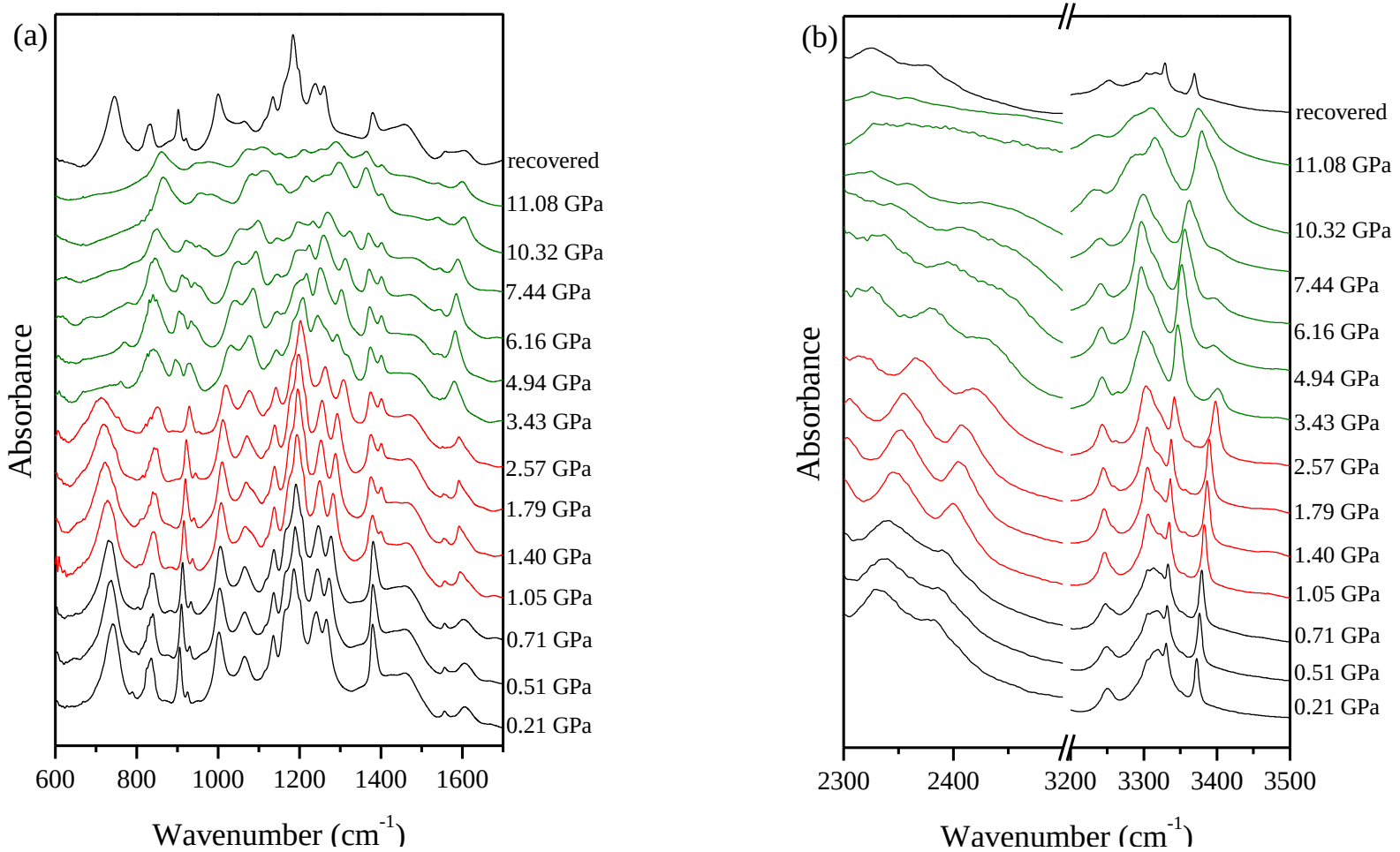

Figure 3.5 IR spectra of NaAB collected at room temperature in the region of 600-3500 cm^{-1}. The peak around 3250 and 3302 cm^{-1} in (b) belongs to the N-H stretching mode of unreacted NH_3BH_3.

www.manaraa.com

3.3.4 In-situ high-pressure Raman spectroscopy

Raman spectra of $NaNH_2BH_3$ were collected as a function of pressure from near ambient pressure to 16.06 GPa, as showed in Figure 3.6. Upon compression to 1.19 GPa, the peak around 128 and 214 cm^{-1} (lattice mode 1 and 3) shift dramatically to the larger Raman shift. Meanwhile, the B-N stretching mode at 912 cm^{-1} shows great blueshift. A new peak around 1192 cm^{-1} appears at 1.19 GPa. All these observations suggests a phase transition at around 1.19 GPa. With the increase of the pressure, the shape of the spectra reveals more difference from the previous one. In Figure 3.6 (a), when the pressure was increased to 2.7 GPa, the lattice mode at 298 cm^{-1} (lattice mode 5) disappears and a new peak at 912 cm^{-1} arises in B-N stretching region. Moreover, the profile of spectrum changes tremendously from 1.73 GPa to 2.7 GPa in Figure 3.6 (b). The B-H stretching mode at 2208 cm^{-1} almost vanishes and displays great blueshift with the increase of the pressure. In Figure 3.6 (c), the N-H stretching mode at 3390 cm^{-1} nearly disappears when the pressure was 2.7 GPa. Such observation indicates another phase transition at around 2.7 GPa. With the further compression, all peaks become broadened gradually until 12.57 GPa. No obvious peaks could be distinguished under such pressure, which suggests the amorphous structure of the material. In order to understand the high-pressure structural stability and the reversibility of the pressure-induced phase transition of $NaNH_2BH_3$, Raman spectra were collected on decompression to near ambient pressure. As illustrated in Figure 3.6, the recovered Raman spectrum shows a different profile to the initial one when the pressure was close to ambient. Therefore, the pressure-induced phase transitions of $NaNH_2BH_3$ is irreversible.

www.manaraa.com

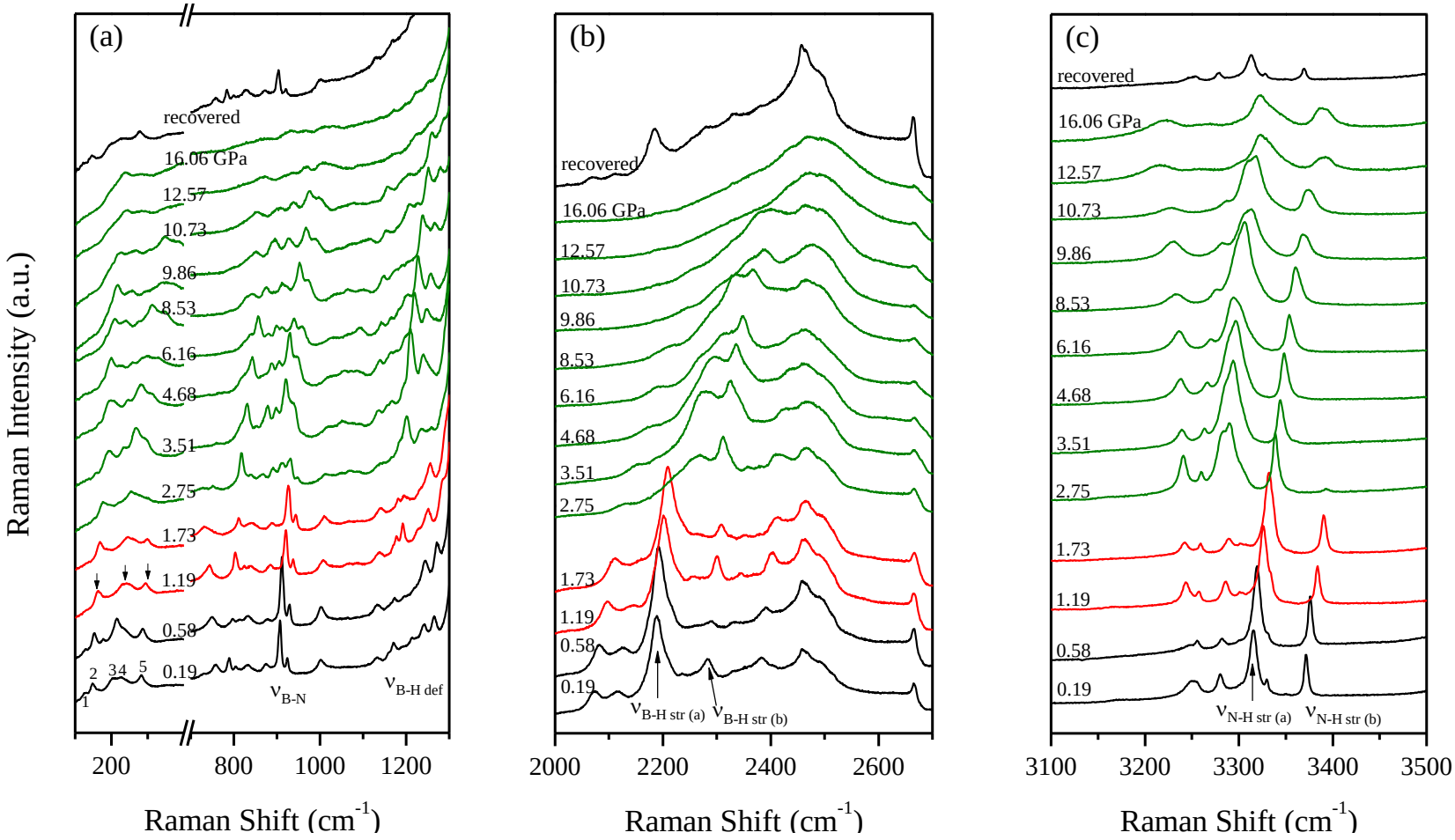

Figure 3.6 Raman spectra of NaAB collected at room temperature in the region of 100-3500 cm^{-1}. The peaks around 3255 and 3281 cm^{-1} in (c) belong to the N-H stretching mode of unreacted NH_3BH_3.

www.manaraa.com

3.3.5 Pressure effects on IR and Raman modes

Moreover, the pressure dependences of the selected IR and Raman internal modes of $NaNH_2BH_3$ were studied by plotting the vibrational frequencies as a function of pressure and shown in Figure 3.7 and 3.8. The pressure coefficients were analyzed by linear fit of the experimental and listed in Table 3.2 and 3.3. The possible phase transitions could be further determined due to the large changes of the pressure coefficients in different pressure regions. Overall, most of the Raman and IR modes exhibit pressure-induced blue shifts, except NBH rocking mode and B-H deformation mode in Figure 3.7, indicating the strengthened chemical bonds upon compression. Additionally, the distinct changes of pressure dependence as well as the appearance or disappearance of several modes also confirmed the phase boundaries consistently, such as the N-B stretching mode, the B-H deformation mode and N-H stretching mode in both figures. Moreover, the largest pressure coefficients were discovered in the pressure region below 1.0 GPa and decreased gradually with the increase of pressure, which means the structure becomes less compressible upon compression.

Furthermore, most of the pressure coefficients show the positive values, indicating the blueshift of the chemical bonds. It is also noticeable that the pressure coefficients of N-H and B-H stretching mods are positive during the whole compression region.

www.manaraa.com

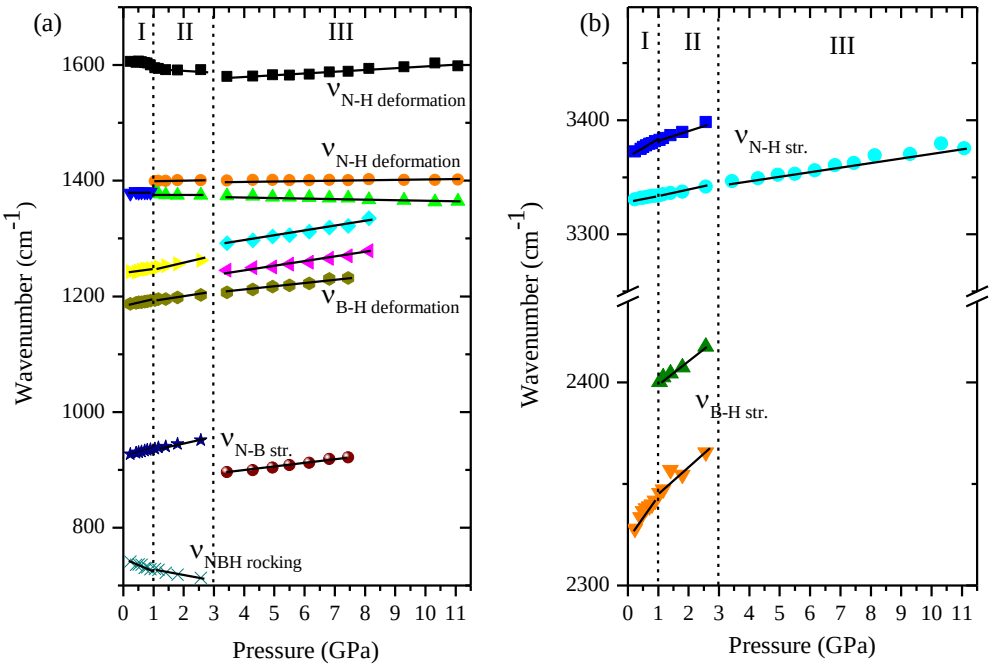

Figure 3.7 Pressure dependence of selected IR modes of NaAB on compression. The vertical dashed lines indicate the proposed phase boundaries.

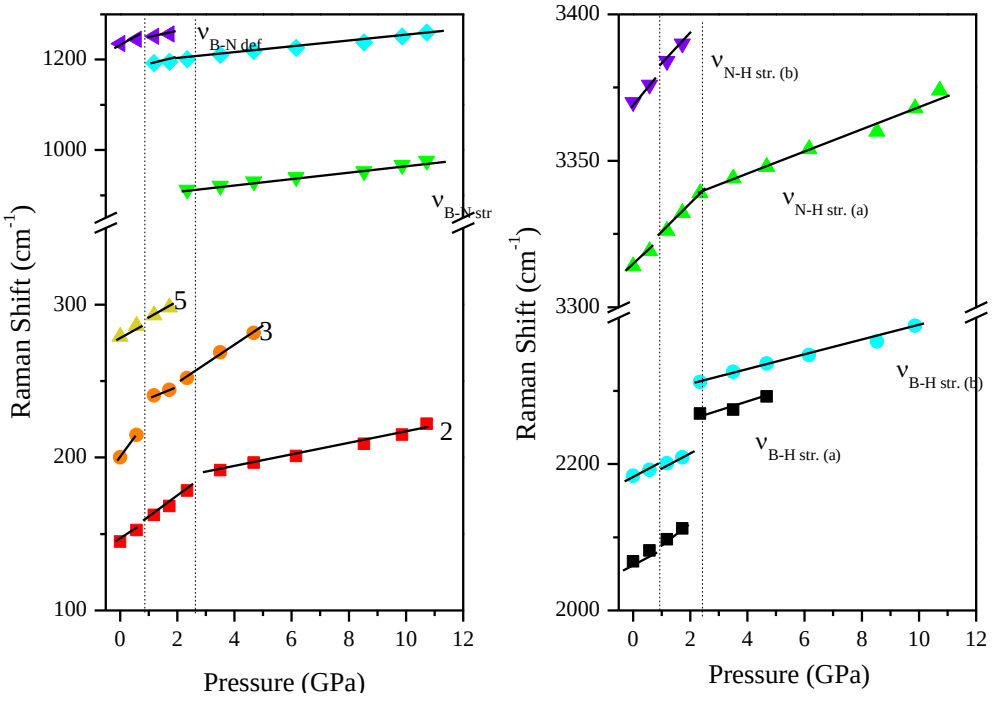

Figure 3.8 Pressure dependence of selected Raman modes of NaAB on compression. The vertical dashed lines indicate the proposed phase boundaries.

www.manaraa.com

Table 3.2 Pressure dependence of vibrational modes of $NaNH_2BH_3$ on compression from IR spectra

Vibrational mode	Frequency (cm^{-1})	dv/dP ($cm^{-1}\cdot GPa^{-1}$)[a]		
		Phase I (<1.0 GPa)	Phase II (1.0 – 2.7 Pa)	Phase III (> 2.7 GPa)
v (N-H) str (a)	3372	13.4	9.9	
v (N-H) str (b)	3330	4.7	4.7	4.4
v (B-H) str (a)	2381		11.0	
v (B-H) str (b)	2328	19.7	12.1	
v (N-H) def (a)	1606	-7.7	-1.9	3.1
v (N-H) def (b)	1380	1.9	1.1 -2.2	0.1 -1.4
v (B-H) def (a)	1242	9.9	8.6	8.6 7.0
v (B-H) def (b)	1185	8.0	5.6	6.4
v (N-B) str (a)	924	13.0	9.6	
v (N-B) str (b)				6.7
NBH rocking	741	-18.4	-9.9	

[a] Multiple entries for each mode correspond to the split. str (a) and str (b) mean the two different stretching modes, def (a) and def (b) mean the two different deformation modes.

www.manaraa.com

Table 3.3 Pressure dependence of vibrational modes of $NaNH_2BH_3$ on compression from Raman spectra

Vibrational mode	Frequency (cm^{-1})	dv/dP ($cm^{-1}\cdot GPa^{-1}$)[a]		
		Phase I (<1.0 GPa)	Phase II (1.0 – 2.7 GPa)	Phase III (> 2.7 GPa)
v (N-H) str (a)	3370	11.8	11.1	
v (N-H) str (b)	3314	12.0	11.0	3.9
v (B-H) str (a)	2184	13.8	14.8	9.6
v (B-H) str (b)	2067	25.9	27.8	9.9
v (N-H) def (b)	1235	17.2	9.3	
v (B-H) def			5.6	6.6
v (N-B) str				7.3
Mode 3	279	12.4	9.6	
Mode 2	200	25.3	6.7	12.6
Mode 1	145	14.0	13.8	4.7

[a] Multiple entries for each mode correspond to the split. str (a) and str (b) mean the two different stretching modes.

3.3.6 In-situ Synchrotron X-ray diffraction

In-situ high-pressure X-ray diffraction measurements of $NaNH_2BH_3$ were performed upon compression up to 22.61 GPa. As shown in Figure 3.9, all peaks shift to the larger 2θ direction, suggesting that the *d* value decreases with the increasing pressure. Upon compression to 1.33 GPa, the shape and intensity of the XRD pattern changes

www.manaraa.com

prominently. Specifically, the intensity of reflections of (121) and (040) decreases with a great extent, labeled as ◆, indicating a phase transition might occur. The theoretical calculation suggests that the phase II is still orthorhombic structure with the space group *Pbca*, suggesting an isostructural phase transition. As shown in Figure 3.2 and 3.10 (b), although the space groups of phase I and II remain the same, the orientation of the NaAB molecules are different. The cell parameters for phase II were refined to be a = 7.2708 Å, b = 14.1705 Å, c = 5.5783 Å and V = 574.74 $Å^3$ at the pressure of 1.75 GPa, using Rietveld refinement (Figure 3.10 (a)).

Upon further compression to 2.85 GPa, several new peaks appear at 2θ = 5.1, 6.7 and 7.3°, labelled as green square symbols, indicating the appearance of the phase III. However, the peaks belonging to phase II still exist upon further compression, suggesting the coexistence of phase II and phase III above 2.85 GPa. Moreover, the phase III was identified as a monoclinic structure with the space group of $P2_1/c$, with the refined cell parameters a = 5.1455 Å, b = 12.6664 Å, c = 5.5471 Å and V = 355.63 $Å^3$ at the pressure of 3.27 GPa, as shown in Fig 3.10 (c). Upon further compression, no obvious change was observed other than the peaks broadening and weakening. Finally, when the pressure was above 14.31 GPa, the structure of material becomes amorphous as indicated by all the peaks becoming broadened. We also calculated the enthalpies of new proposed crystal structures for $NaNH_2BH_3$ as a function of pressure (Figure 3.11), which shows that $P2_1/c$ has the lowest enthalpy at the high-pressure region. Furthermore, X-ray diffraction patterns of $NaNH_2BH_3$ were collected on decompression to near ambient pressure. As shown in Figure 3.9, the recovered XRD pattern is similar with the pattern of phase II, suggesting that the pressure-induced phase transition in $NaNH_2BH_3$ is irreversible.

www.manaraa.com

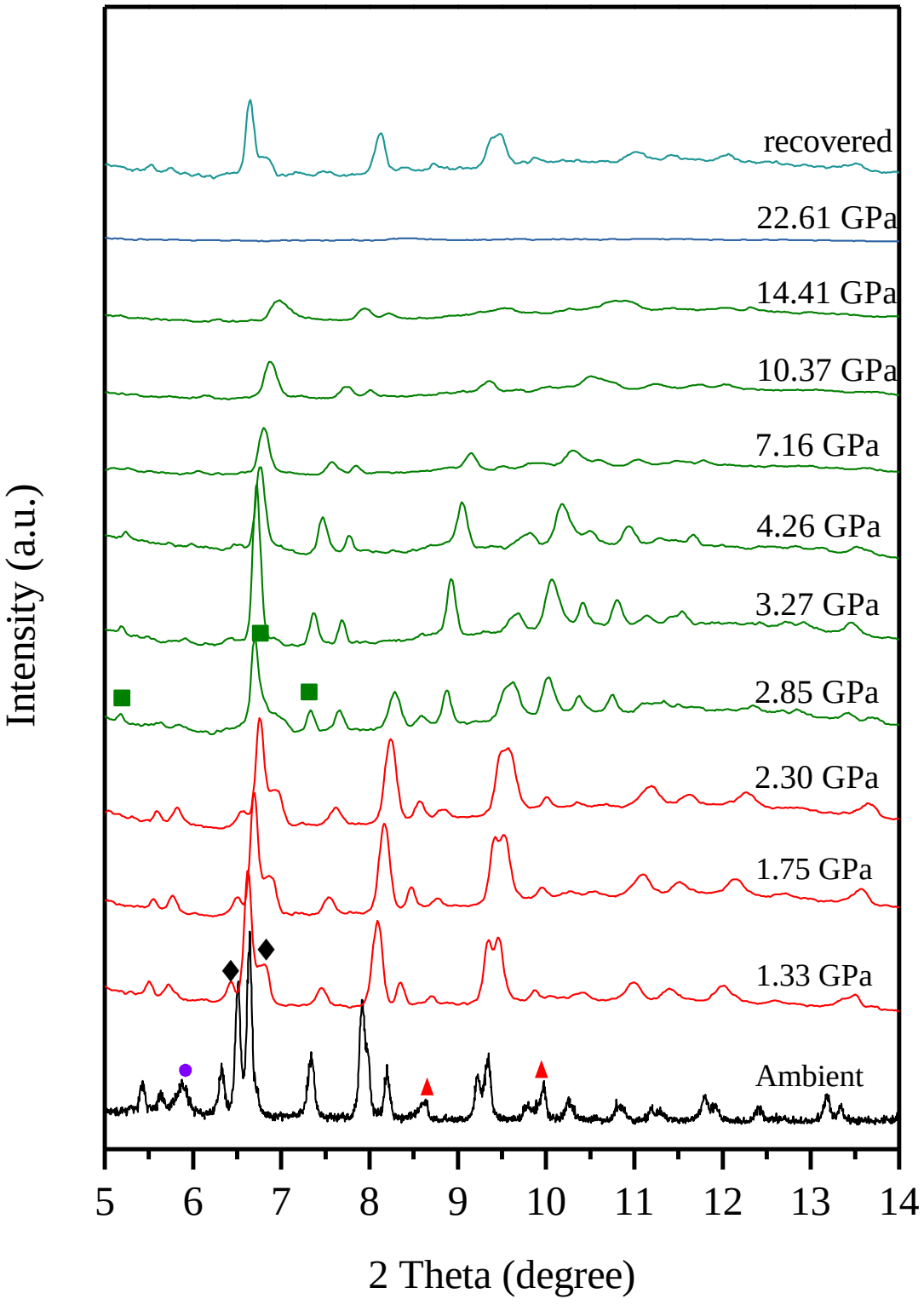

Figure 3.9 XRD patterns of $NaNH_2BH_3$ upon compression, the square and triangle symbols at ambient pressure represent the plastic wrap and unreacted NaH.

www.manaraa.com

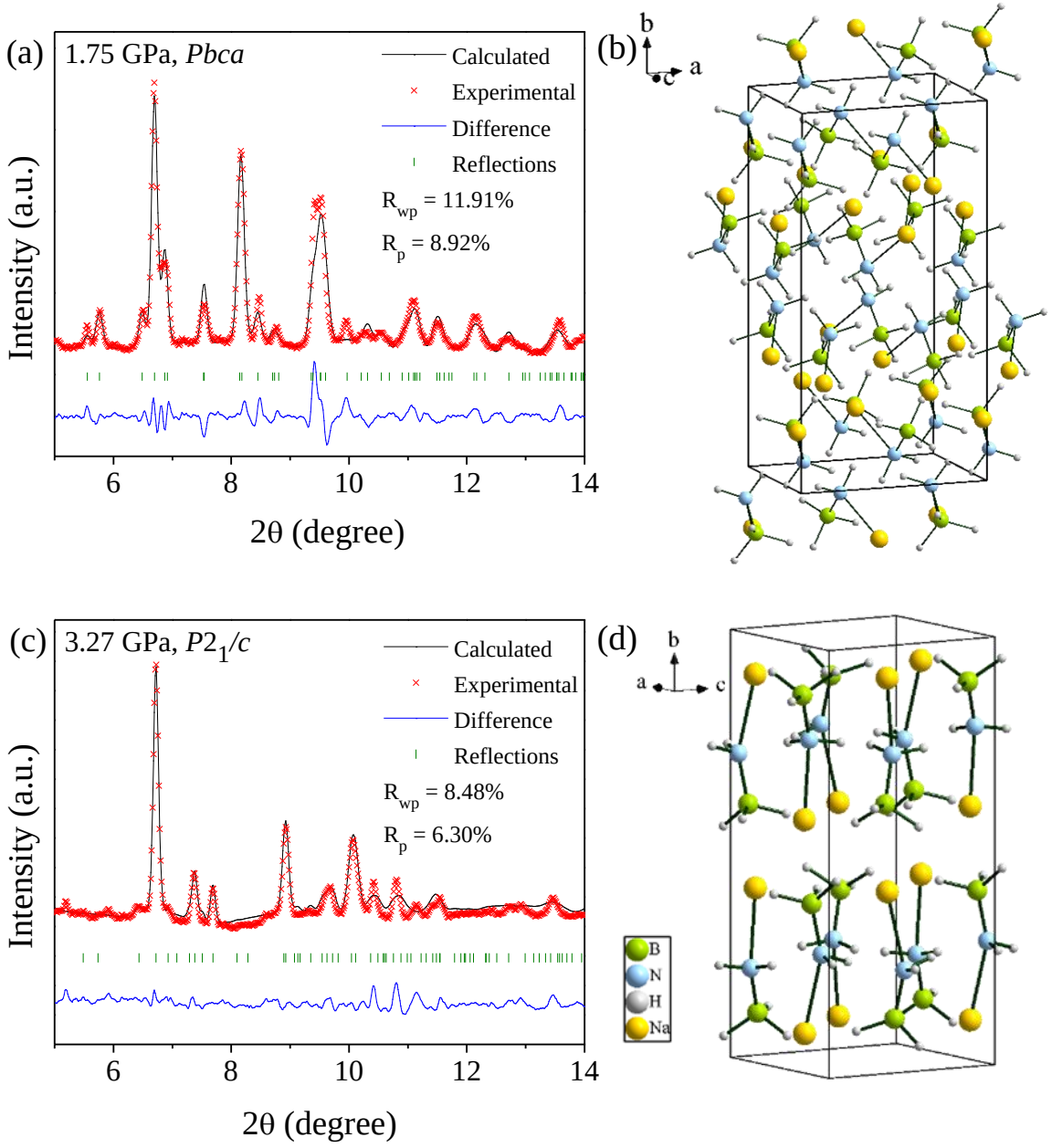

Figure 3.10 Calculated XRD patterns in comparison with experimental results at 1.75 (a) and 3.27 GPa (c) using Rietveld refinement. Proposed crystal structures of high-pressure phase II (b) and phase III (d) based on MD simulations.

www.manaraa.com

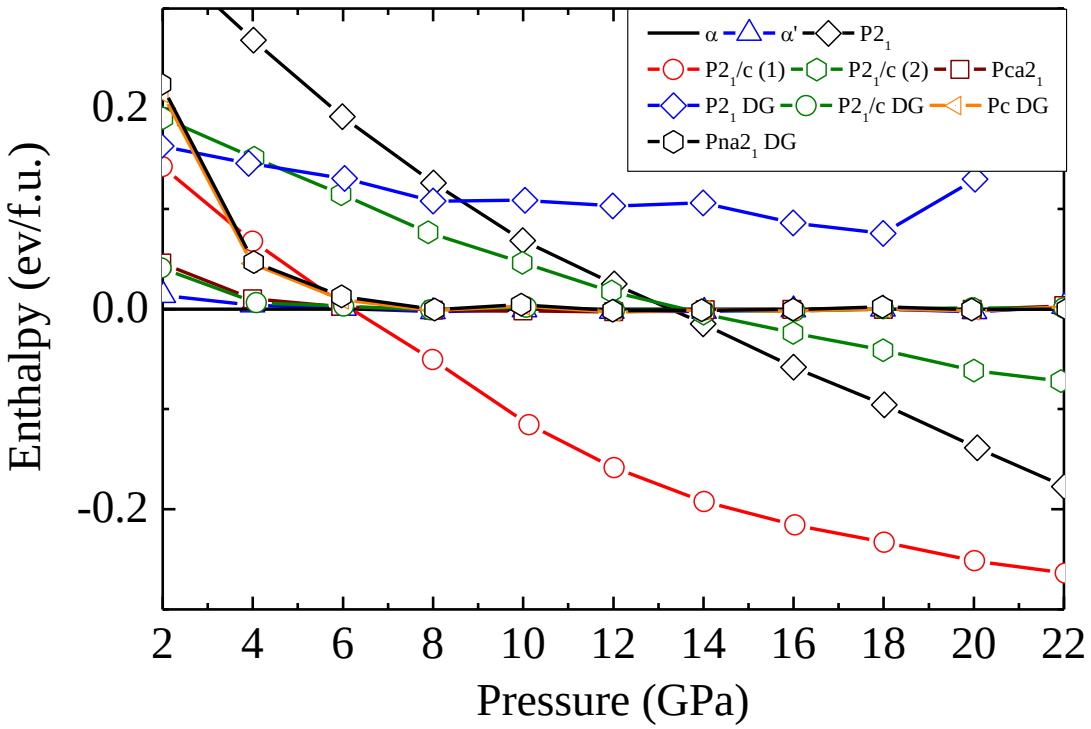

Figure 3.11 Enthalpies of several new possible crystal structures for phase III as a function of pressure. Note that the *P*2$_1$/*c* structure always has the lowest enthalpy at high pressure region

Moreover, we refined all the cell parameters of $NaNH_2BH_3$ under high pressure from the XRD patterns, which are listed in Tables 3.4. The calculated XRD patterns in comparison with experimental results are shown in Appendix A. Figure 3.12 displays the cell parameters and volume of $NaNH_2BH_3$ as a function of pressure. The cell parameters reduce steadily in the first two phases, due to the reorientation of the NaAB molecules in the orthorhombic structures. Upon compression to near 3.0 GPa, the cell parameters reduce sharply and discontinuously, indicating the major structural transformation of NaAB. The cell volume decreases by nearly 35.3 % due to a complete crystal structure transformation from orthorhombic to monoclinic.

www.manaraa.com

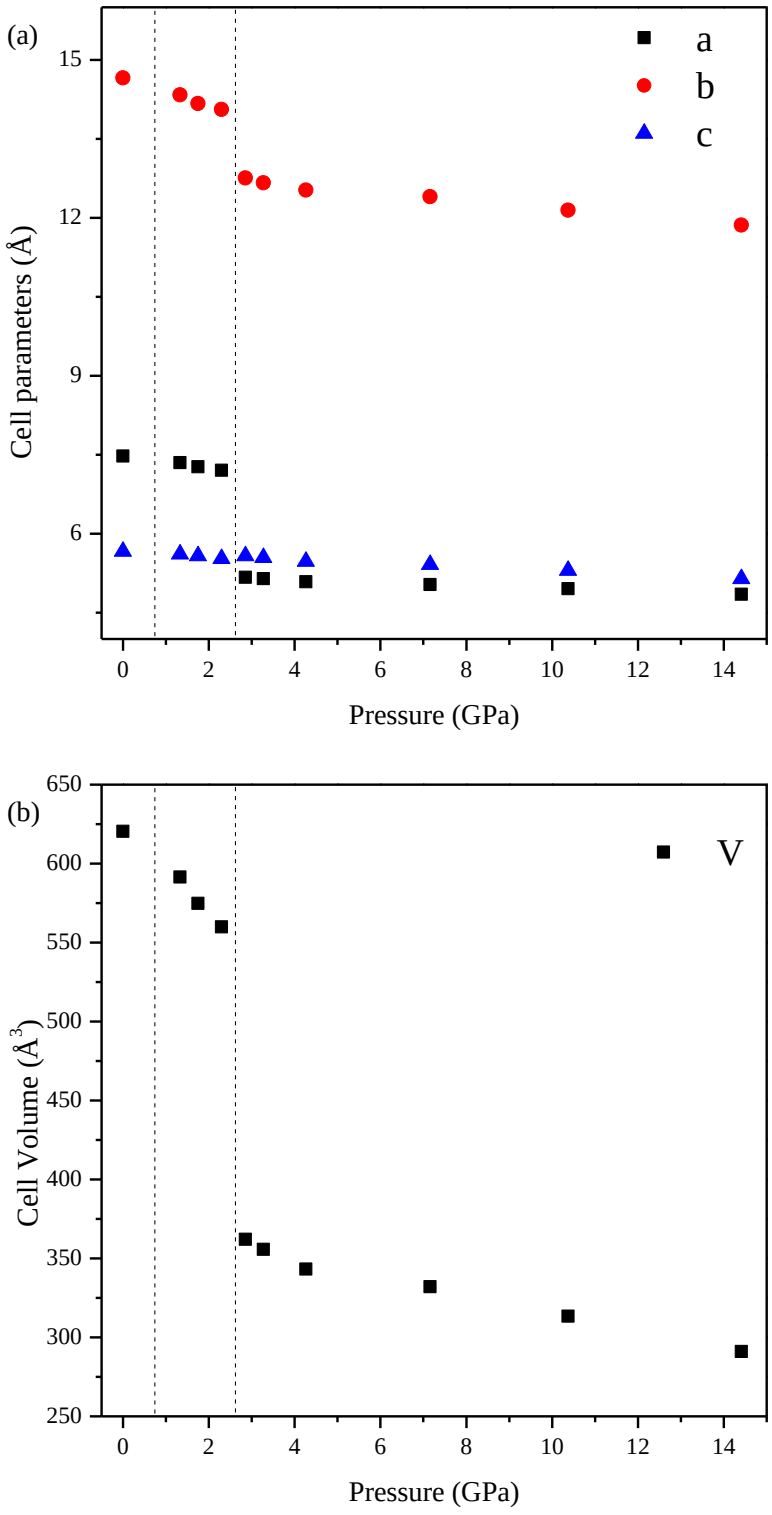

Figure 3.12 Cell parameters (a) and volume (b) of $NaNH_2BH_3$ as a function of pressure

www.manaraa.com

Table 3.4 Unit cell parameters of $NaNH_2BH_3$ at presentative pressures

Phase	Pressure (GPa)	a (Å)	b (Å)	c (Å)	V (Å^3)
Phase I	ambient	7.4741	14.6590	5.6625	620.41
Phase II	1.33	7.3509	14.3329	5.6136	591.45
	1.75	7.2708	14.1705	5.5783	574.74
	2.30	7.2021	14.0605	5.5286	559.85
Phase III	2.85	5.1678	12.7573	5.5776	362.01
	3.27	5.1455	12.6664	5.5471	355.63
	4.26	5.0860	12.5291	5.4755	343.10
	7.16	5.0311	12.3999	5.4149	332.08
	10.37	4.9537	12.1419	5.3031	313.28
	14.41	4.8507	11.8603	5.1474	291.03

The errors of cell parameters in phase II for a, b, c and V are estimated to be ±0.004, ±0.007, ±0.002 and ±0.4, respectively. The errors of cell parameters in phase III for a, b, c and V are estimated to be ±0.002, ±0.008, ±0.003 and ±0.3, respectively.

3.3.7 Discussion

As a result of the formation of dihydrogen bonds, the vibrational spectroscopy studies on NH_3BH_3 shows that the N-H stretching bands were red-shifted under the high pressure,[33] whereas these bands showed blue-shifted trend in $NaNH_2BH_3$, which is consistent with the previous study of lithium amidoborane with two phase transitions at 3.9 and 12.7 GPa.[25] On the basis of the theoretical calculation of NH_3BH_3[23], with the increasing pressure, the intermolecular distance between N and H atoms gets shorter, leading to the stronger dihydrogen bonds. Therefore, the N-H bond length increases, resulting in the redshift of the frequency of N-H stretching modes.[33] However, the N-H stretching bands of $NaNH_2BH_3$ show blueshift with increasing pressure indicated that a likely absence of

www.manaraa.com

dihydrogen bonding in the structure of $NaNH_2BH_3$, which is consistent with the Raman study on $LiNH_2BH_3$.[25] A possible explanation for the absence of dihydrogen bond in the structure of $LiNH_2BH_3$ and $NaNH_2BH_3$ is that the substitution of H by a stronger electron-donating alkali metal will induce considerable changes in the electronic state of N atoms.[5] From the fact that the Na-N bond in $NaNH_2BH_3$ is longer than N-H bond in NH_3BH_3, the substantial ionic character between Na^+ and $(NH_2BH_3)^-$ may exist in $NaNH_2BH_3$ because Na are more electron-donating than H atoms, thus, the Na-N bonds tend to show more ionic character. As a result, the electrostatic interaction between Na^+ and $(NH_2BH_3)^-$ will contribute to the stable structure of $NaNH_2BH_3$ despite the absence of dihydrogen bonding, which was confirmed by the theoretical study of $LiNH_2BH_3$.[35]

3.4 Conclusions

In conclusion, a promising hydrogen storage material, sodium amidoborane was synthesized successfully by ball milling method. The structure and phase transitions under high pressure were firstly investigated via vibrational spectroscopy and synchrotron radiation. Two phase transitions were identified at around 1.0 and 2.7 GPa. The first phase transition is an isostructural phase transition with the different orientation of the $NaNH_2BH_3$ molecules. The structure of $NaNH_2BH_3$ maintains orthorhombic structure with the space group *Pbca*. With the increasing pressure, more significant changes in synchrotron XRD patterns, and Raman and IR bands suggest that the structure of $NaNH_2BH_3$ experiences a major transformation from orthorhombic to monoclinic. $NaNH_2BH_3$ loses the crystallinity structure when the pressure was above 14 GPa. The pressure-induced phase transitions were also found to be irreversible during the decompression process. The recovered phase exhibits a profile similar to phase II. Moreover, the N-H stretching bands of $NaNH_2BH_3$ were observed to be blue-shifted, which is in contrast to NH_3BH_3, but consistent with its isostructural compound $LiNH_2BH_3$, indicating the absence of dihydrogen bonds in the structure of $NaNH_2BH_3$. Finally, the electrostatic interaction between Na^+ and $(NH_2BH_3)^-$ plays an important role to stabilize the structure of $NaNH_2BH_3$ despite of the absence of dihydrogen bonds. Our

www.manaraa.com

findings provide the sufficient structural and the bonding information of $NaNH_2BH_3$ under high pressure, which is important to improve the hydrogen storage properties.

3.5 References

(1) Eberle, U.; Felderhoff, M.; Schuth, F. Chemical and physical solutions for hydrogen storage. *Angewandte Chemie-International Edition* **2009,** *48*, 6608-6630.

(2) Tan, Y. B.; Yu, X. B. Chemical regeneration of hydrogen storage materials. *Rsc Advances* **2013,** *3*, 23879-23894.

(3) Dutta, S. A review on production, storage of hydrogen and its utilization as an energy resource. *Journal of Industrial and Engineering Chemistry* **2014,** *20*, 1148–1156.

(4) Orimo, S. I.; Nakamori, Y.; Eliseo, J. R.; Zuttel, A.; Jensen, C. M. Complex hydrides for hydrogen storage. *Chemical Reviews* **2007,** *107*, 4111-4132.

(5) Xiong, Z. T.; Yong, C. K.; Wu, G. T.; Chen, P.; Shaw, W.; Karkamkar, A.; Autrey, T.; Jones, M. O.; Johnson, S. R.; Edwards, P. P., et al. High-capacity hydrogen storage in lithium and sodium amidoboranes. *Nature Materials* **2008,** *7*, 138-141.

(6) Chua, Y. S.; Chen, P.; Wu, G. T.; Xiong, Z. T. Development of amidoboranes for hydrogen storage. *Chemical Communications* **2011,** *47*, 5116-5129.

(7) Diyabalanage, H. V. K.; Shrestha, R. P.; Semelsberger, T. A.; Scott, B. L.; Bowden, M. E.; Davis, B. L.; Burrell, A. K. Calcium amidotrihydroborate: A hydrogen storage material. *Angewandte Chemie-International Edition* **2007,** *46*, 8995-8997.

(8) Diyabalanage, H. V. K.; Nakagawa, T.; Shrestha, R. P.; Semelsberger, T. A.; Davis, B. L.; Scott, B. L.; Burrell, A. K.; David, W. I. F.; Ryan, K. R.; Jones, M. O., et al. Potassium(I) amidotrihydroborate: structure and hydrogen release. *Journal of the American Chemical Society* **2010,** *132*, 11836-11837.

www.manaraa.com

(9) Wu, H.; Zhou, W.; Yildirim, T. Alkali and alkaline-earth metal amidoboranes: structure, crystal chemistry, and hydrogen storage properties. *Journal of the American Chemical Society* **2008,** *130*, 14834-14839.

(10) Genova, R. V.; Fijalkowski, K. J.; Budzianowski, A.; Grochala, W. Towards $Y(NH_2BH_3)_3$: Probing hydrogen storage properties of YX_3/MNH_2BH_3 (X = F, Cl; M = Li, Na) and $YH_{x\sim3}/NH_3BH_3$ composites. *Journal of Alloys and Compounds* **2010,** *499*, 144-148.

(11) Chen, Y. S.; Fulton, J. L.; Linehan, J. C.; Autrey, T. In situ XAFS and NMR study of rhodium-catalyzed dehydrogenation of dimethylamine borane. *Journal of the American Chemical Society* **2005,** *127*, 3254-3255.

(12) Sewell, L. J.; Huertos, M. A.; Dickinson, M. E.; Weller, A. S.; Lloyd-Jones, G. C. Dehydrocoupling of dimethylamine borane catalyzed by $Rh(PCy_3)_2H_2Cl$. *Inorganic Chemistry* **2013,** *52*, 4509-4516.

(13) Xia, G. L.; Tan, Y. B.; Chen, X. W.; Guo, Z. P.; Liu, H. K.; Yu, X. B. Mixed-metal (Li, Al) amidoborane: synthesis and enhanced hydrogen storage properties. *Journal of Materials Chemistry A* **2013,** *1*, 1810-1820.

(14) Sloan, M. E.; Staubitz, A.; Clark, T. J.; Russell, C. A.; Lloyd-Jones, G. C.; Manners, I. Homogeneous catalytic dehydrocoupling/dehydrogenation of amine-borane adducts by early transition metal, group 4 metallocene complexes. *Journal of the American Chemical Society* **2010,** *132*, 3831-3841.

(15) Grant, D. J.; Matus, M. H.; Anderson, K. D.; Camaioni, D. M.; Neufeldt, S. R.; Lane, C. F.; Dixon, D. A. Thermochemistry for the dehydrogenation of methyl-substituted ammonia borane compounds. *Journal of Physical Chemistry A* **2009,** *113*, 6121-6132.

www.manaraa.com

(16) Sun, C. H.; Yao, X. D.; Du, A. J.; Li, L.; Smith, S.; Lu, G. Q. Computational study of methyl derivatives of ammonia borane for hydrogen storage. *Physical Chemistry Chemical Physics* **2008,** *10*, 6104-6106.

(17) Grochala, W.; Hoffmann, R.; Feng, J.; Ashcroft, N. W. The chemical imagination at work in very tight places. *Angewandte Chemie-International Edition* **2007,** *46*, 3620-3642.

(18) Schettino, V.; Bini, R. Constraining molecules at the closest approach: chemistry at high pressure. *Chemical Society Reviews* **2007,** *36*, 869-880.

(19) Hemley, R. J. Effects of high pressure on molecules. *Annual Review of Physical Chemistry* **2000,** *51*, 763-800.

(20) Song, Y. New perspectives on potential hydrogen storage materials using high pressure. *Physical Chemistry Chemical Physics* **2013,** *15*, 14524-14547.

(21) Trudel, S.; Gilson, D. F. R. High-pressure Raman spectroscopic study of the ammonia-borane complex. Evidence for the dihydrogen bond. *Inorganic Chemistry* **2003,** *42*, 2814-2816.

(22) Custelcean, R.; Dreger, Z. A. Dihydrogen bonding under high pressure: A Raman study of BH_3NH_3 molecular crystal. *Journal of Physical Chemistry B* **2003,** *107*, 9231-9235.

(23) Crabtree, R. H.; Siegbahn, P. E. M.; Eisenstein, O.; Rheingold, A. L. A new intermolecular interaction: Unconventional hydrogen bonds with element-hydride bonds as proton acceptor. *Accounts of Chemical Research* **1996,** *29*, 348-354.

(24) Lin, Y.; Ma, H. W.; Matthews, C. W.; Kolb, B.; Sinogeikin, S.; Thonhauser, T.; Mao, W. L. Experimental and theoretical studies on a high pressure monoclinic phase of ammonia borane. *Journal of Physical Chemistry C* **2012,** *116*, 2172-2178.

www.manaraa.com

(25) Najiba, S.; Chen, J. H. High-pressure study of lithium amidoborane using Raman spectroscopy and insight into dihydrogen bonding absence. *Proceedings of the National Academy of Sciences of the United States of America* **2012,** *109*, 19140-19144.

(26) Ramzan, M.; Silvearv, F.; Blomqvist, A.; Scheicher, R. H.; Lebegue, S.; Ahuja, R. Structural and energetic analysis of the hydrogen storage materials $LiNH_2BH_3$ and $NaNH_2BH_3$ from ab initio calculations. *Physical Review B* **2009,** *79*, 132102.

(27) Zhang, Y. S.; Wolverton, C. Crystal structures, phase stabilities, and hydrogen storage properties of metal amidoboranes. *Journal of Physical Chemistry C* **2012,** *116*, 14224-14231.

(28) Wang, K.; Zhang, J. G.; Zhang, T. L. Crystal and electronic structures of solid $M(NH_2BH_3)_n$ (M = Li, Na, K) and the decomposition mechanisms. *International Journal of Hydrogen Energy* **2014,** *39*, 21372-21379.

(29) Magos-Palasyuk, E.; Fijalkowski, K. J.; Palasyuk, T. Chemically driven negative linear compressibility in sodium amidoborane, $Na(NH_2BH_3)$. *Scientific Reports* **2016,** *6*, 28745.

(30) Stennett, T. E.; Harder, S. s-Block amidoboranes: syntheses, structures, reactivity and applications. *Chemical Society Reviews* **2016,** *45*, 1112-1128.

(31) Klooster, W. T.; Koetzle, T. F.; Siegbahn, P. E. M.; Richardson, T. B.; Crabtree, R. H. Study of the N-H···H-B dihydrogen bond including the crystal structure of BH_3NH_3 by neutron diffraction. *Journal of the American Chemical Society* **1999,** *121*, 6337-6343.

(32) Paolone, A.; Teocoli, F.; Sanna, S.; Palumbo, O.; Autrey, T. Temperature dependence of the infrared spectrum of ammonia borane: Librations, rotations, and molecular vibrations. *Journal of Physical Chemistry C* **2013,** *117*, 729-734.

(33) Xie, S. T.; Song, Y.; Liu, Z. X. In situ high-pressure study of ammonia borane by Raman and IR spectroscopy. *Canadian Journal of Chemistry-Revue Canadienne De Chimie* **2009,** *87*, 1235-1247.

www.manaraa.com

(34) Lee, S. M.; Kang, X. D.; Wang, P.; Cheng, H. M.; Lee, Y. H. A comparative study of the structural, electronic, and vibrational properties of NH_3BH_3 and $LiNH_2BH_3$: Theory and experiment. *Chemphyschem* **2009,** *10*, 1825-1833.

(35) Ryan, K. R.; Ramirez-Cuesta, A. J.; Refson, K.; Jones, M. O.; Edwards, P. P.; David, W. I. F. A combined experimental inelastic neutron scattering, Raman and ab initio lattice dynamics study of alpha-lithium amidoborane. *Physical Chemistry Chemical Physics* **2011,** *13*, 12249-12253.

www.manaraa.com

Chapter 4

4 Pressure effects on structure and dihydrogen bonding in hydrazine borane probed by *in- situ* vibrational spectroscopy and synchrotron X-ray diffraction

4.1 Introduction

Hydrogen has been well considered as a promising energy carrier to replace the fossil fuel sources in the future due to its high gravimetric energy density and the environmental friendly property.[1-4] However, some challenges regarding of the hydrogen storage still hinder the application of hydrogen energy, especially for the mobile applications. The traditional way is to use the compressed hydrogen cylinder, which requires the energy consumption and remains the safety concerns.[5-6] Over the past decades, the development of the hydrogen storage materials has shed light on the novel method for the hydrogen storage. For instance, the chemical hydrides containing B-N bonds, such as ammonia borane (NH_3BH_3) and hydrazine borane ($N_2H_4BH_3$), stood out as the excellent candidates due to their light weight and the ability of bearing multiple hydrogen atoms[5, 7-9] Such B-N compounds have both B-H and N-H bonds, which show the hydridic and protonic properties, respectively, leading to a different dehydrogenation process and a lower dehydrogenation temperature.[10-13]

In particular, ammonia borane (AB) is a well-studied compound, which is a promising hydrogen storage material due to its very high hydrogen content (19.6%) and stability under the ambient conditions.[8, 14-19] However, it was also found that the toxic borazine is released during the decomposition of AB, accompanied by other issues regarding the decomposition temperature, kinetics and the purity of hydrogen.[7-8, 12, 20-22] Finding other alternatives of AB would lead to desirable solutions to these problems.

Similar to AB, hydrazine borane (HB) also possesses high hydrogen content of 15.4%, which could be synthesized via the reaction of hydrazinium sulfate with sodium borohydride in cyclic ethers.[9, 12, 23-24] HB was firstly synthesized in 1961 by Goubeau and

www.manaraa.com

Ricker,[24] the dehydrogenation process and more synthesis routes were also investigated in the next several decades.[12, 25-27] Hügle *et al*. tested the dehydrogenation behavior of both HB and the mixture of HB and LiH, which showed excellent hydrogen release rates at a temperature range of 100-150 °C.[9] Moury *et al*. improved the synthesis procedure of HB with a high yield and purity, the stability and thermal decomposition of HB were also studied.[12] However, some questions about HB remains unclear, such as the dehydrogenation mechanism, the reactivity of N-H and B-H bonds and the regeneration of spent materials.[28-29] In order to anwser these questions, the crystal structure and bond behavior of HB needs further indepth investigation.

High pressure has been demonstrated as an effective tool to modify the crystal structures and to study the bonding behaviors.[30-33] A number of B-N compounds have been studied under high pressure involving phase transitions, the reversibility of structures and the altered electronic properties by both experiments and theoretical calculations. For instance, AB has been examined extensively under high pressure by synchrotron XRD, IR and Raman spectroscopy. Pressure-induced phase transitions were discovered by different researchers and the structures of new phases were also proposed accordingly.[34-37] Moreover, the dihydrogen bonding was also testified by the evidence of redshifts of N-H bond under high pressure, as the result of the strengthening of the dihydrogen bonds, in high-pressure Raman spectroscopy studies on AB.[34-35, 38-39] More recently, the effect of high pressure on structure of HB was explored by synchrotron XRD and the theoretical calculations, but only up to ~2 GPa.[40] No phase transition was observed and the sample maintains ambient pressure crystal structure up to 2 GPa. Therefore, structural transformations and the possibility of new phases of HB under higher pressure region remain to be investigated. Moreover, as an important role in stabilizing the structure of HB, the evolution of dihydrogen bonds as a function of pressure will provide valuable information in understanding the structural stability or transformations of HB.

In this study, we investigate the pressure-induced structural transformation of HB upon compression to ~20 GPa using in-situ IR, Raman and synchrotron XRD. The structural changes and the hydrogen bonding, including the dihydrogen bonding N−H···H−B and

www.manaraa.com

hydrogen bonding N−H···N were investigated with indepth analysis. The new findings in our study will enhance the understanding of the mechanism of dehydrogenation process and guide the design of new AB based hydrogen storage materials.

4.2 Experimental

4.2.1 Synthesis of hydrazine borane

HB were synthesized according to the previous reported method by the following reaction.[12]

$$(N_2H_4)_2{\cdot}H_2SO_4 + 2NaBH_4 \rightarrow 2N_2H_4BH_3 + Na_2SO_4 + 2H_2$$

Hydrazine hemisulfate $(N_2H_4)_2{\cdot}H_2SO_4$ (98%), sodium borohydride $NaBH_4$ (98%), and anhydrous 1,4-dioxane (99.8%) were purchased from Sigma Aldrich with claimed purity and used as received. 4.86 g $(N_2H_4)_2{\cdot}H_2SO_4$ (0.03 mol) and 2.27 g $NaBH_4$ (0.06 mol) were grinded into fine powders separately in a mortar in glovebox, followed by transferring into a 100 mL round bottom flask. 50 mL of dioxane was then added into the flask and the reaction occurred immediately once they were mixed together. The flask was placed into an oil bath and the temperature was set at 30 °C. After the mixture was stirring for 48 hours under 30 °C, the suspension was filtered and the solid was washed with 50 mL of dioxane. Lastly, the filtrate was under the vacuum to remove the solvent. The final product is a white solid, which was dried under vacuum and room temperature overnight. The product was kept in a N_2-filled MBraun LAB Master 130 glovebox with H_2O content of < 1 ppm and O_2 content of < 3 ppm.

4.2.2 Powder X-ray diffraction

The crystallinity and purity of the as-synthesized product was tested by a Rigaku X-ray diffractometer using Co Kα radiation (λ = 1.78890 Å), the scan range was from 2θ = 10 to 80° with a step size of 0.02. The sample was covered by a piece of Kapton film during the measurement to avoid the moisture. The diffraction pattern was refined by Le Bail method using GSAS.

www.manaraa.com

4.2.3 In-situ FTIR spectroscopy

A symmetrical diamond anvil cell with two type II diamonds with the culet size of 400 μm was used for IR measurement. A stainless steel gasket was preindented to 40 μm in thickness. A hole with diameter of 130 μm was drilled in the center of the gasket as a sample chamber. A ruby ball and small amount of KBr were pre-loaded into the sample chamber, followed by the loading of the sample in glovebox. The in-situ high-pressure IR absorption experiments were carried out by a customized IR micro-spectroscopy system with details described in Chapter 2.

4.2.4 In-situ Raman spectroscopy

For Raman spectroscopy measurements, a symmetrical diamond anvil cell with two type I diamonds with the culet size of 400 μm was used. The sample was loaded into sample chamber along with a ruby ball in glovebox. The in-situ high-pressure Raman experiments were carried out by a customized Raman spectrometer with a 532 nm excitation laser. A grating with 1200 lines/mm was used for all measurements. The details of Raman system is provided in Chapter 2.

4.2.5 In-situ synchrotron X-ray diffraction

A symmetrical diamond anvil cell with two type I diamonds with the culet size of 400 μm was used for high-pressure synchrotron XRD study. The measurements were performed at sector 20 in APS, ANL. The sample was loaded into the sample chamber with a ruby ball as pressure calibrant in glovebox. No pressure transmitting medium was used due to the pressure range and the air-sensitivity of the sample. The wavelength of monochromatic X-ray beam is 0.4592 Å.

4.3 Results and Discussion

4.3.1 XRD pattern under ambient conditions

The XRD pattern of as-synthesized HB collected under ambient conditions is shown in Figure 4.1a. The structure of HB could be indexed to be an orthorhombic structure with the space group of *Pbcn*. By using Le Bail refinement (Figure 4.1b), the unit cell

www.manaraa.com

parameters were obtained to be a = 13.1079 Å, b = 5.0995 Å, c = 9.5901 Å, and V = 641.036 V^3, which are consistent with the references.[12, 23, 28, 41]

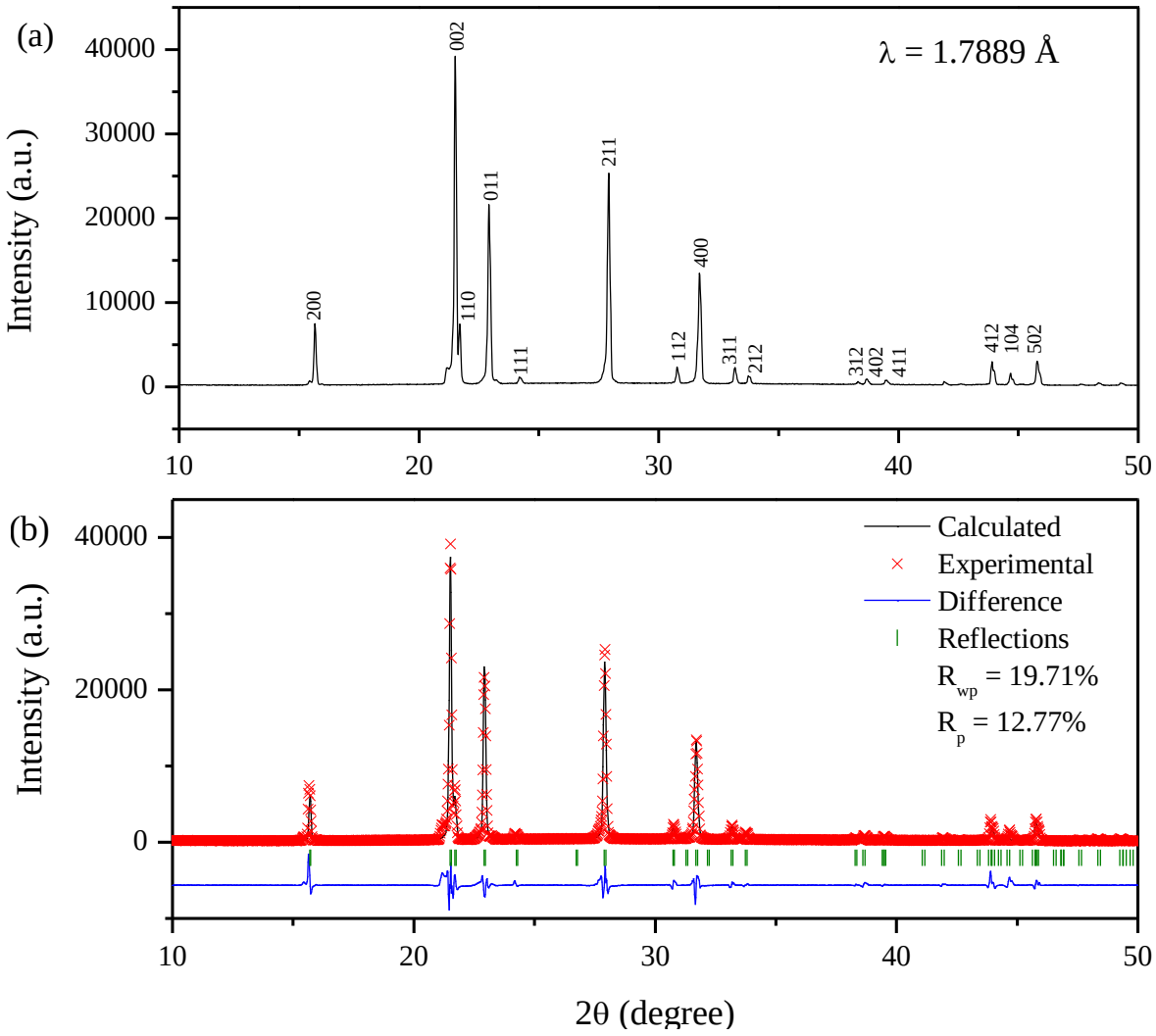

Figure 4.1 Indexed XRD pattern of Hydrazine borane under ambient conditions (a) and calculated XRD patterns in comparison with experimental results under ambient conditions using Le Bail refinement (b)

The previous structural studies of HB revealed that 8 HB molecules reside in a unit cell with each molecule occupying the C_1 site.[12] Due to the different electronegativity of N and B atoms, a dative N-B bond forms in the HB molecule, which was revealed to be both covalent and ionic bond features, but a mainly electrostatic interaction, as suggested

www.manaraa.com

by a previous theoretical study.[41] Similar with ammonia borane, dihydrogen bond N−H···H− B exists between the HB molecules, accompanied with classical N− H···N hydrogen bond, which form a network of the HB molecules to stabilize the solid state of the material, as shown in Figure 4.2a.

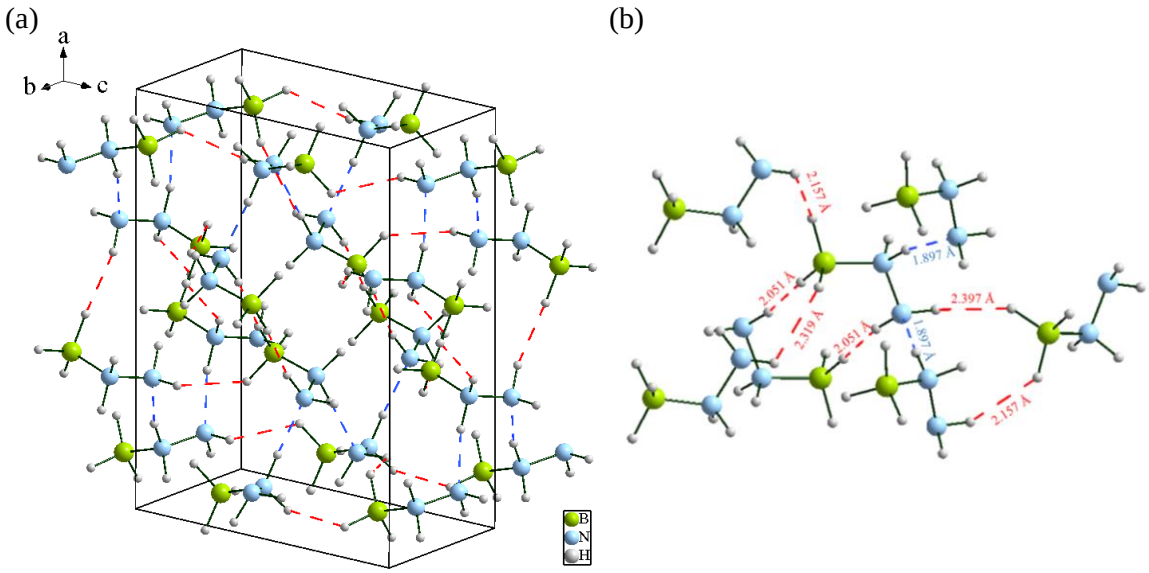

Figure 4.2 Structure of HB unit cell and the network of the HB molecules building by dihydrogen bonds and hydrogen bonds (a), an HB molecule with its nearest neighboring molecules (b). The N−H···H−B dihydrogen bonds were indicated by red dashed lines, while the N−H···N classical hydrogen bonds were presented by blue dashed lines.

To better illustrate the interactions between the HB molecules, an HB molecule with its nearest neighboring molecules are shown in Figure 4.2b. The dihydrogen bonds N−H···H−B are formed by intermolecular interactions in the range of 2.0 to 2.4 Å, which are shorter than twice the van der Waals radius of H atom (i.e., 1.2 Å). Besides, the lengths of the dihydrogen bonds in HB are comparable with those in AB, so that this network will enhance the intermolecular interactions and thus the stability.[15, 42] In addition, the interaction of hydrogen bonding N−H···N is also formed between HB molecules along a direction with a distance of 1.897 Å, which is consistent with the previous theoretical

www.manaraa.com

study.[41] Therefore, such intermolecular interactions stabilize the structure of HB solid under the ambient conditions.

4.3.2 IR and Raman spectra under ambient conditions

We also collected IR and Raman spectra of HB under ambient pressure at room temperature, as shown in Figure 4.3. The spectra reveal characteristic vibrational bands of HB, such as the N−H stretching region (2600 to 3400 cm^{-1}), the B−H stretching region (2200 to 2500 cm^{-1}), the N−H asymmetric bending region (1590 to 1630 cm^{-1}) and the B−H bending region (1100 to 1300 cm^{-1}). Additionally, in Raman spectrum, several lattice modes could be observed from 70 to 400 cm^{-1}. The assignment of the observed IR and Raman vibrational modes are shown in Table 1, in reference with the previous works.[12, 23]

www.manaraa.com

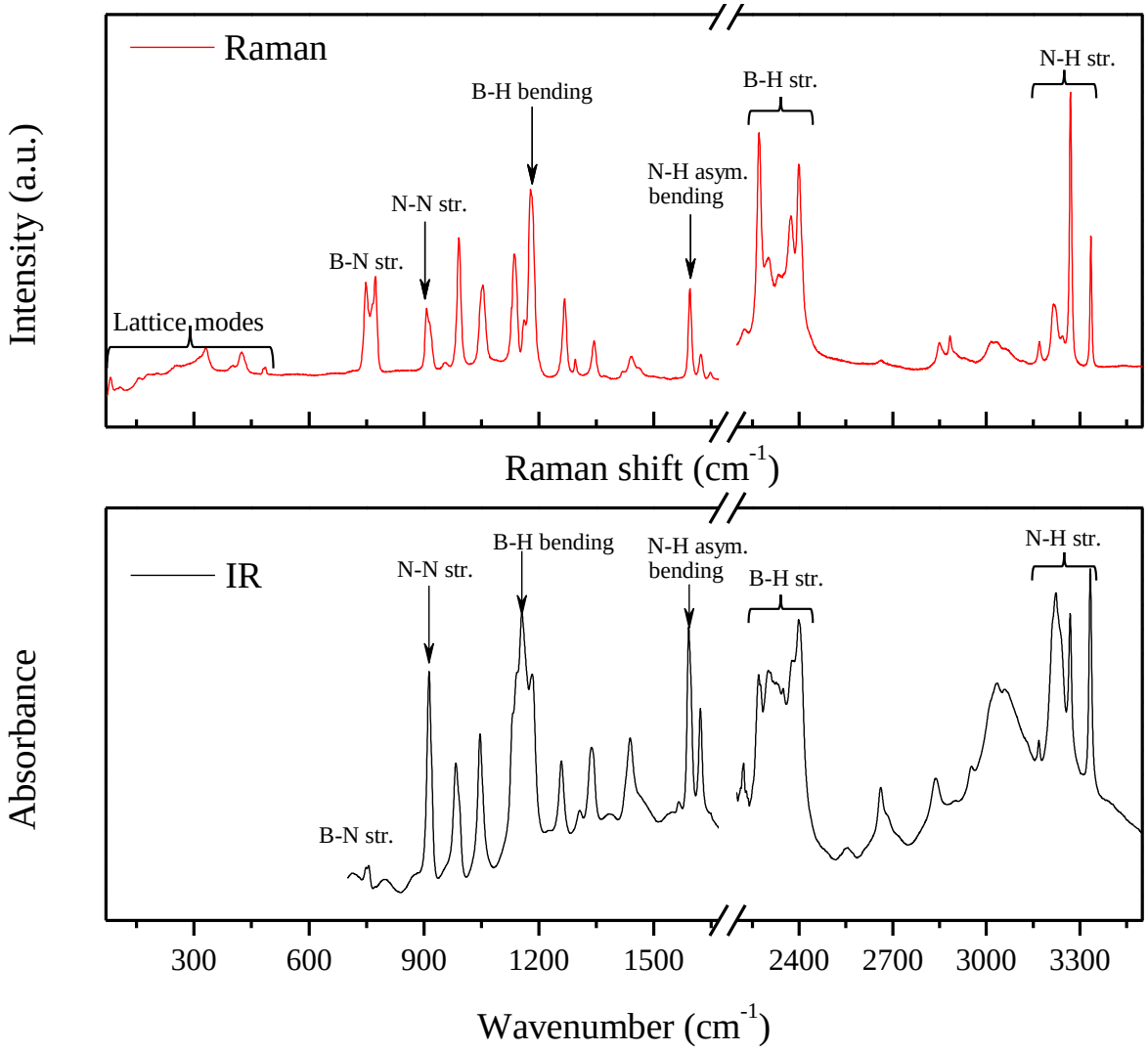

Figure 4.3 Raman and IR spectrum of HB collected at room temperature under ambient pressure

www.manaraa.com

Table 4.1 Assignments and vibrational frequencies (cm^{-1}) of HB at ambient pressure[12, 23]

	IR (cm^{-1})	Raman (cm^{-1})
Lattice modes		81
		107
		156
		178
		330
B-N stretching	749	749
	755	773
N-N stretching	913	907
N-H rocking	986	
	994	992
	1050	1053
B-H bending	1133	1137
	1183	1178
	1260	1269
N-H bending	1337	1341
	1436	1444
N−H asymmetric bending	1591	1594
	1622	1623
B-H stretching	2271	2272
	2300	2303
	2376	2373
	2398	2399
N-H stretching	3168	3170
	3223	3216
	3268	3269
	3333	3334

4.3.3 IR spectra under high pressure

In-situ high-pressure IR spectra of HB were collected under high pressure up to 15 GPa to examine the evolution of the dihydrogen bonding, as shown in Figure 4.4. Overall, the

www.manaraa.com

spectra show a smooth evolution, indicating the absence of phase transition during the entire compression region. Noticeably, a peak at around 1260 cm^{-1} in B-H bending region split into two components at high-pressure region (> 5 GPa), likely due to the distortion of the orthorhombic structure and the altered local structure, leading to the modified interactions between the HB molecules. Upon compression to near 15 GPa, the spectrum exhibits a profile with broadened peaks, suggesting the degree of crystallinity decrease upon compression. Furthermore, we investigated the reversibility of the material. The IR spectra of HB under decompression were shown in Figure 4.5. The recovered spectrum represented the almost same profile as the initial one with all the peaks recovered completely, indicating the high reversibility of HB.

Moreover, the shift of vibrational modes as a function of pressure was further examined, as shown in Figure 4.6. Table 4.2 shows the pressure dependence of selected IR modes on compression. Most of the vibrational modes exhibit blueshift (positive values in Table 4.2), due to the reduced bond length under high pressure. Significantly, compared to AB, the evolution of N-H stretching modes in HB upon compression shows the significant difference. The N-H stretching modes in AB shows the obvious redshift with the increase of the pressure, indicating the strengthening of the dihydrogen bonding $N-H\cdots H-B$, resulting in the weakening of N-H bond.[35] However, the N-H stretching modes in HB shows a minor blueshift, probably due to the rearrangement of the dihydrogen bonding and hydrogen bonding in the network of the structure, leading to a strengthened N-H bond upon compression.[43]

www.manaraa.com

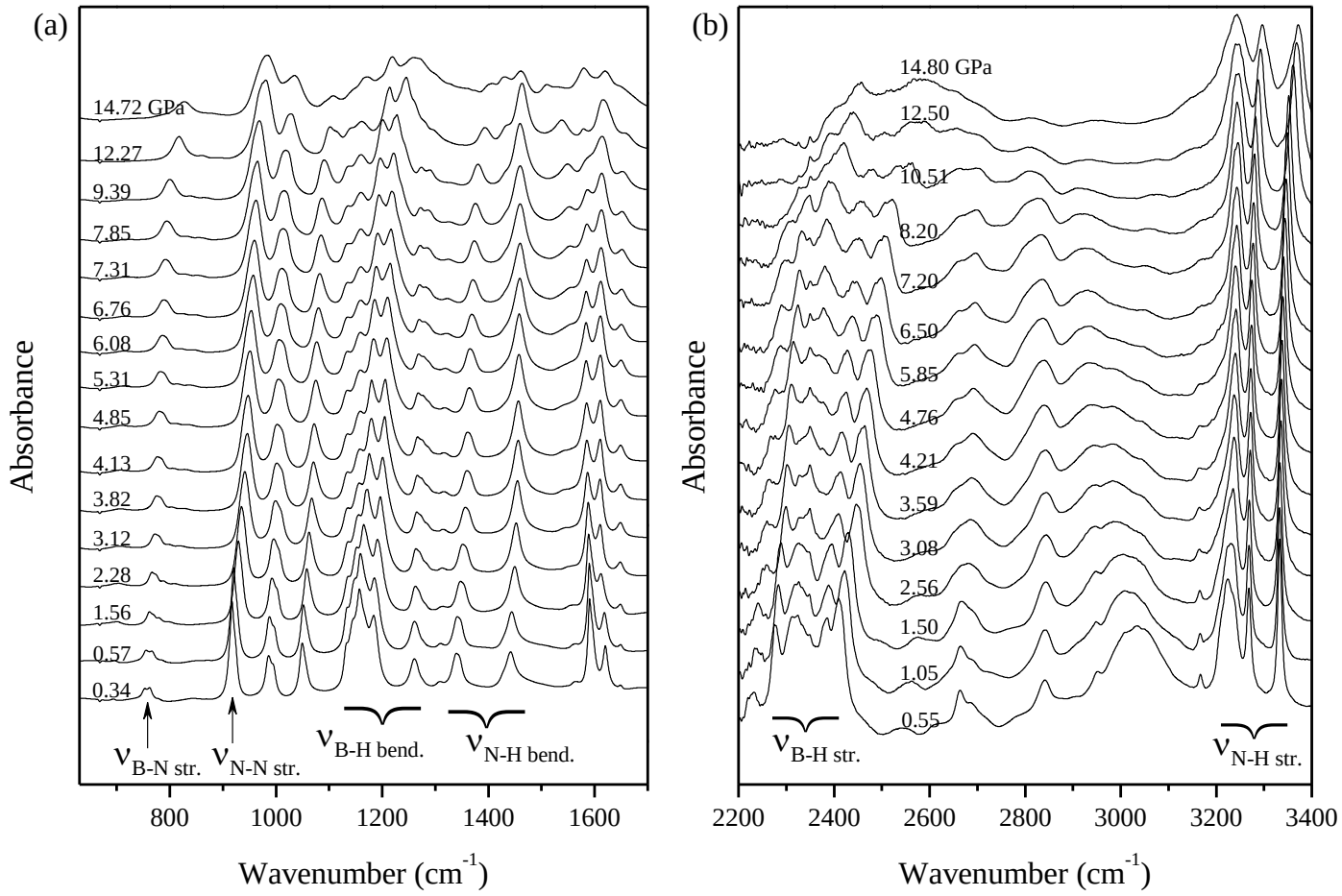

Figure 4.4 IR spectra of HB collected at room temperature on compression in the region of 630-3400 cm^{-1}. The pressures in GPa are labeled for each spectrum and the assignments are labeled for selected IR modes.

www.manaraa.com

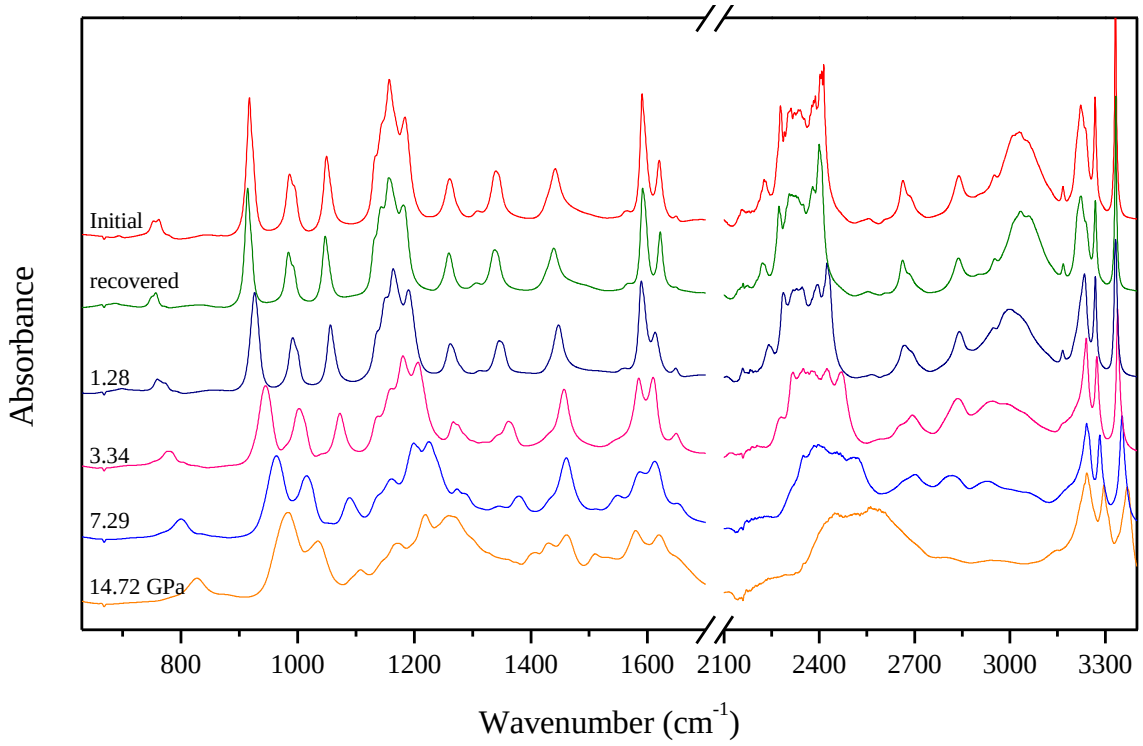

Figure 4.5 Selected IR spectra of HB collected at room temperature on decompression

www.manaraa.com

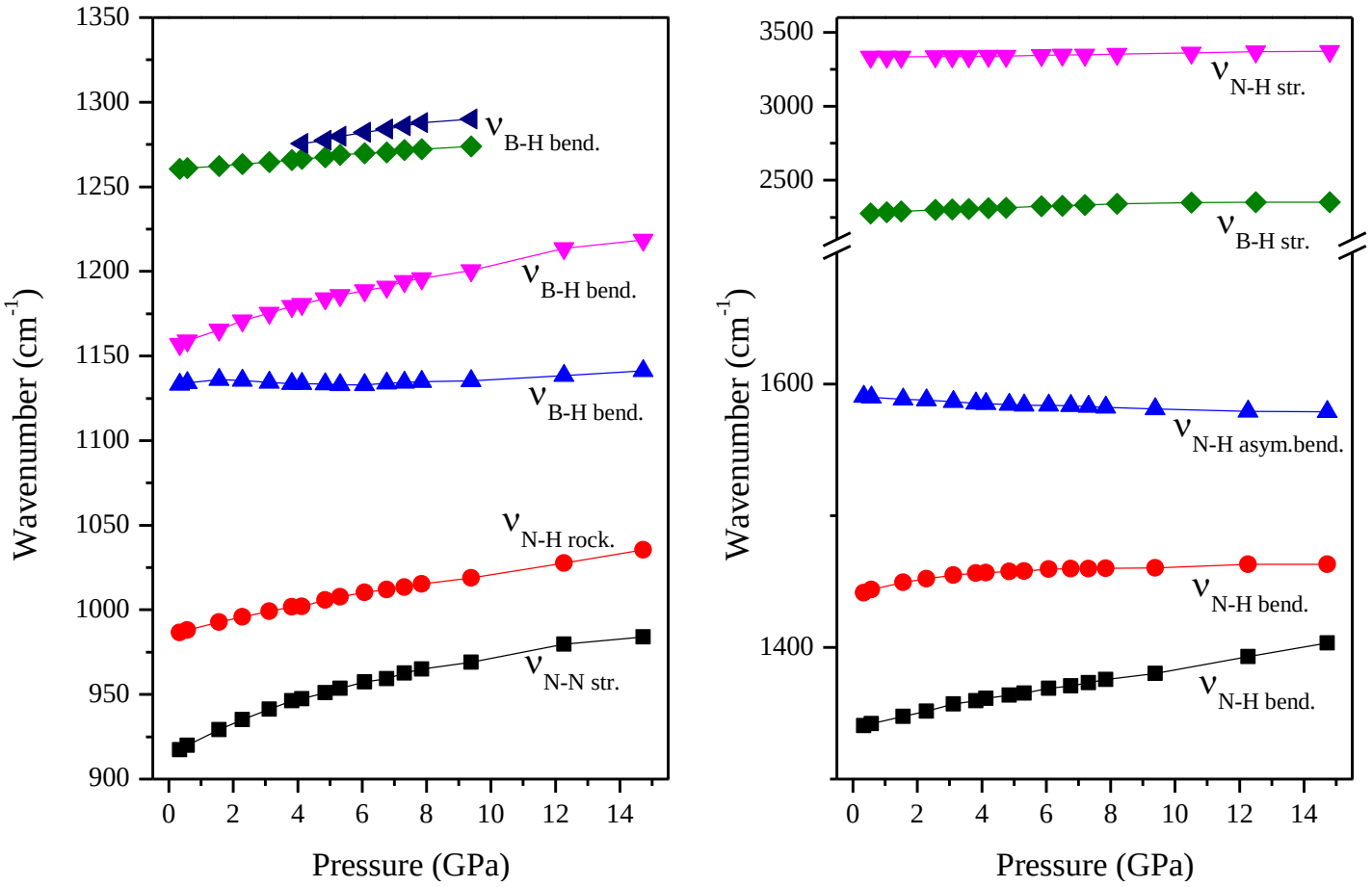

Figure 4.6 Pressure dependence of selected IR modes of HB on compression. Different symbols represent IR modes with different origins.

www.manaraa.com

Table 4.2 The pressure dependence of characteristic IR modes of HB on compression

Assignment	Frequency (cm^{-1})	dν/dp ($cm^{-1}\cdot GPa^{-1}$)
N-N stretching	913	4.65
N-H rocking	986	3.34
B-N bending	1133	0.39
	1156	4.30
	1260	1.54
N-H bending	1337	4.24
	1436	1.34
N-H asym. bending	1591	-0.82
B-H stretching	2271	5.61
N-H stretching	3268	2.97

4.3.4 Raman spectra under high pressure

We also collected in-situ high-pressure Raman spectra of HB from ambient pressure to near 15 GPa, as shown in Figure 4.7. Generally, no significant changes were observed from the spectra, indicating the absence of phase transition. Moreover, the splitting of the lattice mode at 100 cm^{-1} and B-H bending mode at around 1200 cm^{-1} above 5 GPa indicates the minor structure distortion of HB upon compression. When the pressure reaches near 15 GPa, all the peaks become remarkably broadened, suggesting the decreasing of the crystallinity of HB upon compression. Additionally, the Raman spectra under decompression were also collected, as shown in Figure 4.8, the recovered Raman spectra of HB revealed the exact same profile as the initial one, indicating the high reversibility of the material.

www.manaraa.com

Furthermore, the Raman spectra of HB also revealed that all the vibrational modes slightly shifted during the compression, which was further examined by the vibrational modes as a function of pressure and the pressure dependence of the selected Raman modes of HB on compression, as shown in Figure 4.9 and Table 2.3. The results of Raman spectra show the agreement with the IR spectra, all the Raman modes exhibited slight blueshift during the entire compression, indicating the high stability of the material and the strengthening of N-H bond. Further theoretical calculations need to be performed to investigate the orientation of the HB molecules and the evolution of the distance between two H atoms and the distance between H and N atoms under high pressure. The calculations will help us to understand the evolution of the dihydrogen bonding and hydrogen bonding.

Table 4.3 The pressure dependence of characteristic Raman modes of HB on compression

Assignment	Frequency (cm^{-1})	dν/dp ($cm^{-1}\cdot GPa^{-1}$)
Lattice modes	84	6.83
	288	5.72
	425	3.71
B-N stretching	752	6.07
	783	9.37
N-N stretching	909	4.26
	920	6.25
N-H rocking	994	3.62
B-H stretching	2277	8.73
N-H stretching	3269	1.87

www.manaraa.com

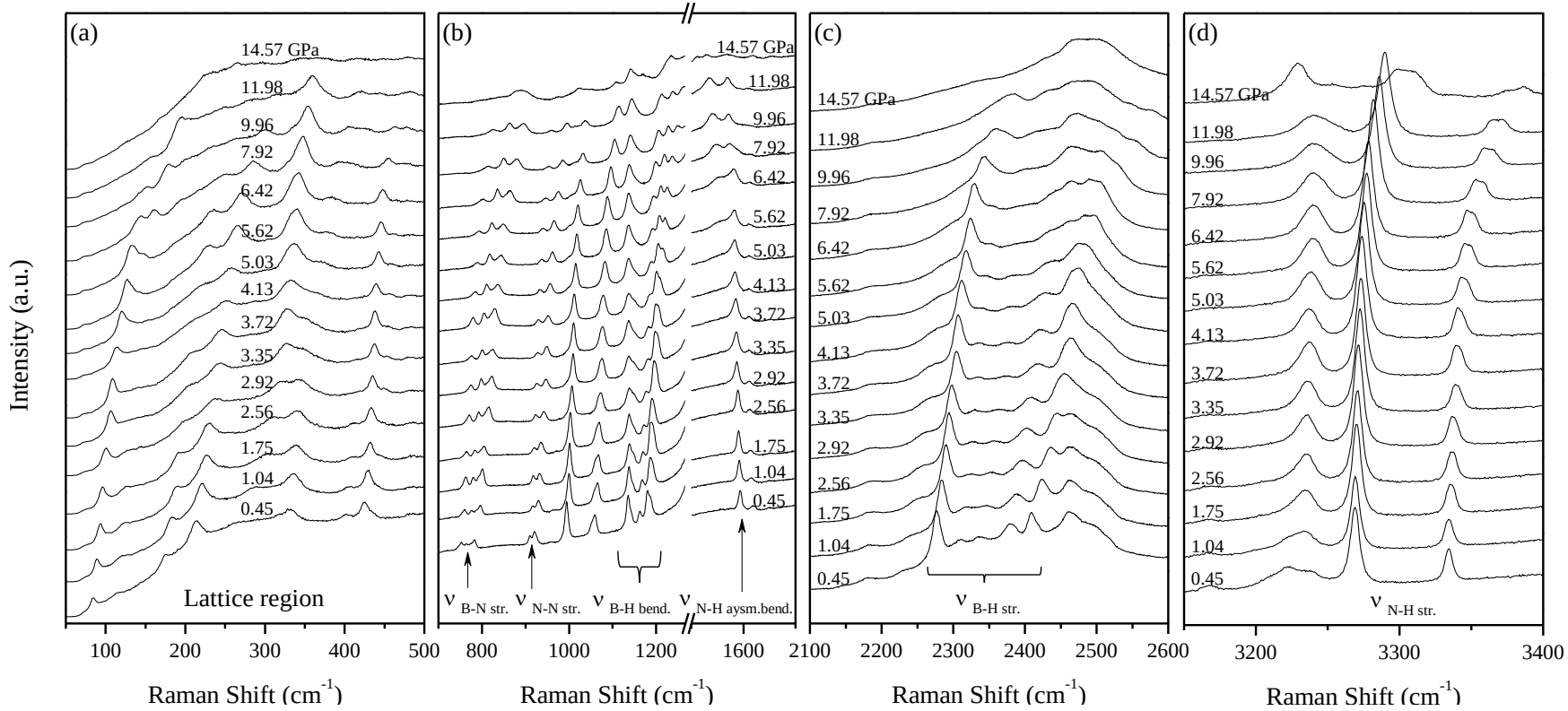

Figure 4.7 Raman spectra of HB collected at room temperature on compression in the region of 50-3400 cm^{-1}. The pressures in GPa are labeled for each spectrum and the assignments are labeled for selected Raman modes.

www.manaraa.com

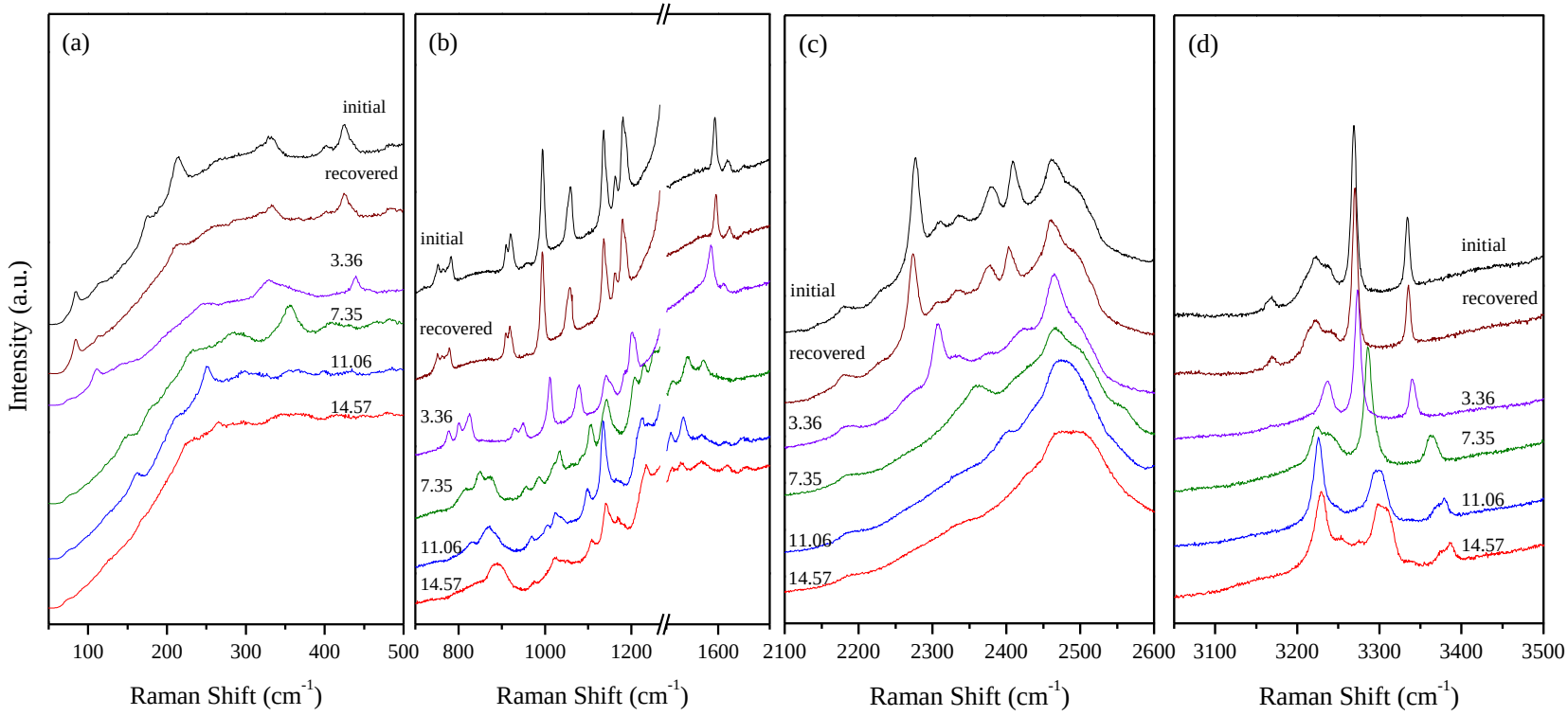

Figure 4.8 Selected Raman spectra of HB collected at room temperature on decompression, the pressures in GPa are labeled for each spectrum.

www.manaraa.com

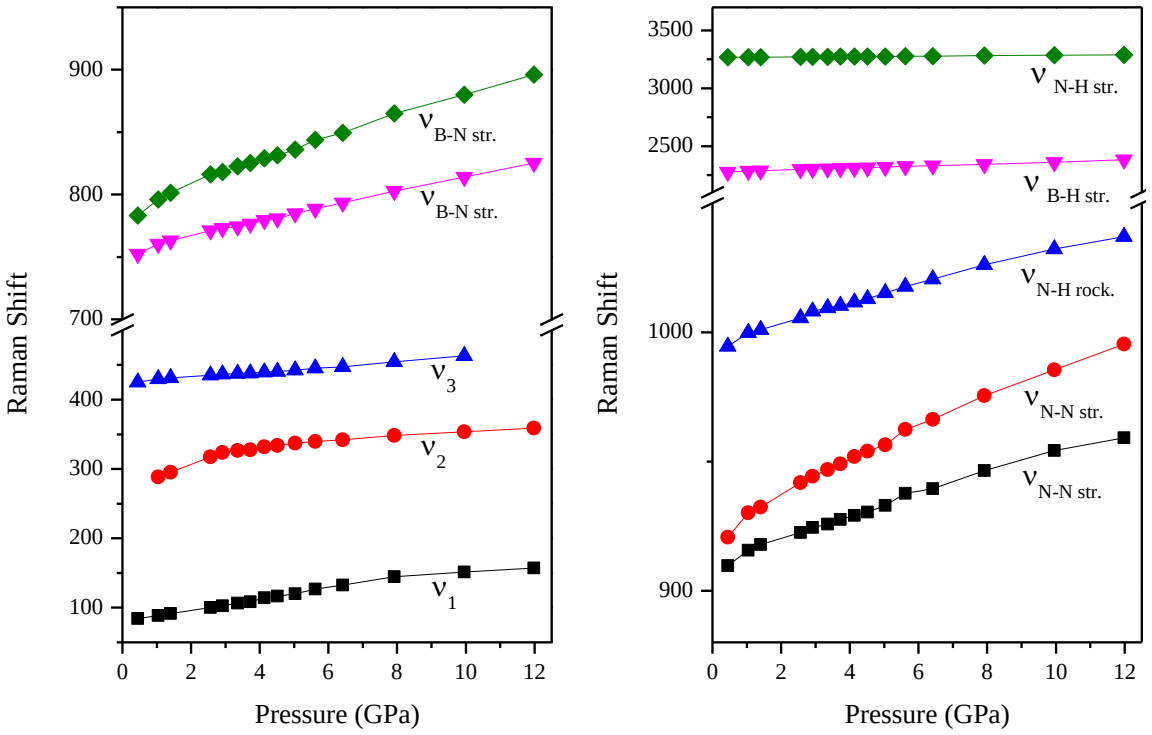

Figure 4.9 Pressure dependence of selected Raman modes of HB on compression. Different symbols represent Raman modes with different origins.

4.3.5 Synchrotron XRD patterns under high pressure

To gain insight into the pressure effect on the structure of HB, we collected the Synchrotron XRD patterns of HB from near ambient pressure to 20 GPa at room temperature, as shown in Figure 4.10. Overall, with the increasing pressure, all the reflections shifted to the higher angle direction, indicating the decreasing d spacing. No new peaks were observed during the whole compression region, indicating the absence of the phase transition. In addition, the XRD pattern at near 20 GPa still shows the profile of the crystallinity of HB without the appearance of the amorphization. Therefore, these observations suggest the high structural stability of the material, which is consistent with the previous low-temperature study of HB over the temperature range of 80–300 K.[44] Furthermore, the cell parameters at every high pressure were refined by Le Bail method

www.manaraa.com

and listed in Table 4.4. The results of calculated XRD patterns in comparison with experimental XRD patterns at 0.82 and 19.68 GPa are shown in Figure 4.11, the refinement results for other high pressures are shown in Appendix.

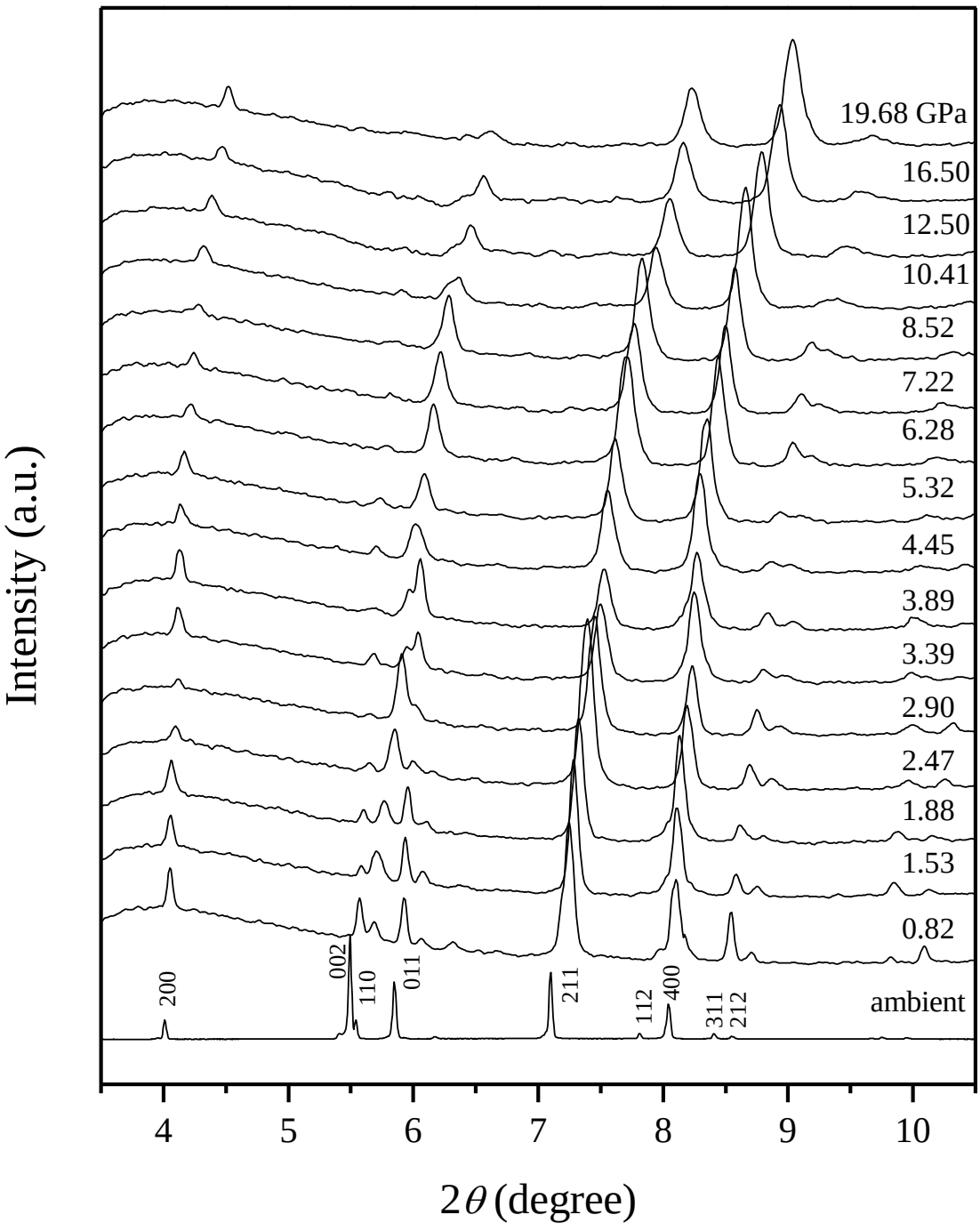

Figure 4.10 In-situ high-pressure Synchrotron XRD patterns of HB on compression

www.manaraa.com

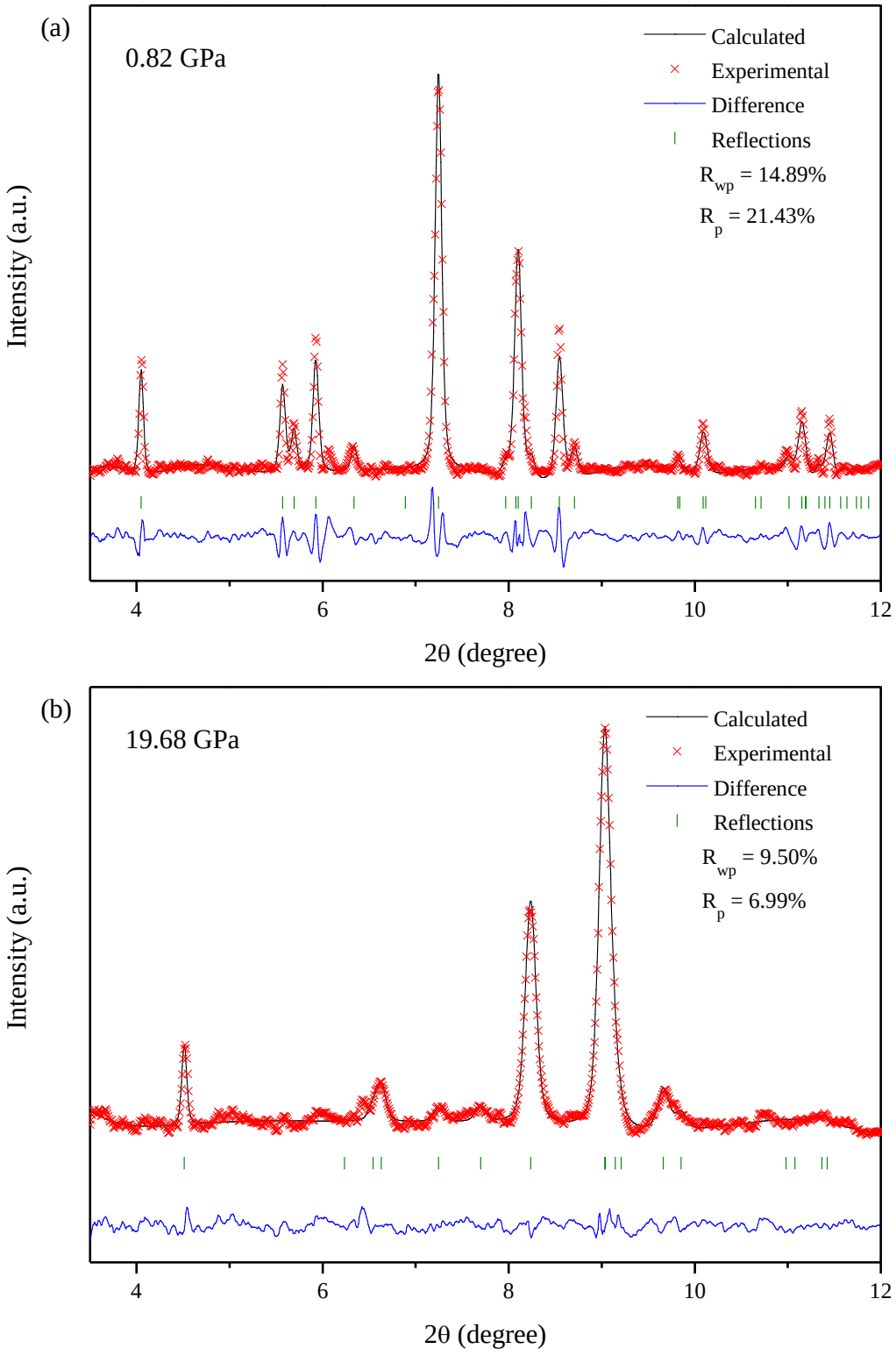

Figure 4.11 Calculated XRD patterns in comparison with experimental results at 0.82 (a) and 19.68 GPa (b) using Le Bail refinement

www.manaraa.com

In addition, the XRD patterns of HB were collected upon decompression, as shown in Figure 4.12, the recovered pattern indicates the similar profile as the initial one, with the modified intensity, indicating the pressure effects on the structure of HB is reversible.

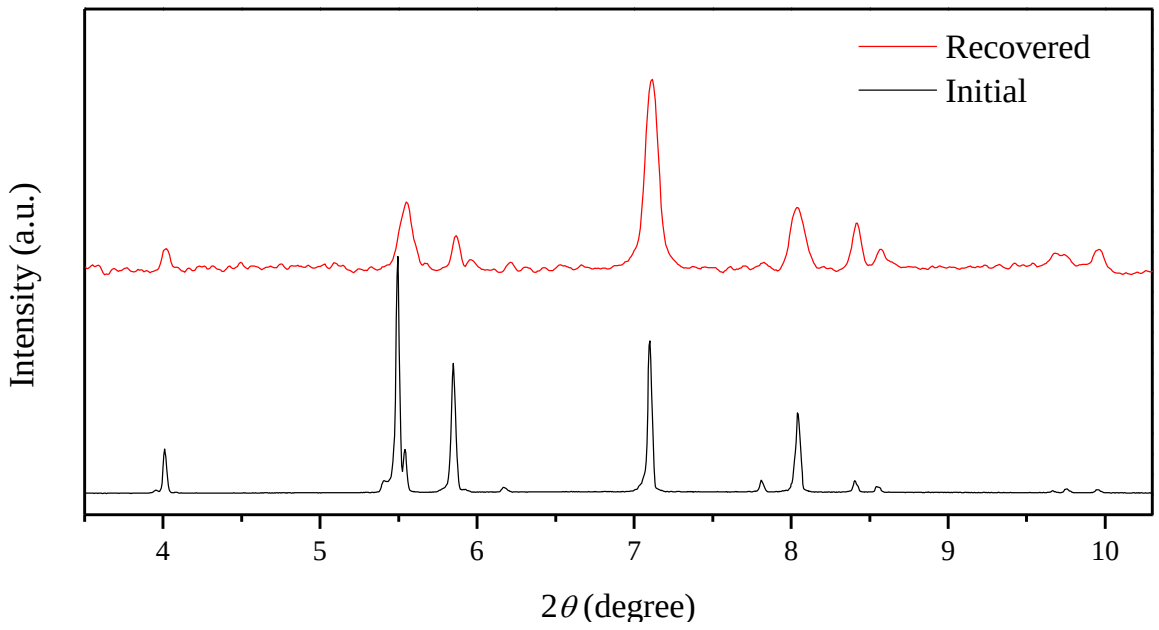

Figure 4.12 The recovered XRD pattern of HB in comparison with the initial one

We also plotted the cell parameters and volumes as a function of pressure (Figure 4.13), which reveal the smooth decrease in all the cell parameters. Moreover, the unit cell volumes obtained under high pressure were further analyzed by the equation of state (EOS) using the Birch–Murnaghan theory and the EoSFit7 software.[45-46] The third-order Birch–Murnaghan isothermal equation of state is given by the Equation 4.1, where P is the pressure, V_0 is the reference unit cell volume, V is the deformed volume, K_0 is the bulk modulus, K_0' is the derivative of the bulk modulus with respect to pressure.[40, 45]

$$P = \frac{3}{2} k_0 [(\frac{V_0}{V})^{\frac{7}{3}} - (\frac{V_0}{V})^{\frac{5}{3}}] \cdot \{1 - \frac{3}{4}(4 - K_0')[(\frac{V_0}{V})^{\frac{2}{3}} - 1]\} \qquad \text{Equation 4.1}$$

Figure 4.13b reports the evolution of the unit cell volume of HB in comparison with the fit obtained by a third order Birch–Murnaghan equation of state. The values of K_0 and K_0' were determined to be 20.53 GPa and 3.48, which are comparable with the previous high

www.manaraa.com

pressure study of HB in the pressure region of 0 - 2 GPa, confirming the high structural stability of this material.[40]

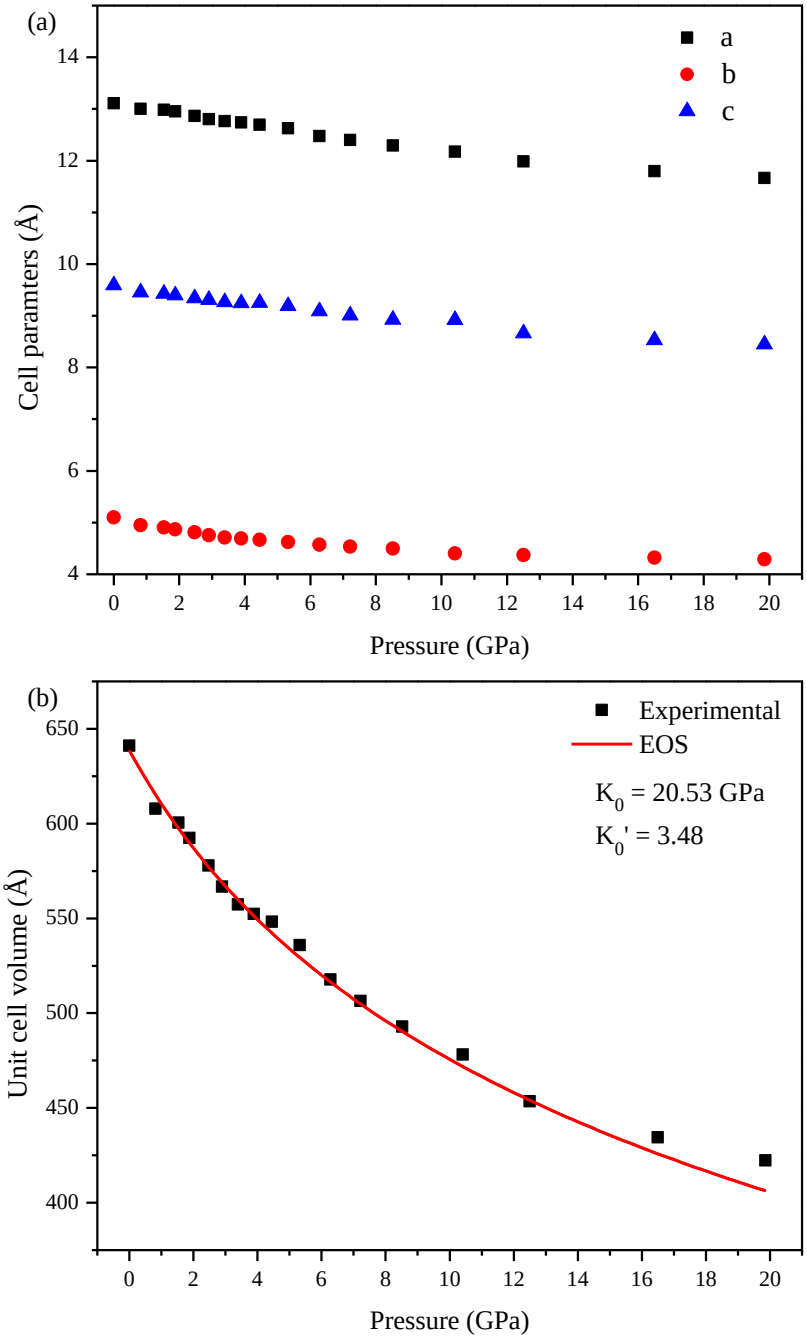

Figure 4.13 Cell parameters of HB as a function of pressure (a), and experimental cell volume of HB in comparison with calculated result using the third-order Birch–Murnaghan isothermal equation of state upon compression (b).

www.manaraa.com

Table 4.4 Refined cell parameters of HB at presentative pressures

Pressure (GPa)	a (Å)	b (Å)	c (Å)	V(Å^3)
ambient	13.1079	5.0995	9.5901	641.04
0.82	13.0002	4.9471	9.4516	607.86
1.53	12.9815	4.9053	9.4293	600.45
1.88	12.9511	4.8673	9.3993	592.50
2.47	12.8635	4.8097	9.3393	577.81
2.90	12.8003	4.7554	9.3111	566.77
3.39	12.7655	4.7122	9.2647	557.30
3.89	12.7415	4.6893	9.2457	552.41
4.45	12.6957	4.6686	9.2489	548.19
5.32	12.6231	4.6197	9.1909	535.96
6.28	12.4727	4.5689	9.0863	517.80
7.22	12.3976	4.5343	9.0077	506.36
8.52	12.2938	4.4932	8.9224	492.86
10.41	12.1751	4.4014	8.9220	478.11
12.50	11.9848	4.3676	8.6617	453.39
16.50	11.7985	4.3173	8.5289	434.45
19.86	11.6634	4.2875	8.4455	422.33

www.manaraa.com

The errors of cell parameters in the lower pressure region (< 8 GPa) for a, b, c and V are estimated to be ±0.006, ±0.003, ±0.007 and ±0.4, respectively. The errors of cell parameters in higher pressure region (> 8 GPa) for a, b, c and V are estimated to be ±0.006, ±0.008, ±0.013 and ±1.7, respectively.

4.3.6 Discussion

The replacement of the NH_3 moiety of NH_3BH_3 by N_2H_4 leads to the formation of HB with an increase of the molecule size and the altered reactivity of the chemical bonds, especially for the N-H bonds, which participate in the intermolecular interaction of HB molecules, i.e., the hydrogen bonding and dihydrogen bonding. Compared with NH_3BH_3 and $BH_3N_2H_4BH_3$ (HBB), the high-pressure effects on these materials reveal a dramatic difference. Firstly, dihydrogen bonding exists in all three materials to maintain the crystal structures, which were revealed by the experimental and theoretical studies.[15, 23, 47] The Raman spectroscopy studies on AB and HBB indicated the obvious redshift of N-H stretching modes upon compression, suggesting the strengthening of the dihydrogen bonding with the reduced intermolecular distance.[35, 47] However, the N-H stretching mode of HB shows slight blueshift, which was also observed in a previous high-pressure study of C-H···O hydrogen bonding system.[43] This observation can be explained by the modified intramolecular distance and N-N-B-H torsion angle, leading to the pressure-induced rearrangement of the dihydrogen bonding.[40] It would be interesting to explore the distance between two H atoms involving in the dihydrogen bonding and the N-N-B-H torsion angle upon compression by the theoretical calculations.

Moreover, in contrast with AB and HBB, HB shows a higher structural stability. Two phase transitions were identified for AB upon compression to 16 GPa, and one phase transition was observed for HBB under 2 GPa.[36, 47] We compressed the HB to near 20 GPa, no phase transition was discovered. This difference may be explained by the different molecular size, molecular conformation and pressure effects on the intermolecular interactions. Furthermore, compared with AB, HB shows a lower compressibility with a K_0 value of 20.53 GPa and K_0' of 3.48. Indeed, the phase I (0 - 1.5 GPa) and phase II (1.5 – 12 GPa) of AB have the K_0 values of 9.9 and 10.3 GPa,

www.manaraa.com

respectively.[48] The enhanced mechanical resilience could be attributed to the difference in the molecular arrangement in the crystal structures.[40] Overall, the high stability of the structure of HB could be explained by the strong intermolecular interactions, which also leads to the high reversibility of HB.

4.4 Conclusions

In summary, a hydrogen storage material hydrazine borane was investigated under high pressure by in-situ IR, Raman spectroscopy and synchrotron XRD. The pressure effect on the structure and chemical bonds of the material was also studied. No phase transition was observed during the whole compression region, indicating the high stability of the structure. In particular, during the whole compression region, the expected strengthening of dihydrogen bonding was not observed by both IR and Raman spectra, which is contrast to other B-N compounds. The possible explanation to this observation could be pressure-induced rearrangement of the dihydrogen bonding in the network of the structure.

4.5 References

(1) Chaubey, R.; Sahu, S.; James, O. O.; Maity, S. A review on development of industrial processes and emerging techniques for production of hydrogen from renewable and sustainable sources. *Renewable & Sustainable Energy Reviews* **2013,** *23*, 443-462.

(2) Schlapbach, L.; Zuttel, A. Hydrogen-storage materials for mobile applications. *Nature* **2001,** *414*, 353-358.

(3) van den Berg, A. W. C.; Arean, C. O. Materials for hydrogen storage: current research trends and perspectives. *Chemical Communications* **2008**, *6*, 668-681.

(4) Sinigaglia, T.; Lewiski, F.; Martins, M. E. S.; Siluk, J. C. M. Production, storage, fuel stations of hydrogen and its utilization in automotive applications-a review. *International Journal of Hydrogen Energy* **2017,** *42*, 24597-24611.

www.manaraa.com

(5) Dalebrook, A. F.; Gan, W. J.; Grasemann, M.; Moret, S.; Laurenczy, G. Hydrogen storage: beyond conventional methods. *Chemical Communications* **2013,** *49*, 8735-8751.

(6) Churchard, A. J.; Banach, E.; Borgschulte, A.; Caputo, R.; Chen, J. C.; Clary, D. C.; Fijalkowski, K. J.; Geerlings, H.; Genova, R. V.; Grochala, W., et al. A multifaceted approach to hydrogen storage. *Physical Chemistry Chemical Physics* **2011,** *13*, 16955-16972.

(7) Hamilton, C. W.; Baker, R. T.; Staubitz, A.; Manners, I. B-N compounds for chemical hydrogen storage. *Chemical Society Reviews* **2009,** *38*, 279-293.

(8) Staubitz, A.; Robertson, A. P. M.; Manners, I. Ammonia-borane and related compounds as dihydrogen sources. *Chemical Reviews* **2010,** *110*, 4079-4124.

(9) Hugle, T.; Kuhnel, M. F.; Lentz, D. Hydrazine borane: A promising hydrogen storage material. *Journal of the American Chemical Society* **2009,** *131*, 7444-7446.

(10) Hoffman, R. Extened huckel theory .3. compounds of boron + nitrogen. *Journal of Chemical Physics* **1964,** *40*, 2474.

(11) Zhang, J. S.; Zhao, Y.; Akins, D. L.; Lee, J. W. Thermal decomposition and spectroscopic studies of preheated ammonia borane. *Journal of Physical Chemistry C* **2010,** *114*, 19529-19534.

(12) Moury, R.; Moussa, G.; Demirci, U. B.; Hannauer, J.; Bernard, S.; Petit, E.; van der Lee, A.; Miele, P. Hydrazine borane: synthesis, characterization, and application prospects in chemical hydrogen storage. *Physical Chemistry Chemical Physics* **2012,** *14*, 1768-1777.

(13) Dovgaliuk, I.; Le Duff, C. S.; Robeyns, K.; Devillers, M.; Filinchuk, Y. Mild dehydrogenation of ammonia borane complexed with aluminum borohydride. *Chemistry of Materials* **2015,** *27*, 768-777.

www.manaraa.com

(14) Patwari, G. N.; Ebata, T.; Mikami, N. Dehydrogenation reaction from a dihydrogen bonded precursor complex in the gas phase. *Journal of Physical Chemistry A* **2001,** *105*, 10753-10758.

(15) Morrison, C. A.; Siddick, M. M. Dihydrogen bonds in solid BH_3NH_3. *Angewandte Chemie-International Edition* **2004,** *43*, 4780-4782.

(16) Crabtree, R. H.; Siegbahn, P. E. M.; Eisenstein, O.; Rheingold, A. L. A new intermolecular interaction: Unconventional hydrogen bonds with element-hydride bonds as proton acceptor. *Accounts of Chemical Research* **1996,** *29*, 348-354.

(17) Richardson, T. B.; deGala, S.; Crabtree, R. H.; Siegbahn, P. E. M. Unconventional hydrogen bonds: Intermolecular B-H···H-N interactions. *Journal of the American Chemical Society* **1995,** *117*, 12875-12876.

(18) Stephens, F. H.; Pons, V.; Baker, R. T. Ammonia - borane: the hydrogen source par excellence? *Dalton Transactions* **2007**, *25*, 2613-2626.

(19) Marder, T. B. Will we soon be fueling our automobiles with ammonia-borane? *Angewandte Chemie-International Edition* **2007,** *46*, 8116-8118.

(20) Peng, B.; Chen, J. Ammonia borane as an efficient and lightweight hydrogen storage medium. *Energy & Environmental Science* **2008,** *1*, 479-483.

(21) Heldebrant, D. J.; Karkamkar, A.; Linehan, J. C.; Autrey, T. Synthesis of ammonia borane for hydrogen storage applications. *Energy & Environmental Science* **2008,** *1*, 156-160.

(22) Sanyal, U.; Demirci, U. B.; Jagirdar, B. R.; Miele, P. Hydrolysis of ammonia borane as a hydrogen source: fundamental issues and potential solutions towards implementation. *Chemsuschem* **2011,** *4*, 1731-1739.

(23) Moury, R.; Demirci, U. B. Hydrazine borane and hydrazinidoboranes as chemical hydrogen storage materials. *Energies* **2015,** *8*, 3118-3141.

www.manaraa.com

(24) Goubeau, J.; Ricker, E. Borinhydrazin und seine pyrolyseprodukte. *Zeitschrift Fur Anorganische Und Allgemeine Chemie* **1961,** *310*, 123-142.

(25) Gunderloy, F.; Spielvogel, B.; Parry, R. W. Hydrazine ‐ mono ‐ and ‐ bisborane. *Inorganic Syntheses*, **1967**, *9*, 13-16.

(26) Gunderloy, J. F. C., Process for preparing hydrazine monoborane. Google Patents: 1968.

(27) Nguyen, V. S.; Swinnen, S.; Matus, M. H.; Minh, T. N.; Dixon, D. A. The effect of the NH_2 substituent on NH_3: hydrazine as an alternative for ammonia in hydrogen release in the presence of boranes and alanes. *Physical Chemistry Chemical Physics* **2009,** *11*, 6339-6344.

(28) Wu, H.; Zhou, W.; Pinkerton, F. E.; Udovic, T. J.; Yildirim, T.; Rush, J. J. Metal hydrazinoborane $LiN_2H_3BH_3$ and $LiN_2H_3BH_3$ center dot $2N_2H_4BH_3$: crystal structures and high-extent dehydrogenation. *Energy & Environmental Science* **2012,** *5*, 7531-7535.

(29) Moury, R.; Demirci, U. B.; Ichikawa, T.; Filinchuk, Y.; Chiriac, R.; van der Lee, A.; Miele, P. Sodium hydrazinidoborane: A chemical hydrogen-storage material. *Chemsuschem* **2013,** *6*, 667-673.

(30) Schettino, V.; Bini, R. Constraining molecules at the closest approach: chemistry at high pressure. *Chemical Society Reviews* **2007,** *36*, 869-880.

(31) Hemley, R. J. Effects of high pressure on molecules. *Annual Review of Physical Chemistry* **2000,** *51*, 763.

(32) Grochala, W.; Hoffmann, R.; Feng, J.; Ashcroft, N. W. The chemical imagination at work in very tight places. *Angewandte Chemie-International Edition* **2007,** *46*, 3620-3642.

(33) Zhang, L. J.; Wang, Y. C.; Lv, J.; Ma, Y. M. Materials discovery at high pressures. *Nature Reviews Materials* **2017,** *2*, 17005.

www.manaraa.com

(34) Liu, A.; Song, Y. In situ high-pressure and low-temperature study of ammonia borane by Raman spectroscopy. *Journal of Physical Chemistry C* **2012,** *116*, 2123-2131.

(35) Xie, S. T.; Song, Y.; Liu, Z. X. In situ high-pressure study of ammonia borane by Raman and IR spectroscopy. *Canadian Journal of Chemistry-Revue Canadienne De Chimie* **2009,** *87*, 1235-1247.

(36) Lin, Y.; Ma, H. W.; Matthews, C. W.; Kolb, B.; Sinogeikin, S.; Thonhauser, T.; Mao, W. L. Experimental and theoretical studies on a high pressure monoclinic phase of ammonia borane. *Journal of Physical Chemistry C* **2012,** *116*, 2172-2178.

(37) Kupenko, I.; Dubrovinsky, L.; Dmitriev, V.; Dubrovinskaia, N. In situ Raman spectroscopic study of the pressure induced structural changes in ammonia borane. *Journal of Chemical Physics* **2012,** *137*, 074506.

(38) Custelcean, R.; Dreger, Z. A. Dihydrogen bonding under high pressure: A Raman study of BH_3NH_3 molecular crystal. *Journal of Physical Chemistry B* **2003,** *107*, 9231-9235.

(39) Trudel, S.; Gilson, D. F. R. High-pressure Raman spectroscopic study of the ammonia-borane complex. Evidence for the dihydrogen bond. *Inorganic Chemistry* **2003,** *42*, 2814-2816.

(40) Yot, P. G.; Yadav, V.; Amara, S. O.; Itie, J. P.; Demirci, U. B.; Maurin, G. Unraveling the mechanical behaviour of hydrazine borane ($NH_2NH_2BH_3$). *Physical Chemistry Chemical Physics* **2018,** *20*, 2845-2850.

(41) Mebs, S.; Grabowsky, S.; Forster, D.; Kickbusch, R.; Hartl, M.; Daemen, L. L.; Morgenroth, W.; Luger, P.; Paulus, B.; Lentz, D. Charge transfer via the dative N-B bond and dihydrogen contacts. Experimental and theoretical electron density studies of small lewis acid-base adducts. *Journal of Physical Chemistry A* **2010,** *114*, 10185-10196.

www.manaraa.com

(42) Klooster, W. T.; Koetzle, T. F.; Siegbahn, P. E. M.; Richardson, T. B.; Crabtree, R. H. Study of the N-H···H-B dihydrogen bond including the crystal structure of BH_3NH_3 by neutron diffraction. *Journal of the American Chemical Society* **1999,** *121*, 6337-6343.

(43) Lee, K. M.; Chang, H. C.; Jiang, J. C.; Chen, J. C. C.; Kao, H. E.; Lin, S. H.; Lin, I. J. B. C-H---O hydrogen bonds in beta-sheetlike networks: Combined X-ray crystallography and high-pressure infrared study. *Journal of the American Chemical Society* **2003,** *125*, 12358-12364.

(44) Yot, P. G.; Miele, P.; Demirci, U. B. In situ Synchrotron X-ray thermodiffraction of boranes. *Crystals* **2016,** *6*, 16.

(45) Birch, F. Finite elastic strain of cubic crystals. *Physical review* **1947,** *71*, 809.

(46) Angel, R. J.; Alvaro, M.; Gonzalez-Platas, J. EosFit7c and a Fortran module (library) for equation of state calculations. *Zeitschrift für Kristallographie-Crystalline Materials* **2014,** *229*, 405-419.

(47) Qi, G.; Wang, K.; Yang, K.; Zou, B. Pressure-induced phase transition of hydrogen storage material hydrazine bisborane: evolution of dihydrogen bonds. *The Journal of Physical Chemistry C* **2016,** *120*, 21293-21298.

(48) Filinchuk, Y.; Nevidomskyy, A. H.; Chernyshov, D.; Dmitriev, V. High-pressure phase and transition phenomena in ammonia borane NH_3BH_3 from X-ray diffraction, Landau theory, and ab initio calculations. *Physical Review B* **2009,** *79*, 214111.

www.manaraa.com

Chapter 5

5 High-pressure structural study of ethane 1,2-diamineborane using in-situ vibrational spectroscopy and synchrotron X-ray diffraction and insight into dihydrogen bonding

5.1 Introduction

Hydrogen is one of the most promising energy sources regarding clean, renewable energy carrier.[1-2] Moreover, the product of the combustion of hydrogen is only water, which makes it the most environmentally-friendly energy in the world. However, hydrogen has a poor energy content per volume, especially under the ambient condition. Therefore, the storage and transportations of hydrogen still hinder the application of hydrogen as a fuel.[2-3]

Recently, the development of hydrogen storage materials, such as simple hydrides, complex hydrides and chemical hydrides, has drawn much attention due to their high hydrogen content. Such hydrogen storage materials have high gravimetric and volumetric hydrogen density and high stability, which makes them promising for the transportation and utilization of hydrogen.[4-6] Among all these hydrogen storage materials, ammonia borane NH_3BH_3 (AB) has gained much attention due to its high hydrogen content, low cost and easy synthesis.[7-8] Moreover, substituting one or more hydrogen atoms in NH_3BH_3 by organic groups or metal ions leads to the formation of various new compounds, such as methylamine-borane ($Me_nH_{3-n}N{\cdot}BH_3$ (n = 1-3)), sodium amidoborane ($NaNH_2BH_3$) and bimetallic amidoborane ($Na[Li(NH_2BH_3)_2]$). These derivatives of NH_3BH_3 show even better dehydrogenation performance than AB.[9-20] Ethane 1,2-Diamineborane (EDAB, $BH_3NH_2CH_2CH_2NH_2BH_3$) is one of the derivatives of NH_3BH_3, which was first synthesized in the 1960s and used as a hydrogen storage material.[21] EDAB is an air-stable compound with a high hydrogen content of 16.0%. It releases ca. 10 wt% of hydrogen below 470K in two steps with less exothermic releasing

www.manaraa.com

of enthalpy than NH_3BH_3,[21-25] which makes EDAB a desirable hydrogen storage material.

High pressure has been proved to be an effective way to alter the structures and the properties of the materials.[26] A number of experimental high-pressure studies on AB and its derivatives by Raman, IR spectroscopy and synchrotron XRD have indicated the structure changes upon compression, as well as the evolution of the dihydrogen bonding network.[7-8, 27-41] Moreover, theoretical calculations on such materials were also implemented for the study of the structural stability and electronic properties of these materials, which could be used to explain their dehydrogenation process.[9, 14, 28, 33, 42-50] As a promising hydrogen storage material, EDAB awaits the exploration under high pressure for the new structures.

Here we report a high-pressure investigation of hydrogen storage material EDAB by in situ Fourier transform infrared (FTIR) spectroscopy, Raman spectroscopy and synchrotron X-ray diffraction. Our results reveal pressure-induced phase transitions and the evolution of hydrogen bonding. The effect of pressure on the behavior of EDAB expands the fundamental understanding of this system and sheds light onto its potential application as a hydrogen-storage material.

5.2 Materials and Characterizations

5.2.1 Materials and preparation

Ethane 1,2-Diamineborane was purchased from Sigma-Aldrich with claimed purity of 96%. The sample was kept in a N_2-filled MBraun LAB Master 130 glovebox with H_2O content of <1 ppm and O_2 content of < 3 ppm. It was used in the high-pressure studies without further purification. Two symmetrical diamond anvil cells with 400 μm culet size were used for the high-pressure studies. A stainless steel gasket was preindented to 50 μm in thickness, followed by a hole with diameter of 150 μm drilled in the center of it as the sample chamber. The sample was loaded into the DAC with a ruby ball in the glovebox.

www.manaraa.com

5.2.2 Powder X-ray diffraction

The crystallinity and purity of the sample were tested by a Rigaku X-ray diffractometer using Co Kα radiation (λ = 1.78890 Å), the scan range was from 2θ = 10 to 80° with a step size of 0.02. The sample was covered by a piece of Kapton film during the measurement to avoid the moisture. The diffraction pattern was refined by the Rietveld method using GSAS.

5.2.3 In-situ FTIR spectroscopy

The in-situ high-pressure IR absorption experiments were carried out by a customized IR micro-spectroscopy system in absorption mode in the infrared range between 400 and 5500 cm^{-1}. A resolution of 4 cm^{-1} and 512 scans were applied for each spectrum collection to achieve an excellent signal-to-noise ratio. Typically, KBr was also loaded into the chamber to dilute the sample.

5.2.4 In-situ Raman spectroscopy

The in-situ high-pressure Raman experiments were carried out by a customized Raman spectrometer and a green laser with the wavelength of 532 nm was used as an excitation source. A grating with 1200 lines/mm was used for all measurements. The signal was recorded using an ultrasensitive, liquid nitrogen cooled, back-illuminated, charge-coupled device (CCD) detector from Acton.

5.2.5 In-situ synchrotron X-ray diffraction

In situ angle dispersive high-pressure X-ray diffraction measurements were performed at beamline of Sector-20ID in Advanced Photon Source (APS), Argonne National Laboratory, with the wavelength of 0.4592 Å. To achieve hydrostatic conditions, neon was loaded together with the sample as the pressure transmitting medium using the gas loading system at GSECARS of APS. The 2D pattern could be converted to 1D pattern using the Dioptas program for the further analysis.[51] The diffraction patterns were refined by Le Bail method.

www.manaraa.com

5.3 Results and discussions

5.3.1 XRD pattern under ambient conditions

The crystal structure of EDAB under ambient pressure was examined by powder X-ray diffraction, as shown in Figure 5.1a, with all the peaks indexed. At ambient condition, EDAB adopts an orthorhombic structure with the space group *Pbca*. By using Rietveld refinement (Figure 5.1b), the cell parameters were refined to be a = 10.761 Å, b = 8.172 Å, c = 8.131 Å, V = 715.03 Å^3, consistent with the reference.[25] The unit cell of EDAB is shown in Figure 5.2, in the solid state, there are 4 EDAB molecules in one unit cell occupying C_i sites.

5.3.2 IR and Raman spectra under ambient conditions

We also collected IR and Raman spectra of EDAB under ambient pressure at room temperature, as shown in Figure 5.3. The assignments of the observed IR and Raman vibrational modes are shown in Table 5.1, in comparison with ammonia borane.[25, 36] 4 lattice modes were observed at 147, 198, 267, 380 cm^{-1} in Raman spectrum. Noticeably, compared to AB,[36] the frequencies of the N−H stretching vibration modes decrease, indicating a weakening of the N−H bond from AB to EDAB. By contrast, we also observed a slight blueshift of the B−H stretching modes in EDAB as compared to AB, which reveals that EDAB present a slightly stronger B−H bond than AB. Moreover, the B−N stretching mode appears at lower wavenumber values in EDAB, suggesting a weakening of B−N bonds. Therefore, the existence of C−N and C−C bonds in the EDAB molecule alters the activity of N-H bond, compared to AB.

www.manaraa.com

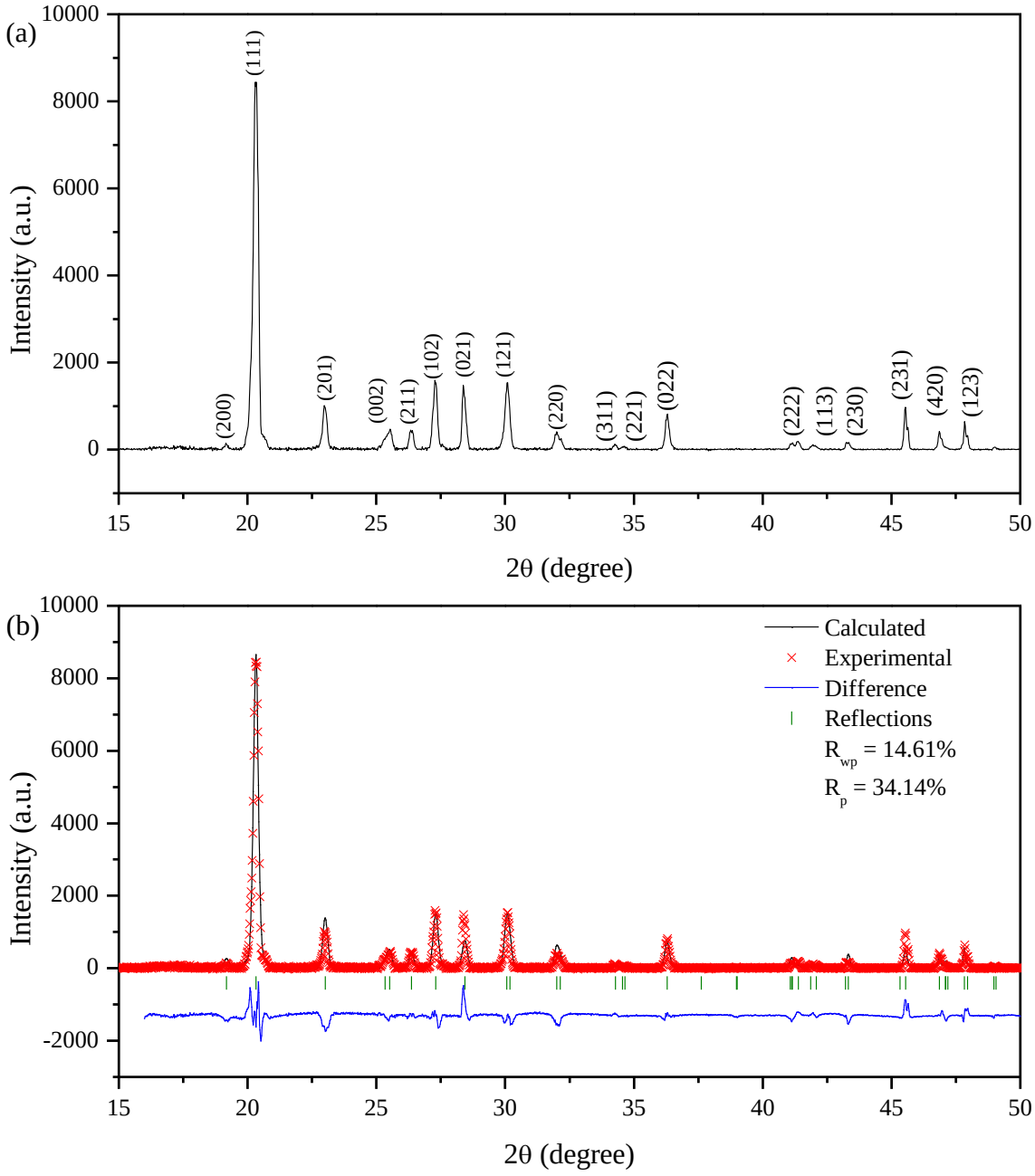

Figure 5.1 XRD pattern of EDAB under ambient conditions (a) and calculated XRD patterns in comparison with experimental results using Rietveld refinement (b)

www.manaraa.com

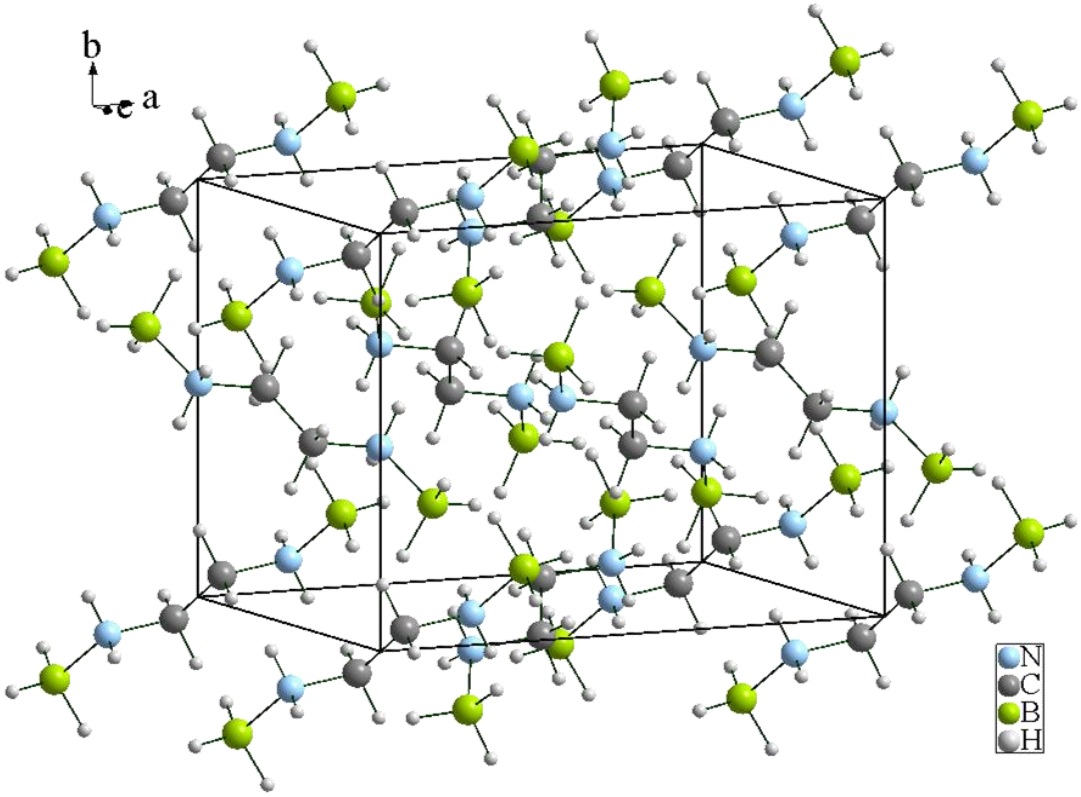

Figure 5.2 Structure of EDAB unit cell

www.manaraa.com

Table 5.1 Assignments and vibrational frequencies (cm^{-1}) of EDAB and AB at ambient pressure[25, 36]

	EDAB		AB	
	IR (cm^{-1})	Raman (cm^{-1})	IR (cm^{-1})	Raman (cm^{-1})
Lattice modes		147		208
		198		345
		267		
		380		
B-N stretch	707	697	799	800
C-N stretch	1046	1053		
C-C stretch		1084		
B-H bend	1166	1167	1186	1189
	1173	1179		
	1191	1197		
C-H bend	1262	1288		
C-H twist		1306		
N-H bend	1361		1343	1357
	1368	1355		
C-H deformation	1466	1443		
		1448		
N-H deformation	1578	1588		
	1585			
	2294	2327		
	2342	2347	2340	2279
	2396	2385	2415	2318
C-H sym. stretch	2895	2886		
overtone	2939	2918		
C-H asym. stretch	2965	2955		
	2992	2970		
N-H sym. str.	3143	3142	3337	3250
N-H asym. str.	3224	3221	3386	3316
	3265	3252		

www.manaraa.com

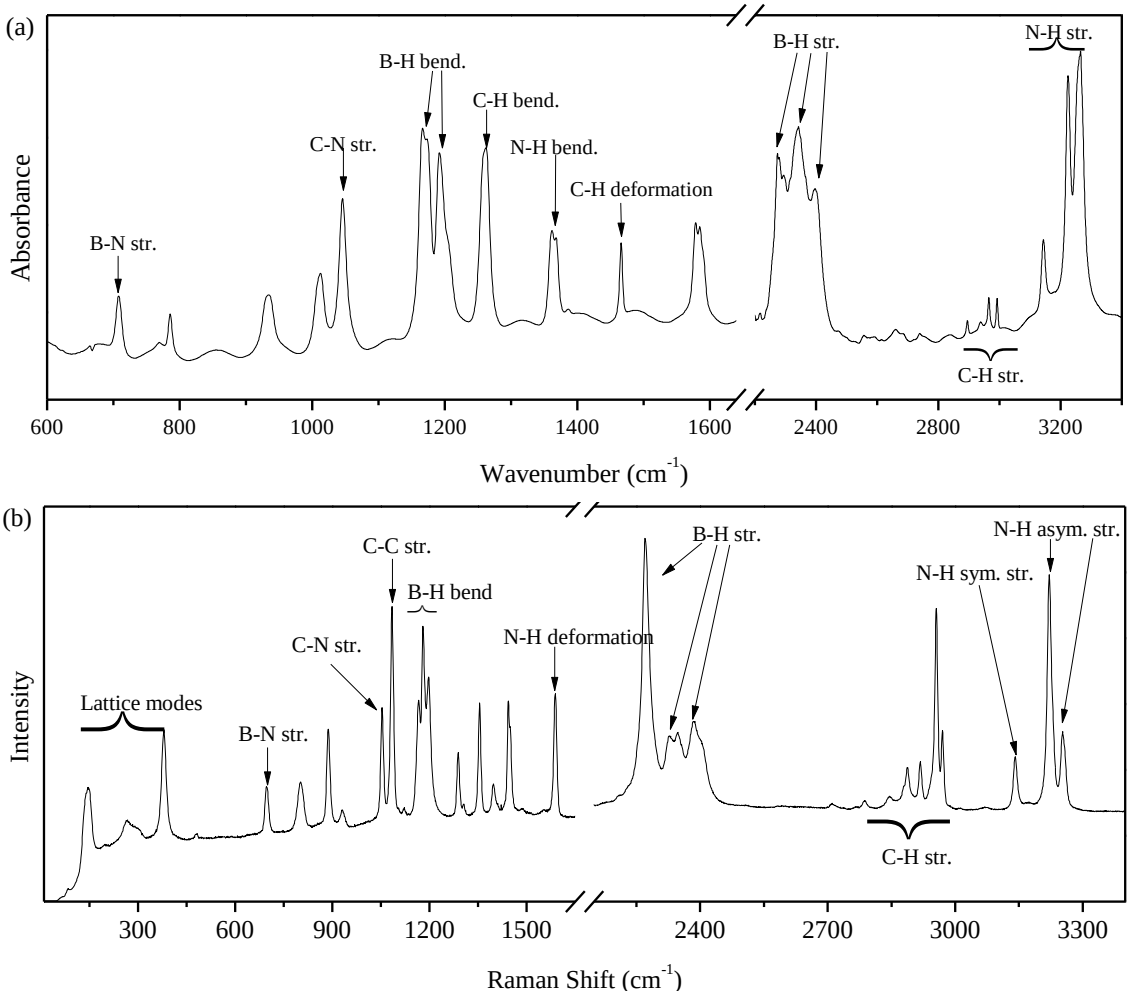

Figure 5.3 IR (a) and Raman (b) spectra of EDAB collected at room temperature under ambient pressure, most of the vibrational modes have been assigned and labeled.

5.3.3 IR spectra under high pressure

In-situ high-pressure IR spectra of EDAB were collected under high pressure to investigate the evolution of various bonds, as shown in Figure 5.4. Upon compression to 0.96 GPa, it is clear to see that abundant major changes were observed in the IR spectrum, indicating the first phase transition. Firstly, in Figure 5.4a, three peaks at around 786, 935 and 1013 cm^{-1} become weaker upon compression and almost vanish at 0.96 GPa. Meanwhile, four new peaks appear at around 759, 801, 926, 991 cm^{-1}.

www.manaraa.com

Additionally, the B-N stretching mode also disappears under such pressure, replaced by a new peak at around 717 cm^{-1}, which could be assigned to ^{10}B-N stretching mode.[25] Then in the bending region (Figure 5.4b), abundant changes were observed upon compression. For the B-H bending mode, the peak at 1166 cm^{-1} becomes stronger and shifts to the lower wavenumber. On the contrary, the peaks at 1175 and 1193 cm^{-1} show blueshift at 0.96 GPa. Besides, there is a new peak appearing at 1213 cm^{-1} when the pressure is higher than 1 GPa. For the N-H bending mode, the peak at 1368 cm^{-1} becomes weaker at 0.96 GPa and eventually vanishes upon further compression. Moreover, the C-H deformation mode disappears as well, replaced by a new peak at 1472 cm^{-1} at the same time. Lastly, the two N-H deformation modes merge into one peak and a new peak shows up at 1561 cm^{-1}. Compared to the previous regions, only slight changes were observed in X-H (X = B, C, N) stretching region, as indicated in Figure 5.4c. The N-H symmetric stretching mode almost disappears at 0.96 GPa, with the emergence of a new peak at 3118 cm^{-1}.

Upon further compression to 6 GPa, several distinct changes were observed, demonstrating the second phase transition. As shown in Figure 5.4b and c, at 6.20 GPa, two new peaks appear at 1600 and 1610 cm^{-1}, as well as another new peak at 3155 cm^{-1}. Upon further compression to near 17 GPa, all the peaks become more and more broadened, indicating the low degree of crystallinity. Therefore, two phase transitions were observed at around 1 and 6 GPa during compression.

Moreover, the phase transitions suggested by the changes in IR spectra were also investigated by plotting the vibrational modes as a function of pressure, as shown in Figure 5.5. The pressure coefficients for some characteristic modes were analyzed by linear fitting and listed in Table 5.2.

www.manaraa.com

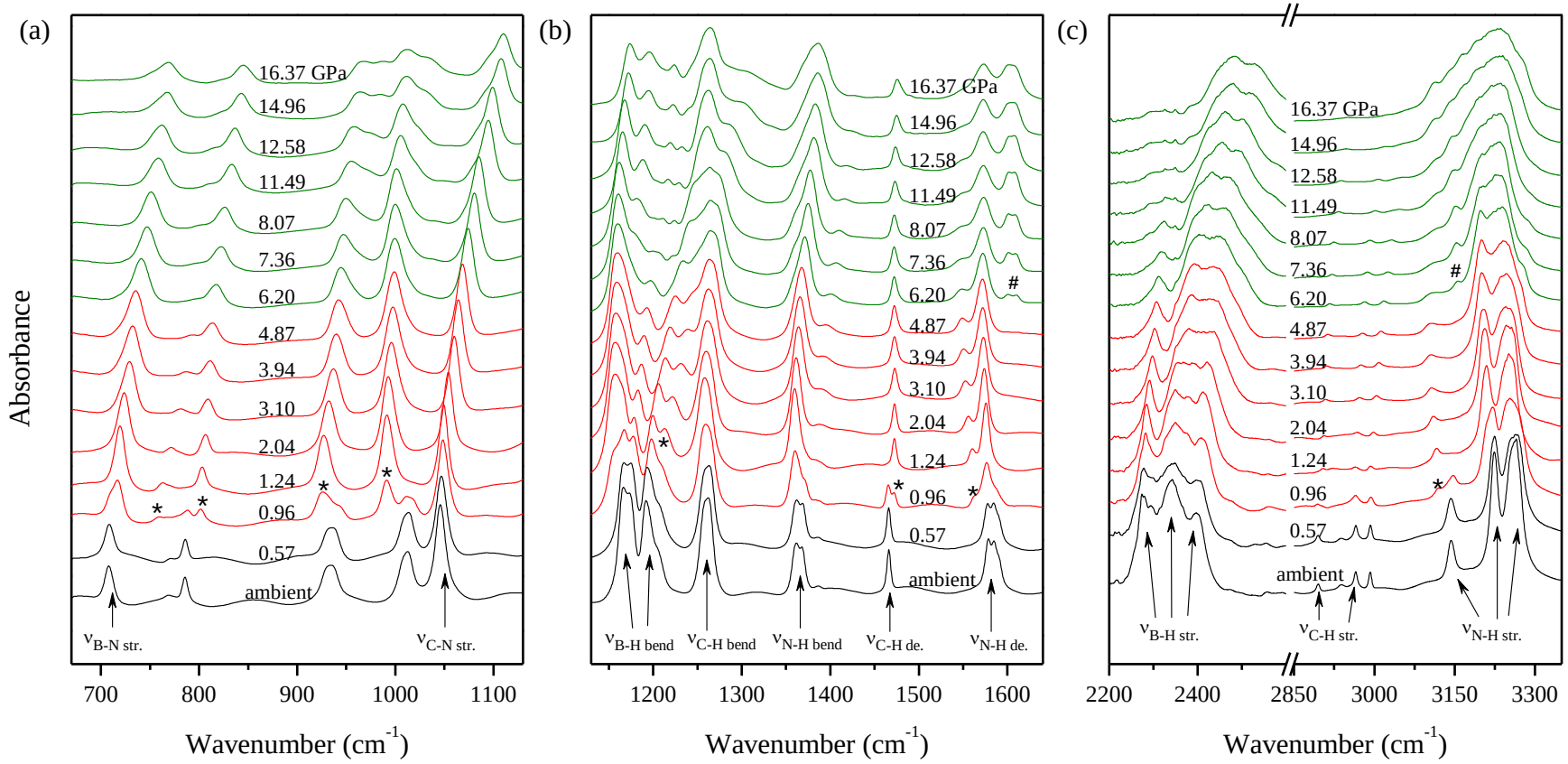

Figure 5.4 IR spectra of EDAB collected at room temperature on compression in the region of 670-3400 cm^{-1}. The pressures in GPa are labeled for each spectrum, and the assignments are labeled for selected IR modes. * and # represent the appearance of new peaks in phase II and phase III.

www.manaraa.com

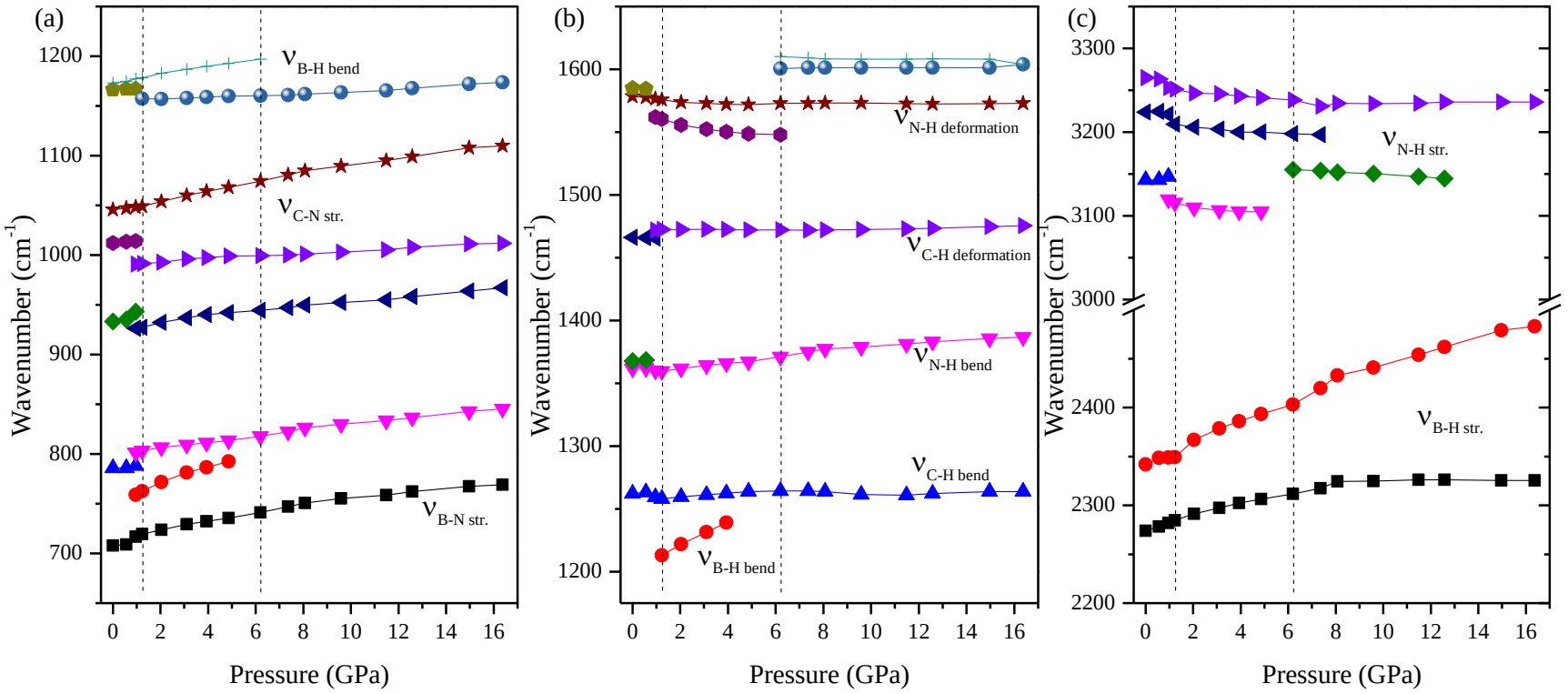

Figure 5.5 Pressure dependence of selected IR modes of HB on compression. Different symbols represent IR modes with different origins.

www.manaraa.com

Table 5.2 Pressure dependence of the selected IR modes of EDAB on compression

Assignment	Frequency (cm^{-1})[a]	dν/dp ($cm^{-1}\cdot GPa^{-1}$)		
		Phase I (< 0.96 GPa)	Phase II (1.0 – 6.0 GPa)	Phase III (>6.0 GPa)
B-N str.	707	8.85	4.70	2.63
B-N str.	759		8.61	
C-N str.	1046	2.80	5.22	3.46
B-H bend	1173	4.42	3.93	
	1191	6.36	6.93	
	1262	-2.62	1.28	-0.07
C-H bend	1361	-1.41	2.02	1.43
N-H bend	1562		-3.44	
	1578	-1.97	-1.18	-0.02
N-H deformation	1600			0.19
	1610			-0.39
B-H str.	2273	8.37	6.24	1.03
	2342	7.66	11.89	7.50
N-H asym. str.	3224	-2.85	-4.33	
	3265	-11.98	-2.84	-0.33

In general, the disappearance and appearance of different vibrational modes clearly show the phase boundaries. Furthermore, most of the pressure coefficients in phase I display the greatest values, suggesting the highest compressibility of phase I. Significantly, the B-H stretching modes exhibit blueshift in entire pressure region (positive pressure coefficients in Table 5.2). On the contrary, the N-H stretching modes show redshift

www.manaraa.com

during all the phases (negative pressure coefficients in Table 5.2), indicating the existence of the dihydrogen bonding in the structure of EDAB.[29-31, 36] With the increase of the pressure, the distance between EDAB molecules is reduced, leading to the strengthening of the dihydrogen bonding B-H···H-N.

Additionally, the reversibility of EDAB was also examined, as shown in Figure 5.6. The recovered IR spectrum shows similar to the initial one, suggesting that the pressure induced phase transition is mostly reversible.

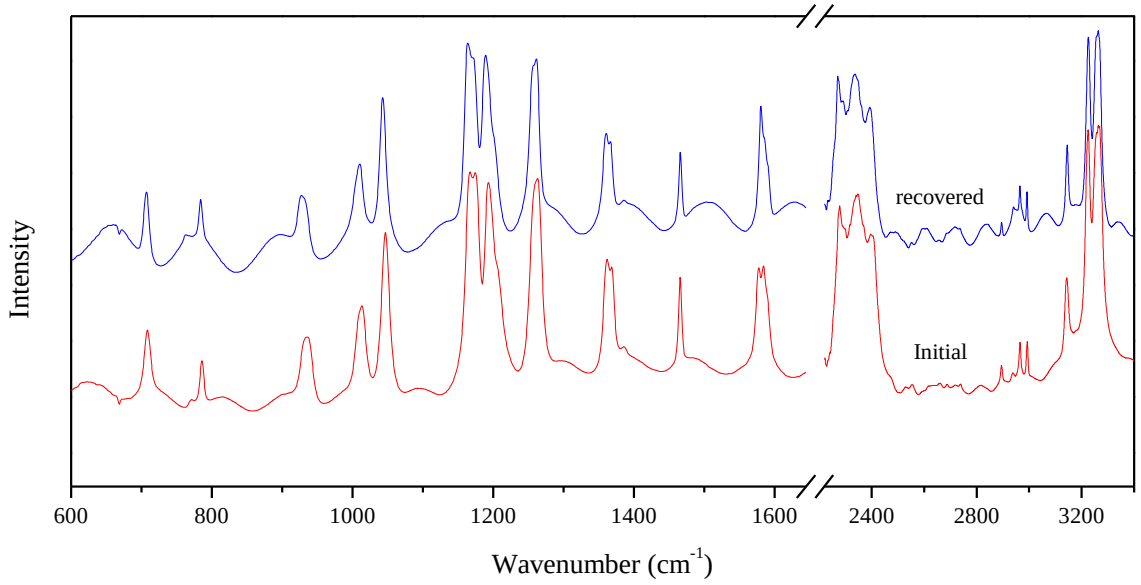

Figure 5.6 Recovered IR spectrum in comparison with the initial one

5.3.4 Raman spectra under high pressure

We also collected in-situ Raman spectra upon compression to near 14 GPa, as shown in Figure 5.7. Abundant changes were observed when the material was compressed to 1.13 GPa, indicating the first phase transition. In Figure 5.7a, three new peaks at 801, 890 and 928 cm^{-1} appear and become stronger with the increasing pressure. Meanwhile, the peaks at around 814 and 900 cm^{-1} vanish. In Figure 5.7b, the C-H deformation mode splits into two peaks upon compression below 1 GPa and they both almost disappear at 1.13 GPa, as well as the N-H deformation mode. Additionally, two new peaks at these two regions appear. Other noticeable changes were observed in B-H stretching mode, as shown in

www.manaraa.com

Figure 5.7c. Upon compression to 1.13 GPa, two peaks at around 2325 and 2346 cm^{-1} merge into one peak with much stronger intensity. Lastly, for C-H and N-H stretching modes, several significant changes were also observed in Figure 5.7d. One of the C-H asymmetric stretching modes at 2955 cm^{-1} splits into two peaks, and the other one at 2970 cm^{-1} disappears completely from the phase transition. Also, the N-H symmetric stretching mode at 3142 cm^{-1} is weakened greatly, with the appearance of a new peak at 3116 cm^{-1} upon compression to phase II. Moreover, one peak of N-H asymmetric stretching mode at 3221 cm^{-1} is weakened significantly and disappears eventually with the increasing pressure above 1 GPa, replaced by a new peak in this region with increasing intensity upon compression.

With the further compression to 6 GPa, some minor changes were noticed. In Figure 5.7a, the peak at around 407 cm^{-1} splits into two peaks, and two new peaks appear at around 795 and 815 cm^{-1}, suggesting the second phase transition. During the further compression, all the peaks became weaker and more broadened, which couldn't be recognized under the highest pressure in Raman measurement (13.79 GPa), demonstrating the low degree of the crystallinity.

Furthermore, the pressure-induced phase transitions were also examined by plotting the Raman shift as a function of pressure for some characteristic vibrational modes, as demonstrated in Figure 5.8, which is clear to recognize the phase boundaries and the different shifts of each mode. Additionally, the pressure coefficients for some characteristic modes were analyzed by linear fitting and listed in Table 5.3. Generally, almost all the modes exhibit blueshift during the whole compression region other than the N-H stretching modes, which show obvious redshift, indicating the strengthening of the dihydrogen bonding, consistent with the observation in IR spectra. Furthermore, the compressibility of EDAB with the increasing pressure becomes weaker by the evidence of reducing pressure coefficients in different phases.

www.manaraa.com

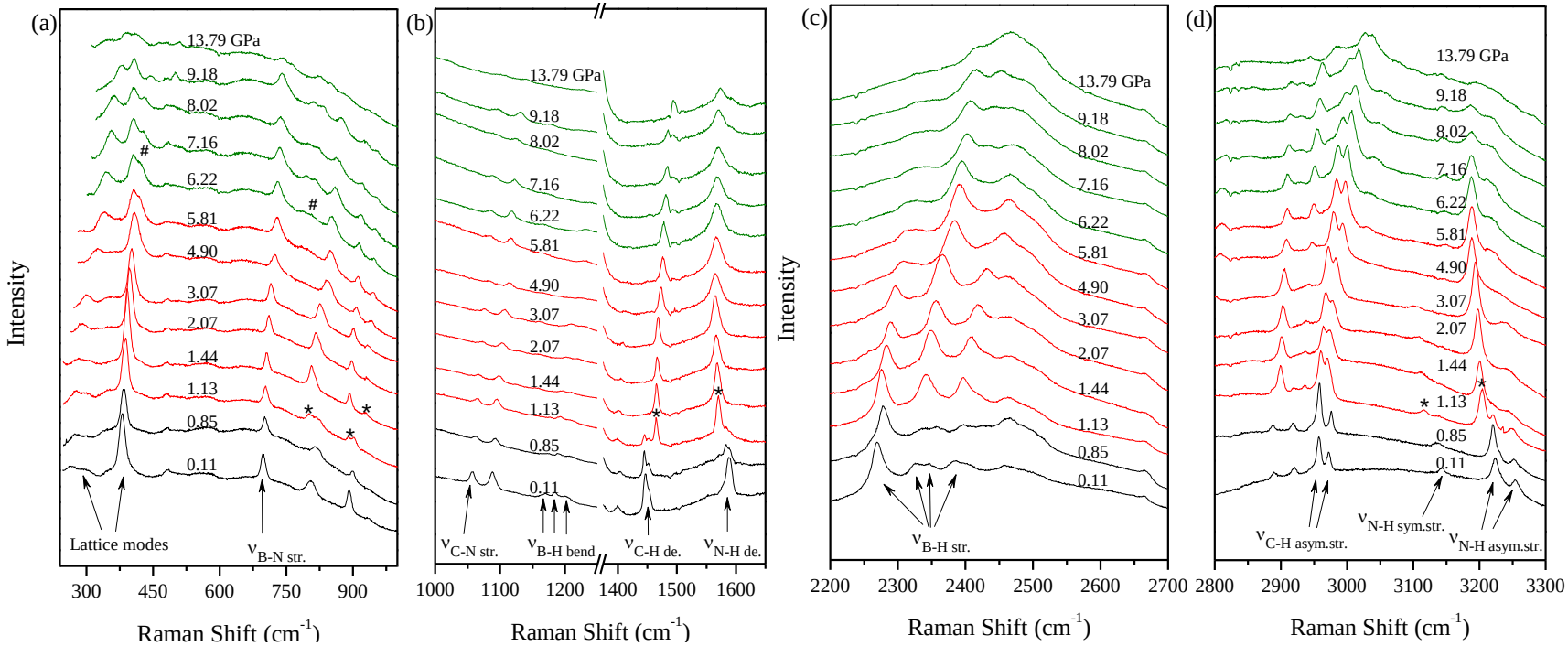

Figure 5.7 Raman spectra of EDAB collected at room temperature on compression in the region of 250-3300 cm^{-1}. The pressures in GPa are labeled for each spectrum, and the assignments are labeled for selected Raman modes. * and # represent the appearance of new peaks in phase II and phase III.

www.manaraa.com

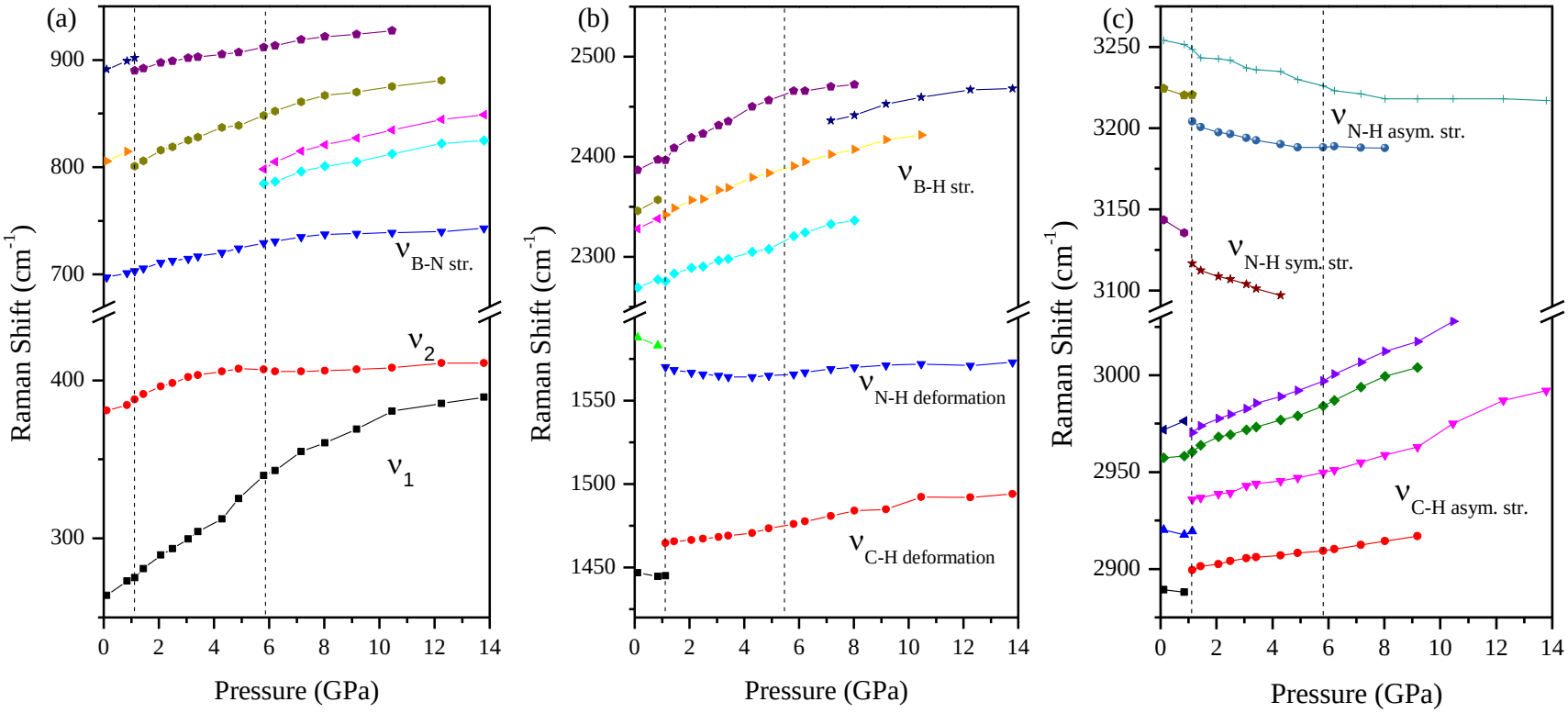

Figure 5.8 Pressure dependence of selected Raman modes of HB on compression. Different symbols represent Raman modes with different origins.

www.manaraa.com

Table 5.3 Pressure dependence of the selected Raman modes of EDAB on compression

Assignment	Frequency (cm^{-1})[a]	dν/dp ($cm^{-1}\cdot GPa^{-1}$)		
		Phase I (< 1.0 GPa)	Phase II (1.0 – 6.0 GPa)	Phase III (>6.0 GPa)
Lattice modes	264	12.16	12.13	6.04
	381	4.32	5.07	0.83
B-N str.	697	5.40	5.30	1.01
	802	/	10.16	4.46
	890	/	4.42	2.53
C-H deformation	1464	/	2.11	2.01
N-H deformation	1570	/	-1.38	0.48
B-H str.	2270	11.08	7.99	4.19
	2342	/	10.81	6.13
	2347	14.86	/	/
N-H str.	3116	/	-5.90	/
	3142	-10.81	/	/
	3204	/	-3.98	-0.35
	3221	-5.40	/	/
	3252	-3.51	-4.10	-0.62

Finally, the reversibility of EDAB was also explored by Raman spectra, as shown in Figure 5.9. The recovered spectrum exhibited very similar profile to the initial one, indicating that the pressure-induced structural transformation is reversible with slight modification.

www.manaraa.com

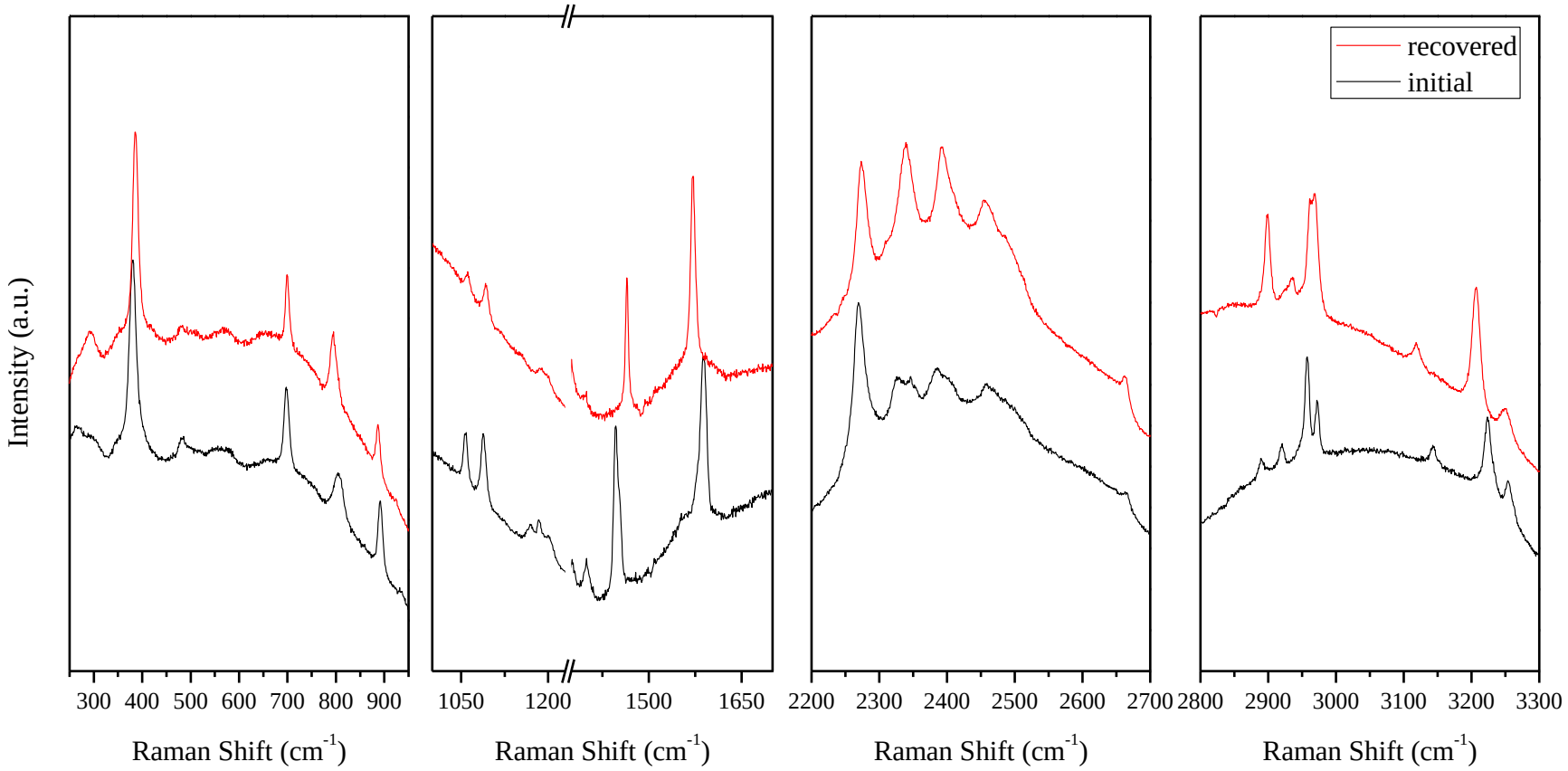

Figure 5.9 Recovered Raman spectrum in comparison with the initial one

www.manaraa.com

5.3.5 Synchrotron XRD patterns under high pressure

The synchrotron XRD patterns of EDAB were collected under compression to 17 GPa, as shown in Figure 5.10. The cell parameters at every high pressure were also refined using Le Bail method and listed in Table 5.4. When the pressure was increased to 1.07 GPa, four new peaks appear at 2θ = 4.73°, 6.43°, 7.98° and 8.54°, indicating the appearance of a new phase (phase II). Meanwhile, all the peaks belonging to phase I still exist, suggesting two phases co-existing under this pressure. With the increasing of the pressure, the intensity of the old peaks decreases greatly, especially the one at 5.20°, which almost disappeared at 1.72 GPa. Moreover, a monoclinic structure was found to be the most probable crystal structure of phase II, and the possible space groups are *P*2, *P*2$_1$, *Pm*, *Pc*, *P*2/*m*, *P*2$_1$/*m*, *P*2/*c*, *P*2$_1$/*c*. The calculated XRD patter using *P*2/*c* structure in comparison with experimental result of EDAB at 1.72 is shown in Figure 5.11a. The cell parameters and volumes as a function of pressure were shown in Figure 5.12. As shown in Figure 5.12 and Table 5.4, the axis a decreases significantly, while the axis b increases greatly, due to a major phase transformation. Additionally, the cell volume also exhibits a drop with the pressure increasing, showing the further contraction of the structure under high pressure. Upon further compression to 6.91 GPa, the profile of XRD patterns change slightly.

Furthermore, upon compression to 7.88 GPa, the XRD pattern shows the other structural transformation in EDAB. As shown in Figure 5.10, two new peaks were observed at 4.98° and 7.20°. Meanwhile, the peaks at 8.51° and 8.76° at 6.91 GPa merge into one peak. With the increasing pressure, no prominent changes were observed other than the disappearing of the peak around 6.5°. Moreover, it is found that the structure of EDAB in this region is an orthorhombic structure, and the possible space groups of phase III are *P*222, *P*222$_1$, *P*2$_1$2$_1$2, *P*2$_1$2$_1$2$_1$, *I*2$_1$2$_1$2$_1$, *Pmm*2, *Aem*2, *Aea*2, *Pmmm*, *Cmme*, *Ccce*. The calculated XRD patter using *Pmmm* structure in comparison with experimental result of EDAB at 7.88 is shown in Figure 5.11b. Additionally, Figure 5.12 shows the major modification of the cell parameters, leading to an increasing a and decreasing b and c, resulting in a contraction of the cell volume.

www.manaraa.com

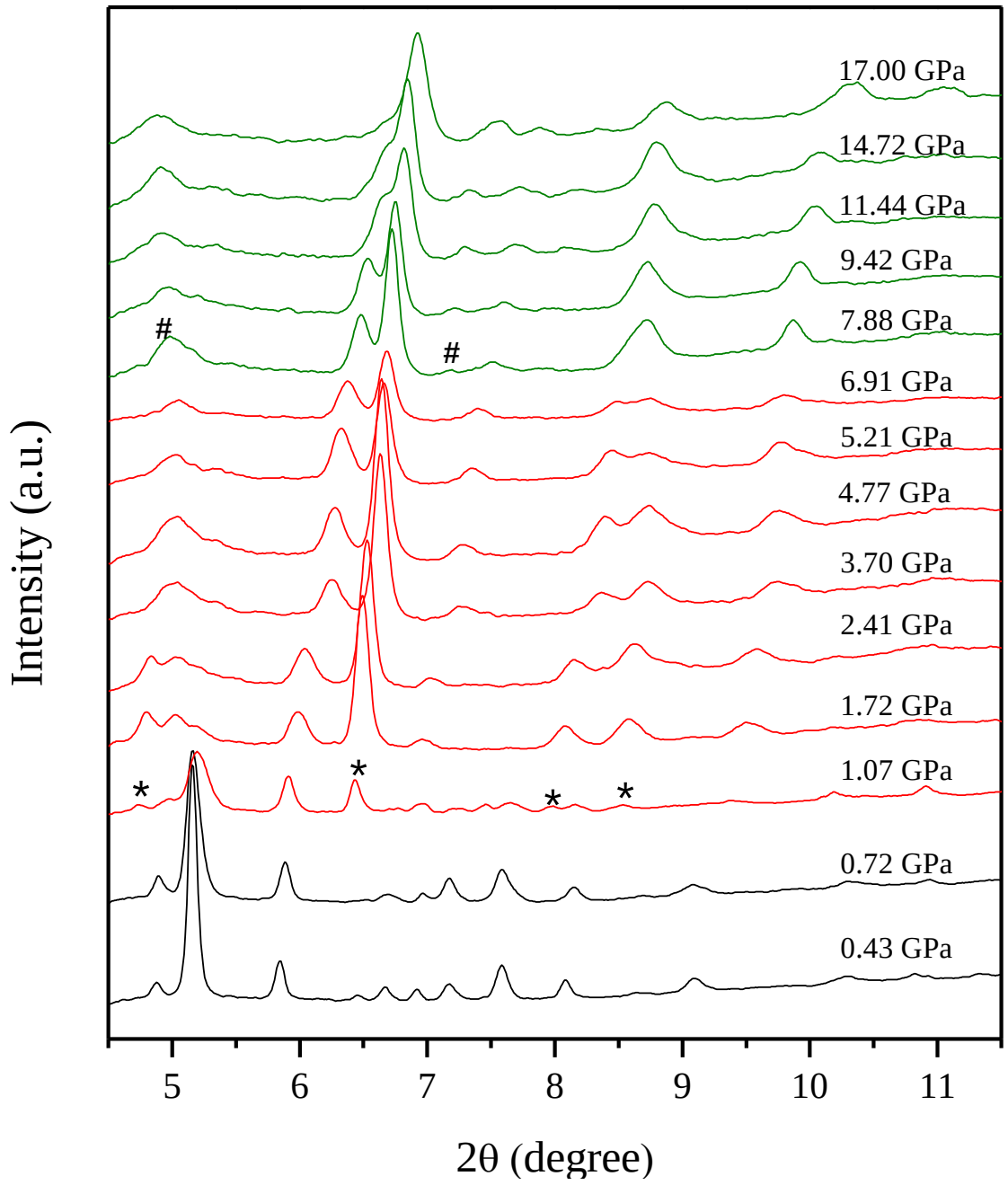

Figure 5.10 Synchrotron XRD patters of EDAB upon compression in room temperature. * and # represent the appearance of new peaks in phase II and phase III.

www.manaraa.com

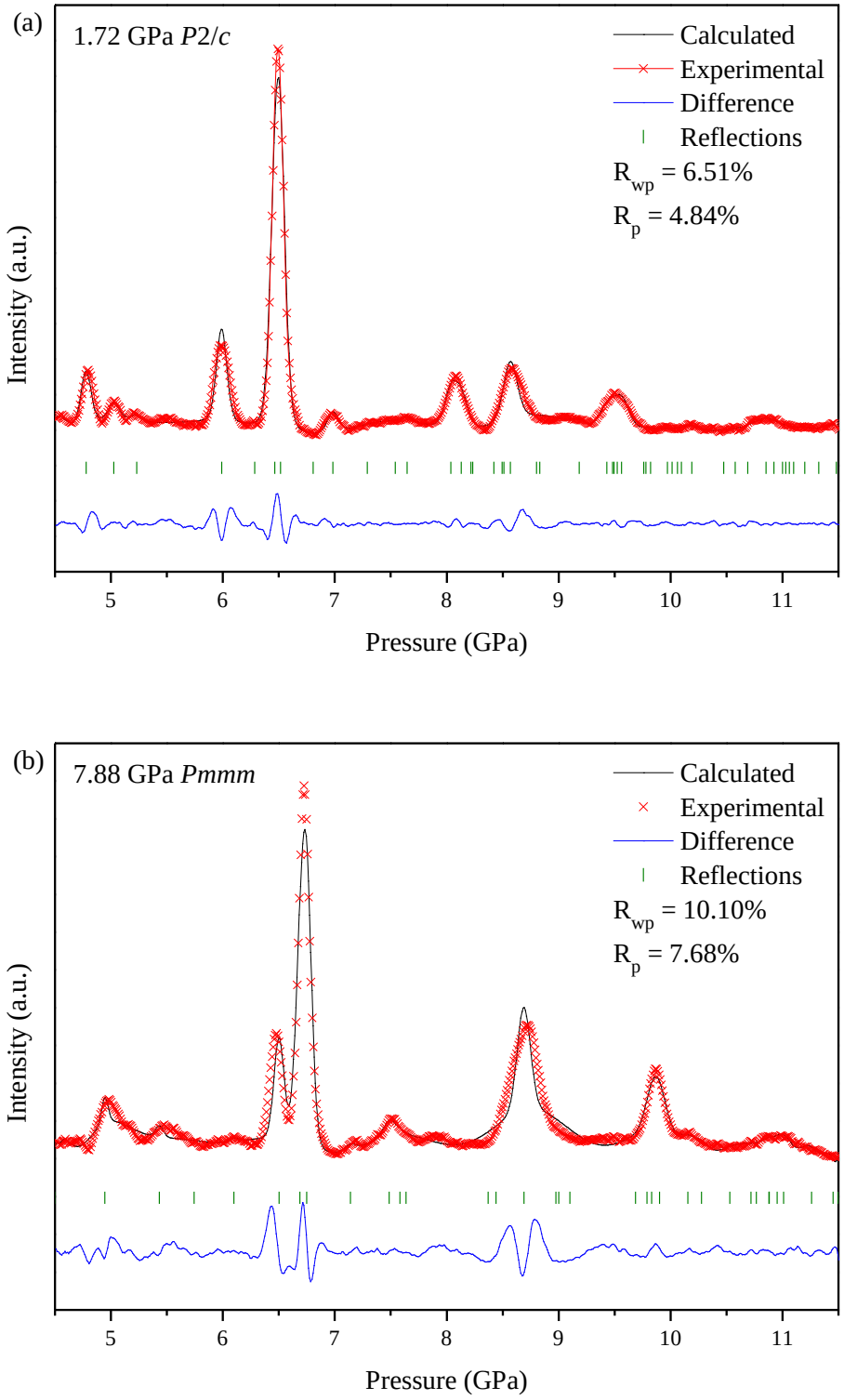

Figure 5.11 Calculated XRD patters in comparison with experimental results of EDAB at 1.72 (a) and 7.88 (b) GPa using Le Bail refinement

www.manaraa.com

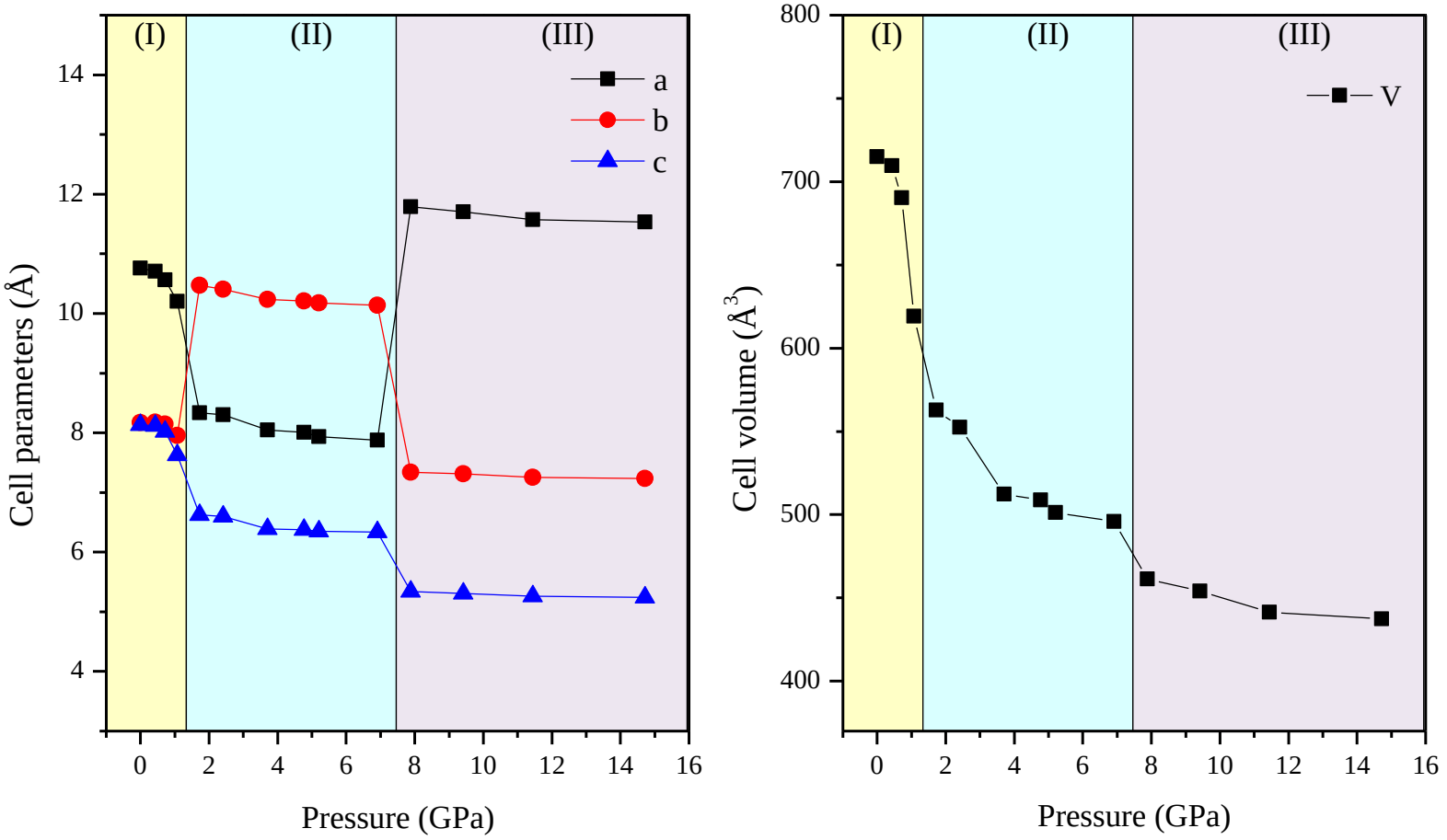

Figure 5.12 Cell parameters and volumes as a function of pressure of EDAB during compression

www.manaraa.com

Table 5.4 Proposed new crystal structures of EDAB on compression and calculated cell parameters of EDAB under different pressures

	Pressure (GPa)	a (Å)	b (Å)	c (Å)	V (Å^3)	β
Orthorhombic	ambient	10.7610	8.1720	8.1310	715.03	
	0.43	10.7100	8.1800	8.1160	711.02	
	0.72	10.5650	8.1440	8.0230	690.36	
Monoclinic	1.07	10.2040	7.9540	7.6290	619.19	
	1.72	8.3377	10.4700	6.6250	562.85	103.29
	2.41	8.3010	10.4060	6.5967	552.47	104.18
	3.70	8.0432	10.2340	6.3869	512.34	102.96
	4.77	8.0100	10.2100	6.3740	508.68	102.62
	5.21	7.9358	10.1784	6.3461	501.26	102.07
	6.91	7.8756	10.1380	6.3333	495.78	101.35
Orthorhombic	7.88	11.7862	7.3355	5.3371	461.43	
	9.42	11.7023	7.3154	5.3047	454.12	
	11.44	11.5723	7.2539	5.2584	441.41	
	14.72	11.5342	7.2345	5.2425	437.46	

The errors of cell parameters in phase I for a, b, c and V are estimated to be ±0.007, ±0.004, ±0.004 and ±0.5, respectively. The errors of cell parameters in phase II for a, b, c and V are estimated to be ±0.006, ±0.007, ±0.004 and ±0.4, respectively. The errors of cell parameters in phase III for a, b, c and V are estimated to be ±0.009, ±0.003, ±0.002 and ±0.4, respectively.

www.manaraa.com

5.3.6 Discussion

The vibrational spectroscopy and synchrotron XRD analysis demonstrated that two phase transitions were observed during compression to 17 GPa. This result is different from the previous low-temperature study of EDAB, which reveals that no phase transition was observed in the low-temperature region of 300 – 16 K, probably due to the different dynamics of the molecule under such conditions. The material undergoes the first phase transition at around 1.0 GPa, which is similar to ammonia borane. AB presents a tetragonal-to-orthorhombic phase transition at 1.6 GPa, which is driven by the displacement of the NH_3 and BH_3 groups in the opposite directions.[52] EDAB consists of chains much longer than AB molecule, the lower phase boundary of EDAB indicates that EDAB is more sensitive to the pressure, which induces the motion of the molecules, leading to the first phase transition. The second phase transition of AB occurs at 12 GPa, which is triggered by the reorganization of the dihydrogen bonding frameworks and the change in the rotational order in the NH_3 and BH_3 groups.[28] Our vibrational spectroscopy study has shown the presence of the dihydrogen bonding in EDAB, which is strengthened during the compression. The rearrangement of the dihydrogen bonding under high pressure may attribute the second phase transition at 7.0 GPa in EDAB.

5.4 Conclusions

In conclusion, our study revealed the structure stability and bonding evolution of EDAB under high pressure by IR spectroscopy, Raman spectroscopy and synchrotron XRD. Two phase transitions were observed at around 1.0 and 7.0 GPa. The origins of these two phase transitions are probably due to the motion of the molecules and the rearrangement of the dihydrogen bonding, respectively. The effect of dihydrogen bonding was also observed during the study by the evolution of B-H and N-H bonds, which may play an important role in the decompostion of EDAB.

www.manaraa.com

5.5 References

(1) Momirlan, M.; Veziroglu, T. N. The properties of hydrogen as fuel tomorrow in sustainable energy system for a cleaner planet. *International Journal of Hydrogen Energy* **2005,** *30*, 795-802.

(2) Hamilton, C. W.; Baker, R. T.; Staubitz, A.; Manners, I. B-N compounds for chemical hydrogen storage. *Chemical Society Reviews* **2009,** *38*, 279-293.

(3) Mazloomi, K.; Gomes, C. Hydrogen as an energy carrier: Prospects and challenges. *Renewable & Sustainable Energy Reviews* **2012,** *16*, 3024-3033.

(4) Song, Y. New perspectives on potential hydrogen storage materials using high pressure. *Physical Chemistry Chemical Physics* **2013,** *15*, 14524-14547.

(5) Orimo, S. I.; Nakamori, Y.; Eliseo, J. R.; Zuttel, A.; Jensen, C. M. Complex hydrides for hydrogen storage. *Chemical Reviews* **2007,** *107*, 4111-4132.

(6) Yang, J.; Sudik, A.; Wolverton, C.; Siegel, D. J. High capacity hydrogen storage materials: attributes for automotive applications and techniques for materials discovery. *Chemical Society Reviews* **2010,** *39*, 656-675.

(7) Staubitz, A.; Robertson, A. P. M.; Manners, I. Ammonia-borane and related compounds as dihydrogen sources. *Chemical Reviews* **2010,** *110*, 4079-4124.

(8) Klooster, W. T.; Koetzle, T. F.; Siegbahn, P. E. M.; Richardson, T. B.; Crabtree, R. H. Study of the N-H···H-B dihydrogen bond including the crystal structure of BH_3NH_3 by neutron diffraction. *Journal of the American Chemical Society* **1999,** *121*, 6337-6343.

(9) Aldridge, S.; Downs, A. J.; Tang, C. Y.; Parsons, S.; Clarke, M. C.; Johnstone, R. D. L.; Robertson, H. E.; Rankin, D. W. H.; Wann, D. A. Structures and aggregation of the methylamine-borane molecules, $Me_nH_{3-n}N{\cdot}BH_3$ (n=1-3), studied by X-ray diffraction, gas-phase electron diffraction, and quantum chemical calculations. *Journal of the American Chemical Society* **2009,** *131*, 2231-2243.

www.manaraa.com

(10) Singh, P. C.; Patwari, G. N. The C-H···H-B dihydrogen bonded borane-trimethylamine dimer: A computational study. *Chemical Physics Letters* **2006,** *419*, 265-268.

(11) Patwari, G. N.; Ebata, T.; Mikami, N. Dehydrogenation reaction from a dihydrogen bonded precursor complex in the gas phase. *Journal of Physical Chemistry A* **2001,** *105*, 10753-10758.

(12) Sloan, M. E.; Staubitz, A.; Clark, T. J.; Russell, C. A.; Lloyd-Jones, G. C.; Manners, I. Homogeneous catalytic dehydrocoupling/dehydrogenation of amine-borane adducts by early transition metal, group 4 metallocene complexes. *Journal of the American Chemical Society* **2010,** *132*, 3831-3841.

(13) Xiong, Z. T.; Yong, C. K.; Wu, G. T.; Chen, P.; Shaw, W.; Karkamkar, A.; Autrey, T.; Jones, M. O.; Johnson, S. R.; Edwards, P. P., et al. High-capacity hydrogen storage in lithium and sodium amidoboranes. *Nature Materials* **2008,** *7*, 138-141.

(14) Wu, H.; Zhou, W.; Yildirim, T. Alkali and alkaline-earth metal amidoboranes: structure, crystal chemistry, and hydrogen storage properties. *Journal of the American Chemical Society* **2008,** *130*, 14834-14839.

(15) Stennett, T. E.; Harder, S. s-Block amidoboranes: syntheses, structures, reactivity and applications. *Chemical Society Reviews* **2016,** *45*, 1112-1128.

(16) Zhang, Y. S.; Wolverton, C. Crystal structures, phase stabilities, and hydrogen storage properties of metal amidoboranes. *Journal of Physical Chemistry C* **2012,** *116*, 14224-14231.

(17) Xiong, Z. T.; Wu, G. T.; Chua, Y. S.; Hu, J. J.; He, T.; Xu, W. L.; Chen, P. Synthesis of sodium amidoborane ($NaNH_2BH_3$) for hydrogen production. *Energy & Environmental Science* **2008,** *1*, 360-363.

www.manaraa.com

(18) Fijalkowski, K. J.; Genova, R. V.; Filinchuk, Y.; Budzianowski, A.; Derzsi, M.; Jaron, T.; Leszczynski, P. J.; Grochala, W. Na Li(NH_2BH_3)$_2$ - the first mixed-cation amidoborane with unusual crystal structure. *Dalton Transactions* **2011,** *40*, 4407-4413.

(19) Chua, Y. S.; Chen, P.; Wu, G. T.; Xiong, Z. T. Development of amidoboranes for hydrogen storage. *Chemical Communications* **2011,** *47*, 5116-5129.

(20) Owarzany, R.; Leszczynski, P. J.; Fijalkowski, K. J.; Grochala, W. Mono- and bimetalic amidoboranes. *Crystals* **2016,** *6*, 88.

(21) Kelly, H. C.; Edwards, J. O. Ethane 1,2-Diamineborane. *Journal of the American Chemical Society* **1960,** *82*, 4842-4846.

(22) Kelly, H. C.; Edwards, J. O. Evidence for the open chain structure of ethane 1, 2-diamineborane. *Inorganic Chemistry* **1963,** *2*, 226-227.

(23) Neiner, D.; Karkamkar, A.; Bowden, M.; Choi, Y. J.; Luedtke, A.; Holladay, J.; Fisher, A.; Szymczak, N.; Autrey, T. Kinetic and thermodynamic investigation of hydrogen release from ethane 1,2-di-amineborane. *Energy & Environmental Science* **2011,** *4*, 4187-4193.

(24) Ting, H.; Watson, W. H.; Kelly, H. C. Molecular and crystal structure of ethylenediamine-bisborane, $C_2H_{14}B_2N_2$. *Inorganic Chemistry* **1972,** *11*, 374-377.

(25) Leardini, F.; Valero-Pedraza, M. J.; Perez-Mayoral, E.; Cantelli, R.; Banares, M. A. Thermolytic decomposition of ethane 1,2-diamineborane investigated by thermoanalytical methods and in situ vibrational spectroscopy. *Journal of Physical Chemistry C* **2014,** *118*, 17221-17230.

(26) Grochala, W.; Hoffmann, R.; Feng, J.; Ashcroft, N. W. The chemical imagination at work in very tight places. *Angewandte Chemie-International Edition* **2007,** *46*, 3620-3642.

www.manaraa.com

(27) Custelcean, R.; Dreger, Z. A. Dihydrogen bonding under high pressure: A Raman study of BH_3NH_3 molecular crystal. *Journal of Physical Chemistry B* **2003,** *107*, 9231-9235.

(28) Lin, Y.; Ma, H. W.; Matthews, C. W.; Kolb, B.; Sinogeikin, S.; Thonhauser, T.; Mao, W. L. Experimental and theoretical studies on a high pressure monoclinic phase of ammonia borane. *Journal of Physical Chemistry C* **2012,** *116*, 2172-2178.

(29) Liu, A.; Song, Y. In situ high-pressure and low-temperature study of ammonia borane by Raman spectroscopy. *Journal of Physical Chemistry C* **2012,** *116*, 2123-2131.

(30) Kupenko, I.; Dubrovinsky, L.; Dmitriev, V.; Dubrovinskaia, N. In situ Raman spectroscopic study of the pressure induced structural changes in ammonia borane. *Journal of Chemical Physics* **2012,** *137*, 074506.

(31) Trudel, S.; Gilson, D. F. R. High-pressure Raman spectroscopic study of the ammonia-borane complex. Evidence for the dihydrogen bond. *Inorganic Chemistry* **2003,** *42*, 2814-2816.

(32) Najiba, S.; Chen, J. H. High-pressure study of lithium amidoborane using Raman spectroscopy and insight into dihydrogen bonding absence. *Proceedings of the National Academy of Sciences of the United States of America* **2012,** *109*, 19140-19144.

(33) Ramzan, M.; Hussain, T.; Ahuja, R. High pressure phase determination and electronic properties of lithiumamidoborane. *Applied Physics Letters* **2012,** *101*, 111902.

(34) Magos-Palasyuk, E.; Fijalkowski, K. J.; Palasyuk, T. Chemically driven negative linear compressibility in sodium amidoborane, $Na(NH_2BH_3)$. *Scientific Reports* **2016,** *6*, 28745.

(35) Qi, G. Y.; Wang, K.; Yang, K.; Zou, B. Pressure-induced phase transition of hydrogen storage material hydrazine bisborane: Evolution of dihydrogen bonds. *Journal of Physical Chemistry C* **2016,** *120*, 21293-21298.

www.manaraa.com

(36) Xie, S. T.; Song, Y.; Liu, Z. X. In situ high-pressure study of ammonia borane by Raman and IR spectroscopy. *Canadian Journal of Chemistry-Revue Canadienne De Chimie* **2009,** *87*, 1235-1247.

(37) Potter, R. G.; Somayazulu, M.; Cody, G.; Hemley, R. J. High pressure equilibria of dimethylamine borane, dihydridobis(dimethylamine)boron(III) tetrahydridoborate(III), and hydrogen. *Journal of Physical Chemistry C* **2014,** *118*, 7280-7287.

(38) Sun, Y. Z.; Chen, J. H.; Drozd, V.; Najiba, S.; Bollinger, C. Behavior of decomposed ammonia borane at high pressure. *Journal of Physics and Chemistry of Solids* **2015,** *84*, 75-79.

(39) Nylen, J.; Sato, T.; Soignard, E.; Yarger, J. L.; Stoyanov, E.; Haussermann, U. Thermal decomposition of ammonia borane at high pressures. *Journal of Chemical Physics* **2009,** *131*, 104506.

(40) Richardson, T. B.; deGala, S.; Crabtree, R. H.; Siegbahn, P. E. M. Unconventional hydrogen bonds: Intermolecular B-H···H-N interactions. *Journal of the American Chemical Society* **1995,** *117*, 12875-12876.

(41) Morrison, C. A.; Siddick, M. M. Dihydrogen bonds in solid BH_3NH_3. *Angewandte Chemie-International Edition* **2004,** *43*, 4780-4782.

(42) Sams, R. L.; Xantheas, S. S.; Blake, T. A. Vapor phase infrared spectroscopy and ab initio fundamental anharmonic frequencies of ammonia borane. *Journal of Physical Chemistry A* **2012,** *116*, 3124-3136.

(43) Wolstenholme, D. J.; Titah, J. T.; Che, F. N.; Traboulsee, K. T.; Flogeras, J.; McGrady, G. S. Homopolar dihydrogen bonding in alkali-metal amidoboranes and its implications for hydrogen storage. *Journal of the American Chemical Society* **2011,** *133*, 16598-16604.

www.manaraa.com

(44) Li, W.; Wu, G. T.; Chua, Y. S.; Feng, Y. P.; Chen, P. Role of NH_3 in the dehydrogenation of calcium amidoborane ammoniate and magnesium amidoborane ammoniate: A first-principles study. *Inorganic Chemistry* **2012,** *51*, 76-87.

(45) Wang, K.; Arcisauskaite, V.; Jiao, J. S.; Zhang, J. G.; Zhang, T. L.; Zhou, Z. N. Structural prediction, analysis and decomposition mechanism of solid $M(NH_2BH_3)_n$ (M = Mg, Ca and Al). *Rsc Advances* **2014,** *4*, 14624-14632.

(46) Chittari, B. L.; Tewari, S. P. First principles calculations of $LiNH_2BH_3$, $LiNH_3BH_4$, and $NaNH_2BH_3$. *Physica Status Solidi B-Basic Solid State Physics* **2014,** *251*, 898-906.

(47) Ramzan, M.; Silvearv, F.; Blomqvist, A.; Scheicher, R. H.; Lebegue, S.; Ahuja, R. Structural and energetic analysis of the hydrogen storage materials $LiNH_2BH_3$ and $NaNH_2BH_3$ from ab initio calculations. *Physical Review B* **2009,** *79*, 132102.

(48) Lee, S. M.; Kang, X. D.; Wang, P.; Cheng, H. M.; Lee, Y. H. A comparative study of the structural, electronic, and vibrational properties of NH_3BH_3 and $LiNH_2BH_3$: Theory and experiment. *Chemphyschem* **2009,** *10*, 1825-1833.

(49) Ryan, K. R.; Ramirez-Cuesta, A. J.; Refson, K.; Jones, M. O.; Edwards, P. P.; David, W. I. F. A combined experimental inelastic neutron scattering, Raman and ab initio lattice dynamics study of alpha-lithium amidoborane. *Physical Chemistry Chemical Physics* **2011,** *13*, 12249-12253.

(50) Shevlin, S. A.; Kerkeni, B.; Guo, Z. X. Dehydrogenation mechanisms and thermodynamics of MNH_2BH_3 (M = Li, Na) metal amidoboranes as predicted from first principles. *Physical Chemistry Chemical Physics* **2011,** *13*, 7649-7659.

(51) Prescher, C.; Prakapenka, V. B. DIOPTAS: a program for reduction of two-dimensional X-ray diffraction data and data exploration. *High Pressure Research* **2015,** *35*, 223-230.

www.manaraa.com

(52) Wang, L.; Bao, K.; Meng, X.; Wang, X.; Jiang, T.; Cui, T.; Liu, B.; Zou, G. Structural and dynamical properties of solid ammonia borane under high pressure. *The Journal of Chemical Physics* **2011,** *134*, 024517.

www.manaraa.com

Chapter 6

6 Pressure-induced polymorphic, optical and electronic transitions of formamidinium lead Iodide perovskite[1]

6.1 Introduction

Recently, organometal halide perovskite-based solar cells have drawn enormous attention due to their superior properties and high power conversion efficiency (PCE).[1-3] Substantial efforts have been made over the past several years to improve the PCE (e.g., from 3.8% to 21.1%)[4] on methylammonium ($CH_3NH_3^+$ or MA) lead triiodide ($CH_3NH_3PbI_3$ or $MAPbI_3$) by tuning the band gap energy (1.5 to 2.3 eV) using different halide ions.[5-6] Compared to MA, the formamidinium cation ($NH_2CH{=}NH_2^+$ or FA) is slightly larger, and therefore, formamidinium lead triiodide ($FAPbI_3$) has a smaller band gap (1.45 eV), a broader absorption spectrum,[3, 7-10] and ultimately a greater PCE in solar cells.[2] Currently, three polymorphs of $FAPbI_3$ are known at ambient conditions (i.e., α-, β- and δ- phases).[11] The α-phase has a trigonal perovskite structure (space group $P3m1$), which is an excellent solar cell material over a broad solar spectrum.[11-12] The δ-$FAPbI_3$ has non-perovskite structure ($P6_3mc$) and is not suitable for photovoltaic applications due to a larger band gap (~2.48 eV).[13] Compared to the well-studied $MAPbI_3$, the understanding of α-$FAPbI_3$ and its phase stabilities is still limited, which poses a challenge in the fabrication.[9]

Application of external static pressure can effectively alter the crystal structures and produce new polymorphs with improved photovoltaic properties and performance. In particular, solar cell materials modified under high pressures may possess novel and tunable electronic, optical, magnetic and mechanical properties.[8, 10, 14-27] For instance, all MA-based perovskites undergo pressure-induced structural transitions and property changes.[10, 14, 16-19, 21-23, 26] The FA-based perovskites, on the other hand, have different

[1] This chapter is based on a published article *J. Phys. Chem. Lett*. 2017, 8, 2119−2125

www.manaraa.com

behaviors at high pressures in that $FAPbBr_3$ undergoes phase transitions[15] whereas $FAPbI_3$ remains stable.[28] Moreover, the influence of the FA moiety in the perovskite materials remains unclear due to limited studies. Here we report a high-pressure investigation of α- and δ-$FAPbI_3$ by in situ synchrotron X-ray diffraction (XRD), Fourier transform infrared (FTIR) spectroscopy, photoluminescence (PL) spectroscopy, electrical conductivity (EC) measurements, and density functional theory (DFT) calculations. Our results reveal pressure-induced new polymorphs of $FAPbI_3$ with contrasting structural stabilities and properties. The demonstrated structure-property correlation provides practical guidance in the design and engineering of new solar cell materials.

6.2 Experimental

6.2.1 Materials

We synthesized both α- and δ-phase $FAPbI_3$ using the previously reported methods,[2, 29] and all chemicals (formamidine acetate, hydroiodic acid (57 wt. %), lead iodide and γ-butyrolactone) were purchased from Sigma Aldrich with claimed purity of 99% for all and used as received.

Firstly, the intermediate reagent, formamidinium iodide (FAI), was prepared by the reaction between formamidine acetate and hydroiodic acid by stirring in an ice bath to get a clear yellow solution, followed by heating in an oil bath at 60 °C to get a colorless solution. Then the solution was evaporated until white crystals were formed, and diethyl ether was used to wash the crystals several times. The white solid was recrystallized twice by hot ethanol followed by cooling to room temperature. Lastly, the fine white crystals were collected through a vacuum filter and dried under vacuum at 70 °C for 12 hours.

δ-$FAPbI_3$ was synthesized by dissolving formamidinium iodide and lead iodide in γ-butyrolactone. The mixture became the bright yellow solution and was heated in an oil bath at 70 °C for 10 minutes, and then the solution was cooled to room temperature and diethyl ether was added to precipitate the yellow powder. The obtained yellow powder

www.manaraa.com

was washed several times with diethyl ether and collected through a vacuum filter. Lastly, the fine product was dried in a 70 °C vacuum oven overnight.

α-$FAPbI_3$ was synthesized by the same procedure, except that the obtained bright yellow solution was heated in an oil bath at around 110 ^oC until all the solution evaporated and black crystals were formed. All the products were kept in a N_2-filled MBraun LAB Master 130 glovebox with H_2O content of < 1 ppm and O_2 content of < 10 ppm.

6.2.2 Powder X-ray diffraction

The crystallinity of the as-synthesized products was investigated by powder X-ray diffraction (XRD) using a Rigaku X-ray diffractometer using Co $K\alpha$ radiation (λ = 1.78890 Å), the scan range was from 2θ = 10 to 80° with a step size of 0.02.

6.2.3 In situ high-pressure X-ray diffraction

The angle-dispersive XRD was performed in Advanced Photon Source (APS), Argonne National Laboratory (ANL), USA, at the Sector 20-ID beamline. A symmetrical diamond anvil cell equipped with type-I diamonds with 400 μm culet size was used for all in situ high-pressure XRD measurements. A stainless steel gasket was pre-indented to 50 μm in thickness, and then a hole with diameter of 150 μm was drilled in the center as the sample chamber. A ruby ball was loaded as pressure calibrant. To achieve hydrostatic conditions, neon was loaded together with the sample as the pressure transmitting medium using the gas loading system at GSECARS of APS. The wavelength of monochromatic X-ray beam is 0.4768 Å, and the 2D Debye-Scherrer diffraction patterns were collected using a MARCCD detector and integrated by using Fit2D program for further analysis. The GSAS software package was used for Rietveld refinement.

6.2.4 FTIR spectroscopy

For IR measurement, KBr was loaded with sample, and no pressure transmitting medium was used. The in-situ high-pressure IR absorption experiments were carried out by a customized IR micro-spectroscopy system. A commercial Fourier transform infrared (FTIR) spectrometer (Model Vertex 80v) from Bruker Optics Inc. equipped with Globar

www.manaraa.com

mid-IR light source constituted the main component of the micro-IR system. The system was operated under a vacuum of < 5 mbar to effectively remove the IR absorption from H_2O and CO_2. The transmitted IR beam was collected by a wide-band mercury cadmium telluride (MCT) detector equipped with a ZnSe window that enables a spectral range of 400 to 10000 cm^{-1} to be measured. A spectral resolution of 4 cm^{-1} was used.

6.2.5 Photoluminescence measurements

For photoluminescence measurements, the sample was loaded into the sample chamber and no pressure transmitting medium was used, and the in situ high-pressure photoluminescence experiments were carried out by a customized Raman spectrometer with a 532 nm diode pumped solid state laser as the excitation source. The signal was recorded using an ultrasensitive, liquid nitrogen cooled, back-illuminated, charge-coupled device (CCD) detector from Acton.

6.2.6 Electrical conductivity measurements

We used DAC in combination with Maglab system to investigate the electronic transport properties under pressure at low temperatures. Pressure was generated by a DAC made of CuBe with anvil culet of 300 μm for α phase and beveled anvil of 100/300 (100 μm diameter culet on the top of a 300 μm diameter face) for δ phase. The sample was loaded into a 100 μm hole in a T301 stainless-steel gasket that is preindented from the thickness of 250 μm to 40 μm. The size of α phase sample was ~ 60 μm in diameter and 10 μm thick, while the size of δ phase was ~ 30 μm in diameter and 5 μm thick. Four gold probes are pressed on the sample, and cubic boron nitride (cBN) was used as insulating layer between the gasket and the electrodes. Gold wire of 18 μm in diameter was used as the electrode leads outside of the culet. When the magnitude of resistance is higher than 10^3 ohm, we used only two adjacent electrode leads. The BeCu cell was connected to the sample holder and put into Maglab system for in situ low-temperature measurements. The pressure was determined by ruby fluorescence method at room temperature before and after each cooling cycle.

www.manaraa.com

6.2.7 Computational Methods

High-pressure phase transitions of $FAPbI_3$ were simulated using *ab initio* molecular dynamics (MD) method as implemented in the Vienna Ab Initio Simulation (VASP) program with Langevin dynamics. Projector-augmented plane-wave (PAW) potentials[30] and Perdew-Burke-Ernzerhof (PBE) functional were used, with $6s^2 6p^2$ for Pb, $5s^2 5p^5$ for I, $2s^2 2p^2$ for C, $2s^2 2p^3$ for N, and $1s^1$ for H treated as valence states. A plane-wave cut-off of 500 eV was used. Supercells consisted of 144, 192, and 240 atoms were employed for both α and γ phases along with a 2×2×2 *k*-point mesh for Brillouin zone (BZ) sampling. Thermal trajectories were sampled by a time step of 1.0 fs at 300 K, and electronic self-consistency criteria was set to 10^{-5} eV. Enthalpy calculation was performed using the VASP program[31] and a dense *k*-point mesh with a spacing of $2\pi \times 0.03$ $Å^{-1}$. The van der Waals (vdW) interactions were taken into account using the optPBE-vdW functional.

6.3 Results and discussion

6.3.1 XRD analysis of $FAPbI_3$

The XRD patterns of synthesized materials are in excellent agreement with the literature data indicating the high purity of as-made samples. As shown in Figure 6.1, structural refinement suggests that the α-phase has a $Pm\bar{3}m$ structure, consistent with recently reported cubic structure[13], while the δ-phase has a $P6_3mc$ structure[2, 11]. The unit cell parameters are a = 6.3558 Å for α- and $a = b$ = 8.6838 Å, c = 7.9365 Å for δ-phase.

Figure 6.2a shows selected XRD patterns of α-$FAPbI_3$ at high pressure. At 0.34 GPa, the XRD pattern of α-$FAPbI_3$ exhibits new reflection peaks, indicating the formation of a new structure (designated as phase II). At 1.67 GPa, another new reflection appeared at 8.8° together with the asymmetrization of several other reflections, indicating the transition to another phase (phase III). The XRD pattern upon compression to 4 GPa displays a broad profile at 9.5°, indicating lattice amorphization, although a small portion of the sublattice remains crystalline, similar to other perovskite materials.[14-16, 22]

www.manaraa.com

Upon decompression, remarkably, the recovered phase at near ambient pressure exhibits a pattern similar to phase II instead of the ambient phase I, which can be refined using phase II structure, indicating an irreversible transition. The refined cell parameters of α-$FAPbI_3$ upon compression and decompression are shown in Table 6.1. This observation is in direct contrast to the recently reported high-pressure behavior of $FAPbI_3$,[28] where a different starting structure was used, which showed no structural transitions at high pressure. The starting structure of α-$FAPbI_3$ is therefore highly sensitive to the detailed preparation procedures.

www.manaraa.com

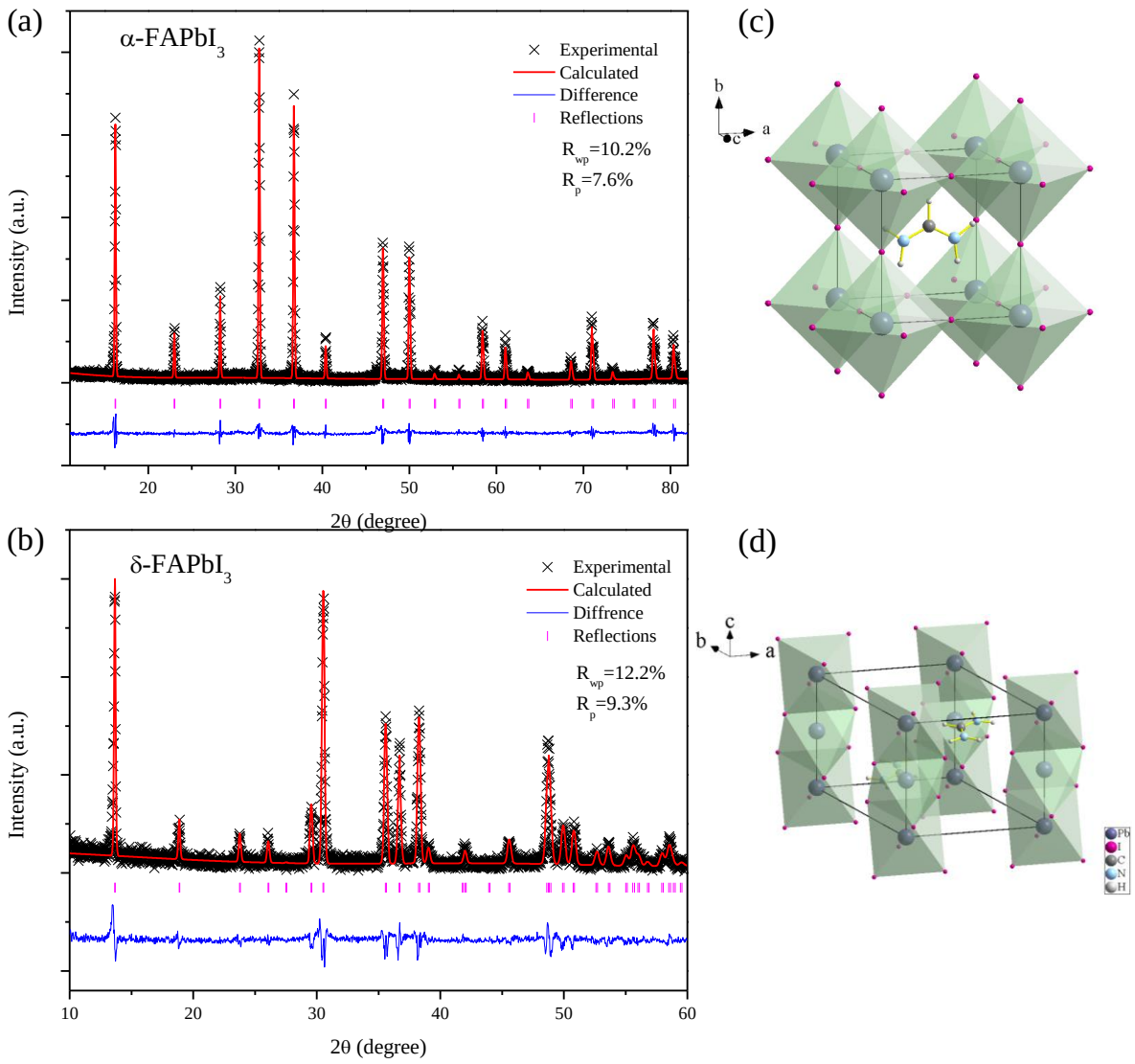

Figure 6.1 X-ray diffraction patterns of *α*- (a) and *δ*- (b) $FAPbI_3$ at ambient conditions using Co *K*α radiation of λ=1.7890 Å in comparison with structural refinement using $Pm\bar{3}m$ (c) and $P6_3mc$ (d) crystal structures respectively.

www.manaraa.com

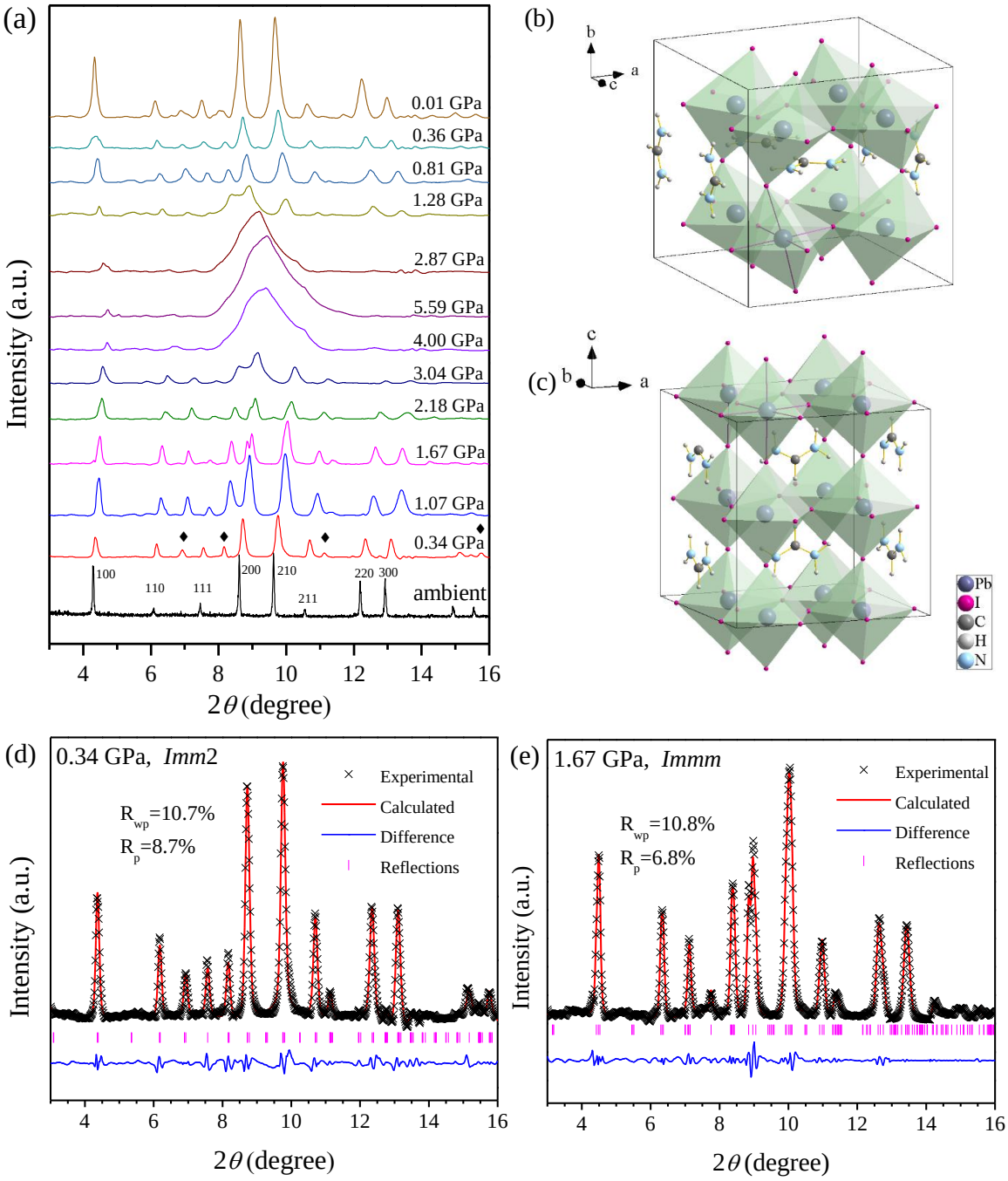

Figure 6.2 XRD patterns of *α*-FAPbI$_3$ upon compression and decompression (a), proposed crystal structures of high-pressure phase II (b) and phase III (c) based on MD simulations, and calculated XRD patterns in comparison with experimental results at 0.34 GPa (d) and 1.67 GPa (e) using Rietveld refinement.

www.manaraa.com

Table 6.1 Unit cell parameters of α-$FAPbI_3$ and δ-$FAPbI_3$ at presentative pressures

α-$FAPbI_3$						
Structure	Pressure (GPa)	a (Å)	b (Å)	c (Å)	V ($Å^3$)	V' ($Å^3$) [a]
Phase I $Pm\bar{3}m$	ambient	6.3558	6.3558	6.3558	256.75	256.75
Phase II *Imm*2	0.34	12.495	12.490	12.543	1957.5	244.68
	1.07	12.245	12.288	12.236	1841.9	230.24
Phase III *Immm*	1.67	12.226	12.184	12.358	1841.0	230.12
	2.18	12.036	11.986	12.227	1763.9	220.49
	3.04	11.911	11.900	12.132	1719.6	214.95
Recovered *Imm*2	0.01	12.631	12.451	12.660	1991.1	248.89

[a] V' is the volume per molecular unit.

δ-$FAPbI_3$				
Pressure (GPa)	a (Å)	b (Å)	c (Å)	V ($Å^3$)
ambient	8.6838	8.6838	7.9365	518.30
0.34	8.5815	8.5815	7.8337	499.60
0.40	8.5815	8.5815	7.8273	499.19
0.90	8.4508	8.4508	7.7513	479.40
1.77	8.3416	8.3416	7.1443	430.51

[b] The crystal structure used is *C*2/*c* in primitive cell with the distorted hexagonal setting (i.e., $\alpha = \beta \approx 90°$ and $\gamma \approx 120°$). See text.

www.manaraa.com

α-$FAPbI_3$ has been reported to gradually transform to the δ-phase at ambient conditions.[2, 32] However, the diffraction patterns of phase II and III clearly do not match that of the δ-phase structure, indicating that both are new phases. We performed ab initio molecular dynamics (MD) simulations to search for possible structures for phase II and III. The simulation at ambient conditions reveals free rotations of FA molecules and an average cubic structure, consistent with experimental result. With increasing pressure, the interactions between FA and PbI_6 octahedrons are enhanced, which leads to confined FA vibrations and unit cell distortions. The most probable structures discovered in the MD simulations for phase II and III are both orthorhombic with space group *Imm*2 and *Immm*, respectively (Figure 6.2b and 6.2c). Using these structures, the calculated diffraction patterns excellently reproduced experimental data (Fig 6.2d and 2e), giving reduced cell parameters of a = 6.2475 Å, b = 6.2450 Å, and c = 6.2714 Å for phase II and a = 6.1132 Å, b = 6.0920 Å and c = 6.1792 Å for phase III structures. Interestingly, the *Imm*2 structure for α-$FAPbI_3$ is similar to that of β-$FASnI_3$[11] while the *Immm* structure is similar to a $MAPbI_3$ structure found favorable above 2.7 GPa.[16] In addition, the enthalpy calculation (Figure 6.3a) indicates that *Imm*2 and *Immm* are indeed low-energy structures not only with increasing pressures but even at ambient pressure, consistent with the experimental observation that the recovered phase retains *Imm*2 structure. Upon compression, the first phase transition ($Pm\bar{3}m$ to *Imm*2) can be characterized by tilting between two adjacent PbI_6 octahedra as well as distortion of an individual PbI_6 octahedron leading to modified Pb-I-Pb angles (166.8, 144.0, and 177.8°). The subsequent *Imm*2-to-*Immm* transition features a further distortion of the unit cell, leading to considerable change of Pb-I-Pb angles to 143.0° and 154.5° but no tilting along the c-axis (i.e., Pb-I-Pb angle remains 180°). The unit cell parameters as a function of pressure (Table 6.1 and Figure 6.4a) suggest that the first transition is smooth and continuous but the second transition at 1.67 GPa has an unusual expansion of the c-axis, and an anomaly of the unit cell volume at the phase boundary. This unusual behavior could be associated with the tilting of the PbI_6 polyhedron as a result of anisotropic compressibility of the crystal axes.

www.manaraa.com

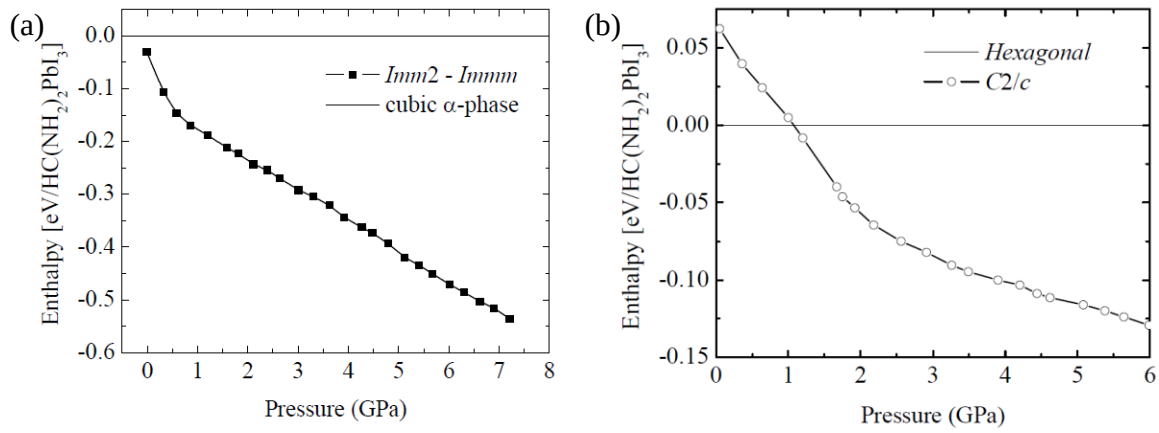

Figure 6.3 Enthalpies of new crystal structures for *α*- (a) and *δ*- (b) phase of $FAPbI_3$ as a function of pressure. Note that the *Imm*2/*Immm* structure always has a lower enthalpy than the cubic *α*-phase even at ambient pressure. This could be due to an inadequate estimate of the enthalpy of the cubic *α*-phase by a static calculation. The cubic *α*-phase has free molecule rotations which cannot be accounted for in this calculation.

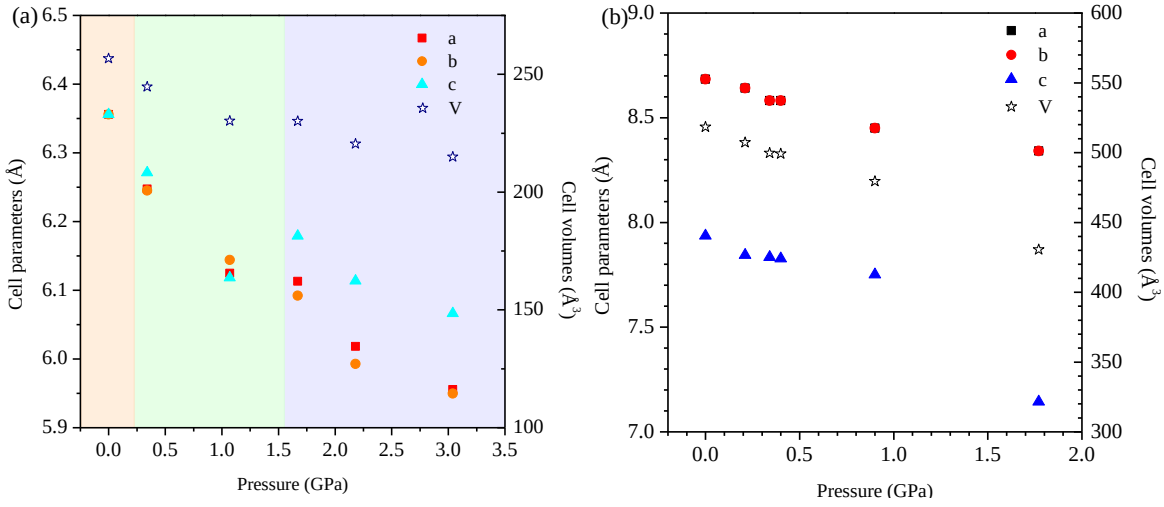

Figure 6.4 Reduced unit cell parameters and volumes of *α*- (a) and *δ*- (b) phase of $FAPbI_3$ as a function of pressure.

www.manaraa.com

We comparatively investigated the structural stability of δ-$FAPbI_3$ at high pressures using in situ XRD with selected patterns shown in Figure 6.5a. In contrast to α-$FAPbI_3$, no distinctive changes of the reflection patterns were observed prior to the amorphization, indicating that the crystal lattice of δ-$FAPbI_3$ undergoes pressure-induced distortion rather than major phase transitions. Moreover, partially irreversible structural modifications were also evident depending on the highest pressure achieved. A*b initio* MD simulations suggest that a monoclinic distortion to a *C*2/*c* structure becomes apparent upon compression, which can also best reproduce the XRD pattern of the δ-$FAPbI_3$ at high pressures (Figure 6.5b). The cell parameters of the *C*2/*c* structure (at 0.34 GPa) are a = 8.7081 Å, b = 14.9724 Å, c = 7.9022 Å and β = 90.6291°. The primitive cell of the *C*2/*c* structure resembles a distorted hexagonal cell, with $a = b$ = 8.6603 Å, c = 7.9022 Å, α = β = 90.3163°, and γ = 119.6346°. In addition, for the high-pressure phase of δ phase, the enthalpy of *C*2/*c* vs. pressures suggests that this structure is more favorable above 1 GPa (Figure 6.3b). Figure 6.6 further illustrates the structural relationship between the hexagonal and *C*2/c structures. Evidently, the *C*2/*c* structure has almost identical projection profile as the original hexagonal structure, consistent with the only slightly modified cell angles. In addition, we found that the δ-phase has confined FA molecular motions already at ambient conditions so that no rotation modes for the FA molecules were observed at high pressure. This indicates that the δ-phase has stronger cation-anion interactions than α-phase, which contributes to the thermodynamic stability of the former.

www.manaraa.com

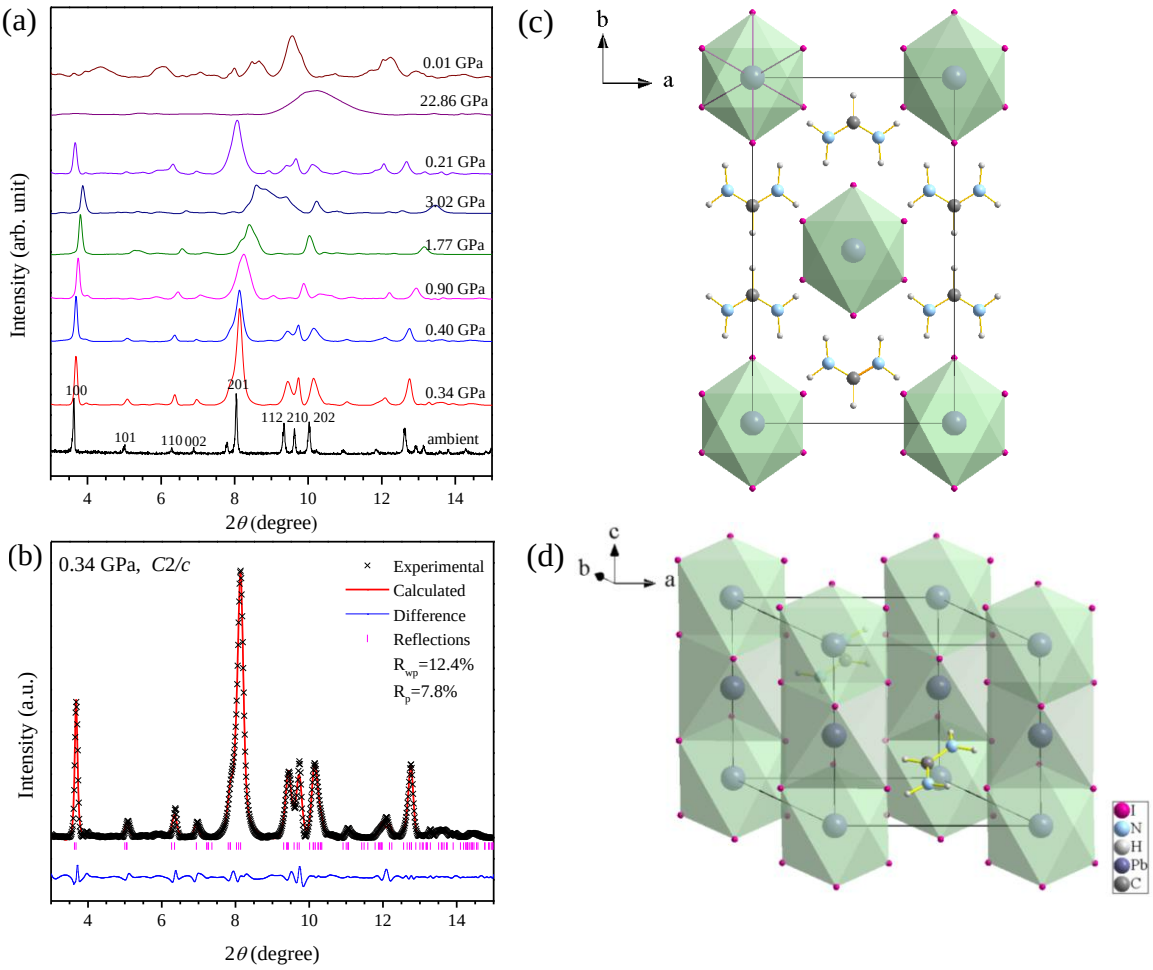

Figure 6.5 XRD patterns of *δ*-FAPbI$_3$ upon compression and decompression (a). Calculated XRD patterns of FAPbI$_3$ in comparison with experimental results at 0.34 GPa for *δ*-FAPbI$_3$ (b) and the corresponding crystal structure in *C*2/*c* (c) and primitive cell representations (d).

www.manaraa.com

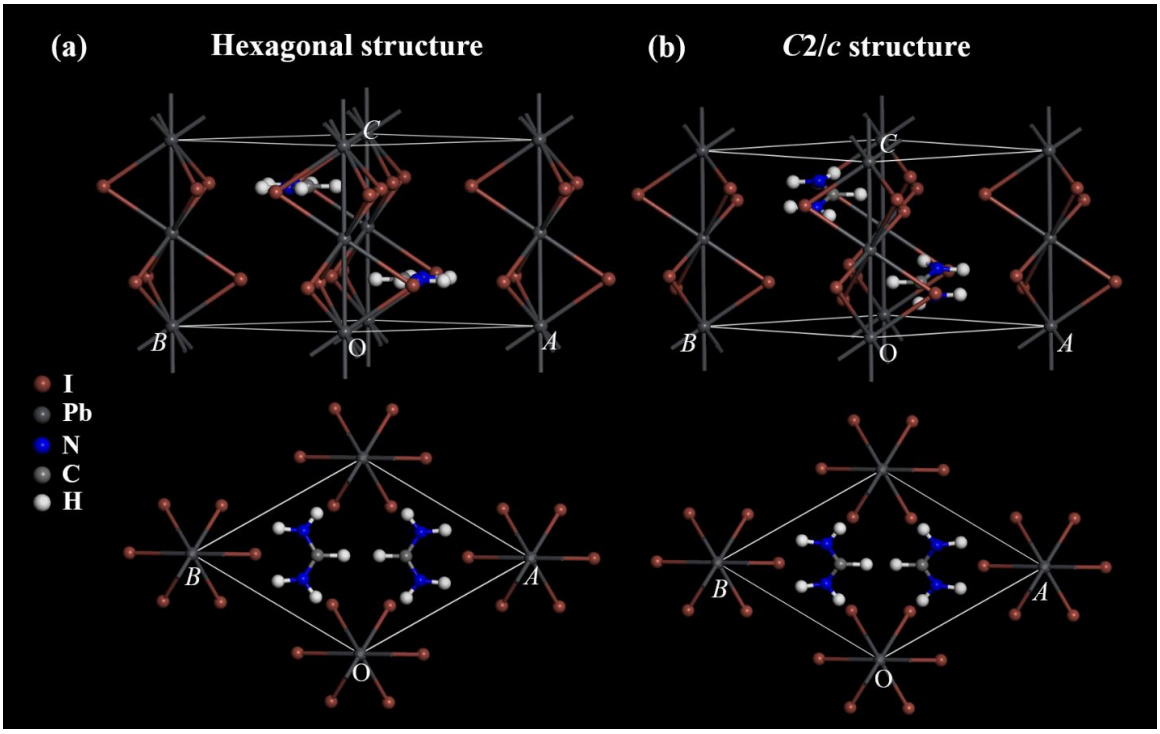

Figure 6.6 The relationship between original hexagonal structure (a) and monoclinic *C*2/*c* structure (b) for *δ*-phase of $FAPbI_3$ upon compression. The *C*2/*c* structure is shown in the primitive unit cell for comparison.

6.3.2 IR analysis of $FAPbI_3$

To explore the pressure effects on the FA moiety and cation-anion interactions, we performed in situ FTIR spectroscopy (Figure 6.7 and 6.8). In the mid-IR region, the optical absorption is exclusively attributed to the vibrations from organic FA (H_2N^+=$CHNH_2$) (Table 6.2). Upon compression, the pressure dependence (Table 6.3) collectively exhibits discontinuities at 0.5 and 1.7 GPa for *α*-$FAPbI_3$, in agreement with the identified transition boundaries. The pressure-induced profile broadening above 4 GPa is also consistent with the structural amorphization suggested by XRD measurements. Most of observed IR modes, especially the N-H and C-H stretching region (3250-3400 cm^{-1}), exhibit a prominent red shift in the entire compression region for both

www.manaraa.com

α- and δ-$FAPbI_3$ (Table 6.3 and 6.4), indicating pressure-induced enhancement of hydrogen bond interactions. The pressure-induced mode softening of the X-H bond has been widely accepted as strong evidence for the formation and enhancement of the X-H···Y hydrogen bond causing the weakening of the X-H bond.[33] MD simulation reveals that the rotations of FA molecules are reduced at high pressure to ordered oscillations (C as the pivot point), which engages a stronger hydrogen bonding between the FA and PbI_6 via highly effective H···I interactions, with the shortest H···I distance of 2.4 Å (Figure 6.9). In contrast to the MA-based counterparts, the FA perovskite is clearly influenced by hydrogen bonding, which, in turn, causes the polymorphic transitions to be significantly different from the former.

www.manaraa.com

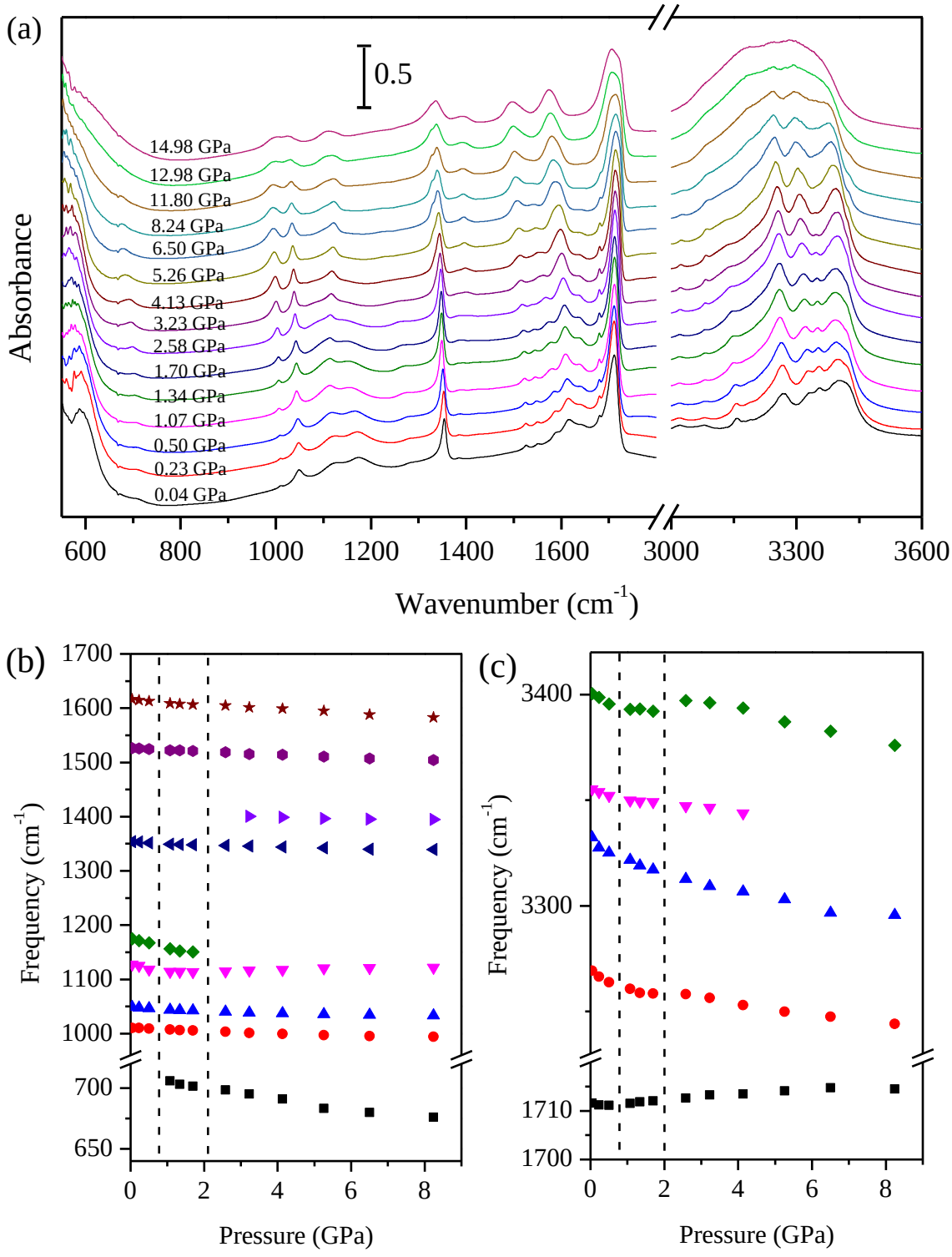

Figure 6.7 FTIR spectra of *α*-FAPbI$_3$ upon compression (a) and pressure dependence of selected IR modes (b) and (c).

www.manaraa.com

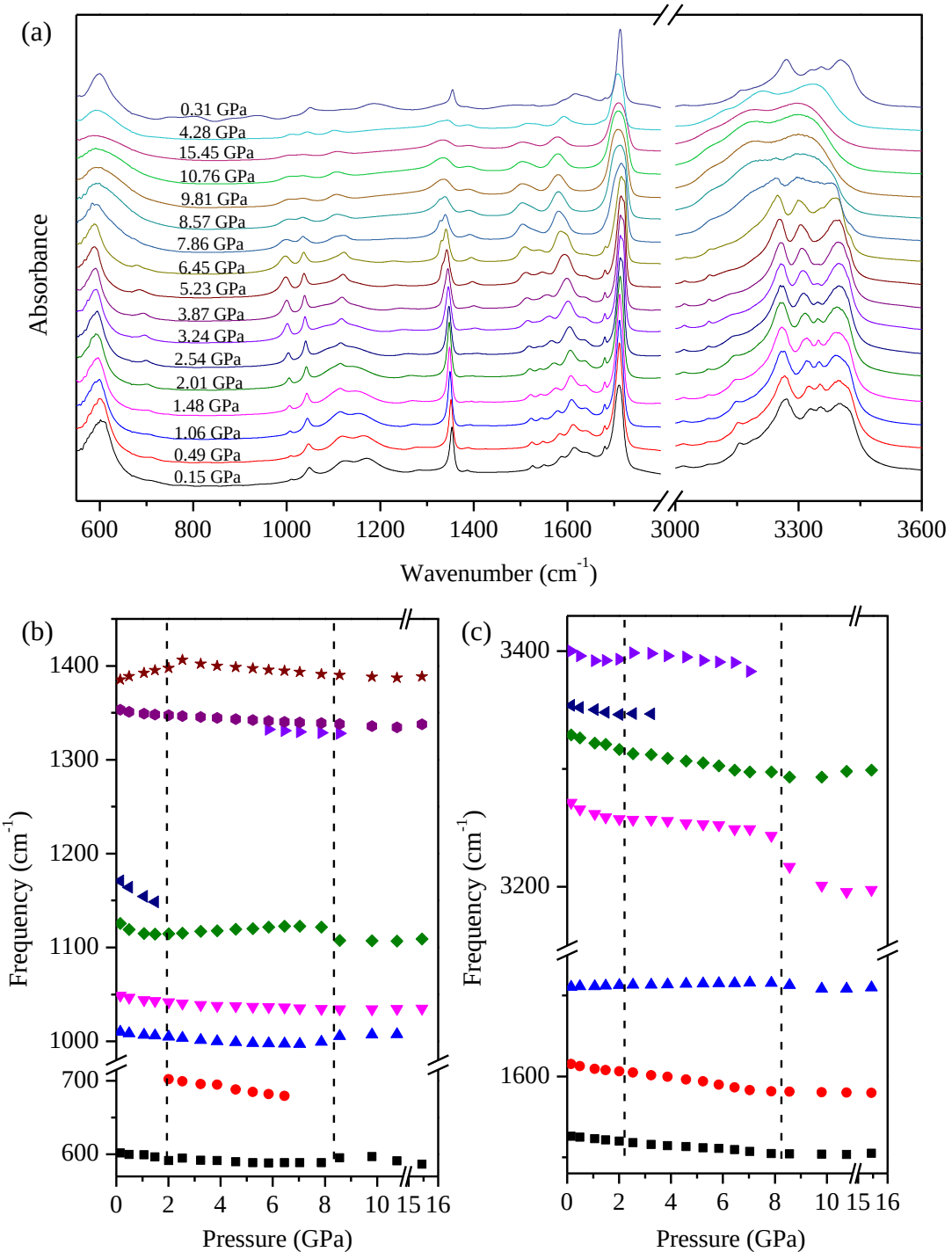

Figure 6.8 FTIR spectra of *δ*-phase of $FAPbI_3$ upon compression and decompression, (a) and pressure dependence of selected IR modes for *δ*-phase (b) and (c).

www.manaraa.com

Table 6.2 Assignment of IR peaks of α-$FAPbI_3$ and δ-$FAPbI_3$

Frequency (cm^{-1})		Assignment
α-$FAPbI_3$	δ-$FAPbI_3$	
587	602	-C-H rock
1049	1048	=C-H bending
1173	1171	C-N stretching
1354	1353	C-N stretching
1616	1615	N-H bending
1712	1711	C=N stretching
3268	3268	C-H stretching
3332	3329	Overtone of N-H bending
3355	3354	N-H symmetric stretching
3403	3399	N-H asymmetric stretching

www.manaraa.com

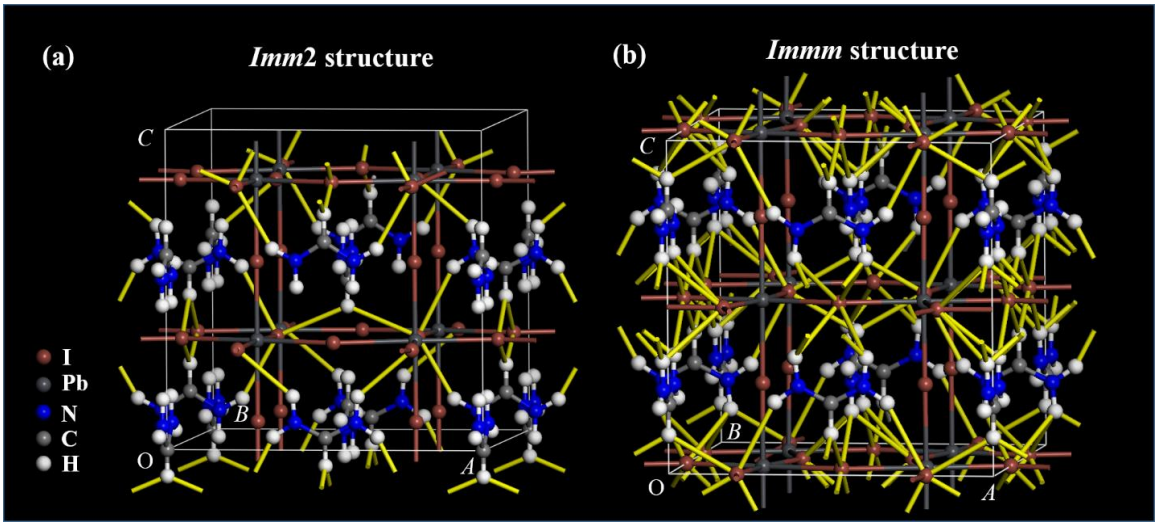

Figure 6.9 Schematic hydrogen bonding interactions between FA and PbI_6 polyhedra in *Imm*2 structure at 0.34 GPa (a) and in *Immm* structure at 1.67GPa (b). The distances of H···I ranging from 2.4 Å to 3.2 Å, i.e., those in strong to moderate hydrogen bonding region, are highlighted by yellow lines. Hydrogen bonds are clearly more populated and symmetric, in the *Immm* structure.

www.manaraa.com

Table 6.3 Pressure dependence of selected IR modes of *α*-$FAPbI_3$ on compression

Frequency (cm^{-1})[a]	d*ν*/dp ($cm^{-1}\cdot GPa^{-1}$)		
	Phase I (< 0.5 GPa)	Phase II (0.5 – 1.7 GPa)	Phase III (1.7 – 8.2 GPa)
705		-6.8	-4.1
1010	-3.7	-2.8	-1.6
1049	-5.4	-3.4	-1.2
1127	-19.9	-0.8	1.3
1175	-16.4	-9.2	
1354	-5.9	-1.9	-1.4
1400			-1.2
1526	-3.7	-2.0	-2.4
1712	-0.9	0.8	0.3
3269	-11.7	-3.4	-2.5
3332	-15.4	-7.2	-3.1
3355	-6.7	-1.0	
3400	-10.6	-1.5	-3.9

[a] Data measured at 0.04 GPa and room temperature.

www.manaraa.com

Table 6.4 Pressure dependence of selected IR modes of δ-$FAPbI_3$ on compression

Frequency (cm^{-1})[a]	$d\nu/dp$ ($cm^{-1}\cdot GPa^{-1}$)	
	Phase I (< 2.0 GPa)	Phase II (2.0 – 8.5 GPa)
602	-3.5	-0.9
702		-5.3
1010	-2.8	-1.6
1125	-8.1	1.7
1171	-16.9	
1332		-1.9
1353	-3.8	-1.5
1385	7.3	-1.9
1615	-5.6	-4.5
1711	0.9	0.6
3271	-8.8	-2.2
3329	-6.1	-3.4
3354	-4.3	
3400	-6.0	-2.2

[a] Data measured at 0.15 GPa and room temperature.

www.manaraa.com

6.3.3 Optical response of $FAPbI_3$

Critical to photovoltaics applications, optical response of $FAPbI_3$ was examined as a function of pressure using an optical microscope (Figure 6.10a and 6.11) and PL spectroscopy (Figure 6.10b and 6.10c). Upon compression to 4.5 GPa near the amorphization threshold, α-$FAPbI_3$ gradually changes from black to a prominent red and maintains this color at higher pressures. The color reverses to black after pressure release. In contrast, the δ-phase initially remains yellow but gradually darkens to orange at 6.4 GPa, and finally becomes red at higher pressures. Unique piezochromism observed here when compared to other organolead halide perovskite materials[14-15, 22] suggests that the optical properties of perovskite materials are structure-dependent and cation-specific.

At ambient pressure, a PL peak was observed at 838 nm (1.48 eV) for α-$FAPbI_3$, close to the band gap energy (1.45 eV). On compression, the peak shifted to red and exhibited a split profile with an additional PL channel. The pressure-induced additional PL channel was also observed in hybrid organolead halide perovskite materials (e.g., $MAPb(Br_{0.6}I_{0.4})_3$)[14]. Therefore, it is highly likely that the non-equivalent iodine ligands in the pressure-distorted PbI_6 octahedra give rise to new PL states. Upon further compression, the major PL channel underwent an abrupt red shift at 1.73 GPa. Above 3.6 GPa, both channels were suppressed. Upon decompression, the PL was recovered with a modified profile and peak position of 824 nm. The evolution of PL peaks shows that the band gap energy reaches a minimum of 1.42 eV at about 3 GPa and then increases. This is in contrast to a recent optical measurement on α-$FAPbI_3$, where the band gap has a monotonic reduction under pressure (to 1.337 eV)[28] in a single structure. Without structural changes, the lattice contraction would play the major role in regulating the PL energy levels. With the lattice distortion and amorphization, however, they outweigh the lattice contraction and lead to the widening of the band gap and total suppression of the PL activity.[22] Moreover, the pressure-induced new PL channels provide a new approach in tuning optical properties in addition to traditional chemical approaches.

www.manaraa.com

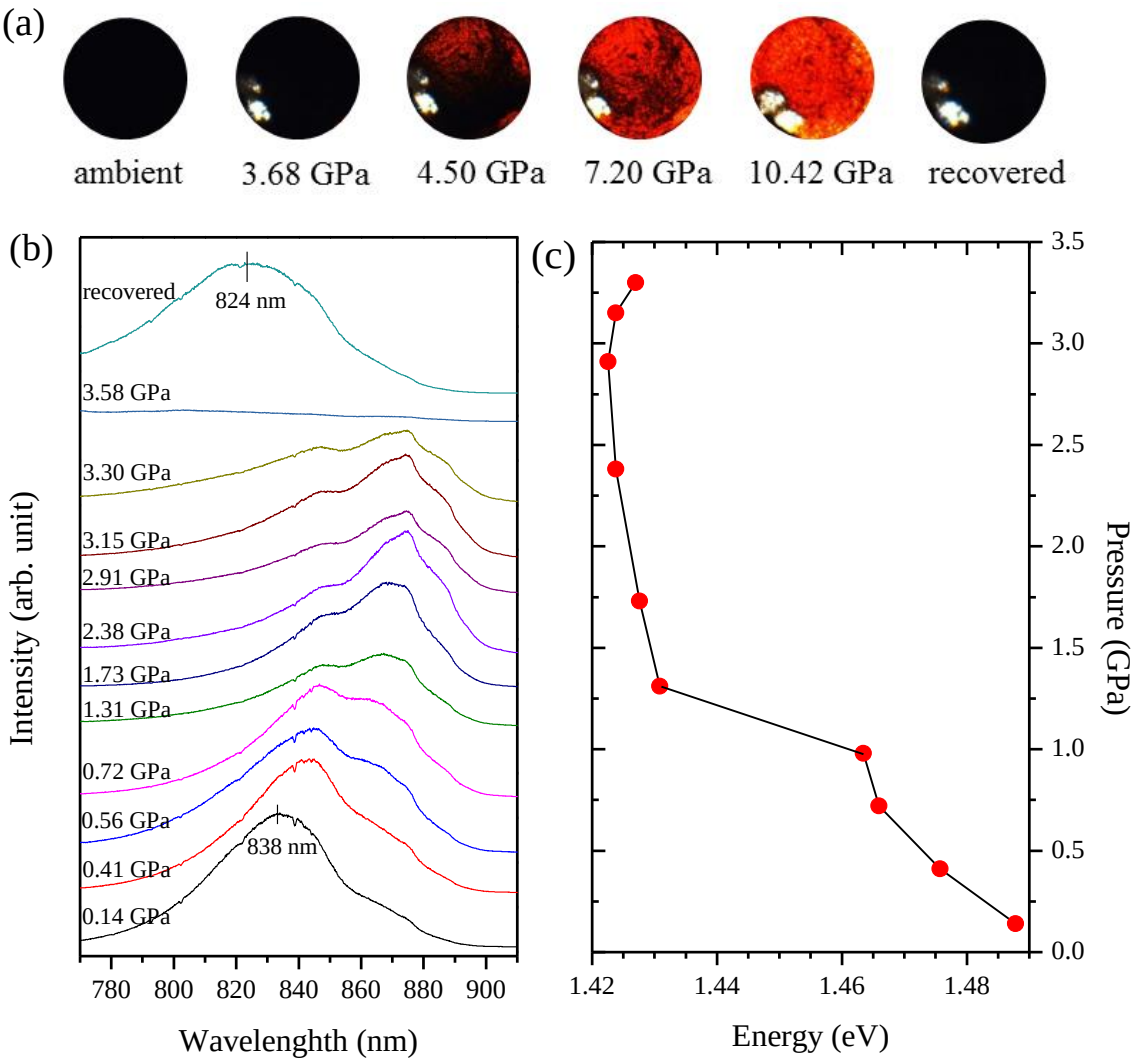

Figure 6.10 Optical micrographs of *α*-$FAPbI_3$ upon compression and recovery (a), PL spectra of *α*-$FAPbI_3$ upon compression and decompression (b) and the corresponding pressure dependence (c).

www.manaraa.com

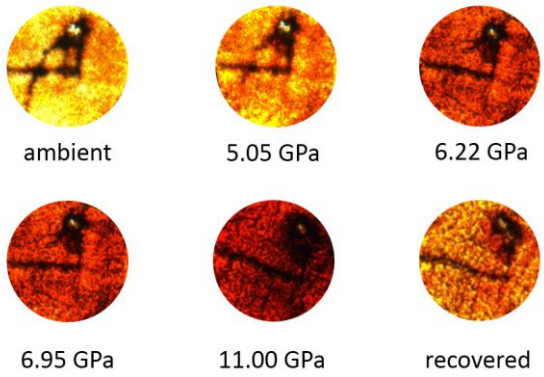

Figure 6.11 In situ high-pressure optical micrographs of δ-$FAPbI_3$ in a diamond anvil cell.

The electronic band structure and density of states (DOS) (Figure 6.12 and 6.13) reveal that in $FAPbI_3$ the valence bands are dominated by I 5p orbitals. The FA cation has notable contributions to only the conduction bands. The α-$FAPbI_3$ is a direct band gap semiconductor with a calculated band gap energy of 1.35 eV at ambient pressure. The experimental band gap energies are well matched to the *Imm*2 and *Immm* structures. With increasing pressure, the band structures do not have fundamental changes (Figure 6.13), but the band gap energy decreases (Figure 6.12b). This agrees with the experiment except the amorphization-induced band gap change near 3 GPa cannot be examined in crystalline phase. The reduction of the band gap suggests a greater level of orbital overlap in the PbI_6 octahedra, which is naturally induced by the Pb-I bond contraction at high pressure. The FA cations, on the other hand, only have a minor role in determining the band gap. The δ-$FAPbI_3$ has an indirect band gap with E_g=2.5 eV at ambient pressure, which also reduces with pressure (Figure 6.14). At high pressure, the δ-phase is distorted to a *C*2/*c* structure, which has a larger band gap compared to the undistorted $P6_3mc$ phase. Here the increase of the band gap is due to the distortion within the PbI_6 octahedra, which deviates from ideal O_h geometry to a distorted square-planar configuration, as a result of molecular tiling and meshing at high pressure. Apparently, the band gaps in both structures can be tuned effectively within a few GPa range. This suggests the possibility of functional manipulation of larger band gap materials to photovoltaic active materials utilizing the externally applied pressure.

www.manaraa.com

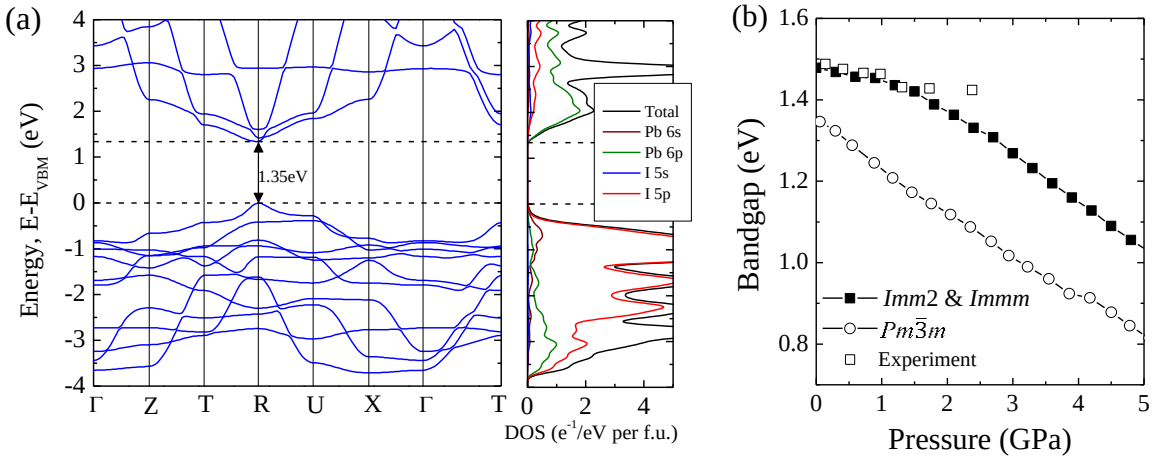

Figure 6.12 Band structures and projected DOS of *α*-FAPbI$_3$ (a) at ambient pressure and calculated bandgap energy vs pressure (b).

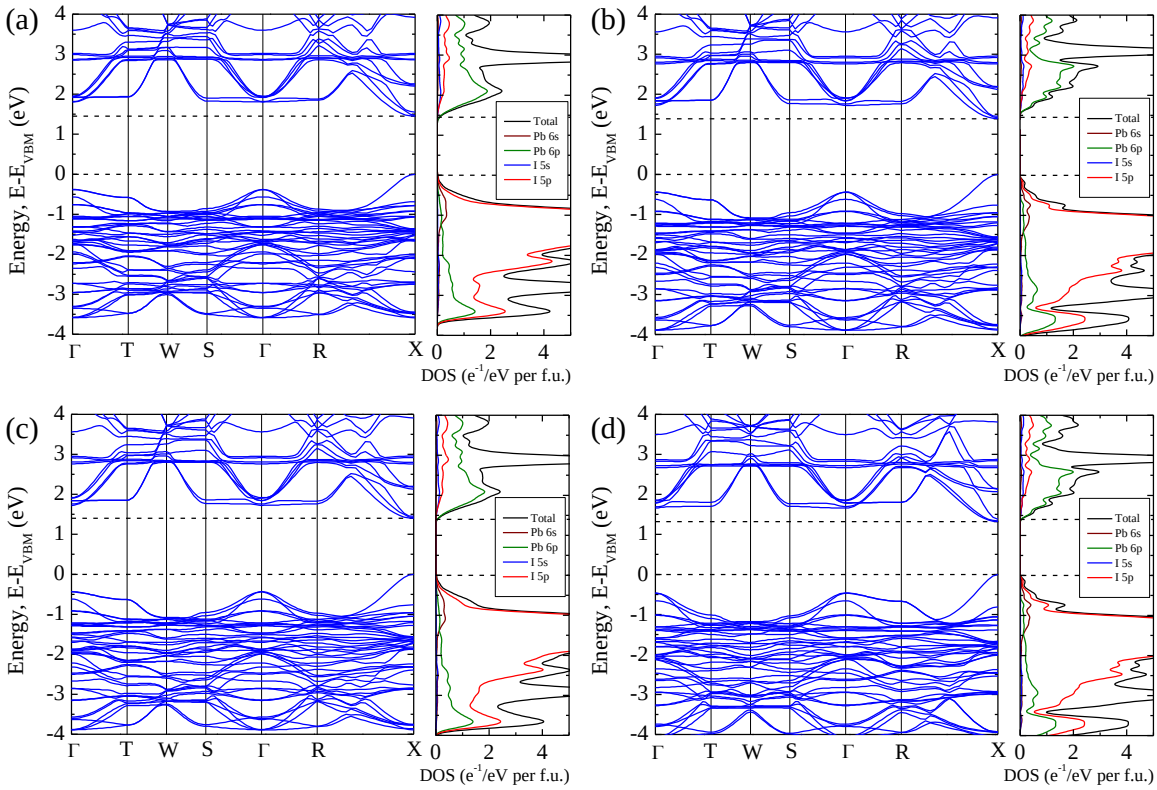

Figure 6.13 Band structures and projected density of states (DOS) of *α*-FAPbI$_3$ for phase II at ambient pressure (a) and 1.6 GPa (b), and for phase III at ambient pressure (c) and 2.0 GPa (d).

www.manaraa.com

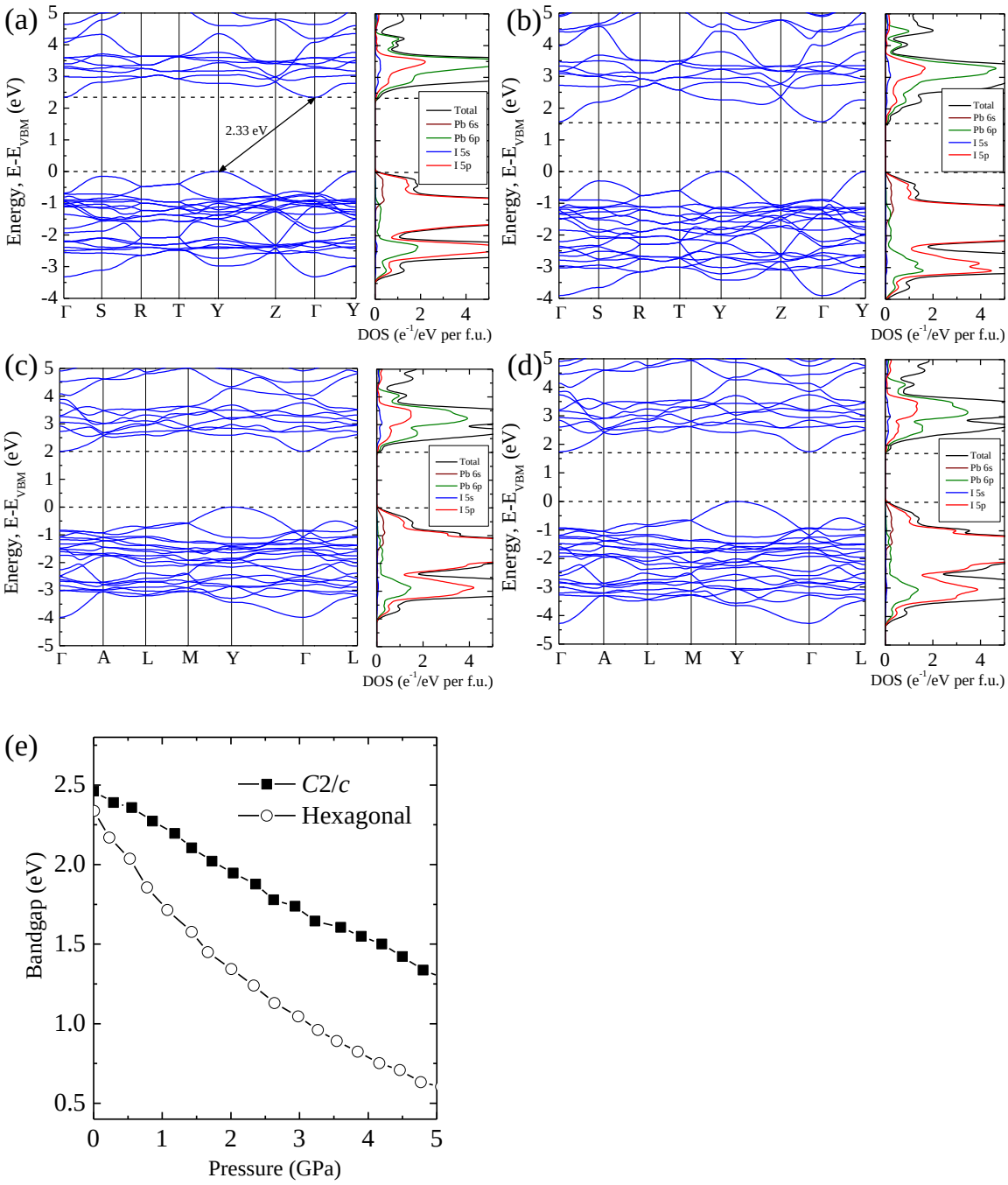

Figure 6.14 Band structures and projected density of states (DOS) of *δ*-FAPbI$_3$ for the hexagonal phase at ambient pressure (a) and 1.4 GPa (b), and for the *C*2/*c* phase at 1.7 GPa (c) and 3.0 GPa (d), as well as the calculated bandgap energy as a function of pressure (e).

www.manaraa.com

6.3.4 Electrical measurements of $FAPbI_3$

Finally, we investigated the EC of both polymorphs, as shown in Figure 6.15. Near ambient pressure, the α- and δ-$FAPbI_3$ have respective resistance of 1.1×10^9 and 1.7×10^{11} Ohm. The resistance difference is consistent with the relative order of the band gap energies (i.e., 1.45 vs 2.48 eV) and the direct vs indirect band structures as well. However, the absolute values for both polymorphs are surprisingly high for a semiconductor. Here the sample size, thickness, particle packing, grain boundaries, as well as the distortion of the FA cations may physically influence the electrical measurement.

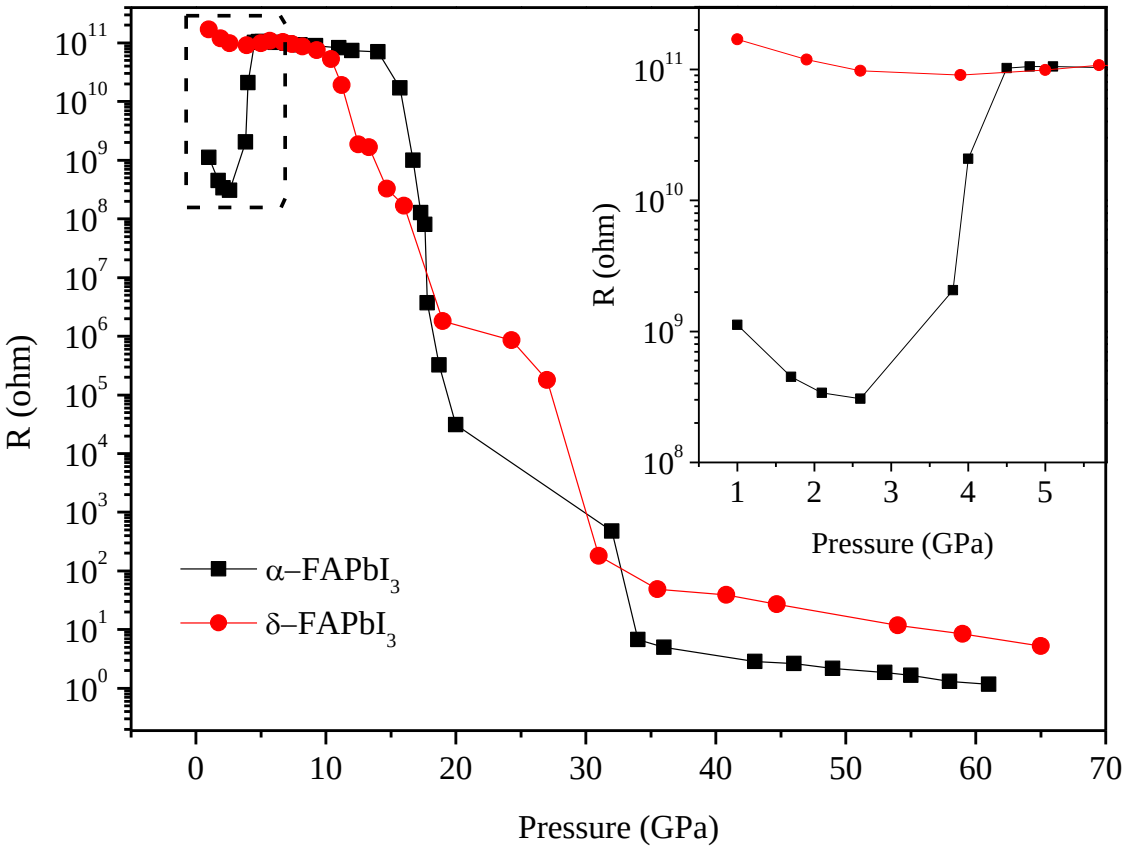

Figure 6.15 Electrical resistance of α- and δ-phase of $FAPbI_3$ as a function of pressure. The inset shows detailed comparison of the electrical resistance of α- and δ-phase of $FAPbI_3$ in the pressure region of 0-5 GPa.

www.manaraa.com

With increasing pressure, the resistance of α-$FAPbI_3$ reduced significantly to 3.1×10^8 Ohm at 2.6 GPa, but for δ-$FAPbI_3$, the reduction was minor (Figure 6.15 inset). The dramatic reduction in the former coincides with the structural transitions, while the minor change in the latter is a reflection of structural distortion to a less degree. For both cases, the pressure-induced reduction can be attributed to contraction of the PbI_6 octahedra. Upon compression to 4.5 GPa, the resistance of α-$FAPbI_3$ rapidly increased by 2 orders of magnitude followed by a plateau region until 15 GPa (11 GPa for δ-phase), where the conductivity was predominated by amorphization.[22] After that, the conductivity dramatically increased by over 9 orders of magnitude as a result of compression to around 35 GPa for both polymorphs, indicating the appearance of a metallic state. To verify this, we performed low-temperature measurements of resistance at different pressures (Figure 6.16). From the contrasting temperature dependence of resistance of semiconductors and metals, we can propose that the semiconductor-to-metal transitions for α- and δ-$FAPbI_3$ occur at 53 GPa and 41 GPa, respectively. The pressure-induced metallization of $FAPbI_3$ is consistent with theoretical predictions of monotonic decreasing band gap energies.

www.manaraa.com

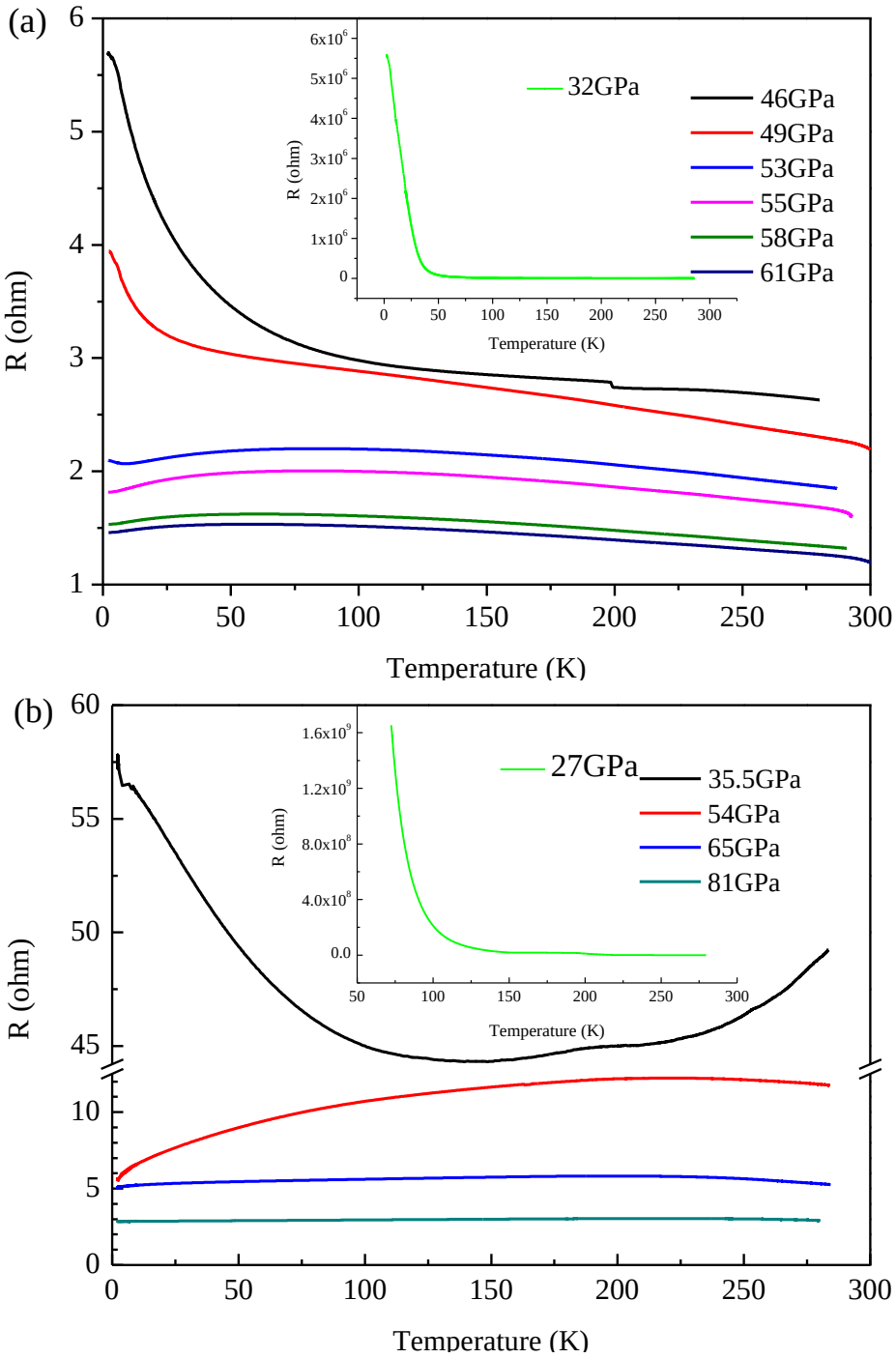

Figure 6.16 Temperature dependence of DC electrical resistance of α- (a) and δ- (b) phase $FAPbI_3$ measured at different pressures. The inset shows the DC electrical resistance of α (a) and δ (b) at 32 GPa and 27 GPa respectively.

www.manaraa.com

6.4 Conclusions and Summary

Overall, the XRD, IR, PL and electrical measurements collectively revealed contrasting stabilities of two polymorphs of $FAPbI_3$. The optical and electrical properties of α-$FAPbI_3$ are more susceptible to external compression, indicating lower stability compared to δ-$FAPbI_3$, which is consistent with reported relative chemical stabilities. In photovoltaic applications, pressure-tuned new polymorphs from promising precursors offer excellent opportunities to develop performance-improved devices. It would be particularly interesting to evaluate the pressure-modified materials (e.g., recovered *Imm*2 structure) in the fabrication of solar cell devices. Moreover, our observations suggest that although the FA cations have limited contribution to the properties, they influence the overall structural stability via cation-anion interactions topologically. So far, studies on perovskite materials are primarily focused on the mixed halide moiety in the form of $MAPbI_xBr_{3-x}$. It would be interesting to explore the possibility of mixing cations, such as $MA_xFA_{(1-x)}PbBr_3$ or $MA_xFA_{(1-x)}PbI_3$ for structural studies and photovoltaic applications.

In summary, we investigated structures and properties of $FAPbI_3$ in two polymorphs comparatively by using in situ synchrotron XRD, FTIR spectroscopy, PL spectroscopy, EC measurements, and ab initio simulations. We observed two phase transitions for α-$FAPbI_3$ at 0.3 and 1.7 GPa but only structural distortions for δ-$FAPbI_3$ upon compression. The new structures were identified using XRD with the assistance of MD simulations. The structural modifications in both polymorphs are strongly mediated by the hydrogen bond, as manifested by in situ FTIR spectroscopy unambiguously. The α-$FAPbI_3$ exhibits pressure-dependent PL activities revealing structure-regulated band gaps, which was excellently reproduced by DFT calculations. Finally, α- and δ-$FAPbI_3$ exhibit strongly contrasting pressure-regulated dc conductivities in the low-pressure region, but both approach to metallic states at high pressures. These observations suggest that external compression can not only reveal contrasting structural stabilities but effectively tune the optoelectric properties of both polymorphs. Our study thus provides valuable insight into the design and engineering of organolead halide perovskite-based solar cell materials.

www.manaraa.com

6.5 References

(1) Service, R. F. Perovskite solar cells keep on surging. *Science* **2014,** *344*, 458-458.

(2) Jeon, N. J.; Noh, J. H.; Yang, W. S.; Kim, Y. C.; Ryu, S.; Seo, J.; Seok, S. I. Compositional engineering of perovskite materials for high-performance solar cells. *Nature* **2015,** *517*, 476-480.

(3) Eperon, G. E.; Stranks, S. D.; Menelaou, C.; Johnston, M. B.; Herz, L. M.; Snaith, H. J. Formamidinium lead trihalide: A broadly tunable perovskite for efficient planar heterojunction solar cells. *Energy & Environmental Science* **2014,** *7*, 982-988.

(4) Saliba, M.; Matsui, T.; Seo, J. Y.; Domanski, K.; Correa-Baena, J. P.; Nazeeruddin, M. K.; Zakeeruddin, S. M.; Tress, W.; Abate, A.; Hagfeldt, A., et al. Cesium-containing triple cation perovskite solar cells: Improved stability, reproducibility and high efficiency. *Energy & Environmental Science* **2016,** *9*, 1989-1997.

(5) Zhou, H. P.; Chen, Q.; Li, G.; Luo, S.; Song, T. B.; Duan, H. S.; Hong, Z. R.; You, J. B.; Liu, Y. S.; Yang, Y. Interface engineering of highly efficient perovskite solar cells. *Science* **2014,** *345*, 542-546.

(6) Noh, J. H.; Im, S. H.; Heo, J. H.; Mandal, T. N.; Seok, S. I. Chemical management for colorful, efficient, and stable inorganic-organic hybrid nanostructured solar cells. *Nano Letters* **2013,** *13*, 1764-1769.

(7) Pang, S. P.; Hu, H.; Zhang, J. L.; Lv, S. L.; Yu, Y. M.; Wei, F.; Qin, T. S.; Xu, H. X.; Liu, Z. H.; Cui, G. L. $NH_2CH{=}NH_2PbI_3$: An alternative organolead iodide perovskite sensitizer for mesoscopic solar cells. *Chemistry of Materials* **2014,** *26*, 1485-1491.

(8) Grochala, W.; Hoffmann, R.; Feng, J.; Ashcroft, N. W. The chemical imagination at work in very tight places. *Angewandte Chemie International Edition* **2007,** *46*, 3620-3642.

www.manaraa.com

(9) Yang, W. S.; Noh, J. H.; Jeon, N. J.; Kim, Y. C.; Ryu, S.; Seo, J.; Seok, S. I. High-performance photovoltaic perovskite layers fabricated through intramolecular exchange. *Science* **2015,** *348*, 1234-1237.

(10) Capitani, F.; Marini, C.; Caramazza, S.; Postorino, P.; Garbarino, G.; Hanfland, M.; Pisanu, A.; Quadrelli, P.; Malavasi, L. High-pressure behavior of methylammonium lead iodide ($MAPbI_3$) hybrid perovskite. *Journal of Applied Physics* **2016,** *119*, 185901.

(11) Stoumpos, C. C.; Malliakas, C. D.; Kanatzidis, M. G. Semiconducting tin and lead iodide perovskites with organic cations: Phase transitions, high mobilities, and near-infrared photoluminescent properties. *Inorganic Chemistry* **2013,** *52*, 9019-9038.

(12) Wang, Z. W.; Zhou, Y. Y.; Pang, S. P.; Xiao, Z. W.; Zhang, J. L.; Chai, W. Q.; Xu, H. X.; Liu, Z. H.; Padture, N. P.; Cui, G. L. Additive-modulated evolution of $HC(NH_2)_2PbI_3$ black polymorph for mesoscopic perovskite solar cells. *Chemistry of Materials* **2015,** *27*, 7149-7155.

(13) Weller, M. T.; Weber, O. J.; Frost, J. M.; Walsh, A. Cubic perovskite structure of black formamidinium lead iodide, α-$[HC(NH_2)_2]PbI_3$, at 298 K. *Journal of Physical Chemistry Letters* **2015,** *6*, 3209-3212.

(14) Jaffe, A.; Lin, Y.; Beavers, C. M.; Voss, J.; Mao, W. L.; Karunadasa, H. I. High-pressure single-crystal structures of 3D lead-halide hybrid perovskites and pressure effects on their electronic and optical properties. *Acs Central Science* **2016,** *2*, 201-209.

(15) Wang, L. R.; Wang, K.; Zou, B. Pressure-induced structural and optical properties of organometal halide perovskite-based formamidinium lead bromide. *Journal of Physical Chemistry Letters* **2016,** *7*, 2556-2562.

(16) Jiang, S. J.; Fang, Y. A.; Li, R. P.; Xiao, H.; Crowley, J.; Wang, C. Y.; White, T. J.; Goddard, W. A.; Wang, Z. W.; Baikie, T., et al. Pressure-dependent polymorphism and band-gap tuning of methylammonium lead iodide perovskite. *Angewandte Chemie International Edition* **2016,** *55*, 6540-6544.

www.manaraa.com

(17) Ou, T. J.; Yan, J. J.; Xiao, C. H.; Shen, W. S.; Liu, C. L.; Liu, X. Z.; Han, Y. H.; Ma, Y. Z.; Gao, C. X. Visible light response, electrical transport, and amorphization in compressed organolead iodine perovskites. *Nanoscale* **2016,** *8*, 11426-11431.

(18) Szafranski, M.; Katrusiak, A. Mechanism of pressure-induced phase transitions, amorphization, and absorption-edge shift in photovoltaic methylammonium lead iodide. *Journal of Physical Chemistry Letters* **2016,** *7*, 3458-3466.

(19) Wang, K.; Liu, R.; Qiao, Y.; Cui, J.; Song, B.; Liu, B.; Zou, B. Pressure-induced reversible phase transition and amorphization of $CH_3NH_3PbI_3$. *Acta Physica Sinica* **2017,** *66*, 030701.

(20) Lee, Y.; Mitzi, D. B.; Barnes, P. W.; Vogt, T. Pressure-induced phase transitions and templating effect in three-dimensional organic-inorganic hybrid perovskites. *Physical Review B* **2003,** *68*, 020103.

(21) Swainson, I. P.; Tucker, M. G.; Wilson, D. J.; Winkler, B.; Milman, V. Pressure response of an organic-inorganic perovskite: Methylammonium lead bromide. *Chemistry of Materials* **2007,** *19*, 2401-2405.

(22) Wang, Y. H.; Lu, X. J.; Yang, W. G.; Wen, T.; Yang, L. X.; Ren, X. T.; Wang, L.; Lin, Z. S.; Zhao, Y. S. Pressure-induced phase transformation, reversible amorphization, and anomalous visible light response in organolead bromide perovskite. *Journal of the American Chemical Society* **2015,** *137*, 11144-11149.

(23) Lü, X.; Wang, Y.; Stoumpos, C. C.; Hu, Q.; Guo, X.; Chen, H.; Yang, L.; Smith, J. S.; Yang, W.; Zhao, Y. Enhanced structural stability and photo responsiveness of $CH_3NH_3SnI_3$ perovskite via pressure-induced amorphization and recrystallization. *Advanced Materials* **2016,** *28*, 8663-8668.

(24) Matsuishi, K.; Ishihara, T.; Onari, S.; Chang, Y.; Park, C. Optical properties and structural phase transitions of lead-halide based inorganic-organic 3D and 2D perovskite semiconductors under high pressure. *Physica Status Solidi B* **2004,** *241*, 3328-3333.

www.manaraa.com

(25) Li, Q.; Li, S. R.; Wang, K.; Quan, Z. W.; Meng, Y.; Zou, B. High-pressure study of perovskite-like organometal halide: Band-gap narrowing and structural evolution of $[NH_3\text{-}(CH_2)_4\text{-}NH_3]CuCl_4$. *Journal of Physical Chemistry Letters* **2017,** *8*, 500-506.

(26) Wang, L. R.; Wang, K.; Xiao, G. J.; Zeng, Q. S.; Zou, B. Pressure-induced structural evolution and band gap shifts of organometal halide perovskite-based methylammonium lead chloride. *Journal of Physical Chemistry Letters* **2016,** *7*, 5273-5279.

(27) Jaffe, A.; Lin, Y.; Mao, W. L.; Karunadasa, H. I. Pressure-induced conductivity and yellow-to-black piezochromism in a layered Cu-Cl hybrid perovskite. *Journal of the American Chemical Society* **2015,** *137*, 1673-1678.

(28) Liu, G.; Kong, L. P.; Gong, J.; Yang, W. G.; Mao, H. K.; Hu, Q. Y.; Liu, Z. X.; Schaller, R. D.; Zhang, D. Z.; Xu, T. Pressure-induced bandgap optimization in lead-based perovskites with prolonged carrier lifetime and ambient retainability. *Advanced Functional Materials* **2017,** *27*, 1604208.

(29) Wozny, S.; Yang, M. J.; Nardes, A. M.; Mercado, C. C.; Ferrere, S.; Reese, M. O.; Zhou, W. L.; Zhu, K. Controlled humidity study on the formation of higher efficiency formamidinium lead triiodide-based solar cells. *Chemistry of Materials* **2015,** *27*, 4814-4820.

(30) Kresse, G.; Joubert, D. From ultrasoft pseudopotentials to the projector augmented-wave method. *Physical Review B* **1999,** *59*, 1758-1775.

(31) Kresse, G.; Hafner, J. Abinitio molecular-dynamics for liquid-metals. *Physical Review B* **1993,** *47*, 558-561.

(32) Koh, T. M.; Fu, K. W.; Fang, Y. N.; Chen, S.; Sum, T. C.; Mathews, N.; Mhaisalkar, S. G.; Boix, P. P.; Baikie, T. Formamidinium-containing metal-halide: An alternative material for near-IR absorption perovskite solar cells. *Journal of Physical Chemistry C* **2014,** *118*, 16458-16462.

www.manaraa.com

(33) Zhou, L.; Shinde, N.; Hu, A. G.; Cook, C.; Murugesu, M.; Song, Y. Structural tuning of energetic material bis(1H-tetrazol-5-yl)amine monohydrate under pressures probed by vibrational spectroscopy and X-ray diffraction. *Journal of Physical Chemistry C* **2014,** *118*, 26504-26512.

www.manaraa.com

Chapter 7

7 Summary and future work

7.1 Summary

Energy storage materials have attracted increasing attention due to the environmental concerns and the reducing energy reserves, such as hydrogen storage materials and perovskite solar cell materials. Much progress has been made to develop new materials and improve their properties in the recent years. Moreover, pressure has been widely used as a powerful tool in the discovery of new materials with peculiar structures and properties. Therefore, applying high pressure on energy storage materials will provide a unique chance to reveal the pressure-induced phase transitions and the modified properties of these materials. In this thesis, we used in-situ high-pressure vibrational spectroscopy and synchrotron radiation to examine the structural stability of three hydrogen storage materials ($NaNH_2BH_3$, $N_2H_4BH_3$ and $BH_3NH_2CH_2CH_2NH_2BH_3$) and solar cell material $FAPbI_3$. Furthermore, the evolution of intermolecular interactions of all materials and pressure-tuned properties of $FAPbI_3$ were also investigated under high pressure.

In chapter 3, $NaNH_2BH_3$ was synthesized by ball-milling method. Two phase transitions were identified at around 1.0 and 2.7 GPa by IR, Raman spectroscopy and synchrotron XRD. The first phase transition is an isostructural phase transition with the different orientation of the $NaNH_2BH_3$ molecules. While the second phase transition is a major structural transformation from orthorhombic to monoclinic. The crystal structures of two new phases are proposed to be *Pbca* and $P2_1/c$. The pressure-induced phase transition is irreversible because the recovered phase exhibits a profile similar to phase II. Moreover, the N-H stretching bands of $NaNH_2BH_3$ were observed to be blue-shifted, indicating the absence of dihydrogen bonds in the structure of $NaNH_2BH_3$. Finally, the electrostatic interaction between Na^+ and $(NH_2BH_3)^-$ plays an important role to stabilize the structure of $NaNH_2BH_3$.

www.manaraa.com

In chapter 4, $N_2H_4BH_3$ was synthesized by wet-chemistry method. No phase transition was observed upon compression to near 20 GPa, indicating the high stability of the structure. In contrast to other B-N compounds, dihydrogen bonding in HB exhibits blueshift during the compression, which could be explained by the rearrangement of the dihydrogen bonding in the network of the structure.

In chapter5, another hydrogen storage material EDAB was investigated under high pressure by IR spectroscopy, Raman spectroscopy and synchrotron XRD. Two phase transitions were observed at around 1.0 and 7.0 GPa. The new phase were proposed to be *P*2/*c* and *Pmmm*. Our analysis suggests that the motion of the molecules and the rearrangement of the dihydrogen bonding should be responsible for the phase transitions. The pressure-induced dihydrogen bonding enhancement was also observed during the compression. The pressure-induced phase transitions is mostly reversible with slight modifications.

In chapter 6, $FAPbI_3$ perovskite was investigated in two polymorphs at high pressures using *in situ* synchrotron X-ray diffraction, FTIR spectroscopy, photoluminescence (PL) spectroscopy, electrical conductivity (EC) measurements, and *ab initio* calculations. We identified two new structures (i.e., *Imm*2 and *Immm*) for α-$FAPbI_3$, but only a structural distortion (in *C*2/*c*) for δ-$FAPbI_3$ on compression. Pressure-enhanced hydrogen bond plays a prominent role in structural modifications, as corroborated by FTIR spectroscopy. PL measurements and calculations consistently show pressure-tuned bandgap energies. Finally, EC measurements reveal drastically different transport properties of α and δ $FAPbI_3$ at low pressures, but a common trend to metallic states at high pressures. All these observations suggest strongly contrasting structural stabilities and pressure-tuned optoelectric properties of the two $FAPbI_3$ polymorphs.

Therefore, our studies provide insights into the pressure-tuned structures and properties of the materials. The structures and intermolecular interaction of these energy storage materials could be effectively tuned under high pressure, which could shed light on the designing of the new hydrogen storage material by substituting the hydrogen atoms on either B or N atoms to modify the reactivity of B-H and N-H bonds. Finally, our

www.manaraa.com

investigation provides valuable insight into the design and engineering of perovskite-based solar cell materials.

7.2 Future work

For the hydrogen storage materials, it would be particularly interesting to study the hydrogen containing complex under high pressure. As introduced in Chapter 1, the formation of NH_3BH_3-H_2 complex would inspire the synthesis of more such materials under high pressure.[1] These novel complexes can store a substantial amount of extra hydrogen. Therefore, investigating the possibility of synthesizing hydrogen containing complexes, such as NaAB-H_2, HB-H_2 and EDAB-H_2 under high pressure can further enhance the understanding of the structures of these materials, leading to the formation of more hydrogen containing complexes. Moreover, theoretical calculations can greatly help us to understand the origin of the phase transitions and the behavior of dihydrogen bonding of these materials under high pressure.

On the other hand, the studies on perovskite materials are primarily focused on the mixed halide moiety in the form of $MAPbI_xBr_{3-x}$. It would be interesting to explore the possibility of mixing cations, such as $MA_xFA_{(1-x)}PbBr_3$ or $MA_xFA_{(1-x)}PbI_3$ for structural studies and photovoltaic applications. Moreover, the environmental concern of heavy metal content of organic lead halide have led to the design of new metal-halide perovskite materials, such as $CsSnX_3$ (X = Cl, $Cl_{0.5}Br_{0.5}$, Br, $Br_{0.5}I_{0.5}$, I).[2] Therefore, the development of Sn- and Sb-based perovskites will offer new insights into the suitability of these materials for PV applications.

7.3 References

(1) Lin, Y.; Mao, W. L.; Mao, H.-k. Storage of molecular hydrogen in an ammonia borane compound at high pressure. *Proceedings of the National Academy of Sciences* **2009,** *106*, 8113-8116.

(2) Jellicoe, T. C.; Richter, J. M.; Glass, H. F.; Tabachnyk, M.; Brady, R.; Dutton, S. n. E.; Rao, A.; Friend, R. H.; Credgington, D.; Greenham, N. C. Synthesis and optical

www.manaraa.com

properties of lead-free cesium tin halide perovskite nanocrystals. *Journal of the American Chemical Society* **2016,** *138,* 2941-2944.

www.manaraa.com

Appendix A Refinement results of NaAB

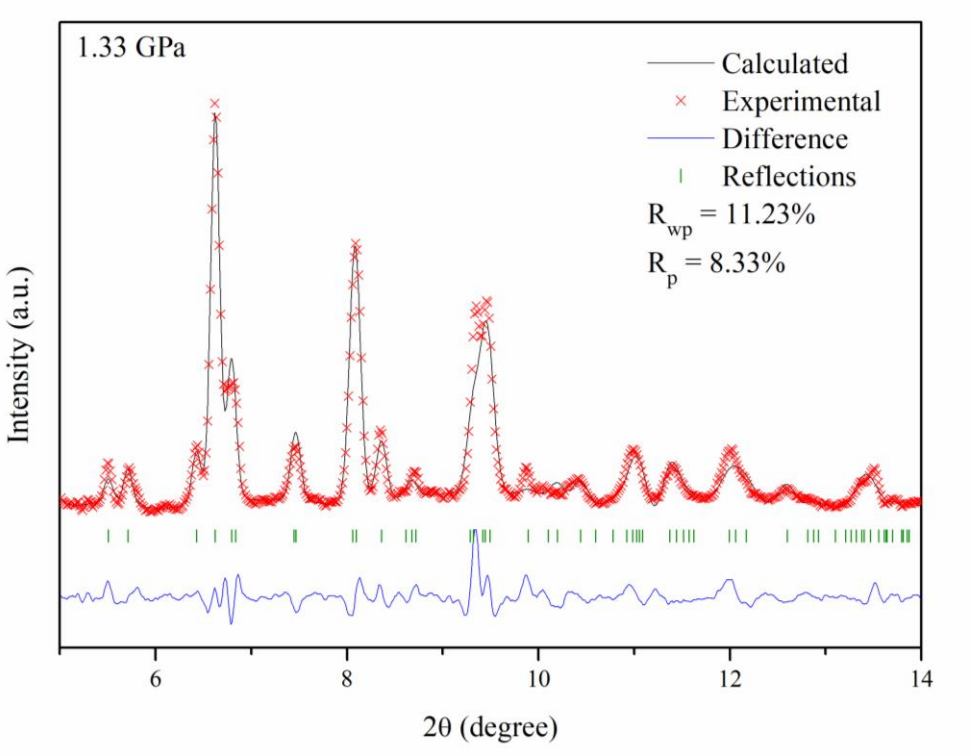

Figure A 1 Calculated XRD pattern in comparison with experimental results of NaAB at 1.33 GPa using Rietveld refinement

www.manaraa.com

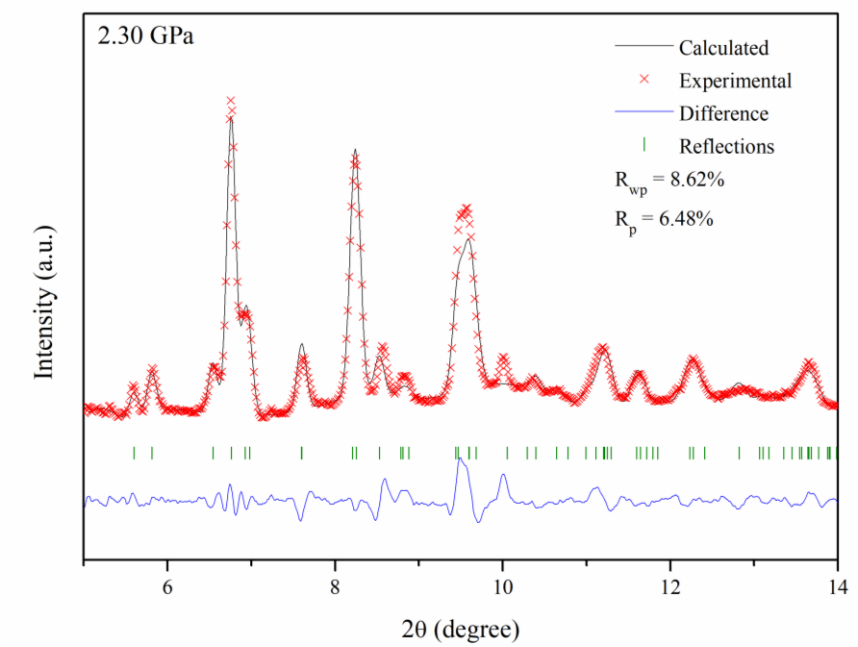

Figure A 2 Calculated XRD pattern in comparison with experimental results of NaAB at 2.30 GPa using Rietveld refinement

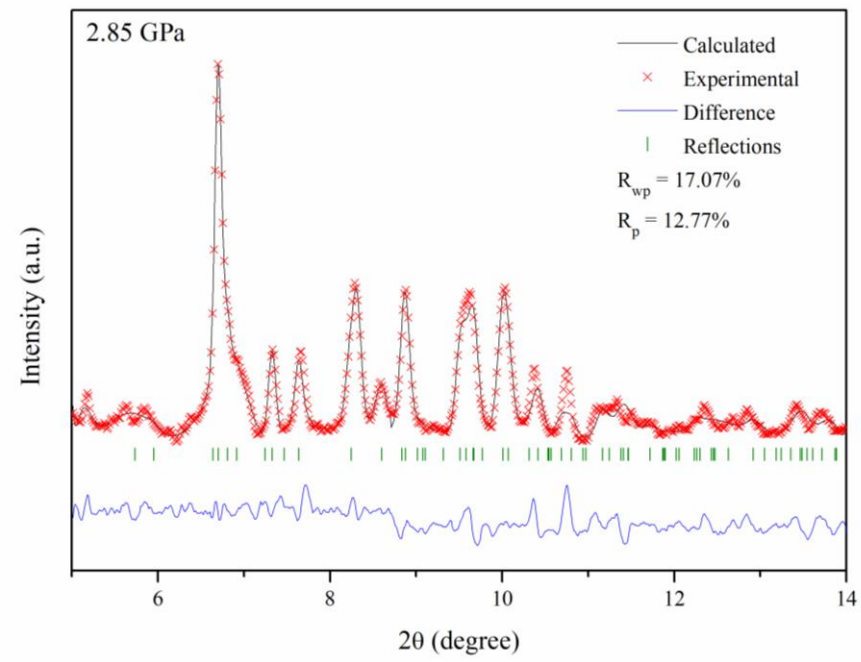

Figure A 3 Calculated XRD pattern in comparison with experimental results of NaAB at 2.85 GPa using Rietveld refinement

www.manaraa.com

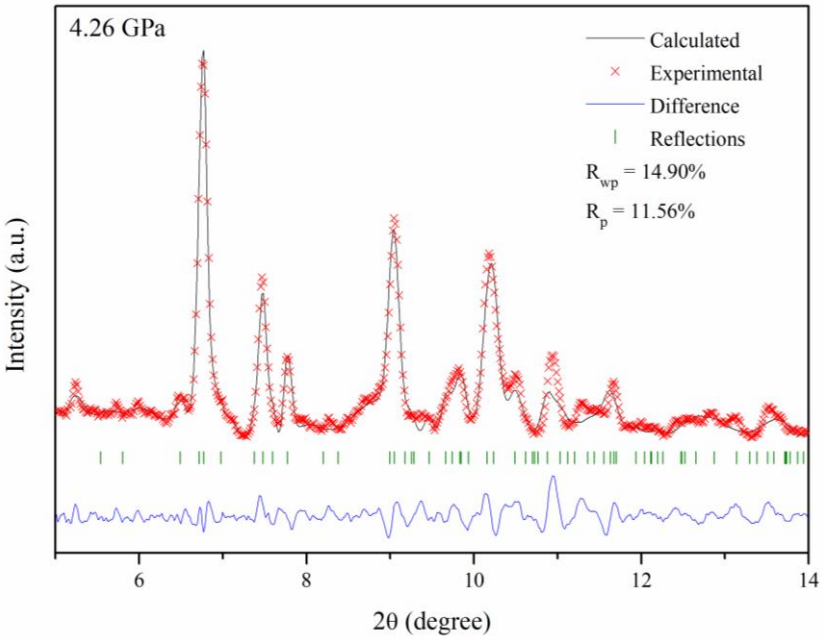

Figure A 4 Calculated XRD pattern in comparison with experimental results of NaAB at 4.26 GPa using Rietveld refinement

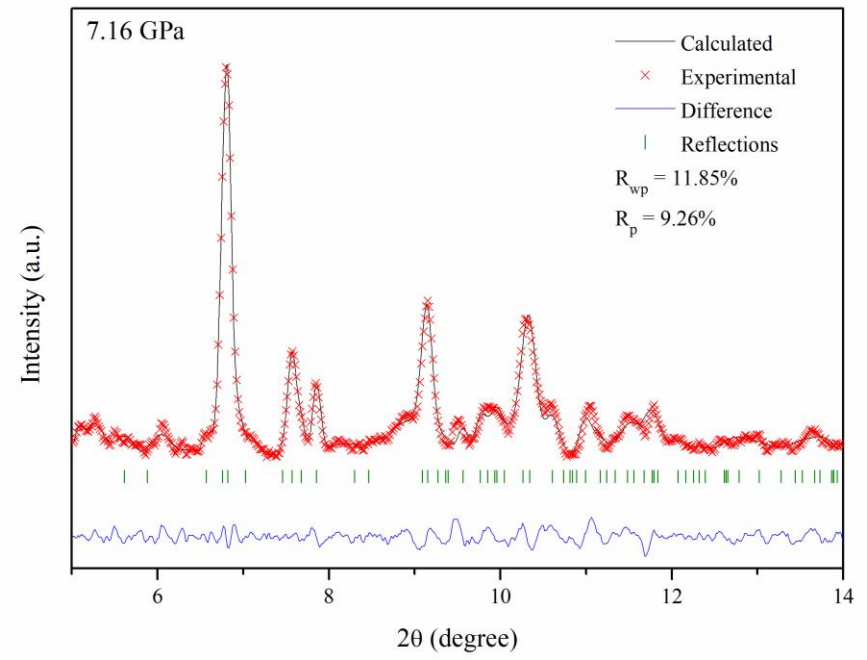

Figure A 5 Calculated XRD pattern in comparison with experimental results of NaAB at 7.16 GPa using Rietveld refinement

www.manaraa.com

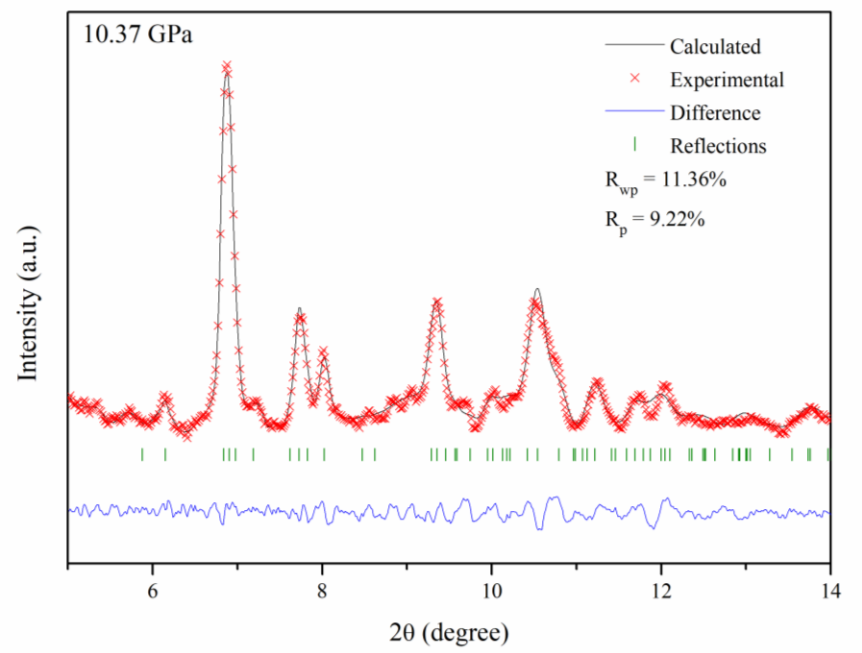

Figure A 6 Calculated XRD pattern in comparison with experimental results of NaAB at 10.37 GPa using Rietveld refinement

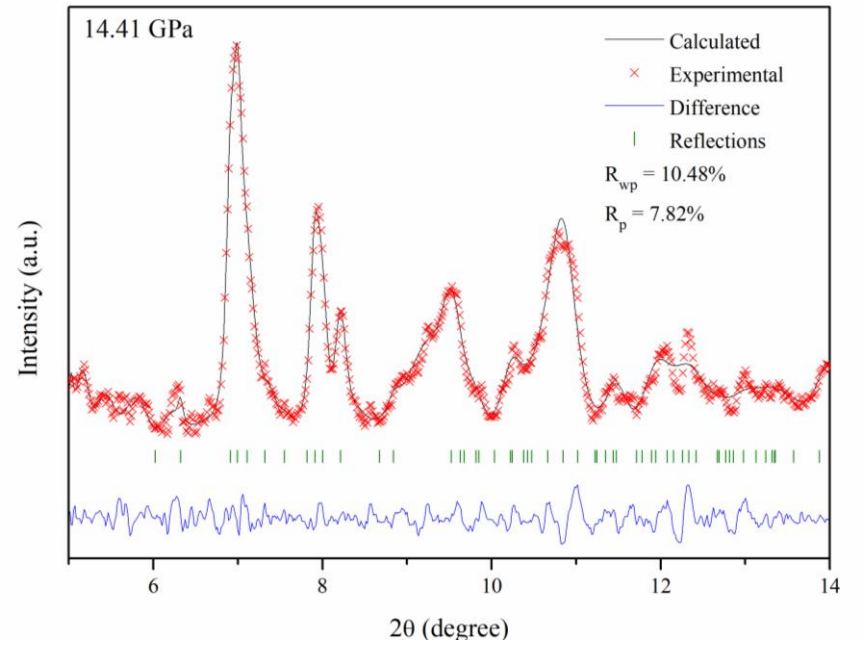

Figure A 7 Calculated XRD pattern in comparison with experimental results of NaAB at 14.41 GPa using Rietveld refinement

www.manaraa.com

Appendix B Refinement results of HB

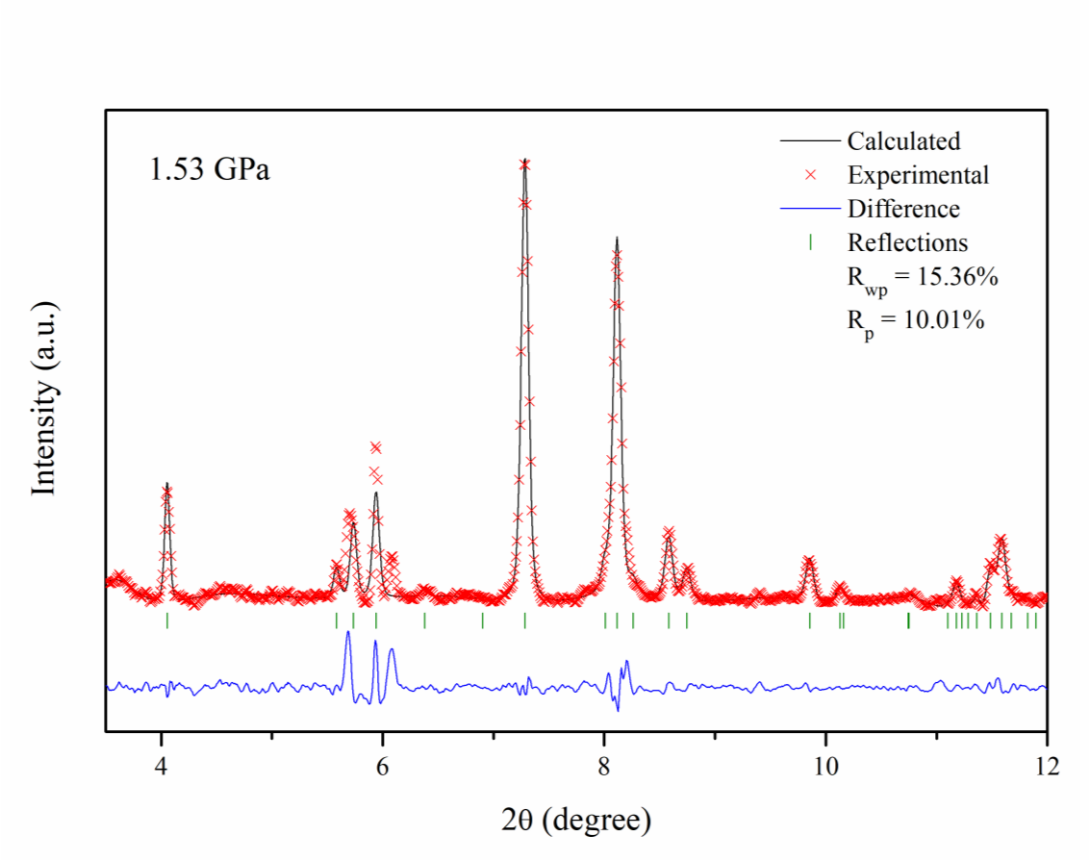

Figure B 1 Calculated XRD pattern in comparison with experimental results of HB at 1.53 GPa using Le Bail refinement

www.manaraa.com

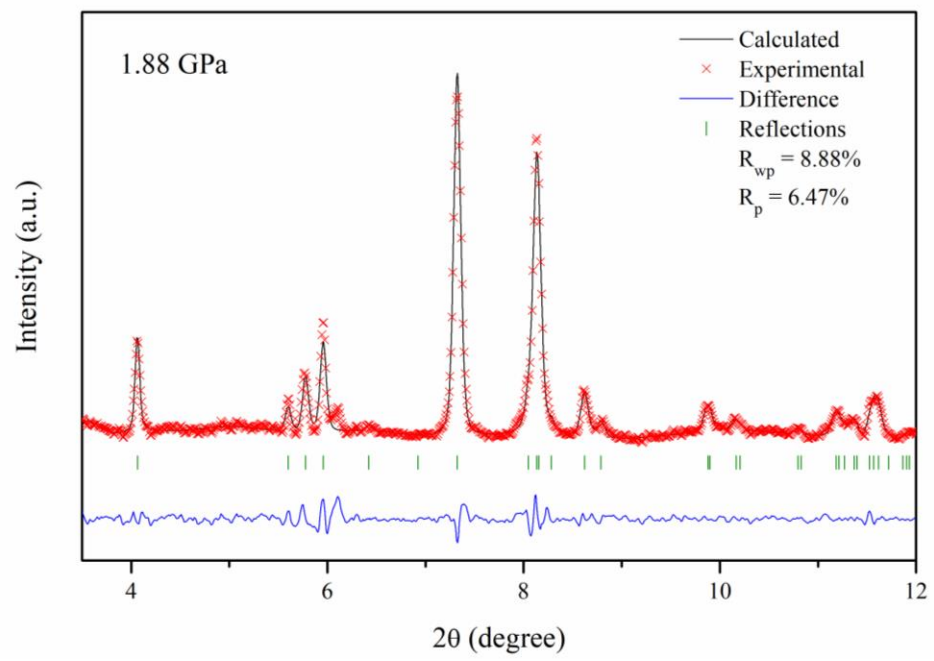

Figure B 2 Calculated XRD pattern in comparison with experimental results of HB at 1.88 GPa using Le Bail refinement

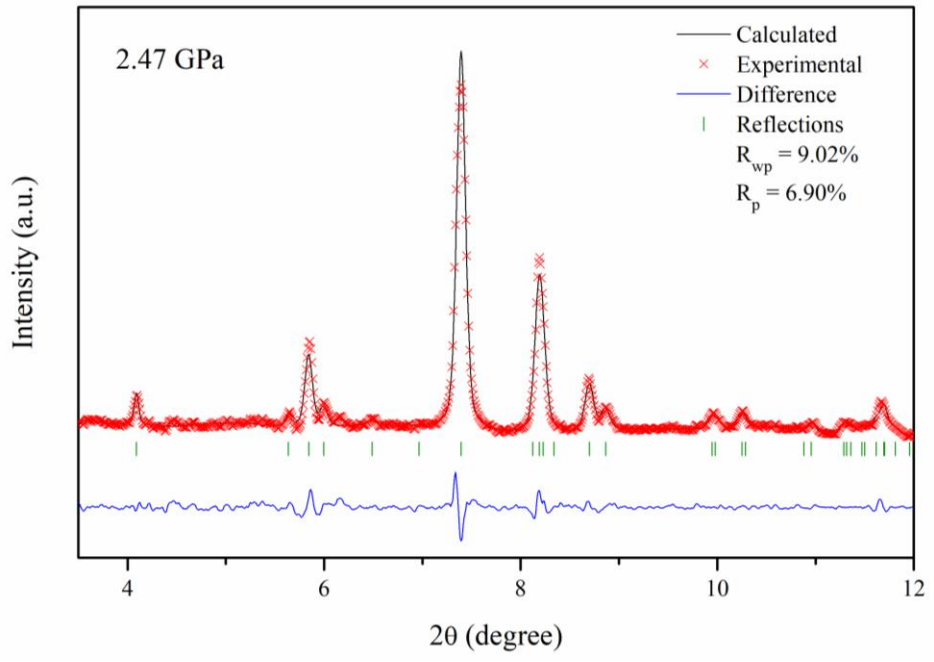

Figure B 3 Calculated XRD pattern in comparison with experimental results of HB at 2.47 GPa using Le Bail refinement

www.manaraa.com

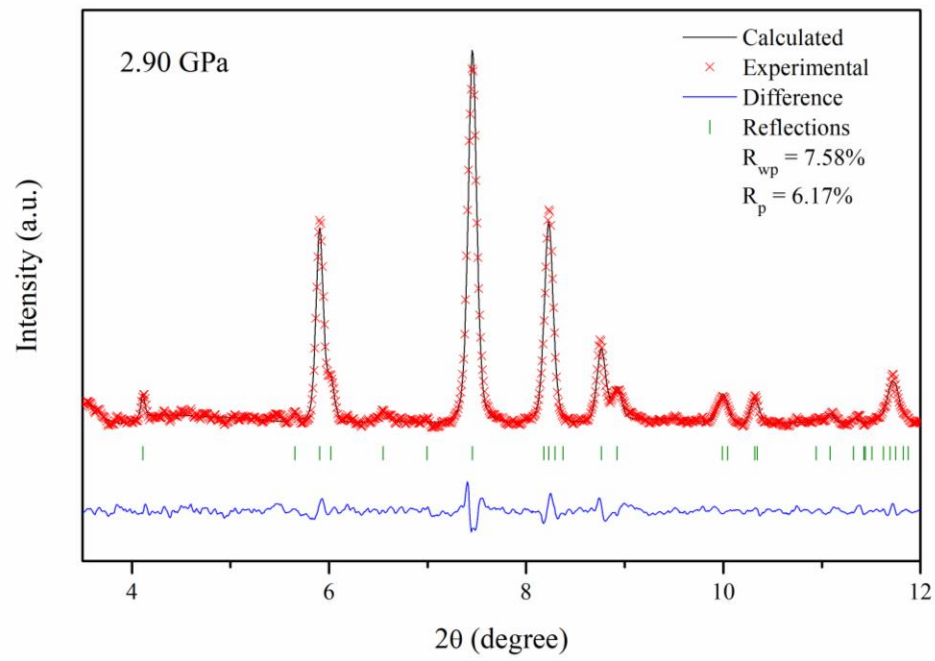

Figure B 4 Calculated XRD pattern in comparison with experimental results of HB at 2.90 GPa using Le Bail refinement

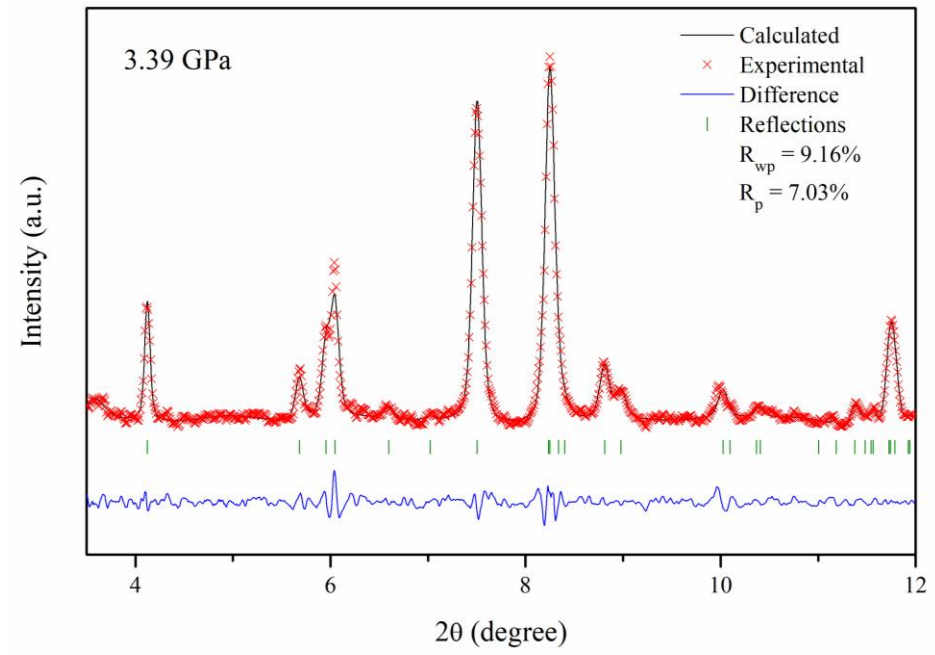

Figure B 5 Calculated XRD pattern in comparison with experimental results of HB at 3.39 GPa using Le Bail refinement

www.manaraa.com

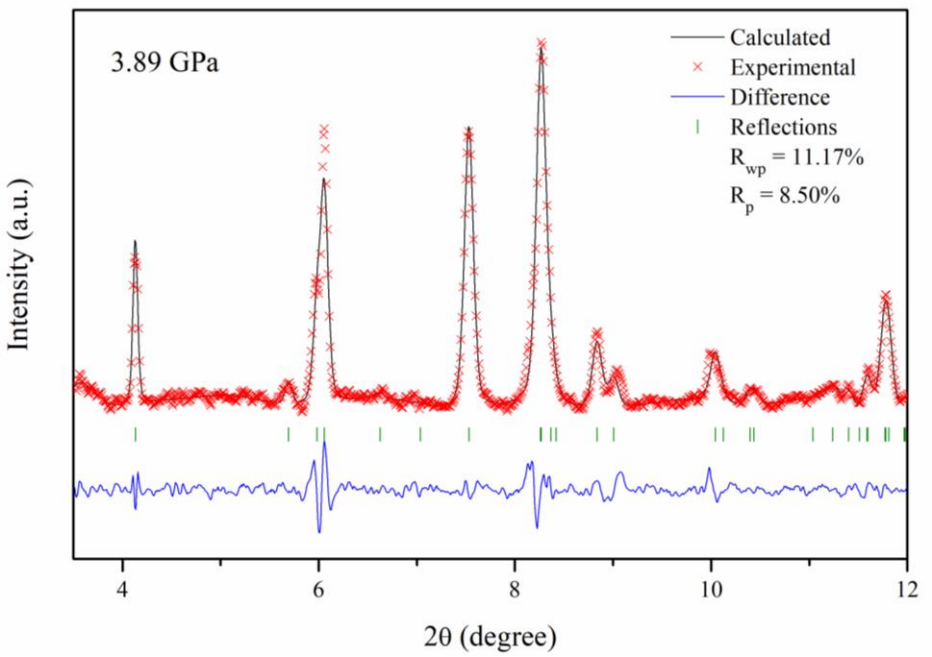

Figure B 6 Calculated XRD pattern in comparison with experimental results of HB at 3.89 GPa using Le Bail refinement

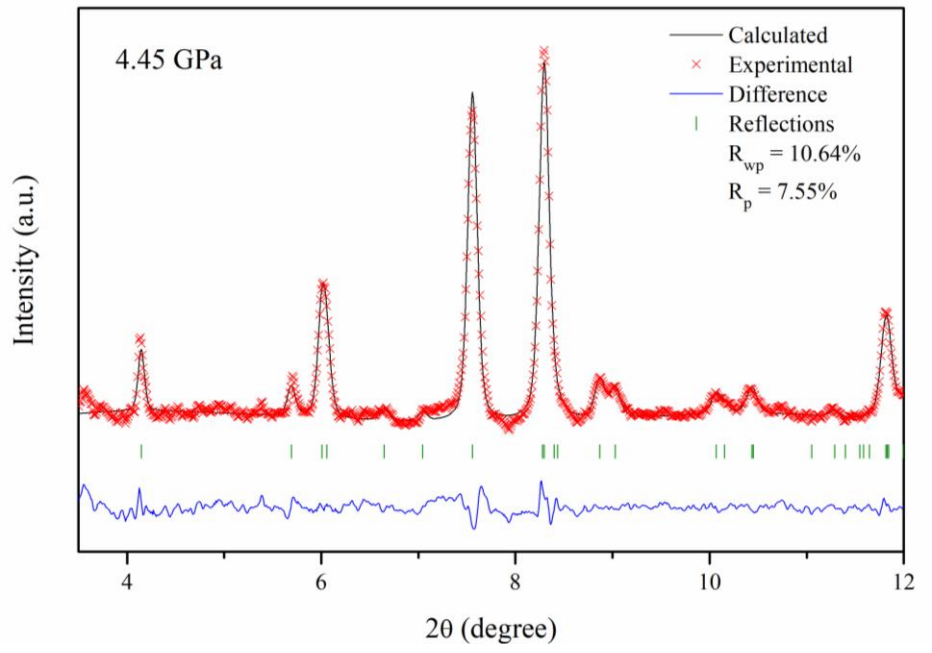

Figure B 7 Calculated XRD pattern in comparison with experimental results of HB at 4.45 GPa using Le Bail refinement

www.manaraa.com

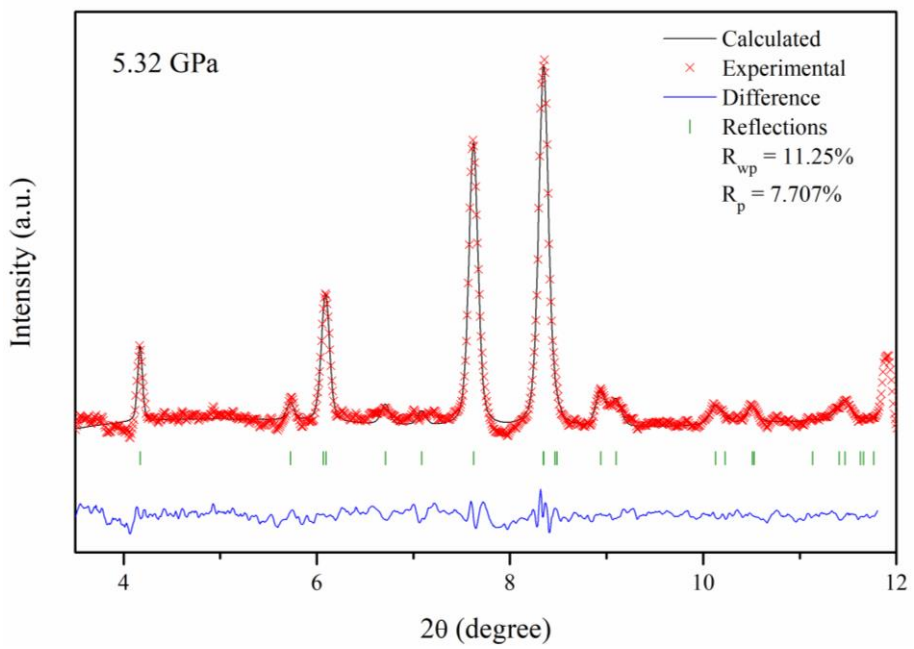

Figure B 8 Calculated XRD pattern in comparison with experimental results of HB at 5.32 GPa using Le Bail refinement

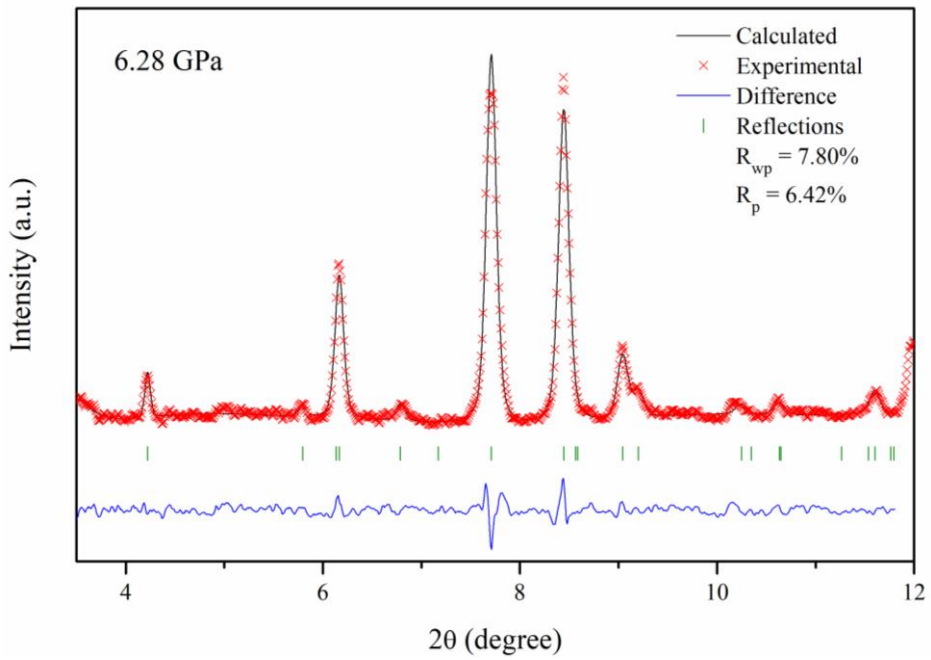

Figure B 9 Calculated XRD pattern in comparison with experimental results of HB at 6.28 GPa using Le Bail refinement

www.manaraa.com

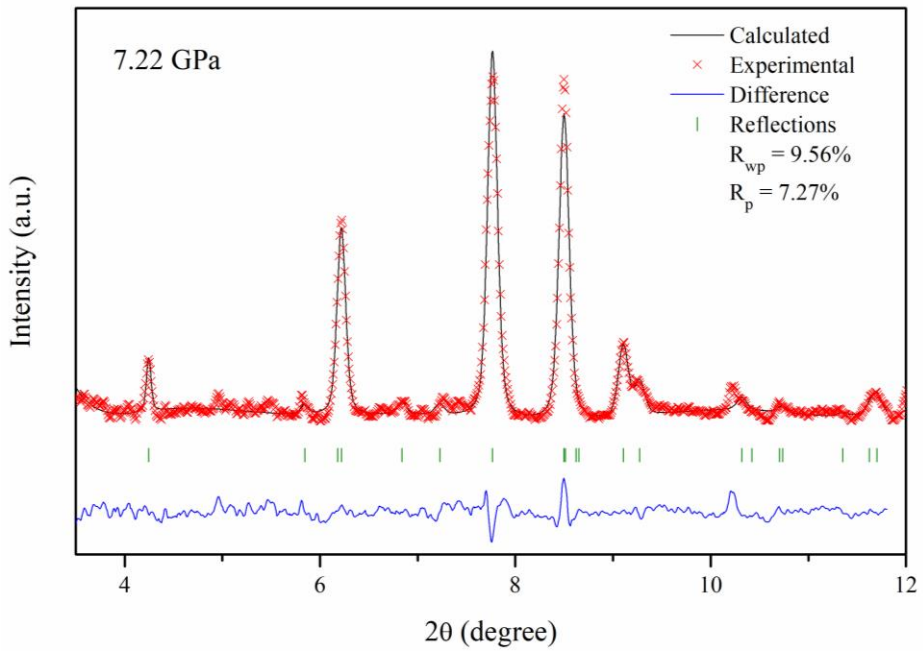

Figure B 10 Calculated XRD pattern in comparison with experimental results of HB at 7.22 GPa using Le Bail refinement

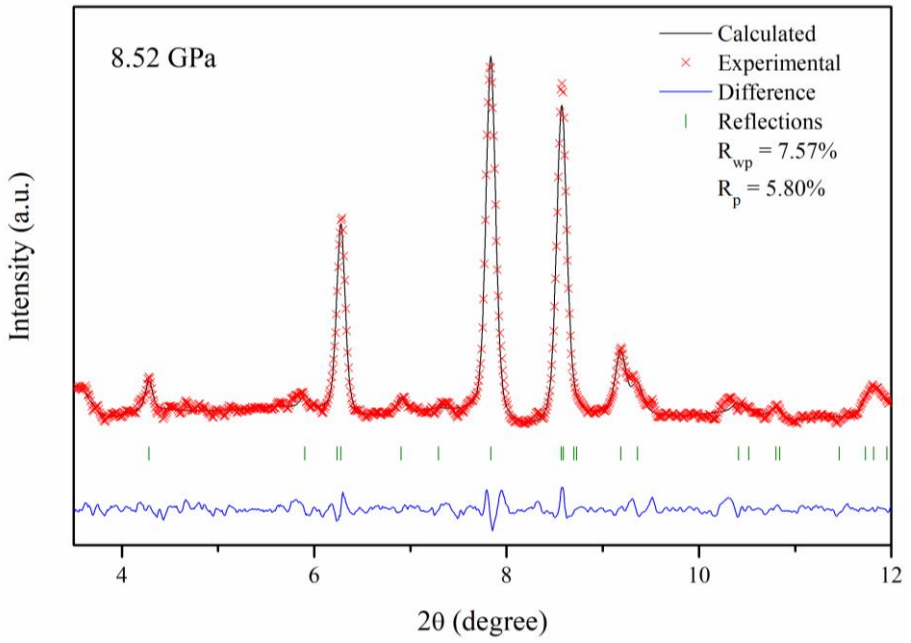

Figure B 11 Calculated XRD pattern in comparison with experimental results of HB at 8.52 GPa using Le Bail refinement

www.manaraa.com

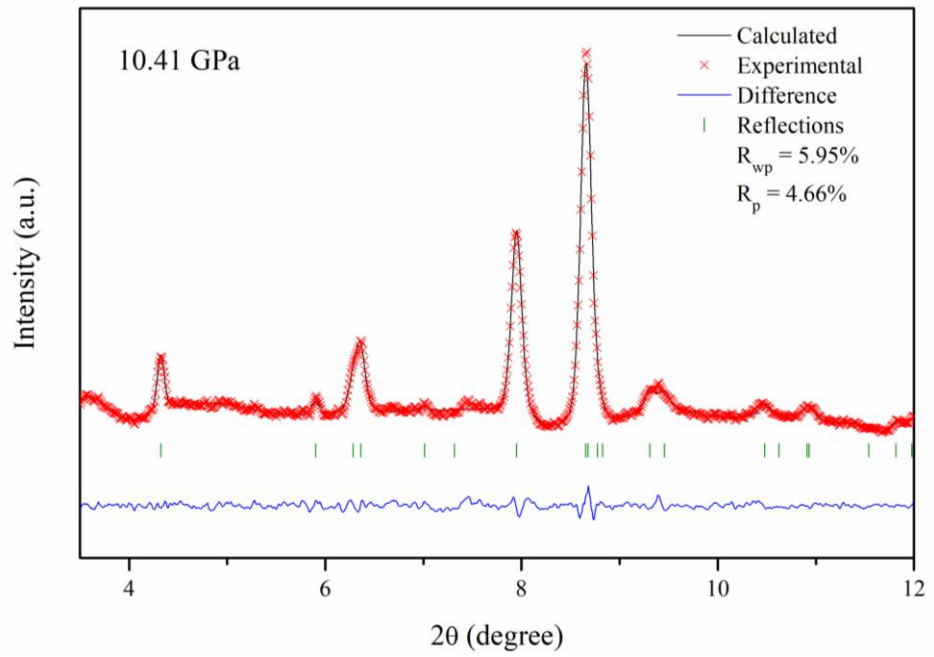

Figure B 12 Calculated XRD pattern in comparison with experimental results of HB at 10.41 GPa using Le Bail refinement

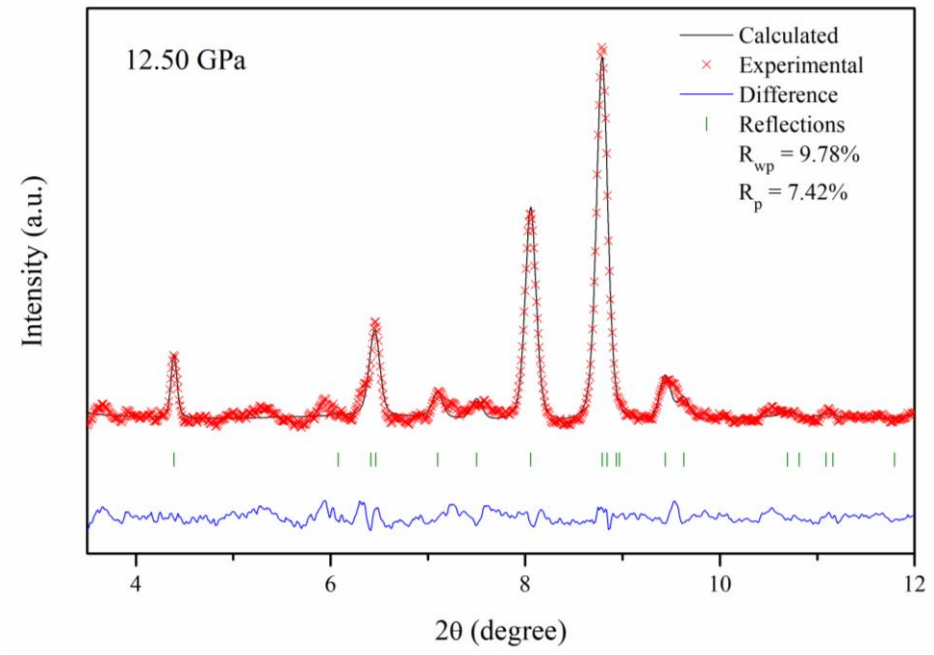

Figure B 13 Calculated XRD pattern in comparison with experimental results of HB at 12.50 GPa using Le Bail refinement

www.manaraa.com

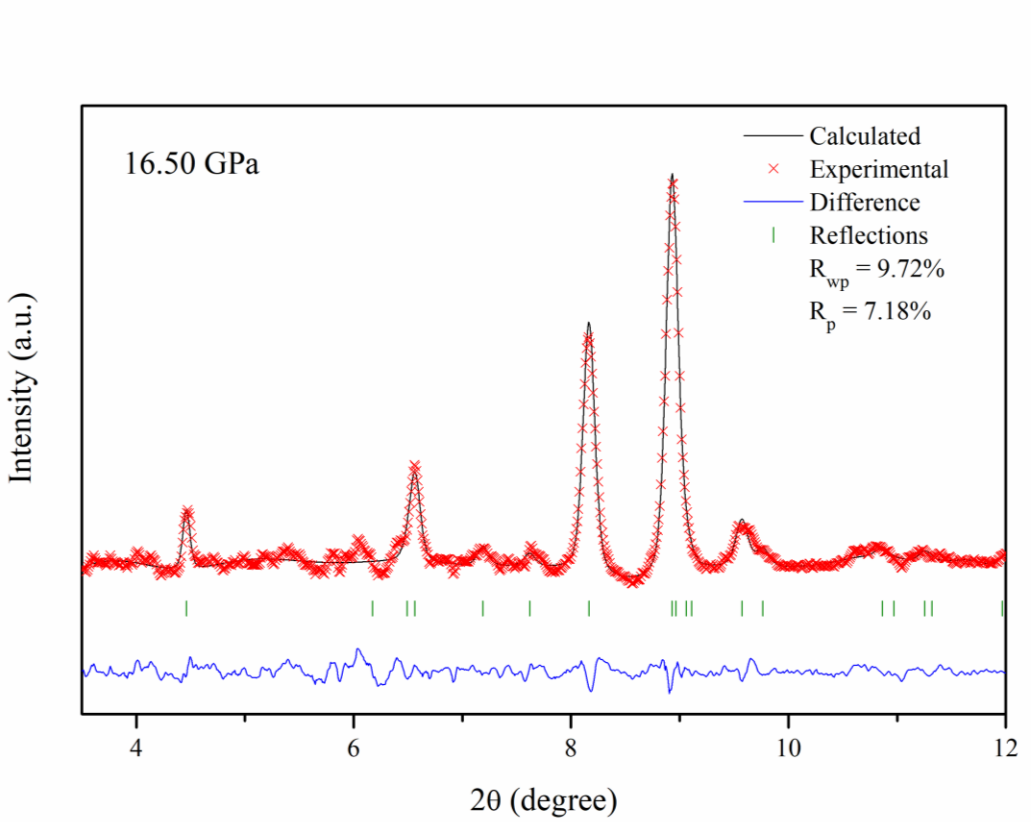

Figure B 14 Calculated XRD pattern in comparison with experimental results of HB at 16.50 GPa using Le Bail refinement

www.manaraa.com

Appendix C Refinement results of EDAB

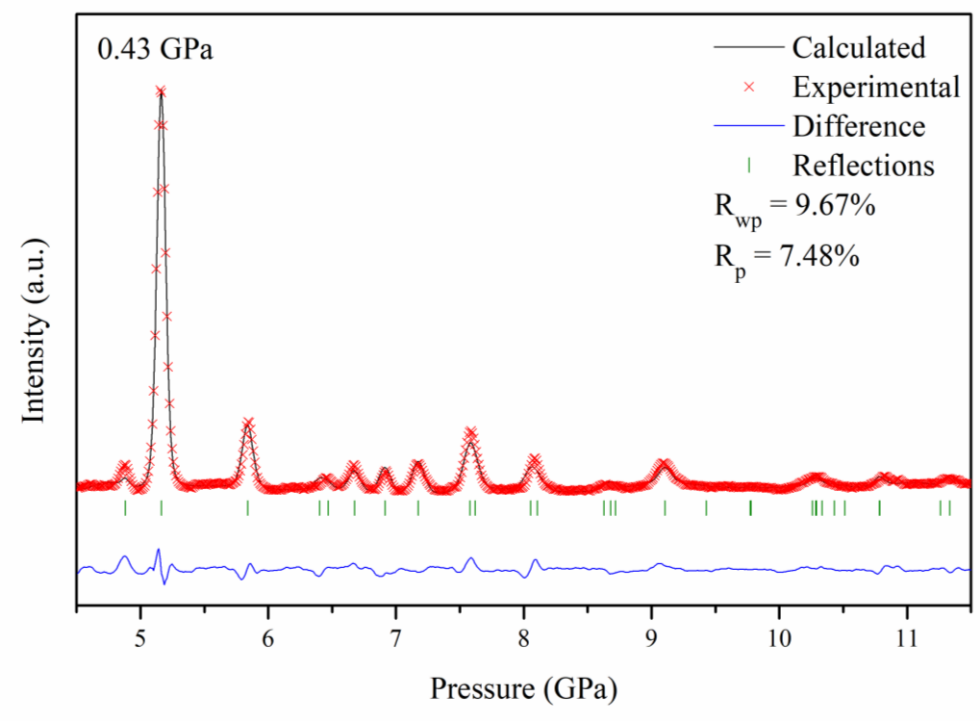

Figure C 1 Calculated XRD pattern in comparison with experimental results of EDAB at 0.43 GPa using Rietveld refinement

www.manaraa.com

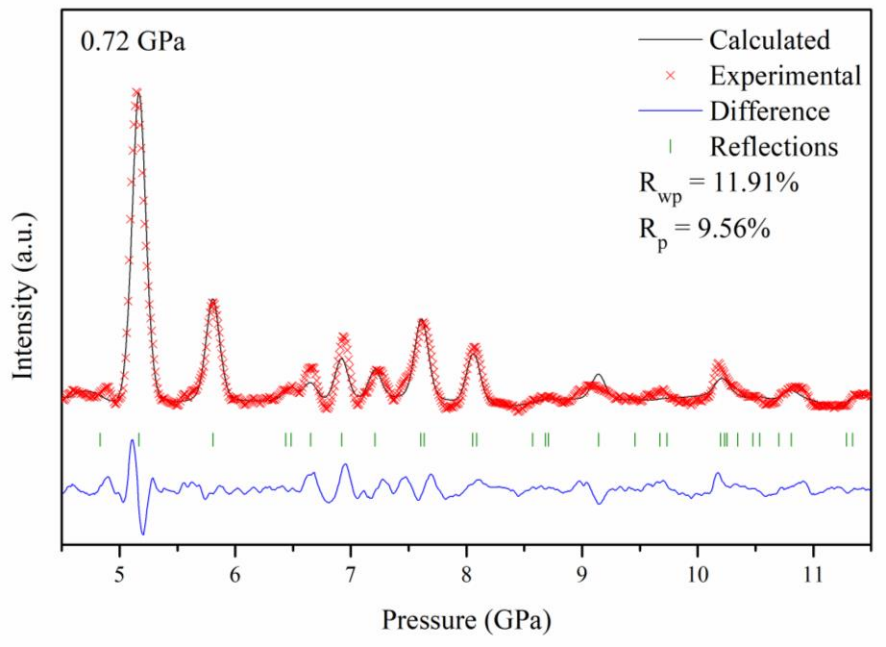

Figure C 2 Calculated XRD pattern in comparison with experimental results of EDAB at 0.72 GPa using Rietveld refinement

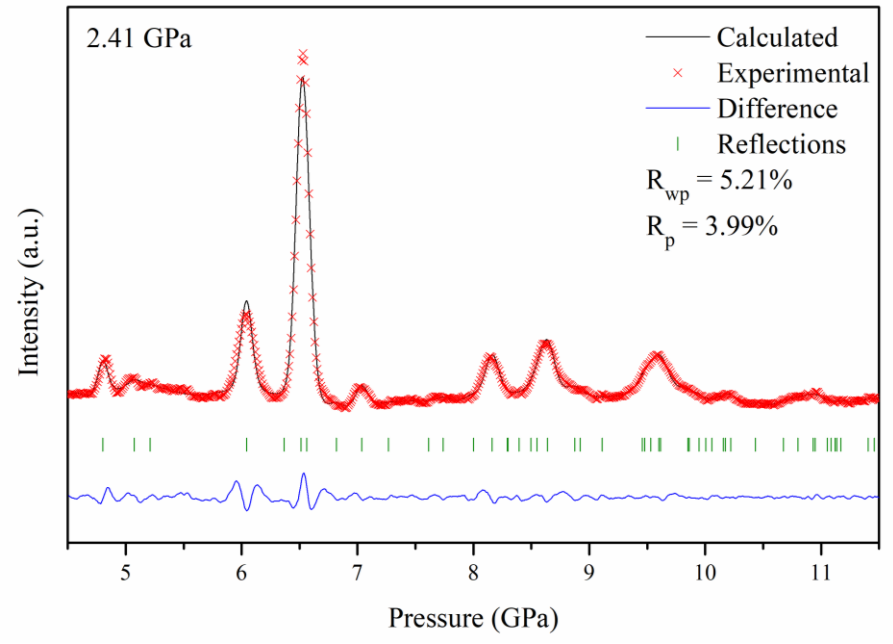

Figure C 3 Calculated XRD pattern in comparison with experimental results of EDAB at 2.41 GPa using Le Bail refinement

www.manaraa.com

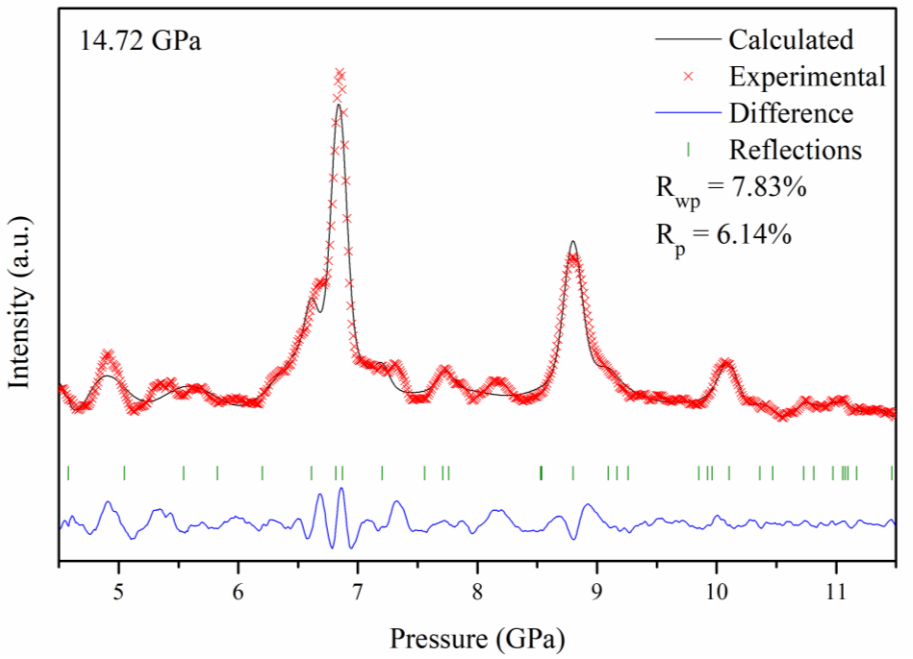

Figure C 4 Calculated XRD pattern in comparison with experimental results of EDAB at 14.72 GPa using Le Bail refinement

www.manaraa.com

Appendix D Copyright Permission

Copyright Clearance Center RightsLink®

Home | Create Account | Help

ACS Publications
Most Trusted. Most Cited. Most Read.

Title: Pressure-Induced Polymorphic, Optical, and Electronic Transitions of Formamidinium Lead Iodide Perovskite

Author: Pan Wang, Jiwen Guan, Draven T. K. Galeschuk, et al

Publication: Journal of Physical Chemistry Letters

Publisher: American Chemical Society

Date: May 1, 2017

Copyright © 2017, American Chemical Society

LOGIN

If you're a copyright.com user, you can login to RightsLink using your copyright.com credentials.

Already **a RightsLink user** or want to learn more?

PERMISSION/LICENSE IS GRANTED FOR YOUR ORDER AT NO CHARGE

This type of permission/license, instead of the standard Terms & Conditions, is sent to you because no fee is being charged for your order. Please note the following:

- Permission is granted for your request in both print and electronic formats, and translations.
- If figures and/or tables were requested, they may be adapted or used in part.
- Please print this page for your records and send a copy of it to your publisher/graduate school.
- Appropriate credit for the requested material should be given as follows: "Reprinted (adapted) with permission from (COMPLETE REFERENCE CITATION). Copyright (YEAR) American Chemical Society." Insert appropriate information in place of the capitalized words.
- One-time permission is granted only for the use specified in your request. No additional uses are granted (such as derivative works or other editions). For any other uses, please submit a new request.

BACK | CLOSE WINDOW

Copyright © 2018 Copyright Clearance Center, Inc. All Rights Reserved. Privacy statement. Terms and Conditions.
Comments? We would like to hear from you. E-mail us at customercare@copyright.com

www.manaraa.com

Curriculum Vitae

Name: Pan Wang

Post-secondary Education and Degrees:

Wuhan University of Technology
Wuhan, Hubei, China
2003-2007 B.A.

Lanzhou University
Lanzhou, Gansu, China
2008-2011 M.A.

The University of Western Ontario
London, Ontario, Canada
2014-2018 Ph.D.

Honours and Awards:

Lanzhou University First-class Scholarship
2009-2011

Lanzhou University Second-class Scholarship
2008

Wuhan University of Technology First-class Scholarship
2006-2007

Wuhan University of Technology Second-class Scholarship
2003-2005

Related Work Experience

Teaching Assistant
The University of Western Ontario
2014-2018

Assistant Engineer
Northwest Institute for Non-ferrous Metal Research
Xi'an, Shaanxi, China
2011-2013

Publications:

[1] **Wang P.**, Guan J., Galeschuk D., Yao Y., He C., Jiang S., Zhang S., Liu Y., Jin M., Jin C., Song Y., Pressure Induced Polymorphic, Optical and Electronic

www.manaraa.com

Transitions of Formamidinium Lead Iodide Perovskite. *J. Phys. Chem. Lett*, **2017**, 8, 2119.

[2] **Wang P.**, Dong Z., Lei Y., Du Y., Li H., Yang., Nie Y., Ma J., High Selective Oxidation of Alcohols Catalyzed by Cu(II)-Schiff base-SBA-15 with Hydrogen Peroxide in Water. *J. Porous Mater*, **2013**, 20, 277.

[3] Wang X., **Wang P.**, Dong Z., Dong Z., Ma Z., Jiang J., Li R., Ma J. Highly Sensitive Fluorescence Probe Based on Functional SBA-15 for Selective Detection of Hg^{2+}. *Nanoscale Res. Lett*, **2010**, 5, 1468

[4] Dong Z., Dong Z., **Wang P.**, Tian X., Geng H., Li R., Ma J., A Fluorescent Probe for Zinc Detection Based on Organically Functionalized SBA-15. *Appl. Surf. Sci.*, **2010**, 257, 802

[5] Li J., Ren J., Yang G., **Wang P.**, Li H., Sun X., Chen L., Ma J., Li R., Simple and Efficient Deposition of Pd Nanoparticles on Fe_3O_4 Hollow Nanospheres: A New Catalytic System for Methanol Oxidation in Alkaline Media. *Mater. Sci. Eng., B.* **2010**, 172(3), 207

[6] Dong Z., Dong Z., Ren J., Jin J., **Wang P.**, Jiang J., Li R., Ma J., A Quinoline Group Modified SBA-15 INHIBIT Logic Gate with [Cu^{2+} and Zn^{2+}] or [Cu^{2+} and Cd^{2+}] as Inputs. *Microporous Mesoporous Mater*, **2010**, 135, 170.

Presentations

[1] Pressure Induced Polymorphic, Optical and Electronic Transitions of $FAPbI_3$ Perovskite; oral presentation, Toronto, CSC 2017

www.manaraa.com